

2005

Experimental investigation of oscillatory heat release mechanisms and stability margin analysis in lean -premixed combustion

Don H. Ferguson
West Virginia University

Follow this and additional works at: <https://researchrepository.wvu.edu/etd>

Recommended Citation

Ferguson, Don H., "Experimental investigation of oscillatory heat release mechanisms and stability margin analysis in lean -premixed combustion" (2005). *Graduate Theses, Dissertations, and Problem Reports*. 2647.

<https://researchrepository.wvu.edu/etd/2647>

This Dissertation is protected by copyright and/or related rights. It has been brought to you by the The Research Repository @ WVU with permission from the rights-holder(s). You are free to use this Dissertation in any way that is permitted by the copyright and related rights legislation that applies to your use. For other uses you must obtain permission from the rights-holder(s) directly, unless additional rights are indicated by a Creative Commons license in the record and/ or on the work itself. This Dissertation has been accepted for inclusion in WVU Graduate Theses, Dissertations, and Problem Reports collection by an authorized administrator of The Research Repository @ WVU. For more information, please contact researchrepository@mail.wvu.edu.

Experimental Investigation of Oscillatory Heat Release
Mechanisms and Stability Margin Analysis in Lean-Premixed
Combustion

DON H. FERGUSON

Dissertation submitted to the
College of Engineering & Mineral Resources
at West Virginia University in partial fulfillment of the
requirements for the degree of

Doctor of Philosophy

Mechanical Engineering

Mridul Gautam, Ph.D., Chair

Larry Banta, Ph.D.

John Loth, Ph.D.

Gary Morris, Ph.D.

George A. Richards, Ph.D.

Department of Mechanical and Aerospace Engineering

Morgantown, West Virginia

2005

Keywords: Thermoacoustic Instabilities, Laminar Flames, Particle Image Velocimetry
Copyright 2005 Don H. Ferguson

ABSTRACT

Experimental Investigation of Oscillatory Heat Release Mechanisms and Stability Margin Analysis in Lean-Premixed Combustion

Don H. Ferguson

Lean-premixed combustion has become an acceptable means of achieving ultra-low NO_x emissions from land-based gas turbines. Further reduction may be possible through the use of hydrogen augmented or syngas fuels. However, advanced combustor designs developed to utilize these technologies often encounter thermoacoustic instabilities that may significantly hamper engine performance and shorten component life-cycles. These dynamics, although not fully understood, occur through a complex interaction between variations in heat release rate and acoustic properties of the system, and can be exacerbated by variable fuel properties in natural gas and syngas applications.

Theoretical models of thermoacoustic instabilities have attempted to describe the coupling process through reduced-order models that represent mechanisms suspected of contributing to variations in the heat release rate such as variations in fuel/air mixing, fluctuations of heat release through vortex shedding and periodic changes in the flame structure. These reduced-order models have demonstrated only a modest ability at predicting instabilities even in relatively simple systems. This may be due to the inherent complexity from interacting processes, the use of over-simplifying assumptions and the lack of experimental verification.

In this study a simple conical flame, used to reduce the number of contributing mechanisms, is utilized to experimentally evaluate the relationship between the heat release rate and variations in the flame surface area. Results indicated that while area perturbations can adequately describe the magnitude of heat release fluctuations, the area perturbations are not a direct indicator of the phase of heat release needed for closed-loop stability analysis.

Time-resolved particle image velocimetry was used to quantify the near-field acoustics and the dilatation rate field in the pre- and post-flame regions of the flow. Measurements indicated that multi-dimensional acoustics dominate the pre-combustion flow field with radial and axial acoustic velocities of similar magnitudes. Variations in the flame structure potentially due to alternating regions of positive and negative flame stretch were also observed and may result in variations in the flame speed. As it is common to assume constant flame speed and one-dimensional acoustics, the experimental identification of these altered mechanisms may help to resolve discrepancies compared to a number of published reduced-order models.

Acknowledgments

I would like to express my gratitude to all my friends, family and colleagues that have supported my efforts on this work. Specifically I would like to thank Dr. Mridul Gautam of the Mechanical and Aerospace Engineering Department at West Virginia University and a number of individuals and groups within the United States Department of Energy – National Energy Technology Laboratory (NETL) for their support.

Dr. Gautam has been a great friend over the years both academically and socially. I thank him for creating opportunities for me and providing just the right level of guidance to get me through the tough times.

Within NETL I would like to extend my appreciation to the Mr. Richard Dennis, Technology Manager Energy Turbine Program for ensuring financial support for this study. And finally there are several individuals that stand out in terms of supporting this project. I would like to thank Dr. Kent Casleton for preventing me from getting too wrapped up in the “red tape” and allowing me to focus directly on the research project. Dr. Steven Woodruff’s guidance in laser diagnostics and imaging was directly responsible for success of most of this work and is owed a huge gratitude for his assistance. As group manager, Dr. Daniel Maloney has displayed unbelievable patience allowing me to primarily focus on the work contained within this dissertation. Through Dr. Maloney’s advice and encouragement I was able to push through until this document was completed. Finally I would like to express my sincere appreciation to Dr. George A. Richards for his assistance and guidance throughout this work. Dr. Richards is recognized as one of the world’s leading experts on combustion dynamics, and the success of this study depended heavily on his expert technical advice and mentoring.

In all I would again like to extend my appreciation to the U.S. Department of Energy – National Energy Technology Laboratory. Through its funding, patience and masterful technical guidance this research study was possible. In the years to come I hope to continue my career with this organization. I hope to repay this enormous debt I have accrued, and assist in advancing science and technology.

Table of Contents

1	Introduction and Objectives	1
1.1	Introduction	1
1.2	Research Objectives	4
1.3	Overview	5
2	Literature Review	6
2.1	Historical Overview of the Study of Thermoacoustic Instabilities	6
2.2	Mechanisms of Heat Release Resulting in Combustion Instabilities	10
2.3	Flame Front Variations as a Mechanism of Heat Release Oscillations	12
2.4	Experimental Heat Release and Flame Surface Identification	13
2.5	Flow Measurement and Visualization in Combustion	17
2.5.1	PIV Seeding	20
2.6	Modeling of Combustion Systems	21
3	Experimental Setup	25
3.1	Rijke Tube Combustor Assembly	26
3.2	Heat Release Measurement	28
3.3	Acoustic Pressure and Velocity Measurements	30
3.4	Flame Excitation	31
3.5	Flame Surface Recording	33
3.6	Flow Measurement and Visualization	33
3.6.1	Seeding Material	33
3.6.2	Particle Illumination	34
3.6.3	CCD array, lens, synchronization	35
3.6.4	PIV Measurement Accuracy	37
3.7	Data Acquisition System	38
3.8	Measurement Uncertainty	41

4	Two-port / one-port analysis	42
4.1	Modeling Thermoacoustic Systems	42
4.2	Classification of Sources as One- or Two-port Sources	45
5	PIV Analysis and Discussion	47
5.1	Image Acquisition and Analysis (Cross-Correlation Analysis)	47
5.2	Dynamic ranges of velocity and spatial resolution	50
5.3	Application of PIV to Reacting Flows	51
5.4	Tracer Particle Mobility	56
5.4.1	Frequency Response of Tracer Particles	56
5.4.2	Thermophoresis	59
6	Acoustic Velocity Measurement	61
6.1	PIV Measurement	61
6.2	Two-Microphone Technique	65
6.3	Comparison between the two-microphone method and PIV measurement	70
7	General Flame Response	74
7.1	Unstable Flame Response	74
7.2	Stability Boundary Analysis and Flame Excitation	86
8	Flame Surface Area	91
8.1	Review of Flame Surface Variations, Fleifel et al. ³⁹	91
8.2	Experimental Determination of the Instantaneous Flame Surface Area	95
8.2.1	Experimental Results and Discussion	97
8.2.2	Spectral Analysis of Oscillating Flames	100
9	Flame Excitation	119
9.1	Various Modes of Flame Excitation	119
9.2	Self-excited and acoustically-forced flames	121
9.2.1	Flame Front Perturbations	123

9.2.2	Response from acoustically-forced flame	127
10	PIV Results and Discussion	138
10.1	Non-Reacting Flows	138
10.1.1	Laminar, non-reacting flow	138
10.1.2	Acoustically forced, non-reacting flow	141
10.2	Reacting Flows	146
10.2.1	Stable Laminar Flames	147
10.2.2	Unstable, Oscillating Flames	154
10.2.3	Unstable, Oscillating Flames: Phase-Resolved	162
10.2.4	Unstable, Oscillating Flames: Near-field Acoustics	167
11	Conclusions and Recommendations	172
11.1	Summary and Conclusions	172
11.2	Recommendations for Future Work	175
11.2.1	Evaluation of marginal stability boundary	176
11.2.2	Further investigate of periodic variations in the flame structure (flame stretch)	177
11.2.3	Variable fuel prosperities to simulate LNG and coal-derived syngas	177
	References	178

Symbols

A	Area
A_f	Flame surface area
A_f'	Flame surface area perturbations
a_f	Flame surface area ratio ($a_f = A_f'/A_{f_mean}$)
c	Speed of sound
C_{i-j}	Cross spectrum analysis between i and j
c_p	Specific heat with constant pressure
C_{ph}	Wave celerity
D	Duct diameter
D	PIV displacement vector of all particles
d_p	Particle diameter
f or f_{ex}	Excitation frequency
F_{TP}	Thermophoretic force
G	Flame Strouhal number
H_f	Flame height
i_p or ε	Acoustic intensity ratio ($i_p = v'/V_{mean}$)
K''	Lewis number defined term
k	Thermal conductivity
L	Duct length
Le	Lewis number ($Le = k/\rho c_p D$)
n	Interaction index
P	Operating pressure
p'	Acoustic pressure
Q	Total heat release rate
q'	Heat release rate perturbations
Δq_r	Heat of reaction per unit mass of the mixture
R	Burner radius
R	Acoustic reflection coefficient
Ra	Rayleigh Criteria
R_C	PIV mean background correlation

R_D	PIV correlation of particle images
Re	Reynold's number
R_F	PIV fluctuation in background noise
R_{II}	PIV correlation function
s	PIV separation vector in the correlation plane
S_u	Laminar flame speed
T	Period of oscillation
T	Temperature
T	Acoustic transmission coefficient
T_b	Burned gas temperature
T_u	Unburned gas temperature
t	Time
U	Instantaneous radial velocity
u'	Radial acoustic velocity
U_{exit_avg}	Average radial velocity at nozzle exit
u_L	Flame speed
V	Instantaneous axial velocity
v'	Axial acoustic velocity
V_{cl}	Centerline axial velocity
V_{exit_avg}	Average axial velocity at nozzle exit
x or r	Radial coordinate
y or z	Axial coordinate
Z	Impedance
z	Characteristic acoustic impedance
α	Half angle of flame cone
Γ	PIV position vector
γ	Specific heat ratio
δ	Flame thickness (thin sheet approximation)
Δ	Characteristic flame thickness

ϕ	Equivalence ratio
ϕ'	Equivalence ratio perturbations
μ_f	Fluid viscosity
ξ	Axial displacement of the flame surface
ρ	Density
$\Theta_{i,j}$	Phase angle difference between i and j
τ	Time delay
τ_c	Characteristic reaction time for a given species
τ_p	particle relaxation time
ω	Acoustic mode frequency

Chapter 1 Introduction and Objectives

1.1 Introduction

Lean pre-mixed (LPM) combustion has become a recognized means of reducing thermal NOx production in land-based gas turbine engines by lowering peak combustion temperatures. However, the presence of combustion instabilities within the desired operating range has complicated the use of this technology. Combustion instabilities of this sort are not a new phenomenon and have been observed in liquid and solid rockets^{22-25,47}, afterburners³⁰, and industrial furnaces^{76,102}, as well as in land-based turbines^{29,49,65}. Unstable combustion can degrade engine and emissions performance; shorten component life through excessive mechanical vibration and enhanced heat transfer; and in some instances result in severe structural damage.

Combustion instabilities can be characterized as either static or dynamic in nature. Static stability addresses the phenomena of flashback and blow-off, and is of particular interest for lean-premixed combustors operating near the lean flammability limit. Of greater concern due to their unpredictability, and the focus of this study, are dynamic (thermoacoustic) instabilities which manifest themselves as large amplitude, organized pressure oscillations. Acoustic waves propagating in a system may influence the combustion process, locally modifying the heat release rate. Given the proper gain-phase relationship heat release oscillations can feed energy back into the instability resulting in an amplification of the acoustic perturbations (Rayleigh¹⁰⁴). The proper phase relationship was established by the Rayleigh Criteria, which states that for amplification to occur variations in the heat release rate need to be in phase with pressure oscillations; and conversely if the heat release rate is out

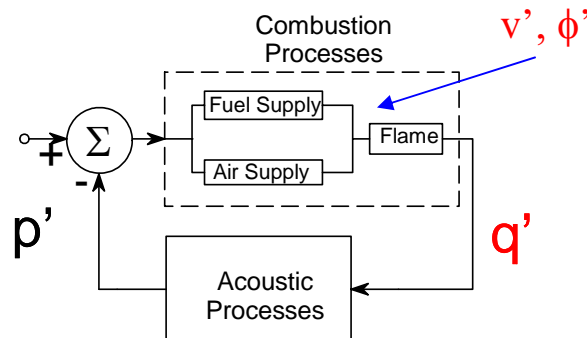


Figure 1.1: System diagram of thermoacoustic instability

of phase with the pressure, the instability is damped. [Figure 1.1](#) provides a systems level diagram of the closed loop feedback cycle common in thermoacoustic instabilities. Nonlinearities within the system may allow the amplitude of the combustion oscillations to grow until a limit-cycle is attained.

Effective mitigation of combustion instabilities depends on a better understanding of the coupling process between acoustics and combustion. A basic criterion for the occurrence of thermoacoustic instabilities exists in the Rayleigh criteria, but it does not provide an explanation of the mechanisms responsible for creating periodic variations in the heat release rate. A significant amount of literature has been devoted to this topic and a number of suspected mechanisms have been identified and include: variations in fuel/air mixing⁶¹, vortex shedding^{45,111,112} and periodic changes in the flame structure^{81,89,116}. However, the inherent complexity of a number of these processes interacting makes determining the impact of individual mechanisms very difficult.

The derivation of analytical models depends on simplifying assumptions of physical processes to describe the flame response to acoustic perturbations. Richards and Janus¹⁰⁷ modeled the combustion process as an unsteady well-stirred reactor. However, the control volume approach taken may neglect some of the dynamic interactions that are likely to occur in reality. A common means of modeling combustion instabilities is with an n - τ analysis which is a linear approach that was originally proposed by Crocco²² to investigate instabilities in rocket engines. The basic concept of the n - τ model is that the flame responds to an acoustic disturbance after some time delay, given by τ , resulting in variations in the heat release rate. The time lag arises from the convective delay associated with premixing, chemical kinetics and other mechanisms such as variations in the flame area, flame position, etc.. The strength of the interaction is governed by the parameter n . This method was later adapted by Culick²⁶ to include nonlinear acoustic effects.

A number of researchers have attempted to describe thermoacoustic instabilities through reduced-order models that utilize transfer functions to relate the heat release fluctuations to pressure or velocity variations within the system^{33,39,64,93,95}. These modeling efforts attempt to describe a phenomenon with a limited number of parameters, focusing on the elements that have the most significant influence on the process. Reduced-order models, unlike CFD models that are system specific, provide a general relationship between the various physical processes that are involved in driving the instabilities. However, studies based on CFD analysis like those of Hobson⁴⁹, Kruger et. al⁶⁴, Hubbard and Dowling⁵¹ and Pascheriet et.al.⁹¹ have provided some insight into the influence of various mechanisms.

Fliefil et al.³⁹ utilized the n - τ analysis to develop a reduced-order model aimed at describing the response of a premixed flame to acoustic velocity perturbations. This model considered the interaction between a one-dimensional acoustic field and a laminar cone-shaped flame (i.e., Bunsen flame). Fliefil et al.³⁹ showed that the acoustic velocity perturbations (v') produce an oscillation in flame surface area (A_f') with a corresponding oscillation in heat release. The heat release oscillation was calculated assuming a constant flame speed over the variable flame surface area, however an experimental validation of the model was not provided. In an earlier study, Blackshear¹¹ also considered flame surface area as the source of variable heat addition and derived a relationship between inlet velocity perturbations and flame surface area based on one-dimensional axial flow. The phasing of A_f' with v' was found to depend primarily on flame speed and appeared to be independent of the magnitude of the velocity perturbations.

More recently, Lee and Lieuwen⁶⁸ have investigated the near-field acoustic behavior of a Bunsen flame. These authors show that if a plane wave arrives at a conical flame, an evanescent wave is formed which decays exponentially in amplitude with distance from the flame and contains an axial as well as a radial component. In the numerical analysis presented by Lee and Lieuwen⁶⁸, radial acoustic velocities were shown to be 70% of the longitudinal component. These large amplitudes suggest that near-field acoustic effects may need to be included in the thermoacoustic models.

Typical transfer functions describe the flame response to an acoustic disturbance as a single-port model in which variations in heat release result solely from a fluctuating inlet velocity (often considered to be one-dimensional) to the flame. Four-pole, or two-port, models such as that of Paschereit and Polifke⁹² have been used to represent the thermoacoustic system as a network of acoustic elements. These transfer matrices describe the change in the acoustic state variables (velocity and pressure) across each element and treat the burner and flame as a black box in which its transfer function must be found numerically (Kruger et.al.^{64,65}) or experimentally (Paschereit and Polifke^{92,93}, Schuermans et.al.¹¹⁴). Ducruix et al.³³ and Khanna⁵⁸ derived empirical transfer functions relating one-dimensional acoustic velocity to the flame response of relatively simple burner geometries. However, even in these relatively simple systems discrepancies existed between theoretical flame response models and experimental results, and in both studies the effects of near-field acoustics were thought to be responsible for these discrepancies to some extent.

The aforementioned studies emphasize the need for experimental investigations of the mechanisms that drive thermoacoustic instabilities. Although most practical burners rely on turbulent three-dimensional flames, these systems tend to be too complex to analyze. By studying simplified systems in a well-controlled environment, it is possible to isolate particular phenomena contributing to fluctuations in heat release. This could then lead to a greater understanding of the coupling process between heat release variations and combustor acoustic properties that creates the feedback cycle that drives thermoacoustic instabilities. Demonstration of this procedure on a simple burner can identify difficulties and limitations in carrying out the complete procedure in more practical problems.

1.2 Research Objectives

The primary focus of this study is to improve the fundamental understanding of the physical processes involved in driving thermoacoustic combustion instabilities in lean-premixed combustion. This is to be accomplished through an experimental analysis of specific mechanisms believed to influence the combustion process and its interactions with the acoustic characterizations of the combustion chamber. In particular, perturbations in the flame surface area are measured and compared to variations in the heat release rate in order to evaluate the predictive capability of the model presented by Fliefil et al.³⁹. Additional mechanisms are considered by obtaining two-dimensional, phase resolved velocity vector maps of the near-flame flow field. Through the time resolved definition of the velocity field, it was possible to experimentally evaluate the effects of the near-field acoustics on the response of the flame and compare these data to that of the theoretical study of Lee and Lieuwen⁶⁸.

Along with comparisons made to the two theoretical studies mentioned above, the experimental analysis performed in this work provided an opportunity to form generalizations with regards to current practice of using reduced-order models to predict the onset and strength of thermoacoustic instabilities. These models, often limited to a single input and known as one-port models, have shown promise in describing combustion instabilities, however their capability is somewhat limited. In this study experimental comparison between self-excited and acoustically-driven flames leads to recommendations for input parameters and empirically derived transfer functions of reduced-order models.

1.3 Overview

In Chapter 2, past works in the area of combustion instabilities are discussed emphasizing the complexity of the problem due to interactions of multiple mechanisms. In order to isolate heat release perturbation mechanisms, steps were taken to prevent equivalence ratio fluctuations and swirl, and will be discussed along with the rest of the experimental setup in Chapter 3. The closed loop feedback system that drives thermoacoustic instabilities is described in Chapter 4 along with a consideration of the general form of the reduced-order models that are commonly employed to study combustion dynamics. In Chapters 5 and 6 a more detailed discussion of velocity measurements is presented, with Chapter 5 focusing on the use of particle image velocimetry (PIV) to measure the pre- and post-flame flow field in an oscillating flame. Chapter 6 provides a comparison between the direct method of phase resolved PIV and the indirect use of acoustic pressure measurements to obtain acoustic velocity.

The inherent instabilities of the flame in the Rijke tube combustor are discussed in Chapter 7 and the measured phase-gain relationship between variations in the heat release rate and acoustic properties is presented. Drawing on the findings presented in the previous chapter, Chapter 8 describes the methodology utilized to measure the flame surface area and its relation to the heat release rate and ultimately the overall response of the flame. Chapter 9 discusses the differences between acoustically-forcing a flame compared to one that is self-excited and how the use of forced flames may affect modeling considerations. Finally in Chapter 10 the results obtained from the flow field measurements are presented along with a discussion on the impact of multi-dimensional acoustics. Chapter 11 provides a brief summary of the study along with conclusions drawn from the experimental analysis and recommendations for future work.

Chapter 2 Literature Review

This chapter attempts to provide a historical perspective on the study of thermoacoustic instabilities that has been underway for more than two centuries. Initial efforts in the 1700's were directed at advancing the fundamental understanding combustion. As industry began relying more and more on combustion-driven processes, understanding instabilities become more of a necessity than a luxury. Through the years, combustion instabilities have been observed in devices such as furnaces, rocket engines, ramjet engines, afterburners and gas turbine engines. Current concerns regarding combustion dynamics revolve around the land-based gas turbine engine used in the power generation industry.

Efforts to reduce environmentally harmful exhaust emissions from gas turbine engines have shown lean pre-mixed combustion to be a promising technology. Unfortunately its wide spread use has been complicated by the unpredictable presence of combustion instabilities. The literature review for this study tends to focus on first gaining an understanding of the fundamental concepts relating to thermoacoustic instabilities by taking a historical look at a number of past works. Through this analysis several predominant physical processes, or mechanisms, were identified that are believed to contribute to the occurrence of these instabilities. Then, as this is primarily an experimental study, literature regarding the measurement of the effects of these processes is discussed along with the application of advanced experimental techniques. Finally, the use of experimental data, as well as theoretical relationships, to derive predictive models is reviewed along with mention of how these models improve our understanding and ultimately the control of thermoacoustic instabilities.

2.1 Historical Overview of the Study of Thermoacoustic Instabilities

One of the first recorded studies of combustion-driven oscillations was published by Higgins⁴⁸ (1777), who produced what has come to be known as organ-pipe oscillations by enclosing a hydrogen diffusion flame in a large tube open at both ends. For certain positions of the flame in the tube and for certain lengths of the tube, the flame could be made to “sing”, or oscillate. The name “organ-pipe oscillation” stems from the fact that the enclosed instabilities vibrate in the same manner as the gas column in a sounding organ pipe (Putnam and Dennis⁹⁹⁻¹⁰¹). Using a similar apparatus as Higgins⁴⁸, Rijke¹⁰⁹ found that by inserting a heated wire mesh gauze into the lower half of an open-ended vertical tube, strong oscillations could be obtained with the maximum intensity occurring when the distance of

the gauze from the lower end of the tube was approximately one-fourth of its entire length. Rijke¹⁰⁹ attributed this phenomenon to the rising convection current expanding in the region of the heated wire mesh and compressing downstream from the heater due to the cooling of the pipe walls. While this explanation provided some insight on the occurrence of organ-pipe oscillations it did not provide detail into the heat exchange mechanism causing the instabilities (Feldman³⁸). Although Higgins⁴⁸ had originally demonstrated the use of an open-ended tube for studying combustion oscillations, the occurrence of oscillations in such a device induced by the placement of a heat source within the tube is referred to as the Rijke phenomena.

The Rijke tube provides an elementary example of thermoacoustic oscillation of the organ-pipe type and has been used extensively in both theoretical and experimental studies (Carrier¹⁷; Yoon et al.¹²⁴; Friedlander et al.⁴¹; Maling⁷⁵; Neuringer and Hudson⁸⁷). Feldman³⁸ provided an extensive review of literature on Rijke thermoacoustic oscillations which included many of the papers listed above. The author noted that although a considerable amount of effort has been directed towards this phenomenon, the detailed heat transfer mechanism causing large amplitude oscillations has yet to be quantified.

A qualitative explanation of this phenomenon was offered by Lord Rayleigh¹⁰⁴. The Rayleigh Criteria, as it has come to be known, states that for a heat-driven oscillation to occur there must be a varying rate of heat release having a component in phase with the varying component of the pressure. It can be expressed mathematically as the following

$$Ra = \int_0^T q'(t)P'(t)dt \quad (2.1)$$

where Ra is the Rayleigh Index, T is the period of oscillation, q' is the varying rate of heat release, P' is the oscillating component of the pressure, and t is the time. When Ra is positive the pressure instability is amplified by the heat release, and when Ra is negative the perturbations are damped.

Organ-pipe oscillations, such as those that occur in the Rijke tube, produce standing waves and for a tube open at both ends the pressure nodes exist at the inlet and outlet for the fundamental mode and the maximum pressure occurs at the center, Figure 2.1. Conversely, the velocity has a node at the center and antinodes (maximums) at the ends, thus the pressure and velocity are 90° out of phase. Assuming that the heat release rate varies in phase with the acoustic velocity, the Rayleigh Index defined in Equation 2.1 is positive in the lower half of the tube and negative in the upper half

thus sustaining self-excited thermoacoustic oscillations when the heat source is added in the lower half, and damping oscillations when the source is located in the upper half.

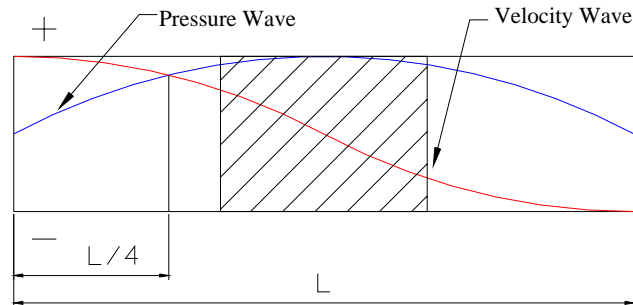


Figure 2.1: Velocity and pressure waves in an open-ended tube.

Putnam and Dennis¹⁰¹ reviewed organ-pipe oscillations in combustion systems in which consideration was given to “singing flames” of the Higgins type, flash tube studies, gauze tones, rocket-shaped burners (gas and solid fuels), refractory tube combustion and ram-jet type combustors. In their own experimental study, Putnam and Dennis¹⁰⁰ investigated organ-pipe oscillations in three burner configurations. A general explanation of the oscillations was obtained for all three cases by considering the system acoustics and heat release location. They demonstrated that in order to sustain oscillations the phase difference between rate of heat release and the pressure fluctuations had to be less than $\pi/4$ and the point of heat release must be “near” the point of maximum pressure in the combustion tube. In response to the second stipulation, the authors suggested that for maximum effectiveness and to overcome damping effects, the heat should be released in the middle third of the pressure wave. This region is indicated by the hatchmarks in Figure 2.1. This assumes that the heat can be arbitrarily added to the combustion tube and is not dependent on the velocity wave. If in fact the heat release rate were subject to the acoustic velocity, then one would expect the largest amplitude thermoacoustic oscillation to occur at $L/4$, as in the Rijke experiment.

In a subsequent paper, Putnam and Dennis⁹⁹ developed a mathematical expression for the driving criteria which depended on: 1) variation of flame-front position with time, 2) flow of gases relative to the flame front, 3) heat release rate of the burning gases, and 4) relation of the heat release rate to the pressure variation along the tube. The model assumed all of the energy from combustion was released at a single point and in general, was a model of the Rayleigh criteria based on determining

the theoretical phase difference between the pressure and heat release. Damping and Lewis number effects were neglected, and no reference was made to the heat release variation mechanisms. However, this study supported the findings that for oscillations to be driven at the peak amplitude, the heat release must occur near the pressure antinode.

Much of our present day understanding of combustion instabilities stems from research initiated in the 1950's and 60's to support the development of advanced rocket motors. Crocco et al.²³ observed instabilities in liquid fuelled rocket motors and applied a time lag theory to predict the effect of the combustion chamber length on the stability boundary. However, the authors noted the difficulty in generalizing the theoretical model developed for this study. The same time lag theory was used by Crocco and Mitchell²⁴, but the oscillations were considered to be nonlinear and possess a limit cycle behavior. Analysis of the nonlinear perturbations resulted in a nonlinear ordinary differential equation governing the shape of the nonlinear periodic wave.

As previously noted, modern stationary gas turbines use lean premixed combustion as a means of meeting restrictive emission limits and designers must address thermoacoustic instabilities. Keller⁵⁶ stated that due to the vast differences between conventional diffusion style and low-NO_x combustors, instabilities occurring in the latter are actually similar to those of rocket motors. Therefore, much of the continuing effects have resembled those of previous rocket motor studies, in particular the use of the time lag theory, which primarily states that thermoacoustic oscillations occur when the time scale of the acoustic pressure field, τ_1 , is similar to that of the combustion characteristic time, τ_2 . In premixed combustion, the characteristic time combines mixing, transport and chemical kinetics.

Richards and Janus¹⁰⁷ investigated combustion instabilities in a rig designed to closely resemble actual gas turbine conditions. A simple time lag model was adopted to experimentally characterize instabilities produced by a premix fuel nozzle. The model suggested that the nozzle velocity played an important role in the stability of the combustor. Tests conducted at conditions between stable and unstable combustion were studied and resulted in intermittent perturbations. Thus, the authors emphasized the need to identify stability boundaries in new combustors. Studies have also been performed on full-scale gas turbine engines (Konrad et al.⁶³; Scholtz and Depietro¹¹³; Hobson et al.⁴⁹). However, these investigations are often system specific and stress the need for more accurate models to help predict the occurrence of instabilities and the stability boundaries.

2.2 Mechanisms of Heat Release Resulting in Combustion Instabilities

Published literature presents evidence of a variety of mechanisms to describe the process that occurs over the characteristic time, τ_2 , which results in a fluctuation of the heat release. Theoretical and experimental studies investigating mechanisms such as: variations in fuel / air mixing and fuel composition, vortex shedding and periodic changes in the flow and flame structure have been performed and will be discussed below.

Equivalence ratio fluctuations, ϕ' , were considered to be the primary driving mechanism by Lieuwen et al.⁷⁴. They concluded that a coupling between the combustion chamber and fuel / air premixer acoustics produces small changes in equivalence ratio, and at lean conditions this could have a significant impact on various combustion characteristics (flame speed, flame temperature, chemical time, etc.), thus causing large fluctuations in the heat release rate. Similar findings were reported by several other authors (Mongia and Dibble⁸⁰; Shih et al.¹¹⁵; Oran and Gardner⁸⁸; Darling et al.²⁹) who also considered equivalence ratio variations alone or in combination with flow instabilities as the primary mechanism for fluctuations in the heat release rate.

Peracchio and Proscia⁹⁵ utilized the methodology of Culik^{26,27} to create a model describing the coupling of linear acoustics and nonlinear heat release. The acoustic model is considered to be one-dimensional and relates the acoustic pressure and velocity through the acoustic impedance at the combustor inlet. The nonlinear heat release rate is coupled to the acoustic velocity via the equivalence ratio which is said vary with the velocity. In a simplifying assumption, the influence of a variable flame front on the heat release was not considered. Bode analysis on the open-loop transfer function that described the coupled system provided a “critical gain value” that could be used to evaluate system stability. This critical gain value depended on a number of parameters including a variable delay that included convective and chemical times, an acoustic damping term, frequency and acoustic impedance. Fairly good qualitative agreement was obtained between model and experimental heat release as a function of acoustic velocity. However, the model was inconsistent on its prediction of the collective time delay and over predicted the limit cycle frequency.

The presence of large-scale coherent structures in the flow can act to enhance the instability if the shear layer instability frequency matches the acoustic frequency. This was shown in Schadow et al.¹¹¹ by acoustically forcing a ducted jet at its resonant frequency and altering the flow rate to obtain a match with the vortex merging frequency in the shear layer. It was found that the size of the stabilized vortex is controlled, to some degree, by the acoustic frequency. The vortices will be smallest when the

acoustic frequency equals the initial vortex shedding frequency and will be largest when the acoustic frequency is near the preferred-mode or vortex merging frequency.

The vortices do not significantly alter the acoustic field in a combustor, however when combustion is present they can feed back and affect the heat release in a variety of ways (Schadow et al.¹¹²). Large-scale coherent structures have the capability of convecting heat away from the primary reaction zone (Poinsot et al.⁹⁷). In addition, the shedding of vortices due to combustor and nozzle geometries can result in the periodic dilution of the unreacted mixture with hot combustion products leading to a sudden change in the heat release (Schadow et al.¹¹², 1992). Flow instabilities leading to fluctuations in the reaction rate caused by a similar mixing process were considered by Keller⁵⁶. By combining schlieren photography and natural C_2 chemiluminescence, Poinsot et al.⁹⁷ were able to determine the phase relationship between vortex formation and heat release. They demonstrated that the interaction between several vortices results in a sudden heat release, and when coupled with the system acoustics results in flame instability. A short note presented by Gutmark et al.⁴⁵ supported this result through an experimental study of a step expansion combustor in which the maximum pressure oscillation amplitude was obtained when the acoustic frequencies were within 20% of the vortex merging frequency.

Conventional modeling efforts are often limited to one-dimensional acoustics. Lee and Lieuwen⁶⁸ presented a numerical model of the acoustic near-field flow characteristics in which a plane disturbance was imposed on the flow upstream of the flame. The authors found the acoustic velocity in the vicinity of the flame, especially at the base of the flame, to be two-dimensional having both an axial and radial component. This would suggest that radial acoustics may alter the flame surface in a manner that is comparable to the effects of the axial acoustic mode.

A study by Richards and Robey¹⁰⁸, although more closely related to the system acoustic properties than heat release mechanisms, developed a simplified model of a variable geometry fuel injection system to evaluate its impact on the dynamic response of the combustion system. Acoustic transfer functions were used to relate acoustic pressure and mass flow at various points along the nozzle, and a dynamic model for the premixer orifice flow was developed from a linearized momentum balance. Although not done, it was suggested that open-loop Bode or Nyquist analysis could be performed as a means of evaluating the system stability. The authors experimentally showed that by changing the acoustic impedance of the fuel system it was possible to significantly modify the phase of fuel fluctuations and under certain conditions enhance the stability of the combustor.

2.3 Flame Front Variations as a Mechanism of Heat Release Oscillations

Variations in the flame front, and subsequently the heat release, resulting from interactions with the plane acoustic waves have been considered by a number of authors (Merk⁷⁷; Mugridge⁸²; Fleifil et al.³⁹; Blackshear¹¹). Equation 2.2 describes the total heat release rate $Q(t)$ and shows its dependence on the flame surface area,

$$Q(t) = \rho S_u A_f \Delta q_r \quad (2.2)$$

where ρ is the mixture density, S_u is the laminar flame speed, A_f is the flame surface area and Δq_r is the heat of reaction per unit mass of the mixture.

An analytical model developed by Fleifil et al.³⁹ predicted variations in the heat release rate through perturbations in the flame surface area brought on by oscillations in the combustor inlet velocity. Their model indicated that the flow Strouhal number, $\omega R/u$ (where ω , R , and u are defined as the acoustic mode frequency, the tube radius and the mean combustor inlet flow, respectively), determines the amplitude of the flame surface oscillation while the flame Strouhal number ($\omega R/S_u$), where the laminar burning velocity (S_u) replaces the mean flow, defines its shape. Thus variations in the heat release rate were believed to be in phase and agree quantitatively with variations in the global flame surface area.

Several other authors have considered flame surface area variations as the mechanism controlling the heat release. In an early study presented by Chu²⁰, the author presented a physical interpretation of the Rayleigh Criteria through an analogy with a piston driving a mechanical spring-mass system. The physical model was then used as a basis for a purely analytical solution that demonstrated how small amplitude disturbances could be amplified by fluctuations in the rate of heat release from the heat source. Chu²⁰ noted that since the rate of heat release from a flame front is controlled, in part by the flame surface area, any change in this variable would result in a change in the heat release rate. Blackshear¹¹ presented a model indicating that velocity perturbations induced by a wave causes a change in the flame area that if in phase with the existing acoustic wave could drive the instability. Studies presented by Markstein⁷⁶ and Kaskan⁵⁵ provide a similar argument for explaining that variations in the flame surface area contributed to thermoacoustic instabilities. In their study of the effects of coherent structures on flame instability, Schadow et al.^{111,112} noted that as vortices are shed they convected downstream causing the flame surface to become distorted. This distortion

results in an oscillatory change in the flame surface area and hence results in an oscillatory heat release rate. Unfortunately, none of these studies provide an experimental verification of the effects of flame surface area variations on the heat release

Models developed on the basis of Equation 2.2 are often done so under the assumption of a constant laminar flame speed. Unfortunately the presence of flame stretch complicates this approximation. Few flames exist without the influence of flame stretch and strain on the surface. Law⁶⁷ classified the influence of strain on the flame surface in two categories: hydrodynamic stretch and flame stretch. Hydrodynamic stretch was considered to occur from an interaction of the normal and tangential velocity gradients at the flame surface. This interaction produces a change of the flame surface and the volumetric burning rate due to a distortion of the flame topography and displacement of the flame surface. Flame stretch occurs when the tangential velocity modifies the heat and mass diffusion and the mass flux of the reactants. The temperature and concentration profiles in the reaction zone are modified by this action, subsequently altering the burning intensity, reaction temperature and completeness.

Law⁶⁷ also noted that except in highly strained cases, stretch has little influence on the reaction zone. In Bunsen flames, flame stretch may be more prevalent in the highly curved tip of the flame more so than along the sides. However, this study focuses on relatively low-frequency oscillations resulting in flame surface perturbations that are much larger than the flame thickness. In addition, by maintaining a laminar flow into the reaction zone the effect of turbulence with length scales on the order of the flame thickness can be lessened.

2.4 Experimental Heat Release and Flame Surface Identification

An experimental evaluation of the impact of flame surface area variation on the rate of heat release requires the measurement of both these parameters. Unfortunately, there is no direct method to quantify either the surface area or heat release rate, and thus they must be inferred from other measurable parameters. This necessary approach assumes an implicit correlation between the particular flame measurables and the rate quantities in question (Najm et al.^{85,86}). A detailed understanding of the reaction mechanisms has provided a means of correlating both chemical (e.g. chemiluminescence and laser-induced fluorescence) and physical (e.g. flow dilatation and temperature) measurements to specific events, such as major heat release reactions, in the flame. A majority of these studies were performed in the fifties and sixties, where overall flame emission was correlated to the reactant flow rates (Gaydon⁴²).

Quantitative analysis of the flame surface area will most likely require a clear definition of the flame surface. One common approach is to define the flame based on temperature within various regions. Using this methodology the flame can be divided into two zones (Borghi¹⁴; Turns¹²⁰): the preheat zone and the reaction zone. The reaction zone is the region in which all of the exothermic chemical reactions (heat release) take place and is often approximated to be a thin-sheet. If the reaction zone were considered “thick”, variations in the release of chemical energy within its bounds could occur without altering the flame surface area. Prior to entering the reaction zone, the unburned mixture passes through the preheat zone where it is heated to the ignition temperature by diffusion and convective processes. Gaydon and Wolfhard⁴² define the start of the preheat zone as the position where the temperature has risen just 1% with reference to the temperature rise in the zone, $T_i = T_u + 0.01*(T_b - T_u)$. Here T_i is the temperature at the upstream boundary of the preheat zone, T_u is the unburned mixture temperature and T_b is the temperature of the burned gases (for an ideal case, this would be the adiabatic flame temperature). For the thin-sheet approximation to be true the temperature of the mixture must increase rapidly to the point of ignition and the subsequent reaction must progress quickly. Borghi¹⁴ provides the following empirical relationship for the flame thickness

$$\delta = K'' * \tau_c * u_L \quad (2.3)$$

where K'' is a Lewis Number defined term ($Le = k/\rho c_p D$ – ratio of thermal diffusivity to mass diffusivity), τ_c is the characteristic reaction time for the given species, and u_L is the flame speed. Equation (2.4) is commonly used to determine the flame or “characteristic” thickness and was first given by Zeldovich (Jarosinski⁵³) and later by Williams¹²³ and Lewis and von Elbe⁷⁰.

$$\Delta = k / c_p \rho_u S_L \quad (2.4)$$

where k , c_p , ρ_u and S_L are the thermal conductivity, specific heat with constant pressure, density of the unburned mixture, and the laminar flame speed, respectively. Turns¹²⁰ provided a similar relationship except the thickness was determined to be twice that given by equation (2.4), 2Δ . However, unlike the previous authors, Turns¹²⁰ assumed a linear temperature profile across the flame front. Using the

definition of the preheat zone given by Gaydon and Wolfhard⁴² and Equation (2.4), the preheat zone thickness was determined to be approximately 4.6Δ .

Jarosinski⁵³ derived a simple experimental method for determining the flame thickness on the basis of the energy equation. Given the temperature profile of the flame, the flame thickness can be approximated by the following

$$\delta = 2 \frac{(T_b - T_u)}{(dT/dz)_{\max}} \quad (2.5)$$

where the $(T_b - T_u)$ and $(dT/dz)_{\max}$ are the measured values of the temperature difference and the maximum temperature gradient, respectively. In general the thin-sheet approximation depends on a short characteristic time lending itself to a steep temperature gradient and a thin reaction zone. As long as the reaction times are short for the major heat producing reactions, the thin-sheet approximation will be valid.

Unfortunately, highly resolved instantaneous temperature measurements over a global region such as a reacting flow field are not practical, unless the steep temperature gradient that makes up the transition between the pre-heat and reaction zone can be inferred from other measures. An option is to use optical techniques based on the measurement of flame emittance from combustion products. These techniques have been utilized as a means to identify the flame surface, as well as the global heat release within hydrocarbon flames by correlating their recorded intensity with fuel flow rates (Najm et al.^{85,86}; Dandy et al.²⁸; Haber et al.⁴⁶; Gaydon and Wolfhard⁴²; Samamiego et al.¹¹⁰). Chemiluminescence occurs in the natural visible and near-ultraviolet range with the primary emitters from hydrocarbon flames considered to be CO_2^* , OH^* , CH^* and C_2^* , with weaker emissions from HCO^* and CH_2O^* . The asterisk (*) indicates molecules in their excited state, as opposed to their ground state. Meaningful interpretation of chemiluminescence measurements requires knowledge of kinetics leading to the formation of the excited state, the exact identity and spectroscopy of the excited state, and the kinetics of physical quenching reactions, which may compete with spontaneous emission to deactivate the excited state (Najm et al.^{85,86}).

Samamiego et al.¹¹⁰ (1995) provided a numerical analysis that included the effects of strain on laminar and turbulent premixed flames supporting the use of CO_2^* as an indicator of fuel consumption and heat release rates. The favored mechanism for the formation of CO_2^* is $\text{CO} + \text{O} + \text{M} \rightarrow \text{CO}_2^* + \text{M}$. While marginal correlation was obtained for fuel consumption, a monotonic

relationship was observed between the predicted heat release rates and intensity of CO_2^* chemiluminescence for all cases considered. However, CO_2^* chemiluminescence occurs over a very broad range, 340-600 nm (Samamiego et al.¹¹⁰), thus a number of narrow band filters would be needed to prevent concurrent measurement of OH^* , CH^* and C_2^* emissions.

Alternatively, OH^* and CH^* chemiluminescence occurs over a very narrow band, 306.4nm (near-ultraviolet) and 431nm (visible), respectively (Gaydon and Wolfhard⁴²). The primary source reaction for OH^* is considered to be $\text{CH} + \text{O}_2 \rightarrow \text{OH}^* + \text{CO}$ (Becker et al.⁹), however Haber et al.⁴⁶ also proposed $\text{HCO} + \text{O} \rightarrow \text{CO} + \text{OH}^*$. This second reaction is somewhat questionable as it is not commonly used and Dandy and Vosen²⁸ suggest the reaction produces ground state OH as opposed to the excited state. A comparison study between the total mean reaction rate and OH^* chemiluminescence measurements in an unstable flame conducted by Lee et al.⁶⁹ showed good agreement.

For CH^* , the primary mechanism is considered to be $\text{C}_2\text{H} + \text{O} \rightarrow \text{CH}^* + \text{CO}$, however Najm et al.^{85,86} advised caution when studying highly turbulent flames where experimental results for CH^* indicated a breakage in the primary flame surface that was not evident in planar laser induced fluorescence (PLIF) images of HCO. However, HCO PLIF emissions (360 nm) are particularly weak, requiring filtration to reject as much natural flame emission as possible and frame averaging to obtain a usable image, thus the simplicity of OH^* and CH^* measurements make an attractive and useful alternative. Additionally, the flow of carbon into CH^* is negligible for methane flames and thus may not be an appropriate indicator of the total heat release (Najm et al.⁸⁶).

Laser induced fluorescence (LIF) offers an alternative spatially resolvable method to natural chemiluminescence and can potentially reveal more detailed information. Unlike chemiluminescence, LIF measures the concentration of a species in the ground state and in the absence of the quantity being measured the signal is zero (Najm et al.⁸⁵). This technique can easily be extended to a planar geometry (PLIF), thus allowing for the 2-D isolation of specific regions within the flame, which is not possible in chemiluminescence.

Lee et al.⁶⁹, Najm et al.^{85,86}, and Paul et al.⁹⁴, provide excellent studies of PLIF imaging of OH, CH and HCO. OH PLIF was successfully used by Lee et al.⁶⁹ to identify flame structure in stable and unstable methane-air flames. However, it was also noted that unlike OH^* , the long-lived, ground state OH exists not only in the flame front but extends into the post-flame region. This may act to "blur" the heat release and the flame structure, especially in highly unstable or wrinkled flames. In stable and

moderately unstable flames, the absence of OH in the pre-heat zone helps to identify the leading edge of the flame front.

CH PLIF has often been used to mark the surface of the flame due to its relatively short life span. However, like CH*, CH PLIF results obtained by Paul et al.⁹⁴ and Najm et al.⁸⁵ indicated a breakage in the primary flame surface when a vortex pair was imposed on the flame. This breakage was not evident when the flame was imaged by HCO PLIF. For this reason, these authors suggested the use of HCO PLIF as a flame marker and additionally demonstrated excellent temporal and spatial correlation between HCO and heat release rate. The latter statement was believed to be due to 1) the rapid decomposition of HCO, and 2) HCO production accounts for a substantial fraction of the carbon flow. However, the weak signal strength of HCO PLIF due in part to the rapid decomposition reaction and quenching of the excited species, requires additional filtration and image averaging. This makes the identification of the instantaneous heat release and flame front locations in turbulent or unsteady flames difficult, if not impossible. Both Paul et al.⁹⁴ and Najm et al.⁸⁵ addressed this issue by considering the concentration product of species responsible for the production of HCO.

The reaction $\text{CH}_2\text{O} + \text{OH} \rightarrow \text{H}_2\text{O} + \text{HCO}$ is a major production path for HCO (Paul et al.⁹⁴). Thus by obtaining single pulse images of CH₂O and OH concentrations, which are both much stronger signals than HCO, and a pixel-by-pixel product of these two images, it was possible to derive an image that was closely correlated to the temporal and spatial heat release rate and flame front topography.

2.5 Flow Measurement and Visualization in Combustion

As part of this study, the author was also interested in characterizing the unsteady flow field in an oscillating flame. Conventional flow measurements that have been used in a combustion research can be divided into qualitative and quantitative methods. Schadow et al.¹¹² reviewed a number of experimental papers focusing on the role of large-scale coherent structures in the combustion process that utilized a variety of techniques, including: hot-wire anemometry, Planar Laser Induced Fluorescence (PLIF), Schlieren photography, spark shadowgraphy, and Laser Doppler Velocimeter (LDV).

Qualitative methods provide a means of visualizing the reacting and non-reacting flow fields and may consist of schlieren photography, spark shadowgraphy, laser sheet visualization and high speed photography. Poinot et al.⁹⁷ used spark Schlieren photography to visualize the flow field in a step combustor. The recorded images provided a visual representation of the flame and flow field at specific instances in the oscillating cycle and were correlated with simultaneously measured heat release

through C_2^* emissions and pressure to obtain a phase relationship between these parameters. Results indicated that the time lag between the vortex formation and the maximum heat release was about $\frac{1}{2}$ of the period of oscillation, and that between the vortex formation and the pressure oscillation maximum was $\frac{1}{4}$ of the period. An alternative approach was taken by Schadow et al.¹¹² in which the fluid dynamic-combustion interaction was visualized by PLIF imaging of in situ OH radicals. Phase-locked average images revealed that the initial reactions occur in the circumference of the vortices and are convected downstream as the reaction reaches the vortex core. While these qualitative techniques may yield estimates of desired parameters and instantaneous images of the flow and flame quality, they fail to provide a detailed quantitative measurement of the flow field that can be compared to other sampled parameters.

Quantitative flow measurements provide the level of detail needed to understand the flow-combustion interactions and build / verify models of this behavior. However the use of conventional techniques is complicated by the existence of a reacting flow field. Hot-wire anemometry has been used in a number of studies (Gutmark et al.⁴⁵; Blackshear¹¹; Schadow et al.¹¹²) but is limited to isothermal flows. Thus flow measurement must be performed in the absence of combustion with the assumption that little change occurs in a reacting environment. The effect of frequency matching between the acoustics and vortices can be determined by acoustically forcing the flow field (Schadow et al.¹¹¹).

Techniques do exist that allow for measurement of the fluid dynamics during combustion. Wagner and Ferguson¹²¹ utilized Laser Doppler Velocimeter (LDV) in an attempt to measure the laminar flame speed in a premixed Bunsen flame. In LDV the flow is seeded with highly refractive material capable of accurately following the flow and a point velocity is obtained by determining the Doppler shift between the scattered laser light and a reference beam. Keller and Saito⁵⁷ investigated the flow-flame interaction through the use of LDV in a pulse combustor. Alumina Oxide (Al_2O_3) powder of approximately $1.0 \mu m$ in size, capable of a frequency response in excess of 1 kHz, was used to seed the combustor flow operating at a frequency of 50 Hz. Measurement of the velocity variance distinctly resolved the large mean velocity fluctuation in the reacting, pulsing flow.

The measurement of the acoustic velocity for use in the development of transfer functions to describe the relationship between the heat release fluctuations and the velocity variations for a given burner geometry using LDV was performed by Ducruix et al.³³ Due to the planar nature of the acoustic wave, its velocity was measured at a single point above the burner exit, while global CH^* emissions of the flame were recorded to indicate heat release. The developed transfer function was

intended to support the model developed by Fleifil et al.³⁹. At moderate and high frequency values the predicted phase difference were significantly smaller than measured.

Methods such as hot-wire anemometry and LDV are point measurements. Thus in order to map an entire flow field a large number of measurements would be needed. This can be quite time consuming and unless the flow is reproducible, only generalized results could be obtained. Additionally, hot-wire anemometry is an intrusive measurement which can influence the fluid dynamics-combustion interaction.

In addition to velocity, the measurement of vorticity, strain rate and dilatation could provide insight into the effect of flame stretch on combustion instabilities. These parameters require the measurement of instantaneous velocity gradients in at least two dimensions, and the spatial resolution of the velocity measurements must be sufficient to resolve the integral length scales (Reuss et al.^{105,106}). Particle Image Velocimetry (PIV) is a flow measurement technique that allows a large portion of the flow field to be evaluated simultaneously. Like LDV, the fluid motion is made visible by adding small tracer particles. The particles are illuminated by a laser sheet pulsed over a short time interval and the subsequent images are recorded on either film or a CCD array. The displacement of the particles between the light pulses is determined by a correlation analysis of the recorded image(s) (Raffel et al.¹⁰³; Westerweel¹²²; Christensen et al.¹⁸).

Reuss et al.^{105,106} utilized PIV to measure the laminar flow field velocity distribution in a Bunsen type burner for reacting and non-reacting flows. For the velocity, vorticity and strain rate results for the non-reacting case correlated quite well with the theoretical profile based on Poiseuille flow. Measurement in the reacting flow was complicated by the poor distribution of seeding particles between the unburned and burned gases. The image of the flame indicated a heavily seeded unburned gas region inside the boundary of the flame, while the burned gas region outside and above the luminous flame zone was very lightly seeded. This light seeding resulted in a failure of the interrogation in the burned gas region. The low seeding density was believed to be a result of two factors: volume expansion due to combustion and a decrease in the scattering cross section of the seeding material, TiO_2 . Utilizing particles that have a constant scattering cross section such as Aluminum Oxide (Al_2O_3) could prevent the second factor.

Unlike Reuss et al.^{105,106}, Mungal et al.⁸³ heavily seeded a laminar Bunsen flame and the turbulent tip region in an unstable premixed flame with Alumina powder in hopes of measuring both the non-reacting and reacting flow fields. As with the previous study, in both cases the unburned region within the flame boundaries was much more heavily seeded, thus indicating the strong volume

expansion associated with the presence of the flame. The heavier seeding level marks the region of the flow up to the preheat region of the flame, in which a thin region exists before the flame surface (location of maximum reaction rate). The authors noted that the error in the analysis increases in regions that overlap the burned and unburned portions of the flow due to the large particle image density gradient. This gradient leads to a bias in the measured velocity towards the non-reacted (heavier seeded) values. However, fairly good results were obtained with a velocity error of less than 3% of the maximum velocity with a portion of the error due to thermophoresis effects in the vicinity of the flame zone. It was also shown that the dilatation ($\nabla \cdot \mathbf{u}$) provided an excellent marker for the flame zone, which was expected as it is directly related to a change in density.

2.5.1 PIV Seeding

Using PIV, the fluid velocity is inferred from the position of the light-scattering tracer particles at two instances in time. The ideal particles would (1) exactly follow the motion of the fluid, (2) not alter the flow or the fluid properties and (3) not interact with each other (Westerweel¹²²). Particles must also be capable of reflecting a significant quantity of light such that their position in the flow field can be recorded onto some media. Therefore, a compromise between reducing the size of the particle to better track the flow and increasing size to improve light scattering is necessary.

For most experiments it is desirable that seeding particles be non-toxic, non-corrosive, non-abrasive, non-volatile and chemically inert. A number of materials, including: TiO₂, Al₂O₃, glass micro-balloons, and various oils (corn oil, olive oil and oil smoke), have been found to meet these requirements and used in a number of gaseous flow studies. However, the presence of a reacting flow field, as in this study, complicates the use of some of these materials.

Several previous studies interested in velocity measurements in flames have attempted to use oil droplets ranging in size from 2-2.5 μm (Ruess et. al¹⁰⁶). While these oils are non-toxic and have a relatively low density in comparison to other seeding material there is a significant drawback to using oils in reacting flow studies. Oil droplets tend to have a low vaporization temperature (olive oil ~ 600 K) and vaporize in the preheat (pre-flame) region, thus no velocity measurements can be made outside of the cold, non-reacting regions. The boundary established by the oil droplet vaporization may or may not be the flame front depending on the temperature in the preheat region. If only the flow into the preheat region of the flame is of interest, then oil

droplets would be beneficial as they would not cloud the windows which is a problem with powder seeding.

Melling⁷⁸ suggests the use of oxide materials such as Al_2O_3 or TiO_2 for seeding flames and high-temperature flows. Both of these materials are inert and can survive the combustion temperatures experienced in this study ($\sim 1800^\circ\text{C}$). For this study $1\ \mu\text{m}$ diameter Al_2O_3 particles with a density of $3970\ \text{kg/m}^3$ were used. Melling⁷⁸ also showed that Al_2O_3 particles up to $2.46\ \mu\text{m}$ in diameter were capable of accurately following flows with a turbulence frequency of up to $1\ \text{kHz}$. This was more than adequate for the laminar flows considered here.

2.6 Modeling of Combustion Systems

Few papers have used *quantitative* measures (or predictions) of transfer function sub-models to actually predict the stability of practical combustors. Instead, most investigations use control theory models to understand trends and predict qualitative behavior. For practical applications, quantitative evaluation of the combustion or acoustic transfer function sub-models is a current research topic, see Lieuwen and Neumeier⁷³ for an example. Thus, complete stability analysis of practical systems has seldom been carried out using quantitatively accurate sub-models. Kruger et al.^{46,65} approaches this goal, but some aspect of the problem is (necessarily) simplified. Therefore, actual prediction of the stability margin, in terms of the phase and gain, is qualitative.

An analytical model resulting in a nonlinear ordinary differential equation was developed to describe periodic oscillations in rocket motors by Crocco and Mitchell²⁴. The nonlinearity of the problem accounts for the limit cycle behavior, which ensures finite oscillation amplitude. The combustion process was represented by the sensitive time-lag, or $n\text{-}\tau$, model and considered to be well distributed over the length of the combustion chamber. An oscillation was imposed onto a reacting environment with and without a shock with feedback provided by the combustion process. The model did not account for the system geometry, thus damping and driving were controlled entirely by the presence and strength of a shock wave, the magnitude of the combustion feedback terms (interaction index, n) and the characteristic (or “stretched”) time lag, τ .

Mitchell⁷⁹ discussed the need to include all of the important driving and damping mechanisms in models developed to predict combustion stability in liquid fuelled rockets. Two general approaches to stability modeling were proposed: 1) attempt a direct analytical solution of the partial differential equations (pde’s) that describe the flowfield of the rocket; or 2) numerical analysis or direct numerical

integration of the pde's. The latter of these two was also subdivided into linear and nonlinear analysis. The bulk of the study focused on the small oscillation amplitude linear model that utilized the time-lag (n- τ) model to represent the combustion response, given as the following:

$$Q' = \bar{Q}n(1 - e^{-i\omega\tau})p' / \bar{p} \quad (2.6)$$

Models were additionally provided for the nozzle response and acoustic absorbers to evaluate the impact of axially distributed combustion on stability. Results indicated that if the time lag, τ , were relatively short, distributing the combustion is stabilizing, whereas if τ were relatively long, distributing the combustion is destabilizing. The author notes the need for nonlinear models to predict the occurrence of the finite amplitude waveform, or limit cycle behavior; and to address the phenomena of triggering in which the introduction of disturbances of sufficient amplitude and correct form can initiate an instability in an intrinsically stable engine.

The primary difficulty in modeling combustion driven oscillations is the description of the response of the flame to various inputs. An early attempt at modeling the flame dynamics in a simple laminar conical flame utilizing a linear stability analysis was presented by Merk⁷⁷. In this analysis, the author described the combustion driven oscillations by a flame transfer function, in which the fluctuations in the heat production were shown to be dependent on perturbations in the inlet flow to the combustion system. The derived characteristic equation, or flame transfer function, predicted the occurrence (or nonoccurrence) of instability based on combustor geometry and the impedance variation across the flame.

Assuming a very small pressure difference in comparison to the “velocity jump” across the flame, Mugridge⁸² derived a simple equation relating the velocity jump to variations in the heat release rate from the flame utilizing basic principles

$$u_2 - u_1 = \left(\frac{\gamma - 1}{\rho c^2} \right) q_{(x_2 - x_1)} \quad (2.7)$$

where q is the fluctuating heat release per unit cross sectional area between planes x_1 and x_2 . The resulting flame transfer function coupled the heat release to system acoustic through the impedance on either side of the flame. Theory suggested that for a given flame transfer function an instability could

be suppressed by altering the supply impedance. However, experimental results displayed nonlinear effects that were not predetermined by the flame transfer function.

As a comparison to Equation (2.7), two aforementioned studies (Chu²⁰; Fleifel et al.³⁹) also provided a relationship between the heat release rate and the change in acoustic velocity across the flame.

$$\text{Chu} \quad (u_2)_h - (u_1)_h = \frac{\gamma_2 - 1}{\gamma_2} \left(\frac{q}{p_1} - \frac{\gamma_1 - \gamma_2}{(\gamma_2 - 1)(\gamma_1 - 1)} (u_1 - S_a)_h \right) \quad (2.8)$$

Where the “h” subscript indicates conditions at the heat source, and S_a is the apparent fluctuating flame speed.

$$\text{Fleifil} \quad n(u_2 - u_1) = \frac{\gamma - 1}{\rho_1 c_1^2} q_{x_2 - x_1} e^{-i\omega\tau} \quad (2.9)$$

Equation 2.8 takes a slightly different approach by considering the ratio of specific heats on either side of the flame. Additionally, variations in characteristic time are accounted for adjusting the apparent flame speed, S_a . The relationship given by Fleifil et al.³⁹ is similar to that given by Mugridge⁸², except for the inclusion of the n- τ model in Equation 2.9.

Baade⁵ investigated combustion driven oscillation by utilizing stability criteria based on feedback loop analysis. Through the use of feedback loop analysis it is possible to quantitatively account for both magnitude and phase of all the cause-effect relationships associated with the instability. Three linear transfer functions were developed to describe the acoustic impedance of the combustion chamber, the dependence of the flame volumetric expansion on the pressure fluctuations in the combustion chamber, and the flame itself. Using these transfer functions, the author re-stated the Rayleigh Criteria, given in Equation (1), into a form that led to the same criteria as the feedback loop analysis. This was verified by comparison to a number of other theoretical models, in which relatively good agreement was obtained for both phase and magnitude at low frequencies.

A number of studies have considered modeling thermoacoustic oscillations as a network of acoustic elements (Paschereit and Polifke⁹²; Paschereit et al.⁹¹; and Schuermans et al.¹¹⁴). The elements, which are defined by transfer matrices, are frequently referred to as an acoustic “two-port” due to fact that the transfer function describes the relation between the acoustic quantities on either side of the element. Schuermans et al.¹¹⁴ developed an adaptation of the classic n- τ model based on this approach

for a premix swirl stabilized burner. Due to the complex nature of the flow field in the burner and the uncertainty of the time lag, several parameters were determined empirically by exciting the burner with and without combustion. Acoustic measurements were conducted at various locations in order to determine the Riemann invariants, which can in turn be used to derive the transfer matrices for the burner and the flame.

In two separate studies, Ducruix et al.³³ and Khanna et al.⁵⁸ experimentally determined the open-loop flame transfer functions for laminar, premixed flames. In both cases an inherently stable flame was excited to evaluate its response to acoustic modulations. Determination of the open-loop flame transfer function is dependent on the measurement of the fluctuating heat release rate and the acoustic velocity upstream of the flame. Global heat release rates were inferred from chemiluminescence measurements of CH* and OH*, respectively. Ducruix et al.³³ utilized laser Doppler velocimetry (LDV) to measure velocity perturbations and Khanna et al.^{58,59} used a velocity probe based on a two-microphone technique and the 1-D Euler equation. The transfer function in the Khanna et al.⁵⁸ study was found to be fourth-order by determining the best fit of the experimental data. For this study a flat flame burner was used in which there was a significant interaction between the honeycomb substrate flame anchor and the flame via heat transfer. The authors believe this may have contributed to the higher order model. Two pairs of complex conjugate poles were obtained, with the first resonant response believed to have been dictated by a fluctuating flame speed and the second resonant response attributed to the chemical kinetics of the combustion process. Results indicated an increase in damping and bandwidth with an increase in the mean energy content of the mixture.

Although Ducruix et al.³³ did not obtain a mathematical description of the flame transfer function, its amplitude and phase were determined from the experimental data and compared to two analytically derived models, including that of Fleifil et al.³⁹. Fairly good agreement was obtained between the experimentally determined amplitude and that of the analytical models, however considerable difference was seen in the phase comparison. The experimental phase difference indicated a nearly constant time lag between the velocity perturbations and the heat release fluctuations, which only agreed with the analytical results at relatively low frequencies. This discrepancy was believed to be due to assumptions made in the modeling, such as constant flame speed.

Chapter 3 Experimental Setup

The combustion system utilized for this study is a ring-stabilized premixed laminar methane-air flame inserted in a Rijke tube combustor operating at atmospheric conditions (Figure 3.1). The Rijke tube provides the necessary acoustic environment needed to generate combustion oscillations for this study, while at the same time provide a simplified system that is capable of nearly isolating the effect of individual mechanisms on the heat release rate.

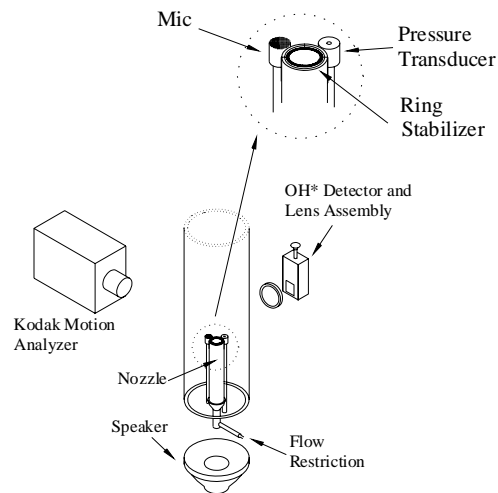


Figure 3.1: Experimental Setup

Metered fuel and air are mixed well upstream of the choked burner and flows are maintained in the laminar regime. Microphones placed at various locations throughout the combustor provide acoustic pressure measurements, which in turn can be used to obtain the acoustic velocity. The arrangement shown in Figure 3.1 allows for self-excited, as well as stable operation. Under stable conditions various speaker arrangements are utilized to impart controlled acoustic velocity fluctuations. The natural visible chemiluminescence emission from the flame is recorded by a high-speed digital camera to provide a general measurement of the flame surface. Utilizing a filtered photomultiplier tube OH* chemiluminescence is collected and related to the global heat release rate from the flame. Particle image velocimetry is utilized to provide velocity, dilatation, and strain measurements in the reacting and non-reacting flows downstream of the burner nozzle. A high-speed

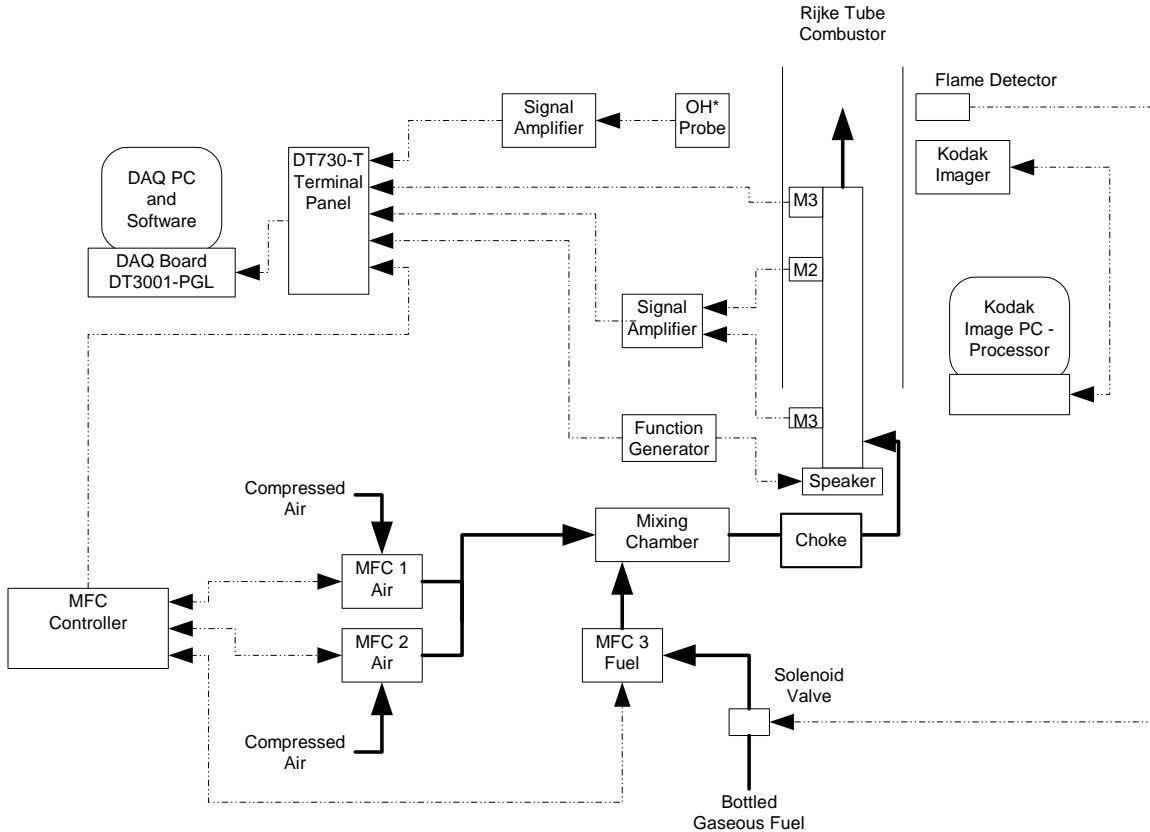


Figure 3.2: Data acquisition flow diagram

data acquisition system has been assembled to collect data and trigger instruments during tests. Figure 3.2 provides a flow diagram of the data acquisition layout.

3.1 Rijke Tube Combustor Assembly

The main body (Figure 3.3) consists of a vertically mounted, 80 cm long, 8.0 cm diameter quartz tube, allowing optical access and suitable transmittance even in the ultraviolet range. The mixture nozzle, a 2.54 cm o.d. / 2.25 cm i.d stainless steel tube, extends 20 cm ($\frac{1}{4}L$) into the main body. The flame is anchored on a 2.04 cm o.d. / 1.68 cm i.d. by 0.25 cm thick ring stabilizer at the top of the nozzle (insert - Figure 3.1 and Figure 3.3). The ring, mounted flush with the top of the nozzle, acts as a bluff-body that provides static stability under lean and high flow operation (Johnson et.al.⁵⁴). Dynamic instabilities could not be attained in initial testing performed without the ring because of flashback and / or blow-off. Johnson et.al.⁵⁴ stressed the necessity of a small gap between the outer

diameter of the ring and the inner diameter of the nozzle in order to create a stable recirculation zone in the wake of the ring. Without the gap the flame would revert back to a rim stabilized flame with limited static stability.

The effective nozzle exit area was determined to be $2.94 \text{ cm}^2 (A_{\text{nozz}} - A_{\text{ring}})$, thus providing a maximum flow velocity of 280 cm/sec and Reynold's number of approximately 3500. However, in order to maintain laminar flow at the nozzle exit, testing was restricted to an average exit velocity of less than 150 cm/sec ($Re \approx 1900$).

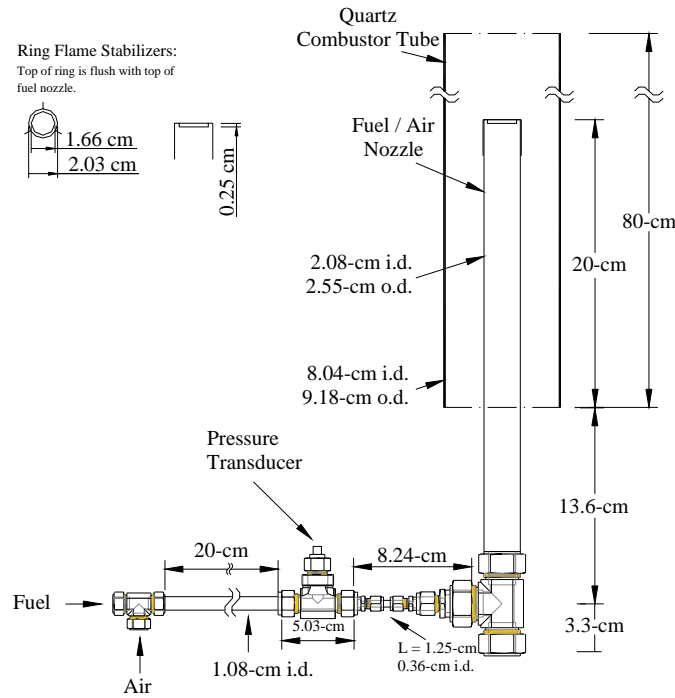


Figure 3.3: Rijke tube combustor experimental assembly

Bottled laboratory grade methane (99.999% methane) and house supplied compressed air (dried to a dew point of -40°C) were mixed well upstream ($L/D = 67$) of the nozzle inlet. Two mass flow controllers (MKS model 1559A) provided a combined flow of air slightly over 45 slpm, with an additional mass flow controller (Tylan model FC-260) regulating fuel flow to a maximum of 5 slpm. A Tylan RO-28 MFC controller was used to vary the flow through each of the three units. This unit was modified to provide an output signal of the measured flow through each MFC. The two air MFC's were calibrated on 20°C dry air with a Gilian Instruments bubble flow meter, while the fuel MFC was

calibrated with the same bubble flow meter using methane as the working gas. The bubble flow meter was calibrated with a NIST traceable venturi.

As a safety precaution, an open/close valve and a solenoid valve were located in the fuel line between the gas cylinder and the fuel MFC. Power to the solenoid was controlled by a Honeywell Flame Detector (C7027A). The flame detector is sensitive to the ultra-violet (UV) emissions from the flame, thus when a flame is present the detector is active and allows power to flow to the fuel shutoff solenoid. However, in the event that the flame was to extinguish the detector would cause the solenoid valve to de-energize interrupting the fuel supply to the combustor. A control override is provided to permit fuel flow for the initial lighting of the flame.

As previously stated, perturbations in the fuel / air mixture composition is considered one of the possible mechanisms driving heat release variations in the reaction zone. Acoustic feedback from combustion or flow instabilities could travel into the mixing region and disproportionately alter the air or fuel flow resulting in perturbations in the mixture composition. However, for this study it was desired that this effect be limited. A small restriction ($d_{res}/d_{noz} = 0.1$) was placed at the base of the nozzle (Figure 3.3), resulting in a 60% pressure drop, to prevent the influence of acoustic feedback on fuel / air mixing. To verify the success of the restriction the pressure signals were monitored, with Kistler model 206 transducers, upstream of the restriction and at the exit plane of the nozzle during operation at the maximum amplitude instability attainable by this system ($P' = 0.68$ psi, $U = 150$ cm/sec, $\phi = 1.0$), Figure 3.4. Figure 3.5 shows the accompanying power spectrum from the two pressure signals.

3.2 Heat Release Measurement

The chemical reactions that occur in hydrocarbon flames produce molecules in an excited state that results in these molecules emitting light. This process is known as chemiluminescence. This spontaneous emission occurs in both the natural visible and ultra-violet spectrum and the presence of specific excited molecules has been related to particular reactions important to the combustion process as detailed in Section 2.4. The chemiluminescence signal from the hydroxyl radical, OH^* (308 nm), was used to provide a means of measuring the dynamic, spatially integrated heat release rate from the flame. The optical arrangement is shown in Figure 3.6. A single fused silica lens ($f = 50.8$ mm) was used to focus the entire image of the flame, centered 1.75 cm above the nozzle exit, onto a filtered, UV sensitive photomultiplier tube (PMT). The lens was positioned approximately 267 mm from the nozzle and 50 mm from the inlet to the filtered PMT. This arrangement would result in a 35 mm x 20

mm object projecting an image of 7.5 mm x 4.3 mm onto the PMT, which has a detection area of 12 mm x 3 mm.

The Hamamatsu model R636-10 photomultiplier tube has an extremely wide detection range of 190 - 925 nm, with peak response occurring between 300 – 800 nm. Thus to eliminate interference from unwanted light, the PMT module was coupled with a UG-11 band-pass filter. Centered at 320 nm, this ± 75 nm band-pass filter has an 85% transmittance at 308 nm. The photomultiplier tube has a quantum efficiency of 20 - 25% at 300 - 350 nm and a response time of 10 - 20 nsec.

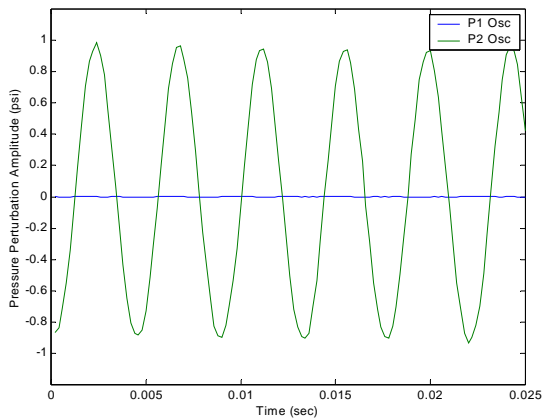


Figure 3.5: Pressure amplitude trace during peak oscillations ($U=150$ cm/sec, $f=1.0$) upstream and downstream of nozzle restriction.

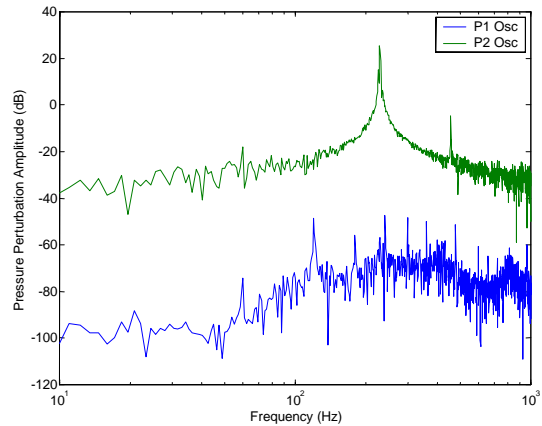


Figure 3.4: Pressure amplitude frequency response during peak oscillations ($U=150$ cm/sec, $f=1.0$) upstream and downstream of nozzle restriction.

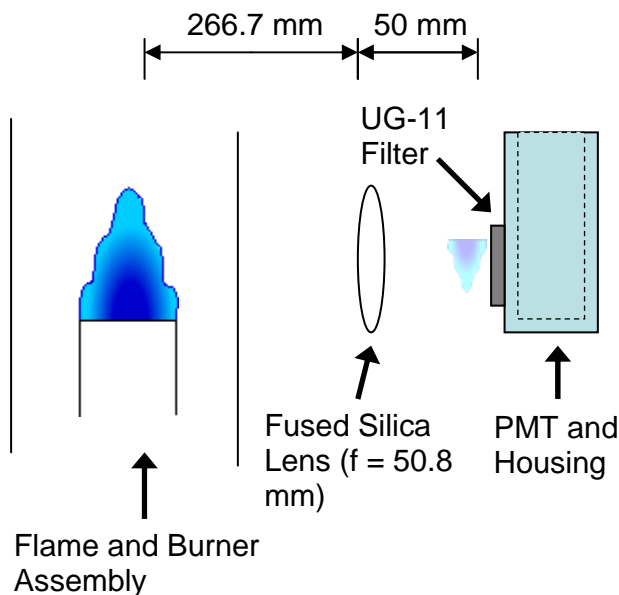


Figure 3.6: OH* optical measurement assembly. Measured OH* is assumed equivalent to heat release.

The PMT produces a current signal in response to photons impinging upon a series of electrodes (dynodes) each held at an ever increase voltage potential. The resulting current is subjected to a 50 ohm load to produce a low-level voltage signal. With a high-voltage power supply providing up to 1500 V, a maximum signal of 50 mV can be obtained. The output signal from the PMT is then sent to a voltage amplifier prior to being recorded by the data acquisition system.

3.3 Acoustic Pressure and Velocity Measurements

In order to evaluate the coupling process between combustion and acoustics, the acoustic pressure and mass velocity at the input to the reaction zone must be known. The acoustic pressure can be measured with the use of a pressure transducer (i.e. microphones). Two methods are used to evaluate acoustic velocity. By applying phase-resolved particle image velocimetry (PIV) at the exit of the nozzle it was possible to obtain instantaneous velocity field measurements at specific times during the oscillating cycle. Post-processing the velocity measurements at all the time instances allowed one to assemble a time history of the velocity at any location within the sampled field. This was a novel approach to measuring the acoustic velocity and had the added benefit of providing both axial and radial velocity.

Acoustic velocity within the nozzle cannot easily be measured, but can be inferred from other parameters. The two-microphone method, described in Section 5.3, was used to determine the acoustic velocity within the Rijke tube combustor assembly by utilizing pressure measurements and acoustic transfer matrices.

Three microphones are placed throughout the burner when testing reacting flows, Figure 3.7. One microphone (Knowles BL 1994) is located at the exit of the nozzle (Mic 3) to measure the acoustic pressure response of the flame. The other two microphones (Knowles FG-3329), which require a 1.5V power source, are positioned in the nozzle upstream of the exit (Mic 1 and Mic 2, Figure 3.7), at 0.19m and 0.34 m from the base, respectively.

Due to the low amplitude response of the two Knowles microphones an adjustable amplifier circuit was constructed (Figure 3.8). Adjustment of the variable resistor (R_b) provided a means of matching amplitude response between microphones. Additionally, the microphone signals were related to pressure through calibration against a sound pressure meter.

3.4 Flame Excitation

One of the most significant advantages of the simple combustor rig being utilized for this study is the capability to investigate the flame under various degrees of flame / flow excitation. Depending upon the nozzle configuration and operating conditions, excitation ranged from stable to self-excited instability to acoustically-driven with an in-line or external speaker at various frequencies and amplitudes.

Acoustically driving a stable flame provides the level of control necessary to investigate the complex response of the heat release rate to variations in flame and flow structure. Although the flame is naturally unstable over a wide range of operating conditions, by replacing the acoustically hard boundary at the base of the burner with an in-line acoustic driver the flame becomes stable when the driver is not operating. Essentially this boundary modification results in a change of the acoustic impedance inside the burner nozzle and while it may prevent self-excited oscillations it does not impact the aerodynamic boundary conditions at the nozzle exit. Thus flow properties at the flame anchor location should be unaffected. It should be noted that impedance variation in combustion systems has been shown to be an effective means of controlling instabilities and work is on-going in this area (Richards and Robey¹⁰⁸).

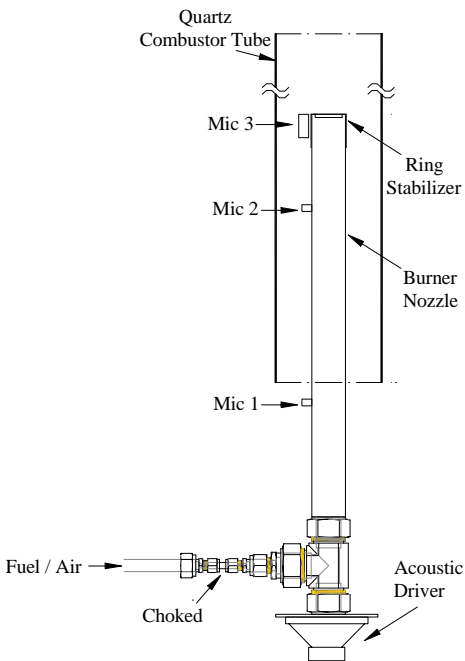


Figure 3.8: Microphone location in flow nozzle.

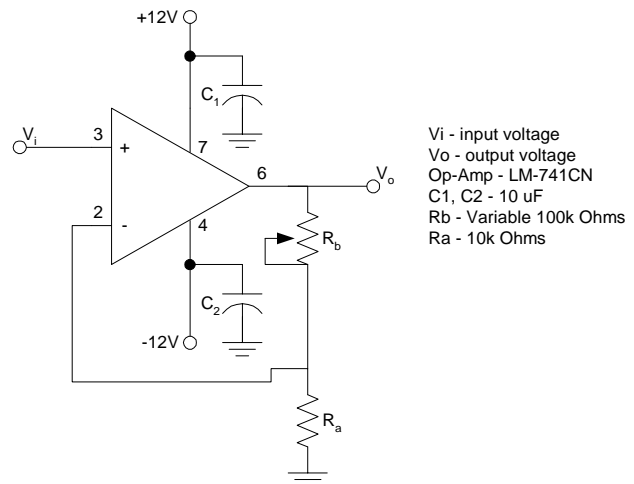


Figure 3.7: Microphone amplifier circuit

Figure 3.9 shows the three speaker / combustor arrangements used for this study. With the burner in the conventional configuration as shown in Figure 3.9a, the flame is self-excited over a given range of operating conditions with a sharp transition from oscillating to stable outside of this envelope. Although a significant amount of the acoustic energy is lost by placing the speaker below the base of the burner assembly (external speaker), Figure 3.9b, it is possible to provide adequate flow excitation to cause a marginally stable flame to oscillate. For this set-up a 20 cm, 100 W subwoofer provides the excitation. A Stanford Research Systems Model DS345 Function Generator controls the frequency, and along with a Realistic 100 W Solid State Amplifier, the amplitude of the excitation being imparted upon the inlet flow.

The in-line speaker configuration, shown in Figure 3.9c, provides a much greater level of controlled inlet velocity perturbation. A 10 cm, 40 W, 8 ohm speaker was attached to the burner nozzle with a coupling device fabricated by welding a 10.5 cm x 10.5 cm, 2 mm flat, stainless steel plate to a 1 1/4" swagelok fitting to facilitate attachment to the bottom of the burner nozzle. The same amplifier and function generator were used to provide a signal to the speaker. With this arrangement the flame can experience upstream velocity perturbations strong enough to dislodge the flame from its anchor resulting in blow-off (much stronger than perturbations that occur for self-excited flames in this combustor).

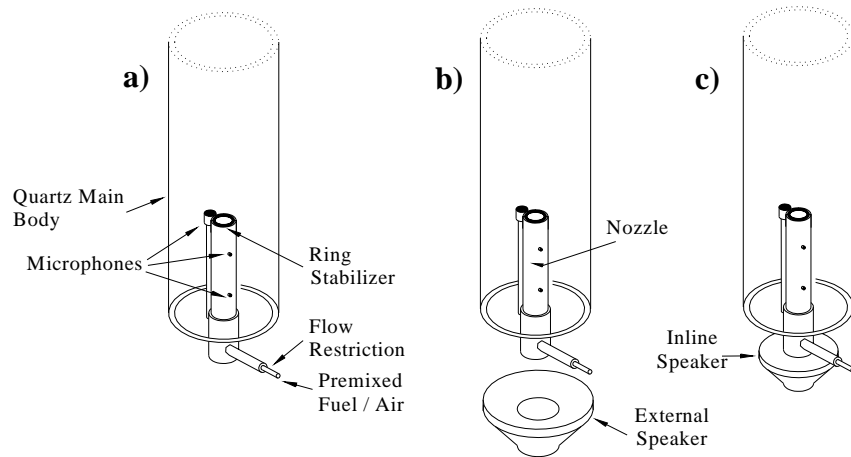


Figure 3.9: Operational configurations for flow and flame excitation

3.5 Flame Surface Recording

A high speed Kodak Motion Analyzer, Model 1000 HRC, capable of recording speeds of 1500 frames per second and a resolution of 512 x 384 pixels, was used to record the visible flame surface which consist primarily of CH* emissions (430 nm). The camera was operated at 1000 frames per second and triggered to allow time alignment with other data. An area of 11.27 cm x 8.45 cm was captured equating to a resolution of 45.4 pixels/cm, which provided sufficient detail of the flame structure. Images were temporarily stored into the local on-board memory and after each session image files were converted to “tif” format and saved to a magnetic tape for subsequent processing.

3.6 Flow Measurement and Visualization

Particle Image Velocimetry (PIV) was used to evaluate the flow characteristics in reacting and non-reacting flows through the Rijke tube burner. As will be further explained, PIV is performed by seeding the flow region of interest with small, highly reflective tracer particles capable of accurately following the flow. These particles are then illuminated in a planar region of the flow by two successive laser pulses within a short time interval. The light reflected from these particles is captured by a recording media, in this case a CCD array, on two separate images. The two images undergo a correlation analysis in order to determine particle displacement, and thus local velocity.

The PIV system used for this study is shown in Figure 3.10. Not all of the instrumentation is shown for clarity. Items shown in gray are added to instrumentation shown in Figure 3.2. The system consists of a particle seeder, laser system, sheet forming optics, CCD array, synchronizer, and data acquisition and analysis system. A description of each of these components is provided in Section 3.3.1.

3.6.1 Seeding Material

Alumina oxide (Al_2O_3) particles were chosen as the seeding material due to their high boiling point and inert behavior. The particles have a nominal diameter of 1 μm and are introduced into one of the two air streams prior to mixing with the fuel, Figure 3.10. By utilizing two separate air supply lines, it is possible to adjust the flow of air into the feeder while maintaining a constant overall mass flow of air to the burner by increasing the flow on MFC 2. Air from one of the mass flow controllers enters a Sylco Fine Powder Feeder thus entraining particles. The powder feed rate can be controlled by one of two mechanisms: 1) adjustment of the air flow into the feeder, or 2) adjustment of the

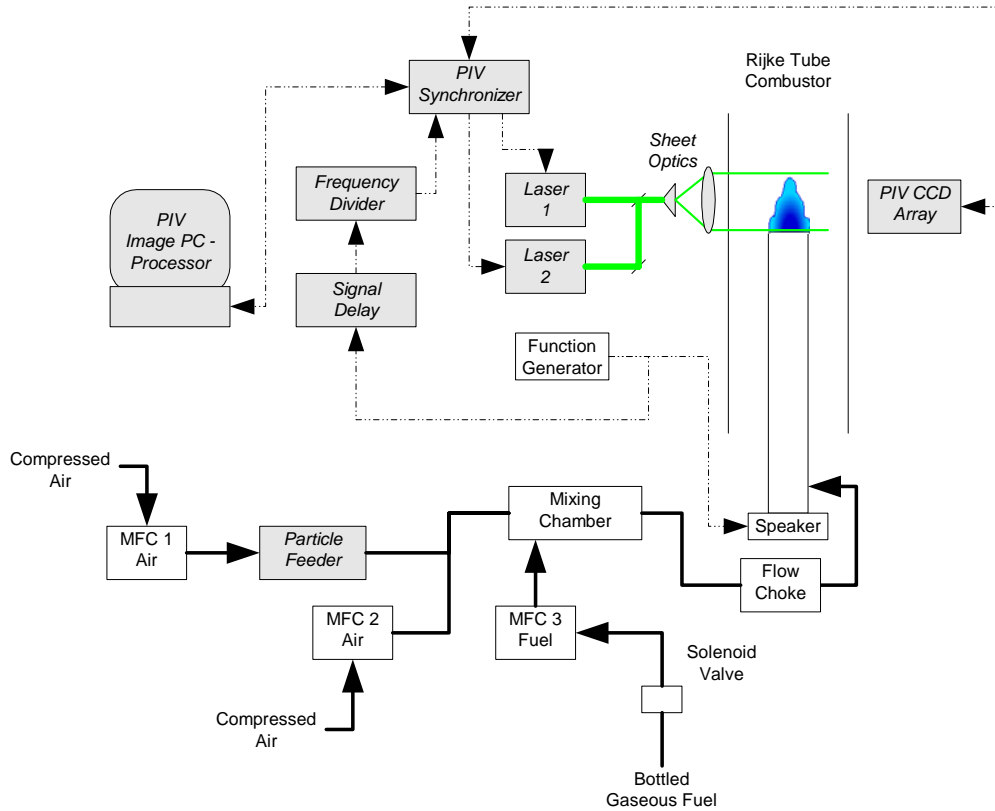


Figure 3.10: System configuration for Particle Image Velocimetry (PIV)

variable speed screw feeder mechanism. The feeder is also equipped with a variable amplitude electromagnetic vibrator which provides a vibratory action to prevent coagulation of particles.

3.6.2 Particle Illumination

Two Continuum Surelite I Nd:YAG lasers provided 532 nm wavelengths beams used to illuminate the tracer particles. Each pulse was 4-6 nsec in length and provided approximately 200 mJ of energy. The beam from each laser was expanded into a sheet by passing it through a series of lenses. Upon leaving the laser head, the 6 mm diameter beam from each unit is translated vertically to the sheet forming optics by two adjustable high-power 45° 532 nm mirrors, Figure 3.11. After passing through the second mirror, the two beams are angled to pass through a small diaphragm and intersect at a 25.4 mm, -25 mm effective focal length (EFL) cylindrical lens at 1.27 m down range.

A 10cm diameter, 600 mm focal length lens is positioned 56 cm away, and focuses the expanding beam to form a laser sheet 9.7 cm in height and 0.5 mm thick at the exit of the burner

59 cm down range from the lens. The intensity quickly falls off at the top and bottom of the sheet due to the Gaussian distribution of the laser. To prevent any biasing of the PIV measurements due to inconsistent illumination only the middle of the sheet was used. The bottom quarter (~2.0 cm) was blocked and the actual PIV image was limited to the region 4.8 cm above the nozzle exit, thus 2.9 cm of the sheet is not used, Figure 3.11. The resulting test volume, or Region of Interest (ROI), for the PIV study was 48.6 mm x 48.6 mm x 0.5 mm.

The arrangement used for this study provides a 2-D measurement of the velocity field, thus motion of the particles outside of the ROI, or out-of-plane motion, is not resolved. Because the correlation algorithm used to process the images assumes only planar motion, laser alignment is critical in order to obtain accurate results. Laser alignment is accomplished using the adjustable steering mirrors in the optical train and verified by the formation of Fraunhofer diffraction fringes through a 0.5mm slit.

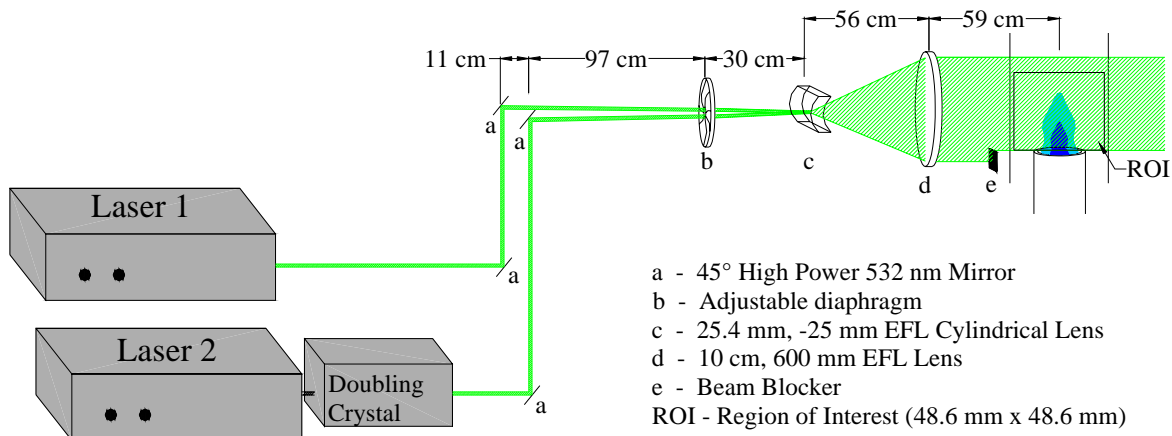


Figure 3.11: PIV laser and optical arrangement.

3.6.3 CCD array, lens, synchronization

For this study a 2048 x 2048 pixel, 12-bit TSI PowerView progressive scan CCD array (Model 630049) fitted with a Nikon 105 mm f/8.0 lens is used to capture the images of the illuminated particles. The TSI PowerView CCD array has a minimum frame separation of 200 nsec. Each pixel of the array is 7.4 x 7.4 μm and has a fill ratio of 60%. Particle illumination to the array is filtered with a 523 nm +/- 10 nm band-pass filter to minimize flame radiation interference. The resulting magnification was 3.2 or 23.73 $\mu\text{m}/\text{pixel}$.

Frame straddling, and PIV in general, requires precise synchronization between laser pulses, CCD array, frame grabber and PC, Figure 3.12. The TSI PIV system uses a TSI model 610034 LaserPulse Synchronizer to provide this service. It is capable of independently controlling the flash lamp trigger and the Q-switch for two separate lasers and can trigger from an internal or external source.

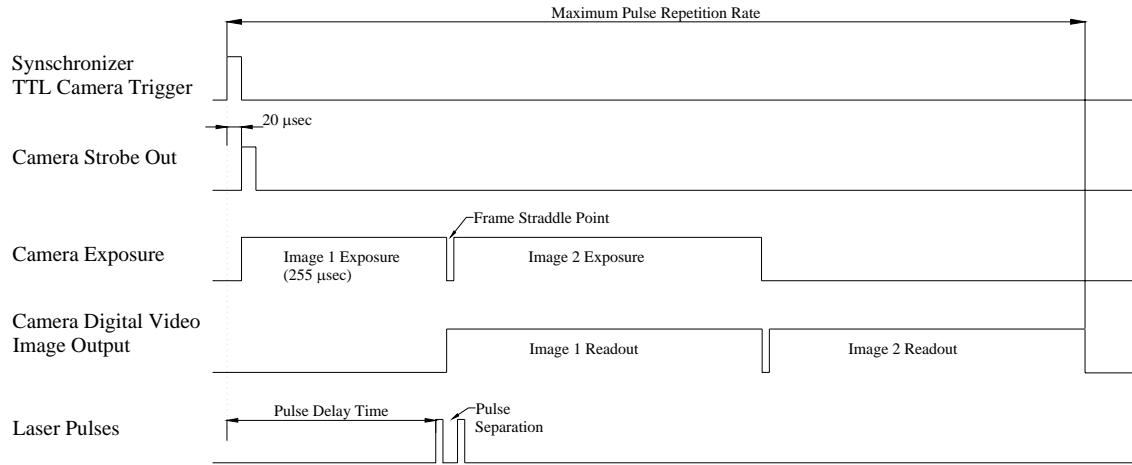


Figure 3.12: PIV frame straddling method and laser pulse synchronization.

The PIV system was phase-locked with the acoustic perturbations in order to provide time resolution of the velocity field. The pressure signal was supplied to a BNC Model 7085 Digital Delay / Width Generator which could provide a delayed trigger to the PIV system in increments of 1 nsec up to a maximum delay of 1 second. However, since the flame typically oscillated at a somewhat higher frequency than the 10 Hz maximum pulse rate of the two lasers, the trigger frequency had to be adjusted so as not to overdrive the system which would result in inconsistent pulsing by the lasers. A frequency divider circuit was constructed using an 8-bit binary counter (Fairchild 74F579) that would divide the input frequency by 32. Thus given a flame oscillating at 230 Hz, a TTL pulse at that frequency is sent to the counter which would produce a subsequent TTL signal at 7.19 Hz.

Although PIV is considered an instantaneous measurement a frame separation is necessary in order to measure the velocity vectors and this essentially results in averaging the flow field over the short separation time. Given a flame perturbation occurring at 230 Hz, a 100 μsec frame separation is equivalent to a phase averaging of 8.28°, and therefore phase-resolution was limited to 10° increments

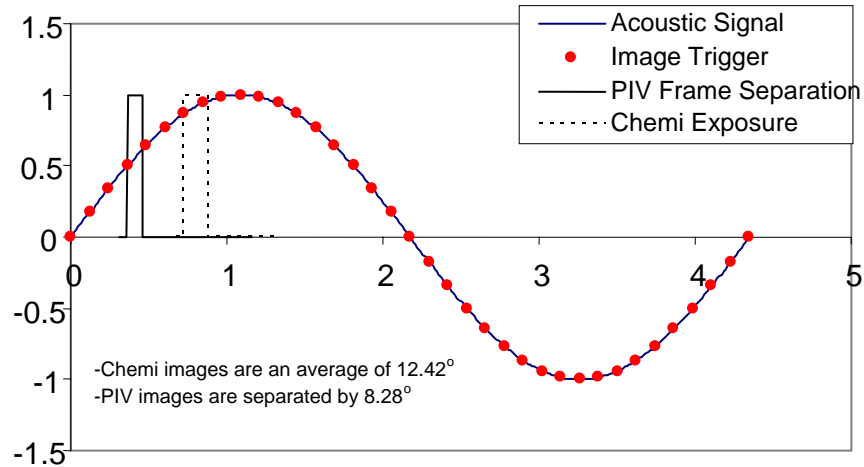


Figure 3.13: Acoustic signal from burner nozzle exit used to trigger PIV sampling. PIV frame separation and chemiluminescent images result in short time averaging.

for this study (Figure 3.13). For a 230 Hz oscillation, this results in a sample rate of $FS = 8280$ Hz. Five images were obtained at each test point.

A TSI model 600067 High-Speed Frame Grabber Board is used to transfer the images captured by the CCD array to storage in a dual Pentium 1.4 GHz PC with 1.7 GBs of RAM. Insight software Version 3.52 developed by TSI controls the CCD and synchronizer operation, as well as managing data collection, storage and preliminary analysis. Proper software calibration is achieved by a comparison of actual length and recorded image length thus providing mm (actual length) / pixel (recorded image). Software calibration was necessary to achieve accurate velocity vectors of the recorded image pairs.

3.6.4 PIV Measurement Accuracy

The accuracy of velocity measurement by particle image velocimetry depends upon the accuracy with which image displacements can be measured and the accuracy with which image displacements can be related to particle locations and their respective particle displacements. A number of studies have considered the errors associated with digital PIV (Adrian³, Huang et al.⁵⁰, Westerweel¹²², Bolinder¹³ 90) and have found three forms: outliers, mean-bias error and root-mean-square (RMS) errors. Outliers are those velocity vectors which result from a mismatch in the particle image pattern (Huang et al⁵⁰) and typically have low correlation peaks (Section 6.1).

The presence of the flame greatly influences the potential for outliers and major factors contributing to this error include insufficient seeding, thermophoresis, and so on, and will be discussed in Chapter 6.

Two forms of error, mean-bias errors and RMS errors, occur in the velocity vectors obtained with sufficiently large correlation peaks. Mean-bias errors are associated with a skewing of the correlation peak due to the width of peak. A significant number of velocity gradients over an interrogation window increase the width of the correlation peak and thus the bias error. Peak-locking is a form of bias error that is also affected by the shape of the correlation peak, but can be reduced through the appropriate choice of interpolation methods used to estimate the center of the correlation peak (i.e. particle displacement).

The RMS error defines the minimum resolvable velocity fluctuation (Adrian) and reflects the deviation of the particle displacements from their mean. In digital PIV this error is primarily associated with electronic noise in the CCD and subsequent digitization. This error can be reduced by proper sampling of the particle images (Huang et al⁵⁰ and Westerweel¹²²).

Simulated particle images or CFD solved flow fields are often used to evaluate the errors associated PIV. These studies have shown that a typical value of the bias for a 32 x 32 pixel interrogation region is about 0.1 pixels (Westerweel¹²²) and a RMS error of 0.026 pixels. Given a particle displacement of 8 pixels (following the 1/4 rule), this would produce an error just over 1%. Methods for reducing the mean-bias error are given by Westerweel¹²², but were not applied to this study.

3.7 Data Acquisition System

Aside from flame and flow images, data was collected by a high-speed data acquisition system consisting of a Data Translation DT 3001-PGL acquisition board and a DT730-T terminal board. The 12-bit, 16 single-ended channels DT 3001-PGL has a maximum throughput of 250 kSamples/sec, however the sampling rates for this study were limited to 5000 Hz. This provides a Nyquist frequency of 2500 Hz which is well above the expect frequencies.

The visual programming language HP Vee (Version 5.01) was used to display and log data, and generate a trigger signal to the PIV system or Kodak High-Speed camera. A graphical user interface (GUI) was created (Figure 3.14) that allowed the operator to monitor test conditions and manually trigger data collection.

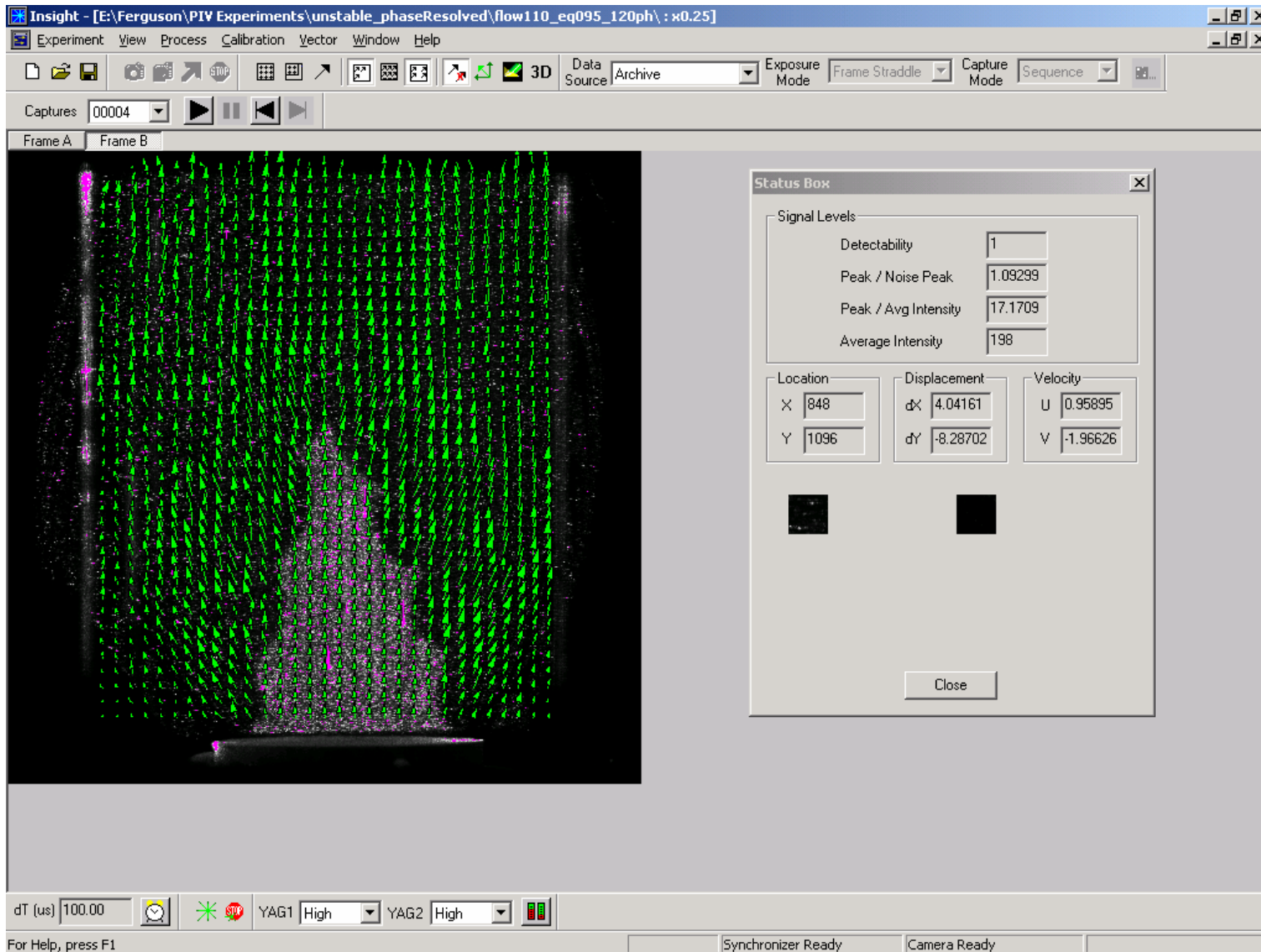


Figure 3.14: Screenshot of PIV Insight software during image analysis.

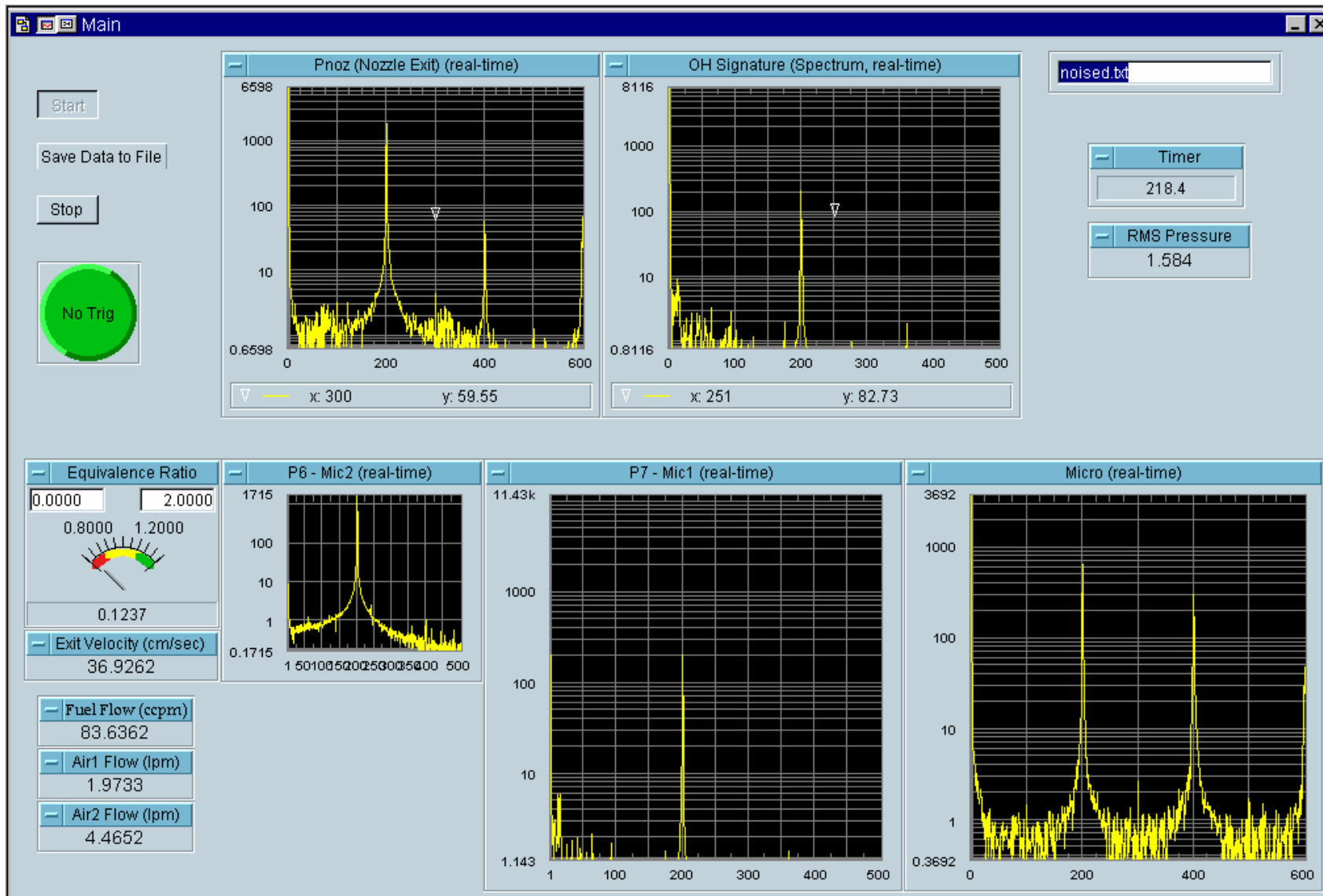


Figure 3.15: Screenshot of data acquisition screen developed using HP VEE software.

3.8 Measurement Uncertainty

In most experimental studies it is common to include an uncertainty analysis of the measurable quantities. However, not all of the measured parameters presented in this study are used to provide a quantitative analysis, and instead are primarily used to provide a qualitative comparison between parameters. Thus a rigorous uncertainty analysis was not performed for all of the measured parameters used throughout this study. Measurable quantities that are considered on a quantitative basis include: equivalence ratio, flame surface area, acoustic velocity determined by acoustic pressure measurement and velocity as determined by PIV method.

Based on a statistical analysis of the repeated experiments an uncertainty of these measurements was obtained. The following uncertainties are based on a 95% confidence interval.

Table 3.1 Uncertainty Analysis of Measurable Parameters

Parameter	Uncertainty as percentage of mean
Equivalence ratio	1%
Flame surface area (based on stable flame)	0.5%
Acoustic pressure (microphones)	10%
Acoustic velocity (two-microphone method)	10%
Velocity (PIV – pre-combustion region)	4%

Chapter 4 Two-port / one-port analysis

Figure 4.1 describes the basic mechanisms that lead to thermoacoustic instabilities. The feedback loop demonstrates the importance of the phase-gain relationship between the heat release rate (due to velocity perturbations) and the acoustics. As a simple example, consider a planar flame at a specific location within a pipe (Figure 4.2). A wave starting downstream of the flame, u_d^+ , travels to the end of the pipe, is reflected and comes back to the flame, u_d^- (Kruger et al.^{64,65}). The wave travels back through the flame (u_u^-) to the upstream end where it is again reflected, returns to the flame (u_u^+) and finally passes back through to its place of origin. Self-excited instabilities occur given adequate gain and proper phasing of this cycle with the oscillation amplitude being constrained by the limit cycle behavior of the non-linear effects.

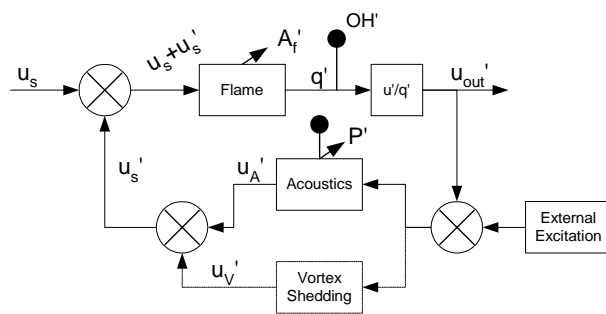


Figure 4.1: Block diagram representation of Rijke tube combustor.

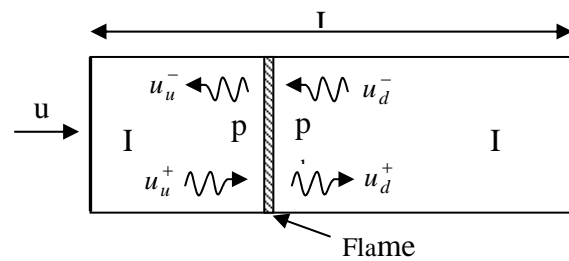


Figure 4.2: Wave propagation in a tube with flame (Kruger et al.).

Describing the response of the simple, planar flame to an acoustic disturbance as shown in Figure 4.2 is possible (Kruger et al.^{64,65}). In turbulent, and even arbitrarily-shaped laminar flames, the interaction between the acoustic waves and the flame surface is much more complex. Wave reflection and transmission is inconsistent across the flame surface which results in area and heat release variations, as well as fluctuations in the acoustic energy.

4.1 Modeling Thermoacoustic Systems

The classic approach to reduced-order modeling of thermoacoustic instabilities is to utilize simple, one-dimensional linear acoustic equations derived from first principles, i.e. conservation of

mass, momentum and energy; coupled to nonlinear heat release rates. Conventional models have typically treated the coupling mechanism between perturbed flow at the inlet of the combustor and heat release rate as a simple time delay with the resulting heat release occurred at a fixed location. The time lag, or $n\tau$ (where n is a gain parameter and τ is the time delay), model was discussed in Section 2.6

An alternative approach that is often used in the analysis of duct and mufflers (Munjal⁸⁴) is to describe the thermoacoustic system as a network of acoustic elements (Paschereit and Polifke⁹³). Each element of the network is defined as either a passive element (fuel and air supply, swirl vanes, cooling channels, etc.) or an active source (coherent structures, burner and flame), and by defining a finite number of degrees of freedom each element can be described as an acoustic multi-port. For a majority of these elements simple analytical models derived from first principles provide an adequate description of their thermoacoustic characteristics. These derivations depend on an understanding of the processes that occur within the element, which for passive, or non-source, components may be limited to simple linear acoustics. Other elements, such as the burner and flame, may have a very complex response which is not fully understood and may be described by analytical, empirical, or numerical methods or a combination of the three. An advantage of the acoustic network approach is that elemental models derived by various methods can be easily combined to form a model of the complete thermoacoustic system.

Assuming a plane wave disturbance with a linear, time-invariant acoustic response and limiting each element to one or two acoustic interfaces, it is possible to describe each element as an acoustic one- or two-port (2- or 4-pole, respectively) in which the unknowns are the acoustic state variables: acoustic pressure (p') and acoustic particle velocity (v'), at the interfaces on either side of the element. Each element can be characterized by the following equation which relates the input state \mathbf{x} to the output state \mathbf{y} (Boden and Abom¹²).

$$\mathbf{y} = \mathbf{K}^* \mathbf{x} + \mathbf{y}_s \quad 4.1$$

Where, in the case of a two-port system, \mathbf{x} and \mathbf{y} are $[2 \times 1]$ vectors containing the acoustic state variables at the inlet and exit of the system, respectively. \mathbf{K} is a $[2 \times 2]$ transfer, or scattering, matrix of the element and contains a passive part and, for an acoustically coupled source, a coupled part. A description of the complete thermoacoustic system is obtained by combining the transfer matrix of all the elements into one “system” matrix by. Finally the variable \mathbf{y}_s is a $[2 \times 1]$ vector that

describes the source strength for active acoustic source elements. For purely passive elements the vector y_s would be set to zero. As an example, consider a plane wave propagating through a fluid contained in a simple straight duct of length, L . The wave originating from the upstream position, “u” subscript, travels downstream, “d” subscript, where it is partially reflected and transmitted.



$$\begin{bmatrix} P_d \\ v_d \end{bmatrix} = \begin{bmatrix} \cos(kL) & i\eta \sin(kL) \\ \frac{i}{\eta} \sin(kL) & \cos(kL) \end{bmatrix} * \begin{bmatrix} P_u \\ v_u \end{bmatrix}$$

4.2

The characteristic impedance of the medium, $\eta = c/A\rho$, is defined as the ratio of acoustic pressure and particle velocity of a plane progressive wave in a given medium, where c is the local speed of sound. The wave number, k , is either k^+ or k^- depending on the direction of travel. Additionally, the length parameter L can be replaced by $(x_d - x_u)$ in order to evaluate the acoustic pressure and velocity at any location within the duct.

Active acoustic elements, or acoustic sources, add energy into the system and in the case of a thermoacoustic instability, sources such as coherent structures in the flow at the burner and variations in the heat release interact with the acoustics field in order to produce a self-excited mechanism that may lead to high amplitude perturbations. In modeling these systems, the sources must be characterized. Equations 4.1 – 4.3 are examples of analytical models of the flame response to an acoustic disturbance, however, as previously mentioned Ducruix et al.³³ has shown that these models are applicable in a limited number of cases, particularly low frequency and low amplitude. Others have tried numerical descriptions (Kruger^{64,65}) but have also been met with limited success. One of the difficulties in using these modeling efforts is that one needs to have an understanding of the processes that are occur inside the element (i.e. how the flame and acoustics interact).

Experimental derivations of the flame transfer function (model of the flame response to acoustic perturbation – active acoustic source) have an advantage in that the burner and flame can be treated as a “black box” in which one is merely concerned with the actual heat release rate response to a given acoustic disturbance and not the actual physical processes that are occurring. This is a method often used in experimental studies (Blackshear¹¹, Khanna⁵⁸ and Ducruix et al.³³) and was described in a

series of studies conducted by Paschereit and Polifke⁹². The resulting flame transfer functions are often in the form of an active acoustic one- or two port.

4.2 Classification of Sources as One- or Two-port Sources

Many attempts at developing empirical models of thermoacoustic instabilities (Khanna⁵⁸, Ducruix et al.³³) as well as many analytical attempts such as Equations 4.1-4.3, result in the characterization of the source (burner and flame) as an acoustic one-port. In these models the response of the burner is directly related to a velocity disturbance without regarding the influence of the upstream characteristic acoustic impedance, where the characteristic impedance is defined as the ratio of the acoustic pressure associated with a progressive wave to the acoustic velocity associated with the same wave (Munjaj⁸³). Assuming the upstream boundary is not acoustically decoupled, for a measured source impedance (flame transfer function) and source strength (u'), the upstream boundary conditions are not allowed to change because they would influence these quantities (Figure 4.3a). Acoustic two-port sources, on the other hand, account for any changes in the upstream boundaries by considering not only the source strength, but also the upstream acoustic pressure (p') which together accounts for changes in the upstream acoustic impedance (Figure 4.xb).



Figure 4.3: Burner / flame characterization as an (a) active acoustic one-port or (b) active acoustic two-port.

Consider the experimental studies conducted by Khanna⁵⁸ and Ducruix³³ in which both works attempted to empirically model the response of the burner and flame to a given acoustic disturbance. In these studies an external acoustic source (loudspeaker) was connected to the burner assembly and used to generate an acoustic disturbance which forced a stable flame to react. Comparing the velocity perturbations leading into the flame and its subsequent response in the form of heat release rate, the researchers derived an empirical relation describing the response of the flame to varying source strength. However, this only considers the open-loop response of the burner to the velocity

disturbance and removal of the loudspeaker results in a change in the acoustically coupled upstream boundary conditions (characteristic impedance) thus violating the one-port assumptions

To characterize the burner as an active acoustic two-port Paschereit and Polifke⁹² utilized the two source-location method (Abom¹, Boden and Abom¹², Lavrentjev and Abom⁶⁶) in which two independent test states were created by externally forcing the flame with loudspeakers placed up and downstream. Measuring the acoustic response of each test state at two locations along with the response of the flame was sufficient to determine the four unknowns of the two-port flame transfer function. Paschereit and Polifke⁹² showed satisfactory results for non-reacting flows, however their results of unstable reacting flows was inconclusive.

Although the derivation of a transfer functions that describe the response of the burner and flame in the Rijke tube combustor is beyond the scope of this study, there is some interest in the manner at which these transfer functions are generated and whether the burner/flame is represented as a one-port or two port acoustic source. This will be discussed in Chapter 8.

Chapter 5 PIV Analysis and Discussion

Clarification of the mechanisms contributing to the occurrence of thermoacoustic instabilities may be possible by studying the structure of the flow within and surrounding the flame. Particle image velocimetry (PIV) offers a means of obtaining an instantaneous, two-dimensional velocity field and has gained considerable acceptance since its inception in the 1970's.

5.1 Image Acquisition and Analysis (Cross-Correlation Analysis)

Fluid velocity is inferred from the distance traveled by the tracer particles between laser pulses. However, due to the high particle density it is not possible to track individual particles so the average particle displacement is measured from small, local groups of particles. These small groups of particles, or interrogation spots, are evaluated by numerical correlation techniques in order to obtain displacement and thus an average velocity for a given interrogation area. Two images of the illuminated seed particles are captured by the TSI INSIGHT software, which uses a two-frame cross-correlation to compare the two images and determine the corresponding velocity field.

The 2048 x 2048 pixel images are divided into a number of 64 x 64 pixel interrogation spots, Figure 5.1a. Each interrogation spot had a corresponding image volume of 1.5 x 1.5 x 0.5 mm³ (23.43 μm/pixel). In nonreacting cases a smaller spot size could be used (i.e. 32x32 pixels), however due to the volume expansion across the flame surface a larger spot size is needed in order to obtain valid data in the less dense post-flame region. In order to improve the resolution, the interrogation spots are overlapped by 75%, satisfying the Nyquist criterion that requires grid spacing of ½ to 1/3 the interrogation spot size. This results in a total of 125 x 125 velocity vectors and a spatial resolution of 0.389 mm.

The cross-correlation of a pair of interrogation spots performs two fast Fourier transforms (FFTs) and produces a correlation function in which the location of the maximum represents the average particle in-plane displacement, and thus the U and V velocity components, for a given interrogation volume, Figure 5.1a. The additional peaks shown in Figure 5.1b are due to the fact that more than one particle pair exists within the interrogation spot. These smaller peaks represent the correlation of each particle image with each other particle image and can be

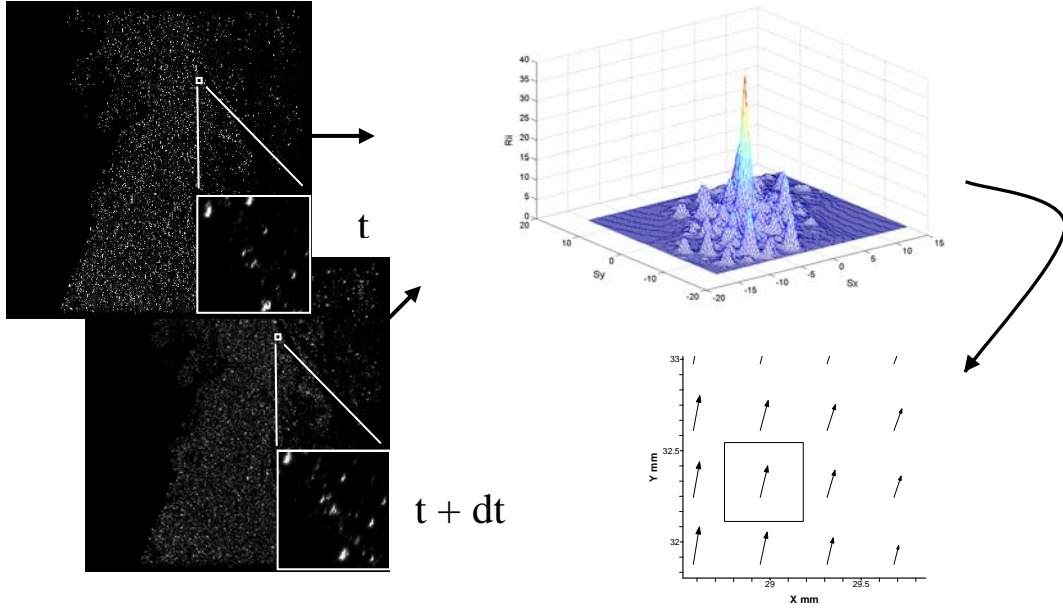


Figure 5.1: Pictorial description of double frame / single exposure cross correlation analysis used in particle image velocimetry.

considered as noise within the process. The resulting correlation function can be represented by the following decomposition

$$R_{II}(s, \Gamma, D) = R_C(s, \Gamma, D) + R_F(s, \Gamma, D) + R_D(s, \Gamma, D) \quad 5.1$$

where s is the separation vector in the correlation plane, Γ is the position vector at time “ t ” for all the particles inside the interrogation volume, and D is the displacement vector of all the particles. The term $R_D(s, \Gamma, D)$ represents the correlation of the of the particle images from the first exposure with the identical particle images from the second. The remaining two terms, R_C and R_F , are the mean background correlation and fluctuation in the background noise, respective. As previously stated, these smaller peaks are considered noise.

Double-frame single-exposure cross-correlation has a much higher signal-to-noise ratio than single-frame, double-exposure auto correlation. This is due to the fact that only particle images from time “ t ” are in image 1 and particles from time “ $t+dt$ ” are in image 2. In single-frame correlations particles images from both time steps are on the same image and this can

result in loss of correlation due to overlapping particles. Additionally, two-frame correlations do not have the directional ambiguity that occurs in single-frame since it is known which image occurs at time “t” and “t+dt”.

Once an initial assessment of the velocity vectors was obtained for an image pair a further validation procedure was performed to remove and replace erroneous, or outlying, data within the vector field. Typically only a small number of vectors (< 10%) were considered as outliers and were generally located at the extremes of the images. Figure 5.2a is an example of a “raw” vector field obtained from a PIV image pair of an oscillating flame and Figure 5.2b is the resulting field after passing through the validation process. Several things happen at the edges of the image which contribute to the erroneous vectors. First, due to the nature in which the flow was seeded not many particles are present at the extreme edges of the sample volume thus effecting the image correlations. Secondly, near the quartz tube wall some of the laser light was refracted resulting in non-homogenous illumination at these outreaching locations. The primary means of negating the effects of these outliers was to make the sample volume larger than the region of interest. However, due to some loss of correlation spurious vectors still occur in the primary region of interest. Following the correlation, the velocity fields are subjected to a validation process that applies a spatial filter to each vector. Vectors that are significantly different from their neighbors are removed and replaced.

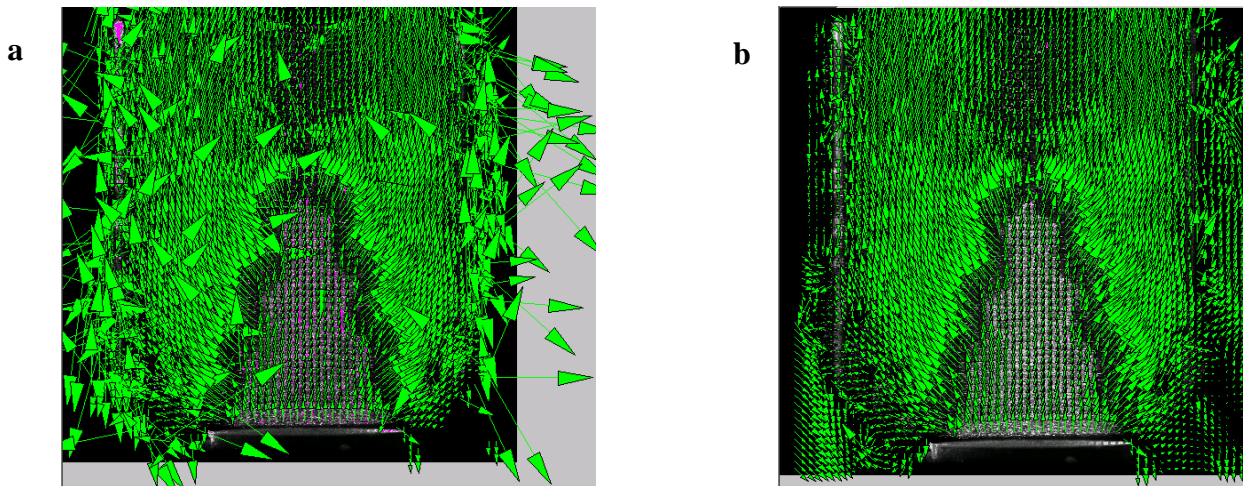


Figure 5.2: (a) Raw velocity vector image contains < 10% outliers. (b) Vector validation process removes outliers.

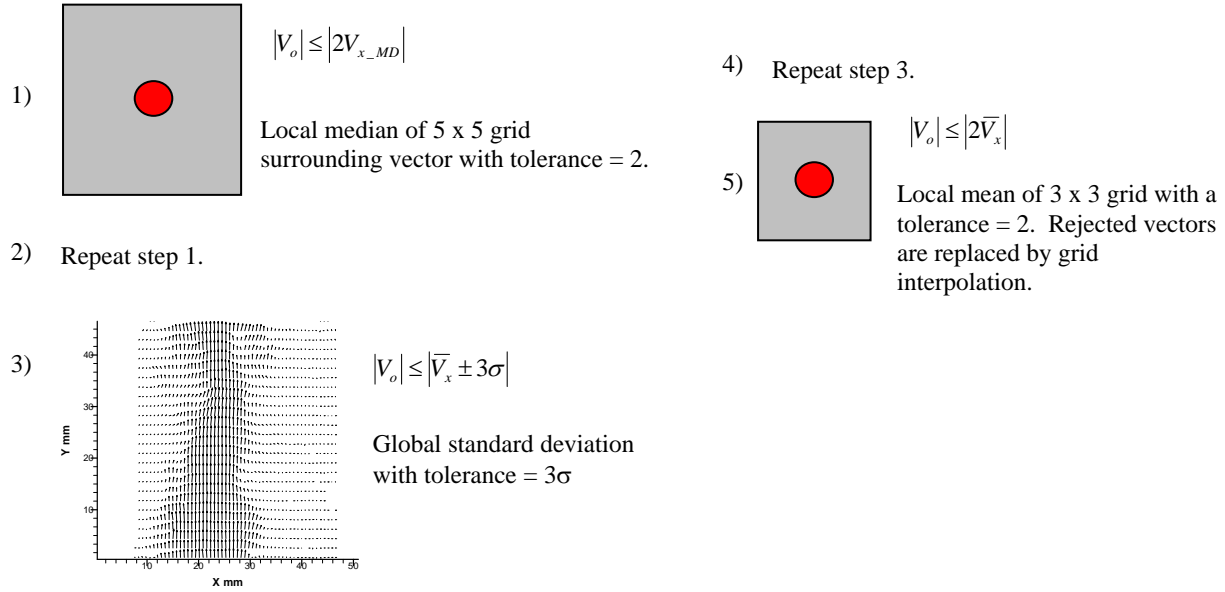


Figure 5.3: Velocity vector validation algorithm that removes spurious results.

The post-processing validation procedure in the TSI Insight software is user specified. For this study each “raw” velocity field was subjected to the same process. Figure 5.3 provides an outline of the validation procedure.

5.2 Dynamic ranges of velocity and spatial resolution

PIV correlation algorithms assign a velocity vector to a region based on the local mean particle displacement within that region. Thus aside from the errors associated with the correlation process, the accuracy of the measurement depends on how well the system can determine particle displacement within a given interrogation area. The uncertainty of this measurement can be described by an RMS error which can be shown to be a function of the optical resolution of the system.

An important parameter in the design of a PIV system is the dynamic velocity range (DVR) which is defined as the ratio between the maximum and minimum velocities that can be measured with a fixed set of instrumental parameters (Adrian³). This can be a significant quantity if a large velocity gradient exists over the field-of-view. Another related parameter is the dynamic spatial range (DSR) which is defined as the field-of-view of the image divided by the smallest resolvable spatial variation. Thus a large DVR and DSR would allow the measurement of small-scale variation embedded in larger-scale motion. Neglecting the noise in

the recorded images and assuming that the time separation between laser pulses can be accurately measured, these quantities depend primarily on the design of the optical system and the characteristics of the recording medium.

For each interrogation area a single velocity vector is given which represents the local mean displacement across the area over the pulse separation. Thus for flows in which there is a large velocity gradient over a small spatial regime (i.e. within the confines of the interrogation area) some of the data is lost due to spatial averaging. This indicates that even by overlapping the interrogation areas, the spatial resolution is limited to the size of the interrogation spot within the fluid, $d_i = D_i/M_o$, where D_i is the interrogation spot size on the image and M_o is the optical magnification.

5.3 Application of PIV to Reacting Flows

A typical PIV image of a stable laminar flame at an equivalence ratio of $\phi = 0.95$ and an average exit velocity of $V_{avg} = 1.63$ m/sec ($Re = 1520$) acquired for this study is presented in Figure 5.4a with the resulting velocity field shown in Figure 5.4b. One of the most pronounced characteristics of the image presented in Figure 5.4a is the large difference in seeding density due to the volume expansion across the flame surface. This volume expansion is a result of the temperature gradient that occurs across the pre-heat and reaction zones. The heavily seeded area is indicative of the cold pre-flame region which is bounded on the downstream side by the pre-heat zone. As expected for this low Reynold's number, the initial velocity profile shown in Figure 5.4b is the typical parabolic shape, which quickly flattens into a more uniform top-hat profile downstream from the exit nozzle. As the flow approaches the pre-heat zone a significant velocity increase occurs (volume expansion) which causes the seeding density to quickly dissipate throughout the downstream region of the burner.

The presence of the flame, and thus the resulting volume expansion across the flame surface, places some unique demands on the seeding density. Because the particles quickly dissipate after they cross the flame surface the use of typical seeding densities has limited reacting flow field analysis by PIV to pre-flame regions. However, in a study presented by Mungal and Lourenco⁸³ the authors were able to simultaneously measure the flow in the pre- and post-flame regions by utilizing a sufficiently high seeding density that was determined by trial and error.

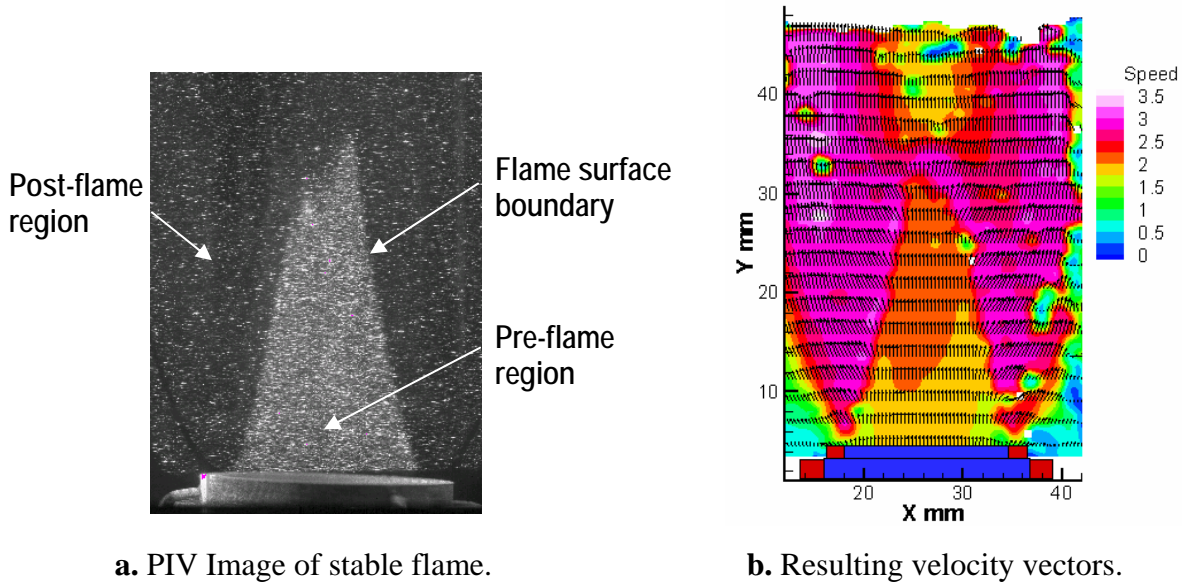


Figure 5.4: (a) PIV image of non-homogeneous seeding in a reacting flow field with pre- and post-flame regions and flame surface indicated. (b) Computed velocity field.

As a general rule of thumb, approximately 10 particle pairs per interrogation spot are suggested for highly reliable data (Adrian^{2,3} and Westerweel¹²²). If this is the desired particle concentration in the flow downstream of the flame, a much higher number density must occur in the cold flow region. As the flow crosses the flame surface, a volume expansion of approximately 6 - 7 times occurs (based on temperature), thus a particle concentration of 70 – 100 particles per interrogation spot is required in the cold flow region. Assuming an interrogation spot size of 64 x 64 pixels, which for this study is equivalent to 1.5 mm² and a sheet thickness of 0.5 mm, the resulting particle number density would be 62 – 89 particles/mm³ or 5.2 – 8.9x10¹⁰ particles/m³.

Figure 5.5a is an example of a conventional seeding level in a non-reacting flow field, $V_{\text{exit_avg}} = 1.25$ m/sec ($Re = 1144$), within the Rijke tube combustor. The accompanying velocity vectors are shown in Figure 5.5b. Based on the algorithms described earlier, only 0.02% of the vectors from this test were considered to be invalid. However, utilizing the same seeding rate in a reacting flow case (Figure 5.5c and 5.5d) at essentially the same conditions, $V_{\text{exit_avg}} = 1.63$ m/sec ($Re = 1520$), resulted in sparse data obtained in the post-flame region with 48.4% of the velocity vectors from Figure 5.5d invalid (thus not displayed).

Increasing the seeding density would produce “typical” seeding levels in the post-flame region, however overseeding could cause the cross-correlation algorithm to fail by overlapping

particles particularly in the cold, pre-flame regions. By utilizing the “real-time” capability of the TSI PIV system it was possible to adjust the seeding density and immediately analyze the images captured by the CCD array. Figure 5.5e is an example of a sufficiently high seeding density that allowed velocity data to be obtained simultaneously in the pre- and post-flame regions of the burner. Other than the seeding density, which was changed by adjusting the powder feeder screw rate and vibration, the operating conditions were left unchanged from those of Figure 5.5c and 5.5d. The resulting velocity field is shown in Figure 5.5f, with only 5.3% of the vectors considered invalid based on the same algorithm tolerances as used above. To ensure the seeding density was not excessive for cold, non-reacting flow conditions of Figure 5.5a were repeated at the high seeding level, Figure 5.5g and 5.5h. Only 0.04% of the vectors were considered invalid which is comparable to the level of invalid vectors obtained with the “typical” non-reacting seed level.

The variation in seeding density across the pre-heat and reaction zones is also the source of a small bias error in calculating the velocity vectors in this thin region. Conventional PIV algorithms depend on homogeneous seeding throughout the flow region of interest. Any variation, or non-homogeneity, in the seeding density could result in a bias of the spatial correlation within the interrogation spot towards the more densely seeded region. A common non-homogeneity occurs due to a Gaussian distribution of the laser sheet intensity so that the center of the image appears brighter than the edges. Unlike the seeding variation due to the large velocity gradients obtained in reacting fields, the length of this non-homogeneity is much larger (spanning the entire image field – e.g. 2048 pixels) than the scale of the interrogation spot size (e.g. 64 pixels) utilized by the algorithms to determine the local velocity field, and can generally be assumed to be negligible.

Previous PIV images of reacting flows from this study (e.g. Figures 5.4a and 5.5e) indicate a significant variation in the seeding density across a small region of the flow field as the gas volume expands across the flame surface. Since this velocity gradient occurs within a very short distance (i.e. across the flame surface), it is possible that the transition could exist within the bounds of the interrogation spot. Because the cross-correlation algorithm attempts to

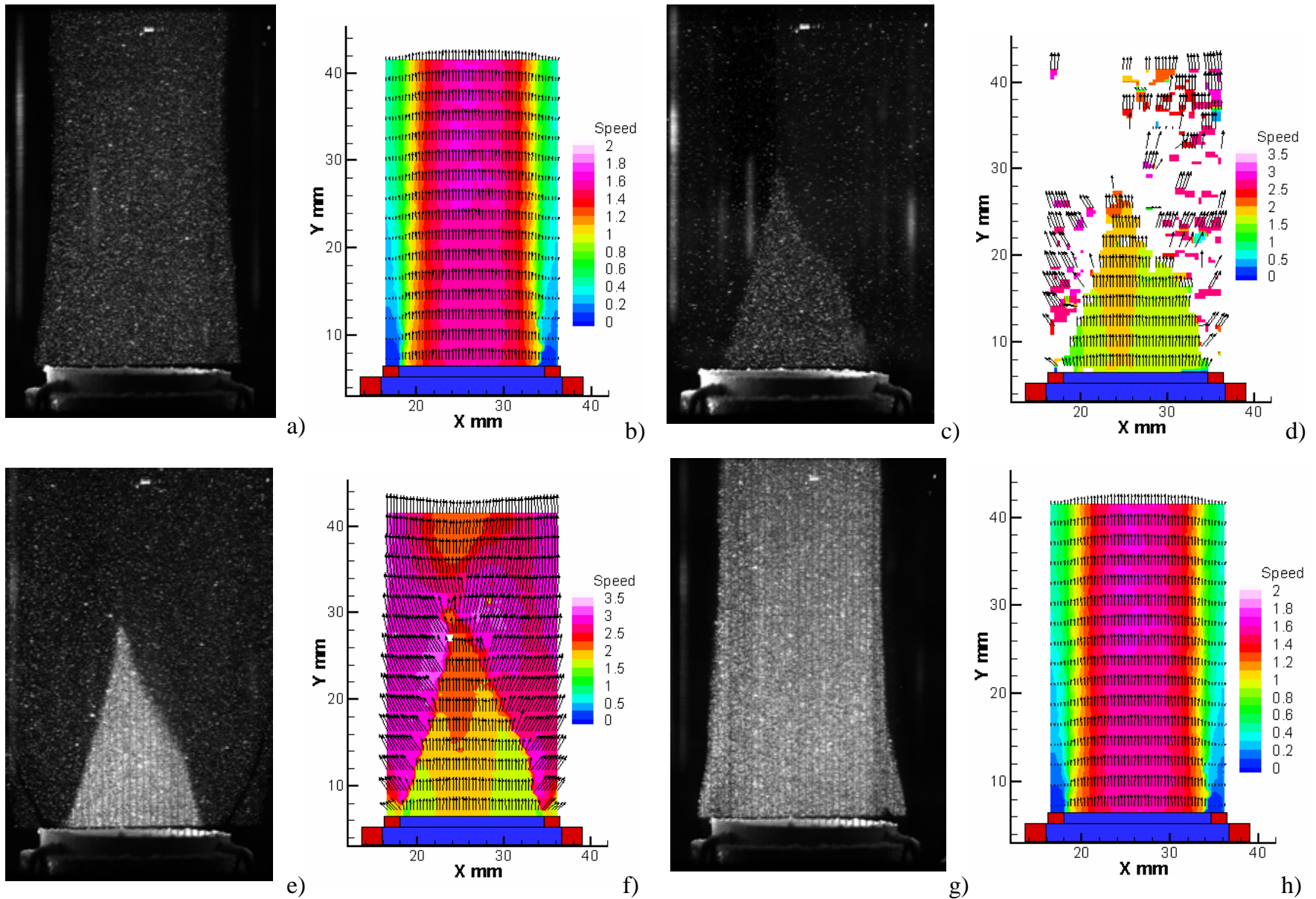


Figure 5.5 a and b) Light seeding for general non-reacting PIV and resulting velocity vectors, c and d) Insufficient seeding due to volume expansion across the flame surface, e and f) Heavy seeding in non-reacting flow, g and h) Valid velocity measurements in the pre- and post-flame regions.

identify a mean particle displacement for each interrogation spot, a bias error is created that results in a shifting of the correlation peak towards the displacement of the higher seeding density areas and a broadening of the peak occurs that increases the uncertainty in the estimation the mean displacement.

Figure 5.6a is again the PIV image of a stable laminar flame and the small highlighted block is the enlarged region shown in Figure 5.6c. The image intensity of this small block is row averaged and normalized by the maximum intensity of the overall PIV particle image, Figure 5.6d. Unlike the described gradual intensity change of the Gaussian laser sheet distribution, Figure 5.6d indicates a very dramatic change that occurs over just 8 pixels (944-952 pixel). This is further illustrated in Figure 5.6b which is a 64 x 64 pixel box similar in size to the interrogation spot size used for this study. As shown in this figure, the interrogation spot can contain a significant amount of both light and heavy seeding, with the light seeding area having fewer number of particle pairs thus biasing the heavily seeded, lower velocity region.

In an analysis of inhomogeneous image fields, Westerwell¹²² reported that the bias error is proportional to the amount of change in the image density across the interrogation spot and is only significant when the heavily seeded region occupies less than $\frac{1}{2}$ the interrogation spot size . For a 64 x 64 pixel interrogation spot size and a gradient of 8 pixels/64 pixel, Raffel et.al.¹⁰³ claims a bias error of approximately 2.0 pixels. This is rather significant given that the cross-correlation algorithm used here typically has a sub-pixel accuracy of less than 0.2 pixels (Westerweel¹²²). In terms of flame structure analysis, this bias error would act to extend the length of the preheat / reaction zone which can be identified by large velocity gradients in this region.

One method of eliminating or reducing the bias is to use uniform interrogation windows of different size, selecting a size for d_2 , the second window, such that a sufficient number of particle pairs will be obtained in both the light and heavily seeded regions. Otsuka and Wolanski⁸⁹ applied a slightly modified version of this method in an attempt to look at the flame structure of a flat flame propagating through a duct. The authors first decomposed the image into “brighter side” and “darker side” images, then analyzing these images individually. For this thesis however, although the bias error (~ 2.0 pixels) could be significant in comparison to the random error (< 0.2 pixels), no attempt to correct for this error was made since the overall effect on the velocity was negligible. The influence of the bias error was additionally decreased

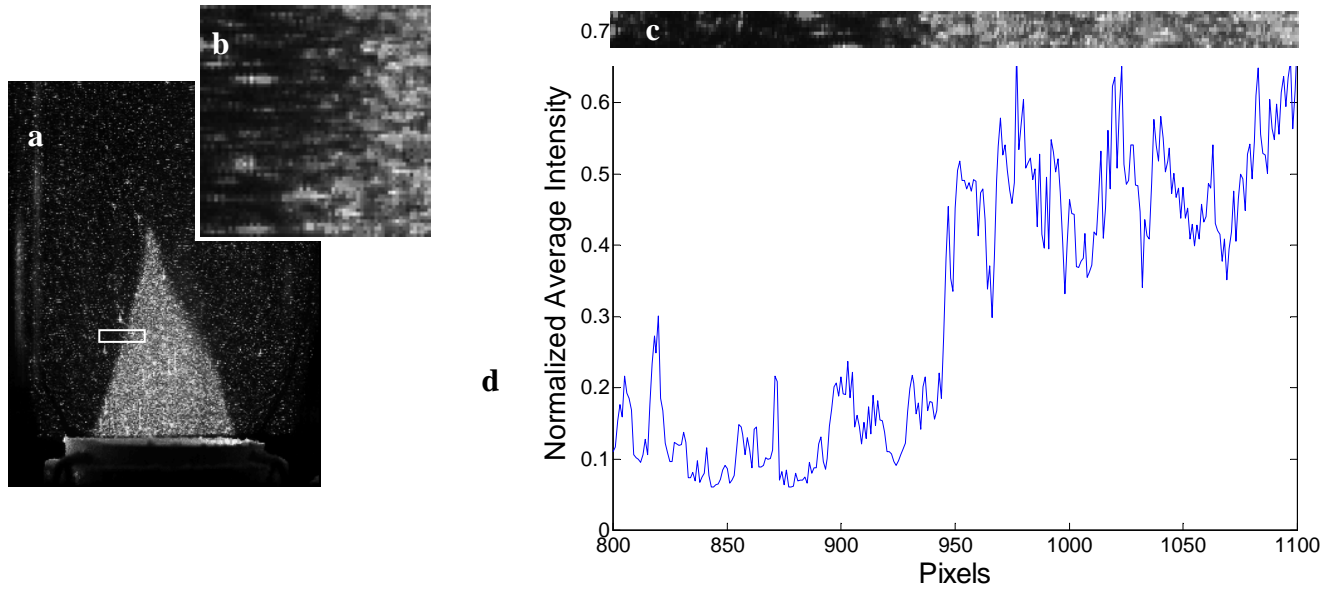


Figure 5.6: a) PIV image indicating large intensity gradient. b) Interrogation window with intensity gradient. c) close-up of region indicated on (a) with accompanying intensity profile (d).

through the use of window overlapping and post-processing validation (median filtering) mentioned above.

5.4 Tracer Particle Mobility

5.4.1 Frequency Response of Tracer Particles

When utilizing particles as a flow marker in a fluid consideration must be given to the particles' ability to accurately track the flow. Neglected electrostatic or magnetic forces and body forces due to centrifugal acceleration and gravity may influence particle motion. Particles unable to follow the flow can potentially lag behind or damp out fluid velocity changes, or may even fall out of the flow all together. Thus selection of tracer particles must compromise between sufficient light scattering efficiency and acceptable particle dynamics.

From Adrian^{2,3} an approximate description of the equation governing particle motion in a fluid is given by

$$\dot{v}_p = \frac{u(t) - v_p(t)}{\tau_p} + b \quad 5.2$$

Here $v_p(t)$ is the velocity of the particle, $u(x,t)$ is the Eulerian velocity of the fluid, and

$$u(t) = u[x_p(t), t] \quad 5.3$$

is the fluid velocity at the location of the particle, $x_p(t)$. The body forces, b , acting on the particle were previously mentioned, and τ_p is a time constant known as the particle relaxation time and is given by

$$\tau_p = \frac{\rho_p d_p^2}{18\mu_f} \quad 5.4$$

For the 1 μm alumina oxide particles used for this study the relaxation time is $\tau_p = 1.42 \times 10^{-5}$ sec.

Figure 5.7 is a representation of the possible error in flow velocity that may result from a departure of the tracer particle from the fluid trajectory due to inertia.

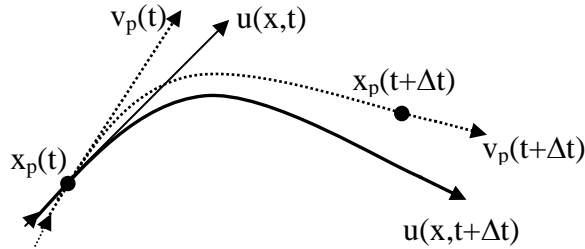


Figure 5.7: Representative difference between fluid pathline and particle trajectory. The marker particle departs from the Lagrangian trajectory of the fluid due to inertia.

For flow measurements in an oscillating field, the tracer particles must have a frequency response comparable or better than the expected fluid motion. In a Stokes regime where the Reynolds number, given as

$$\text{Re} = \frac{\rho_f (u_f - u_p) d_p}{\mu_f} \quad 5.5$$

is less than one, the amplitude frequency response and phase angle is given by Equations 5.5 and 5.6 (Spenik¹⁰¹, (REF), an experimental investigation of particle motion in pulsating turbulent pipe flow).

$$A_p(\omega) = \frac{1}{(1 + (\tau_p \omega)^2)^{1/2}} A_f(\omega) \tag{5.6}$$

$$\phi = \tan^{-1}(-\omega \tau_p)$$

A_f is the amplitude of the fluid oscillation, while A_p is the amplitude of the particle oscillations. For an ideal tracer particle the relaxation time would be equal to zero, thus allowing for the amplitude and phase to match that of the fluid.

Figure 5.8 is a plot of the particle amplitude response relative to the fluid amplitude and phase response at a range of frequencies from 0 to 1000 Hz for one micron alumina oxide particles in air. Based on these results, the particles will achieve at least 99.98% of the amplitude of the flow for the 230 Hz case with a phase difference of 1.176°, or a time lag of 1.42x10⁻⁵ sec. Given the relatively low-speed flows encountered in this study the resulting displacements errors are negligible.

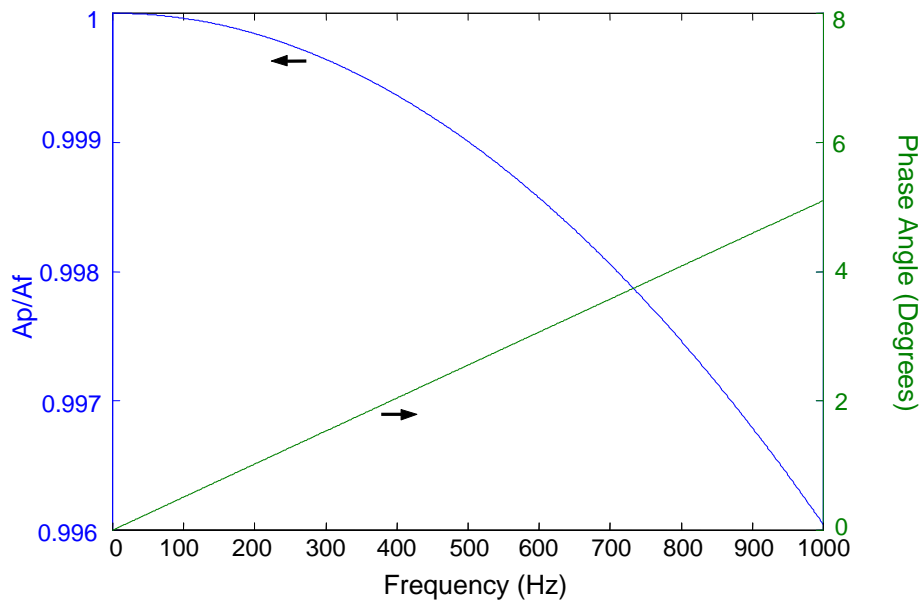


Figure 5.8: Particle amplitude response relative to the fluid amplitude and phase response for one micron alumina oxide particles in air.

5.4.2 Thermophoresis

A number of studies have sighted the effects of thermophoretic forces on particles in flames (Gomez and Rosner⁴⁴, Sung et al.^{118,119}). Thermophoresis is a force that drives particles suspended in a fluid, in which a temperature gradient exists, in a direction opposite of the temperature gradient. The local particle drift velocity due to thermophoretic forces as defined by Sung et al.¹¹⁸ is given by the following expression:

$$v_{TP} = \frac{-C}{3\pi\mu d_p} \cdot F_{TP} \quad 5.7$$

Where the thermophoretic force, F_{TP} , is a function of the temperature gradient and the resulting fluid velocity, v_F , is defined by the particle velocity, v_P , and thermophoretic velocity

$$v_F = v_P + v_{TP} \quad 5.8$$

Sung et al.^{118,119} noted that there was a significant influence on particle motion in regions of the flame with large temperature gradients, such as the preheat zone. As the particle flow approaches the reacting zone from the upstream side, the particles are slowed due to the thermophoretic forces, while the flow begins to speed up due to the temperature increase. Once the particle passes through the flame surface, or the maximum temperature, the thermophoretic force pushes it away from the reaction zone. Thus the speed of the particle will be greater than the speed of the flow. Depending on the magnitude of the velocity difference between the particles and the actual flow, a number of measured parameters may be affected. Under conditions similar to those of the present study, errors as large as 14 cm/sec were observed in the reaction zone. The author also noted that for flames of much higher flame speeds, such as hydrogen or enriched with oxygen, the effect may be even greater.

In a study by Mungal et al.⁸³ in which PIV was used to make velocity measurements in both the reacting and non-reacting regions of a laminar flame, it was estimated that thermophoretic forces slowed the total post-flame velocity from 295 cm/sec to 285 cm/sec resulting in an error of approximately 3.5%, and is comparable to the results of Sung et al.^{118,119}.

It is apparent that velocity variations due to thermophoretic forces can be the source of significant error in PIV measurements. It is possible to correct the measured particle velocity

with the corresponding local thermophoretic velocity if both temperature and velocity can be measured in during the experiment. Since pre- and post-flame flow temperatures were not collected it was not possible to apply a velocity correction, and given the similarity of the experimental flame used by Mungal et al⁸³ it is assumed that the measurements of the flow velocity along the reaction zones for this study include an estimated error of approximately 3.5%.

Chapter 6 Acoustic Velocity Measurement

Due to the measurement complexity, transfer functions describing the relationship between velocity modulations and variations in the heat release rate such as Fliefil et al.³⁹ are often derived from theory (Dowling^{30,31}, Lieuwen^{71,72}). Although limited in number, several studies have attempted to perform experimental derivations of these transfer functions (Kruger et al.^{64,65}, Schuermans et al.¹¹⁴, Paschereit and Polifke⁹²). Khanna⁵⁸ and Ducruix et al.³³ produced flame response models from measured values of velocity modulation and heat release rates. These studies each utilized different methods to measure the acoustic velocity, with Khanna^{58,59} using a variation of the two-microphone technique which solved a 1-D Euler equation to obtain the amplitude of the velocity perturbations and Ducruix et al.³³ measuring velocity modulations at the burner exit by laser Doppler velocimetry (LDV). Both of these measurements have the advantage of being time resolved, which can easily be decomposed in the frequency domain in order to relate it with the acoustic properties of the overall system. However, as both authors pointed out, these measurements lacked two-dimensionality which prohibited the analysis of multi-dimensional near-flame, or near-field, acoustics.

In Chapter 10 of this thesis we will take a closer look at the effects of near-field acoustics on the flame response by comparing experimental results to the theoretical study performed by Lee and Lieuwen⁶⁸. The intent of this chapter is to provide background information on the two methods used to measure the acoustic velocity. The PIV method provides a 2-dimensional analysis of the velocity field both in the cold and hot regions of the flame. However it is difficult to obtain a spectral analysis of the results. The two-microphone technique, on the other hand, can easily be decomposed into its frequency components, but is a 1-D and is not a direct measurement of velocity. Both of the techniques are described in detail below.

6.1 PIV Measurement

It is believed that the acoustic near-field of the flame is composed of a complex superposition of one-dimensional propagating waves and three-dimensional evanescent waves. These evanescent waves only have a local effect on the acoustic fields since they decay exponentially with distance from the flame. Thus having the ability to simultaneously capture both the radial and axial velocities at numerous locations over a relatively large region provides the means to evaluate the evanescent effects of the acoustic waves.

In order to time resolve flow field events with the measured acoustic and heat release rate signals, the PIV measurement was phase locked with the perturbation. The use of this phase-locking process was made possible by the highly repeatable nature of the oscillating flame being studied. PIV sampling occurred at 10° of phase and each time step was averaged over five image pairs. Examples of the localized standard deviations in the axial (v') and radial (u') perturbation velocities with respect to the average bulk velocity at one time step are shown in Figures 6.1a and 6.1b, respectively. In the pre-flame region, which is the area used to evaluate the near-field acoustics, the sample to sample variation is less than 10% of the average bulk flow.

As previously noted, the pressure signal from the microphone at the exit of the nozzle was used as a trigger signal for the PIV synchronizer. In a standing wave configuration, such as this one, the acoustic velocity lags the pressure by $\pi/2$ (Figure 6.2). This can be seen in the maps of the velocity vectors isolating the area at the exit of the burner nozzle in the pre-flame region. Figure 6.3 shows a selection of velocity vector maps that represent particle motion over one cycle. These maps were taken from the results of a self-excited flow with the flame surface indicated by the flow dilatation ($\phi = 0.95$, $U_{\text{mean}} = 1.65$ m/sec). Subtracting the mean flow highlights the sinusoidal variation in the velocity. In reference to the pressure signal measured at the burner outlet, Figure 6.3(a) occurs at a phase angle of 0° and indicates a large downward velocity at the outlet. This agrees with the standing wave shown in Figure 6.2. As we follow the cycle, Figure 6.3(b) represents the acoustic velocity at a phase delay of 80° where the particle velocity has slowed to almost zero. The particle velocity then begins to increase as it reaches its maximum positive amplitude at a phase delay of 180° , Figure 6.3(c). At a phase angle of 270° the acoustic pressure has reached its maximum negative amplitude, thus the acoustic particle velocity once again begins to approach zero as shown in Figure 6.3(d).

Observing the axial velocity at one location ($x/R = 0$, $y/H_f = 0.05$) over the cycle gives a complete time history of the flow at that location, Figure 6.4. Again, Time = 0 msec is in reference to a phase angle of 0° in relation to the acoustic pressure signal. A more detailed analysis of the reacting and non-reacting flow fields at various flow conditions, equivalence ratios and forced excitations is provided in Chapter 8.

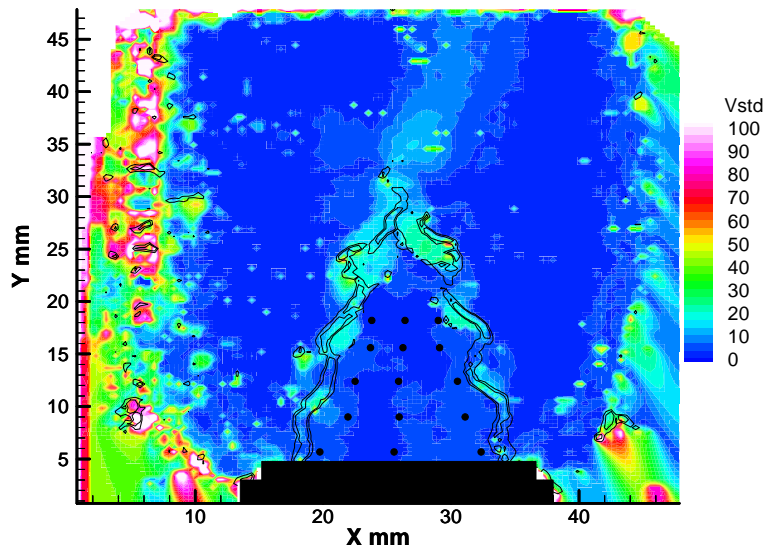


Figure 6.1: (a) Standard deviation of axial velocity, V , as a percentage of localized average for 5 frames of PIV results of a self-excited flame (Phase 120°)

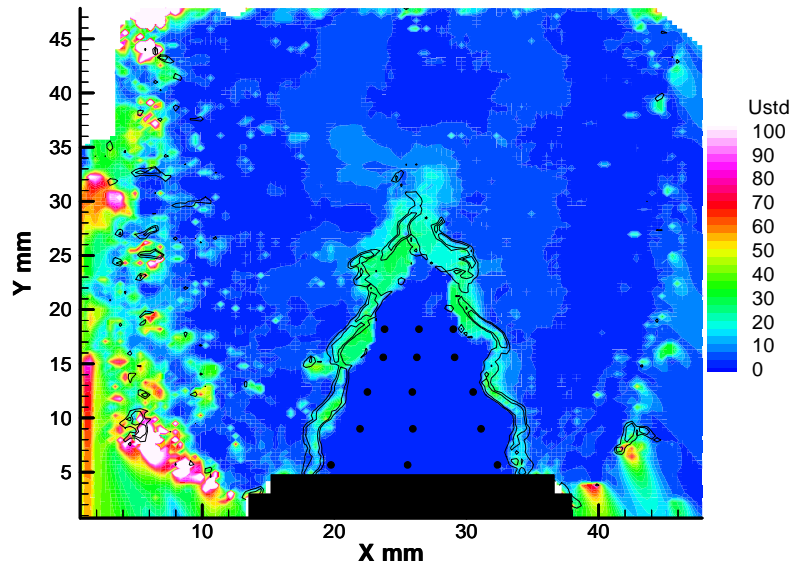


Figure 6.1: (b) Standard deviation of radial velocity, U , as a percentage of localized average for 5 frames of PIV results of a self-excited flame (Phase 120°).

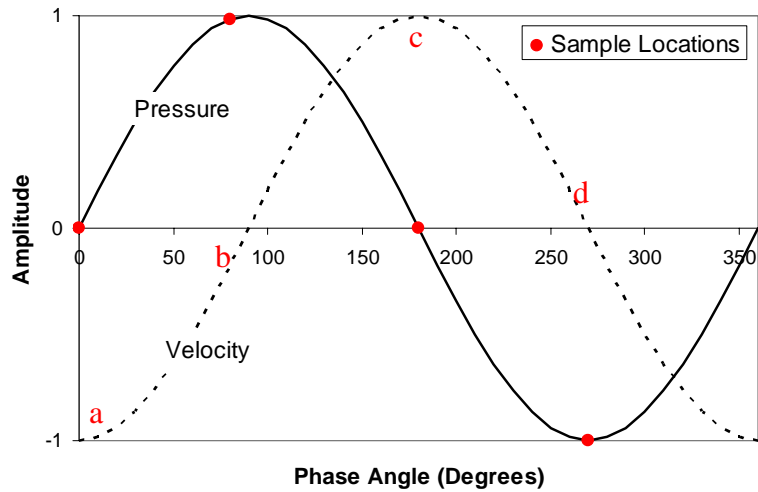


Figure 6.2: Acoustic velocity lags acoustic pressure by 90° in a standing wave. Sample location are indicated for the velocity maps shown in Figure 6.4.

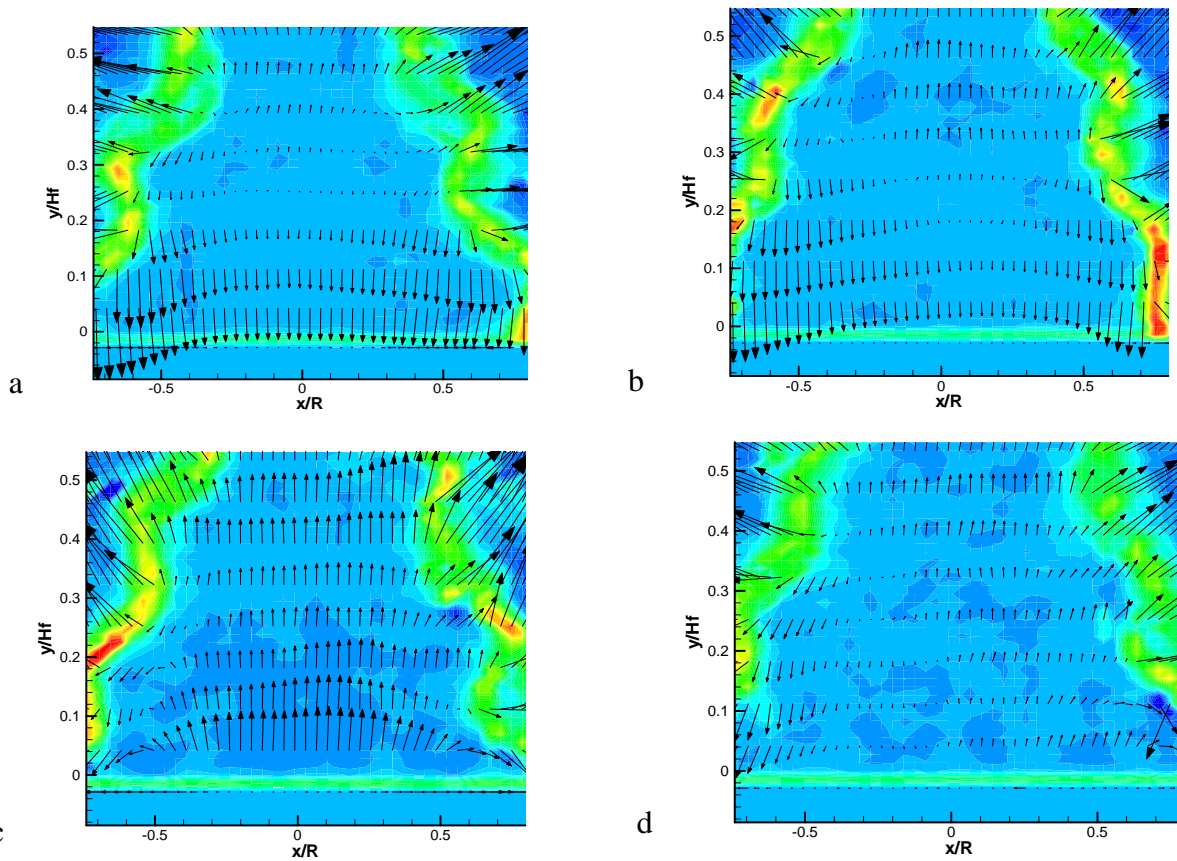


Figure 6.3: Axial velocity vector maps (with bulk mean velocity removed) at the burner exit for self-excited flame showing sinusoidal response of the flow. PIV trigger phase-locked to the acoustic pressure measured at the burner exit: a) 0° , b) 80° , c) 180° , and d) 270° .

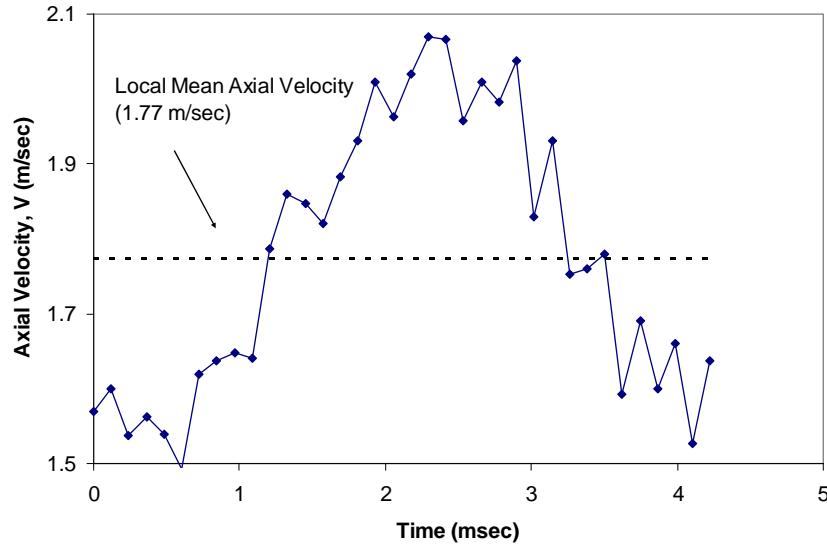


Figure 6.4: Composite time history of the axial velocity measured at $x/R = 0.0$ and $y/Hf = 0.05$.

6.2 Two-Microphone Technique

Experimental techniques such as laser Doppler anemometry (LDA), hot wire anemometry (HWA) and particle image velocimetry (PIV) are all capable of measuring small perturbations within a larger mean flow. However, these methods utilize expensive hardware and the data post-processing necessary to obtain the acoustic velocity can be quite complex. Fortunately, with a simple knowledge of the governing flow equations and / or acoustics it is possible to obtain an accurate measurement of the acoustic mass velocity.

Khanna^{58,59} used a standing wave tube based on the Euler equation in order to determine the acoustic velocity in a similar system.

$$u'(t) = \frac{-1}{\rho} \int \frac{\partial p'}{\partial x} \partial t \quad 6.1$$

However, this approach was somewhat bulky and involved some inherent error due to the approximation of the spatial pressure derivative by finite difference method.

$$\frac{\partial p'}{\partial x} = \frac{P_2 - P_1}{\Delta x} \quad 6.2$$

An alternative is to utilize an adaptation of the two-microphone technique described by Munjal⁸³ and Cheng and Blaser²¹. This method relies on the transfer matrix model discussed in Chapter 4. Two microphones located some distance L apart across an element provide a measure of the acoustic pressures at two locations, Figure 6.5. With the known transfer matrix relating the state variables across the element, the system can be solved for the acoustic velocities.

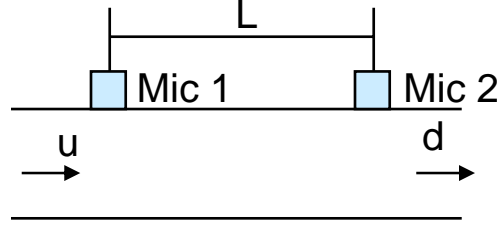


Figure 6.5: Pictorial description of the two microphone method.

The burner nozzle can be modeled as a uniform tube with the transfer matrix given as follows

$$\begin{bmatrix} p_d \\ u_d \end{bmatrix} = \begin{bmatrix} \cos(kL) & i\eta \sin(kL) \\ \frac{i}{\eta} \sin(kL) & \cos(kL) \end{bmatrix} * \begin{bmatrix} p_u \\ u_u \end{bmatrix} \quad 6.3$$

Solving for the velocities

$$\begin{aligned} u_d &= \frac{i}{\eta} \sin(kL) p_u + \cos(kL) \left[\frac{p_d - \cos(kL) p_u}{i\eta \sin(kL)} \right] \\ u_u &= \frac{p_d - \cos(kL) p_u}{i\eta \sin(kL)} \end{aligned} \quad 6.4$$

The signals from the two microphones were collected by the data acquisition system and calculation of the acoustic velocity is handled off-line. During the post processing, the Fourier transforms of the pressure signals were obtained and used to solve Equations 6.4, resulting in a amplitude and phase response of the acoustic velocity at a number of frequencies. Once the acoustic state variables are known at a given location it is possible to find them at other locations within the nozzle by applying Equation 6.3.

Two microphones (Knowles FG-3329 electret condenser microphones) are positioned in the nozzle upstream of the exit (Figure 3.1), at 0.19m and 0.34 m from the base of the nozzle and measure

the acoustic pressure entering the reaction zone. These are AC measurement devices and in order to relate RMS pressures to operating pressures ($\text{Pa} = \text{N}/\text{m}^2$), the frequency response of each microphone was evaluated against a sound level meter in which the output is given in sound pressure level (SPL). SPL can be related to the RMS measured effective pressure of a given acoustic field (P_e) by the following relationship

$$\text{SPL} = 20 \cdot \log(P_e / P_{\text{ref}}) \quad 6.5$$

$P_{\text{ref}} = 20 \mu\text{Pa}$ is the threshold of human hearing and is the effective reference pressure for air. As an example the sound pressure level corresponding to an RMS sound pressure of $1 \text{ N}/\text{m}^2$ is given in decibels as $\text{SPL} = 20 \cdot \log(1/0.00002) = 94 \text{ dB}$. Calibration of the microphones and amplification circuitry ensured that their frequency response characteristics were consistent from one device to another. The calibration included both the microphone and the amplifier circuit.

With microphones “1” and “2” placed adjacent in a varying acoustic field along with the sound pressure meter, it was possible to relate the RMS voltage response of the microphones to an equivalent measurement in units of pressure (Pa). Figure 6.6 indicates that both microphones behave linearly when subjected to an acoustic field and a proportionality constant of $P_{\text{gain}} = 26.6 \text{ Pa}/\text{Volts}$ was used for both microphones.

The response characteristic of the microphones at different frequencies (frequency response function) is also of some concern. Ideally, both microphones would have an identical frequency response characteristic, in which the frequency response function (ratio of the response of MIC 1 to

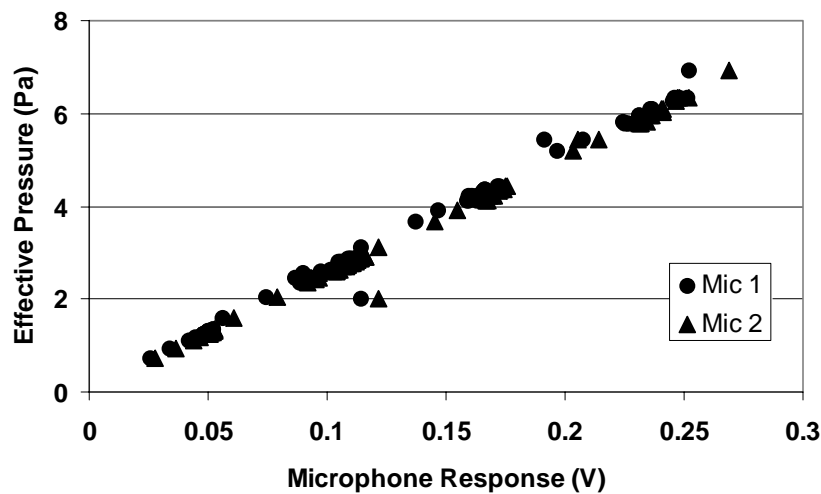


Figure 6.6: Relating microphone response (volts) to effective pressure (Pa)

MIC 2) would have a magnitude of zero dB and a phase of zero. However, this is an unrealistic expectation, thus an acceptable level of tolerance of $0.0 \pm 0.5\text{dB}$ in magnitude and $0.0 \pm 5^\circ$ in phase was set based on the desired accuracy of the two-microphone technique to determine the acoustic mass velocity. The high phase angle allowance is due to the fact that sampling by PIV and CCD result in averaging the flame response over approximately 10° .

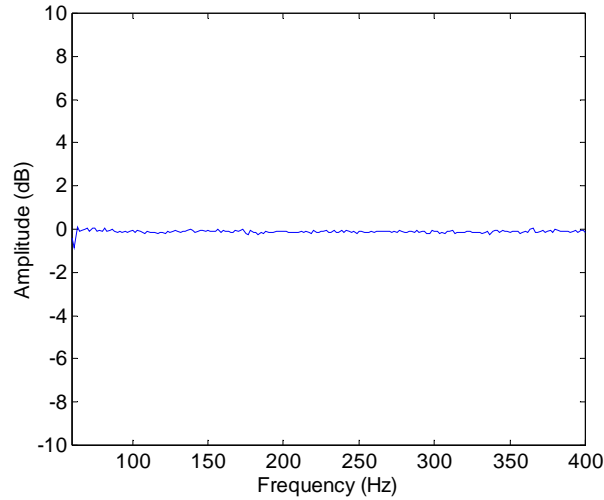


Figure 6.7: Frequency response – magnitude of microphone 1 to microphone 2.

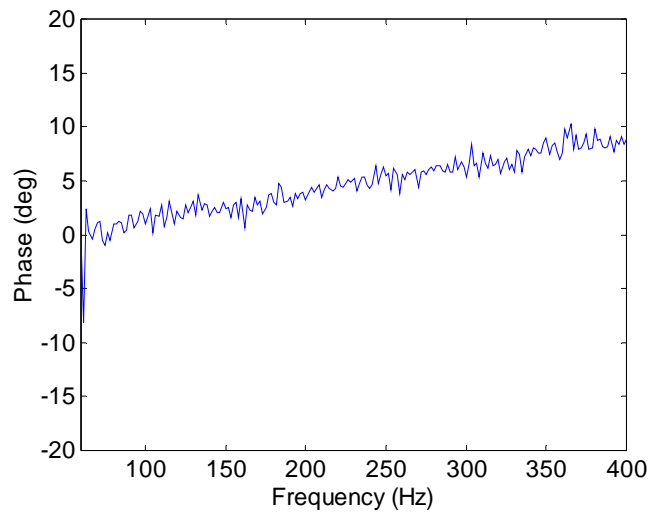


Figure 6.8: Phase response of microphone 1 to microphone 2.

To evaluate the frequency response characteristics from the microphones, they were placed in an acoustic field in which a function generator, whose output was used to drive a speaker, sweep through a frequency range of 1 to 500 Hz in 1 Hz increments at a rate of 500 Hz. Figures 6.7 and 6.8 show the frequency response functions for magnitude and phase, respectively. The magnitude is clearly within the desired tolerance, however at the higher frequencies ($F > 250$ Hz), the phase exceeds the limits with a maximum difference of 8.7° at a frequency of 400 Hz. The monotonically increasing difference in the phase angle suggests a pure time lag between the microphones which is approximately 60 μsec . This was determined to have a maximum impact of 3° on the phase of the resulting acoustic velocity measurement and no effect on its magnitude for a disturbance at 230 Hz which is within the desired tolerance.

The mounting location and separation distance of the two microphones within the Rijke burner nozzle was selected based on the wavelength of the expected perturbations. Cheng and Blaser²¹ indicate the microphone spacing, δ , must not be an integer multiple of the half-wavelength ($\lambda/2$) of the maximum frequency being considered. Thus

$$\delta \leq \frac{c}{2f_{\max}} \quad 6.6$$

In the experimental system shown in Figure 6.6, the microphone spacing is $L = 0.15$ m and with a speed of sound of 330 m/sec, the maximum frequency that could be evaluated is 1100 Hz. This is well above the frequencies considered in this study.

In a standing wave the nodes, plane of zero amplitude, are fixed in space for a given signal (Figure 6.9). To accurately measure the acoustic velocity using the two-microphone technique, the microphones must be located away from the expected pressure nodes. Measuring the coherence between the input to the base mounted speaker (Figure 3.9c) and the response from microphones “1” and “2” over a range of frequencies it is possible to identify frequencies that may produce a node at one of the measurement planes. The speaker supplied a signal sweeping through frequencies between 1 and 500 Hz in increments of 1 Hz. It should be noted that under normal operation perturbations in the burner are limited to one or two frequencies; however sweeping the frequencies as done here is a quick way to evaluate a large number of frequencies.

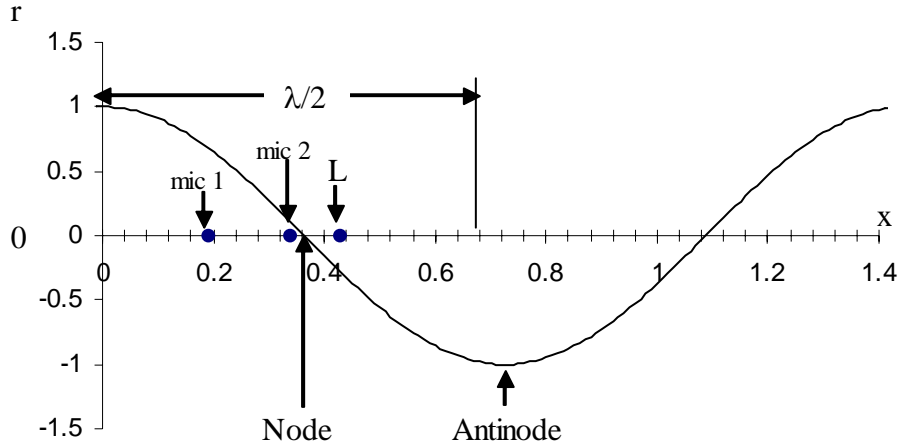


Figure 6.9: Microphone placement with respect to the wavelength of a 230 Hz standing wave in the Rijke tube burner nozzle.

From Figure 6.10 it can be seen that for all frequencies between 50 and 580 the coherence between the speaker input and both microphones is above 0.85, except at 211 and 411 Hz. At 211 a node occurs at 0.39 m from the speaker which is the location of Mic “2”, thus while the coherence is greater than 0.9 between the speaker input and Mic “1”, it is less than 0.7 between Mic “2” and the speaker input. A frequency of 411 Hz results in a pressure node at Mic “1” (0.2 m). The sharp drop in coherence at 314 Hz is an artifact of the frequency sweeping of the function generator. The coherence between Mic “1” and “2” is high at this frequency and single frequency excitation produced high coherence (Figure 6.11). Physically, this means that the two microphones should accurately measure the perturbation velocity (v') at all frequencies in the range of 50 – 580 Hz, except at 211 and 411 Hz due to the presence of pressure nodes at the microphone locations. As will be shown, the proximity of the node to Mic “2” at the flame oscillation frequency complicates the analysis of some of the results when the flame is acoustically-driven at high amplitudes.

6.3 Comparison between the two-microphone method and PIV measurement

The influence of the acoustic velocity on the actual flame response is reserved for a later discussion in this study (Section 8). The current analysis is intended to compare the two previously discussed methods for evaluating the acoustic velocity in the Rijke tube combustor.

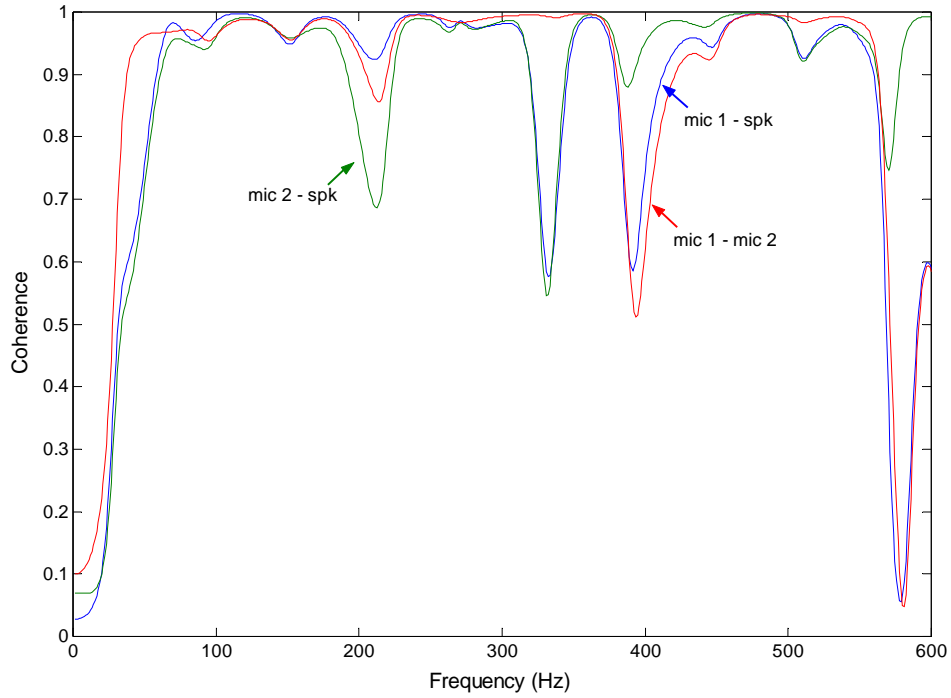


Figure 6.10: Coherence between microphone 1, 2 and speaker input in response to frequency sweep from 1 to 500 Hz.

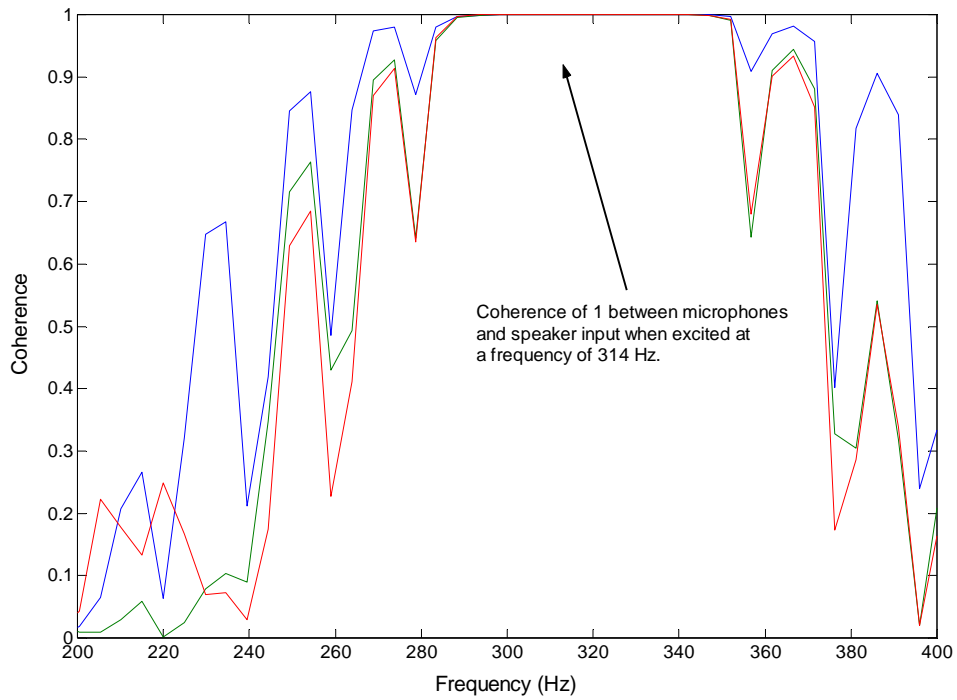


Figure 6.11: Coherence between microphone 1 and 2 and speaker input in response to single frequency input at 314 Hz.

The two methods introduced above are considerably different in their measurement of the acoustic velocity. The PIV method provides a direct measurement of the velocity and by subtracting the mean, the acoustic velocity is readily attained. With the two-microphone method the acoustic velocity is inferred from the acoustic pressure measurement through standing wave relationships. These techniques additionally differ by the fact that the two-microphone process produces a non-dimensional quantity in the frequency domain while PIV provides two-dimensional velocity vectors in the time domain. However, acquisition by the PIV method is considerably more time consuming since the process must be repeated at each time step.

Velocity perturbations in the burner are characterized by a frequency, F , and an intensity, i_p , which is defined as the ratio of the root-mean-squared (rms) amplitude of the velocity fluctuations to the mean flow velocity. Using the transfer matrix approach outlined in the two-microphone method provides a means of extrapolating the velocity fluctuations to the exit of the burner nozzle. The velocity fluctuation intensity, i_p , can be obtained given the fact that the mean square value of the time domain sample is equal to the total area under a curve of the power spectral density function versus frequency, Equation 6.7. The intensity is obtained by taking the square root of Equation 6.7 and dividing by the mean flow velocity.

$$\Psi_v^2 = \int_0^{\infty} G_v(f) df \quad 6.7$$

$$i_p = \Psi_v / \bar{V}$$

Because the PIV method was rather time consuming only four test cases were considered in sufficient detail to properly evaluate the acoustic velocity. Pressure measurements used by the two-microphone method were collected at several instances during a PIV test sequence. The acoustic intensity obtained from PIV are determined from time-resolved measurements at $y/H_f = 0$ and $x/R = 0$ (at the nozzle exit along the centerline). Table 6.1 lists the test conditions and results from each measurement technique. Agreement between the two methods was exceptionally good at the nozzle outlet ($y/H_f = 0.0$) where the flow exiting the nozzle is still primarily one-dimensional. The acoustic velocity will be discussed in greater detail in Chapter 8.

Table 6.1: Measurement method comparison of acoustic velocity intensity at burner exit.

Excitation Method	St_{flow}	ϕ	V_{mean} (m/sec)	i_{p_piv}	i_{p_mic}
SE	1.70	0.95	1.54	0.16 ± 0.006	0.14 ± 0.01
FE	1.64	0.95	1.4	0.22 ± 0.009	0.25 ± 0.02
FE	0.42	0.95	1.78	0.18 ± 0.007	0.12 ± 0.01
FE	0.62	non-reacting	1.21	0.15 ± 0.006	0.12 ± 0.01

SE = Self-excited; FE = Forced excitation

Chapter 7 General Flame Response

The intent of this chapter is to provide a general overview of the response of the flame to various test conditions as outlined in Table 7.1. From these accounts it is possible to establish an operational map that defines the stability boundaries of the Rijke tube combustor used in this study. Utilizing relationships between the velocity intensity ($i_p = v'/V_{\text{mean}}$), acoustic pressure (p') and variable heat release rate (q'), it is possible to show stark difference between a stable and unstable flame as well as the sharp boundary that separates the two regimes. More in depth analysis of the influence of variable flame surface area (Chapter 8), excitation amplitude and transfer function derivation (Chapter 9), and finally near-field acoustics and flow field effects (Chapter 10) will follow in subsequent chapters.

7.1 Unstable Flame Response

Figure 3.9, redrawn here, shows three configurations utilized to control the flame response for this study: a) self-excited flame in which the flame is inherently unstable over much of the operating range, b) acoustically forced by an external driver (loudspeaker) in which flames that appear to be marginally stable are driven to oscillation (no change in nozzle impedance from configuration 3.9a), and c) acoustically forcing a stable flame by an in-line loudspeaker, where the flame is made stable by adjusting the upstream acoustic boundary conditions of the burner nozzle (nozzle impedance altered).

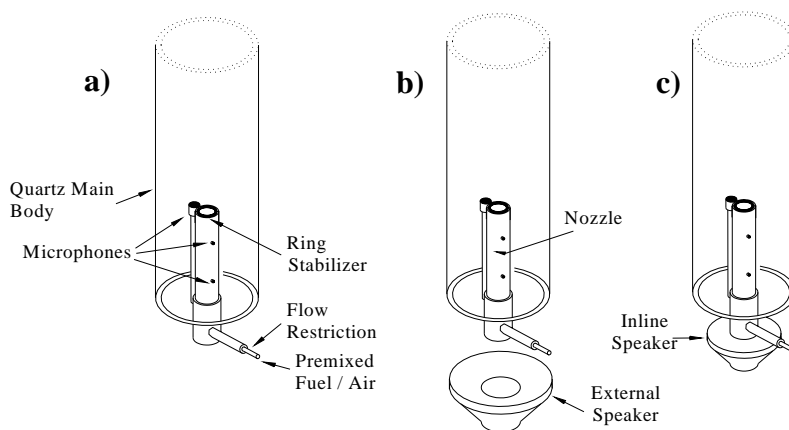


Figure 3.9: Operational configurations for flow and flame excitation.

Table 7.1 provides a general overview of the response of the flame at nozzle exit flows ranging from $V = 1.0 - 2.1$ m/sec and equivalence ratios of $\phi = 0.6 - 1.1$ with the burner in configurations 3.9a and b. For these initial tests the two microphones in the nozzle body were not in place, thus it was not possible to utilize the two-microphone technique to determine the acoustic velocity, v' . An approximate value of v' was obtained from a p' - v' look-up table created by acoustically forcing the flame (discussed in Chapter 9). The velocity intensity is taken as the ratio of rms velocity perturbation to mean flow at the nozzle exit, $i_p = v'/V_{\text{mean}}$, and indicates the intensity of the acoustic disturbance. It is shown in Table 7.1 along with the measured pressure response, p' (Pa), and a corresponding image of the flame.

With the burner assembly in the configuration shown in Figure 3.9(a) the system was found to be inherently unstable at all flows and for equivalence ratios between $\phi = 0.7 - 1.0$. Peak instability occurred at equivalence ratios between $\phi = 0.9 - 1.0$. Instabilities are said to occur when there is a noticeable peak above the background noise in the frequency spectrum as shown in Figure 7.1. Given the operating conditions and burner configuration the frequency range was rather limited, as expected, ranging from $F = 220 - 230$ Hz. These frequencies were close to the theoretical fundamental acoustic frequency of the Rijke tube, which can be considered analogous to a half-wave resonator, and was

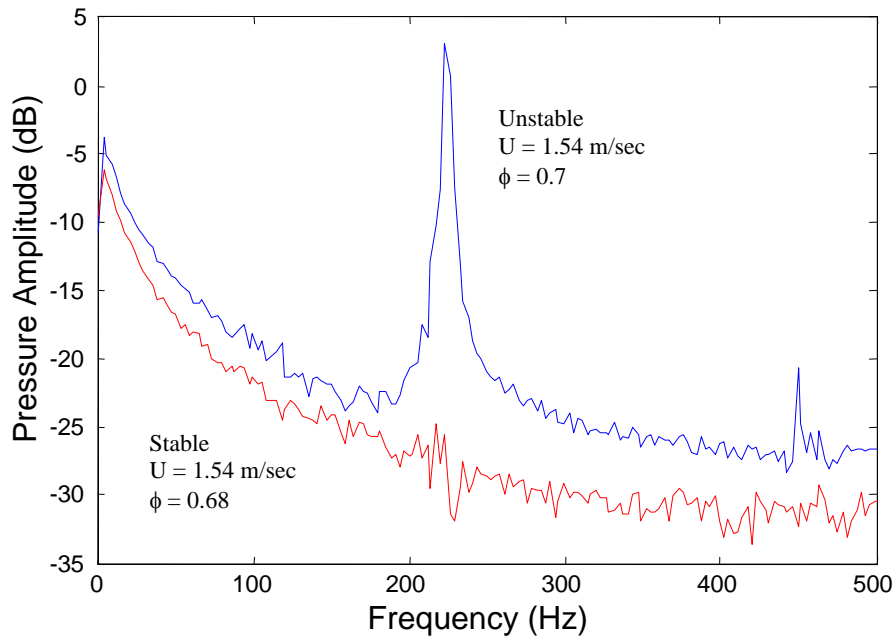
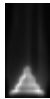
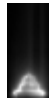
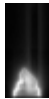

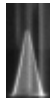

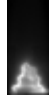
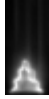






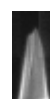

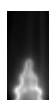
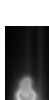

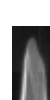

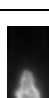

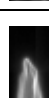
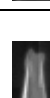
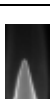
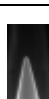

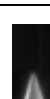
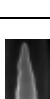
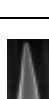




Figure 7.1: Spectral response of the burner under stable and unstable (self-excited) operation. Notice the small change in equivalence ratio between the two conditions.

TABLE 7.1: Flame Response to Changes in Nozzle Exit Velocity and Equivalence Ratio for a laminar Bunsen Flame.

Nozzle Exit Velocity (m/sec)	Equivalence Ratio				
	$\phi=1.0$	$\phi=0.9$	$\phi=0.8$	$\phi=0.7$	$\phi=0.6$
1.0	$P' = 85.0$ $i_p = 0.27$ 	$P' = 87.7$ $i_p = 0.28$ 	$P' = 63.5$ $i_p = 0.21$ 	$P' = 14.4$ $i_p = 0.05$ 	$P' = 8.5$ $i_p = 0.031$ 
1.4	$P' = 89.1$ $i_p = 0.192$ 	$P' = 77.3$ $i_p = 0.165$ 	$P' = 67.3$ $i_p = 0.144$ 	$P' = 31.0$ $i_p = 0.07$ 	$P' = 10.6$ $i_p = 0.027$ 
1.54	$P' = 87.6$ $i_p = 0.168$ 	$P' = 80.1$ $i_p = 0.156$ 	$P' = 64.0$ $i_p = 0.125$ 	$P' = 28.4$ $i_p = 0.058$ 	$P' = 12.8$ $i_p = 0.028$ 
1.75	$P' = 87.3$ $i_p = 0.137$ 	$P' = 78.8$ $i_p = 0.125$ 	$P' = 77.2$ $i_p = 0.122$ 	$P' = 22.1$ $i_p = 0.04$ 	$P' = 12.39$ $i_p = 0.026$ 
2.1	$P' = 75.5$ $i_p = 0.095$ 	$P' = 77.1$ $i_p = 0.096$ 	$P' = 63.9$ $i_p = 0.082$ 	$P' = 17.6$ $i_p = 0.031$ 	$P' = 11.5$ $i_p = 0.025$ 
1.0 Excited	$\phi = 1.1$ $P' = 50.8$ $i_p = .166$ 	$\phi = 1.1$ $P' = 12.1$ $i_p = 0.042$ 		$\phi = 0.68$ $P' = 38.7$ $i_p = 0.127$ 	$\phi = 0.68$ $P' = 10.9$ $i_p = 0.038$ 
1.54 Excited	$\phi = 1.1$ $P' = 48.8$ $i_p = 0.097$ 	$\phi = 1.1$ $P' = 11.3$ $i_p = 0.025$ 		$\phi = 0.68$ $P' = 37.4$ $i_p = 0.075$ 	$\phi = 0.68$ $P' = 11.4$ $i_p = 0.025$ 

(P' – R.M.S. pressure (Pa), i_p = velocity intensity (v^2/V_{mean}))

found to be approximately $F_{\text{fund}} = 214$ Hz for non-reacting flows at standard temperature and pressure. Heat from the flame raises the temperature of the flow downstream of the nozzle exit resulting in an increase in the speed of sound and thus a slightly higher acoustic frequency.

The oscillation frequency can also be given in non-dimensional form as the Strouhal number which represents a ratio of the inertial forces due to the unsteadiness of the flow to the inertial forces due to changes in velocity from point to point in the flow field and is given by the following

$$St_D = \frac{fD}{V_{\text{mean}}} \quad 7.1$$

Here f is the oscillation frequency, D is the nozzle exit diameter and V_{mean} is the mean flow velocity at the nozzle exit. Thus for the self-excited flame discussed in this study the Strouhal number ranges from $St_D \approx 2.0 - 4.0$

The images of the flame in Table 7.1 provide a pictorial representation of the flame response and clearly show the difference between stable and unstable flames. Under stable operations (Figure 7.2a), the flame is relatively quiet and a smooth, conical surface anchors to the ring at the nozzle exit. As the flame becomes unstable, the surface reacts to perturbation in the flow and begins to wrinkle (Figure 7.2b). Blackshear¹¹, Fleifil at al.³⁹, and others speculated that this wrinkling results in a change in the exposed surface area of the flame, which assuming a constant flame speed should have a direct impact on the heat release rate and will be discussed further in Chapter 8.

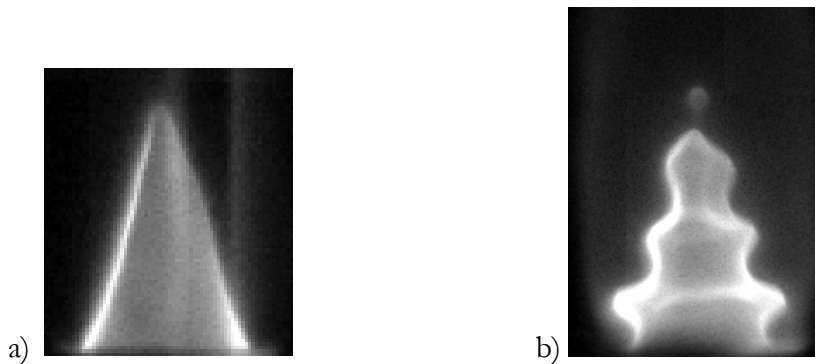


Figure 7.2: a) Stable flame operating at $\phi = 0.68$ and $V_{\text{mean}} = 1.0$ m/sec. b) Self-Excited flame at $\phi = 1.0$ and $V_{\text{mean}} = 1.54$ m/sec ($St_D = 3.0$).

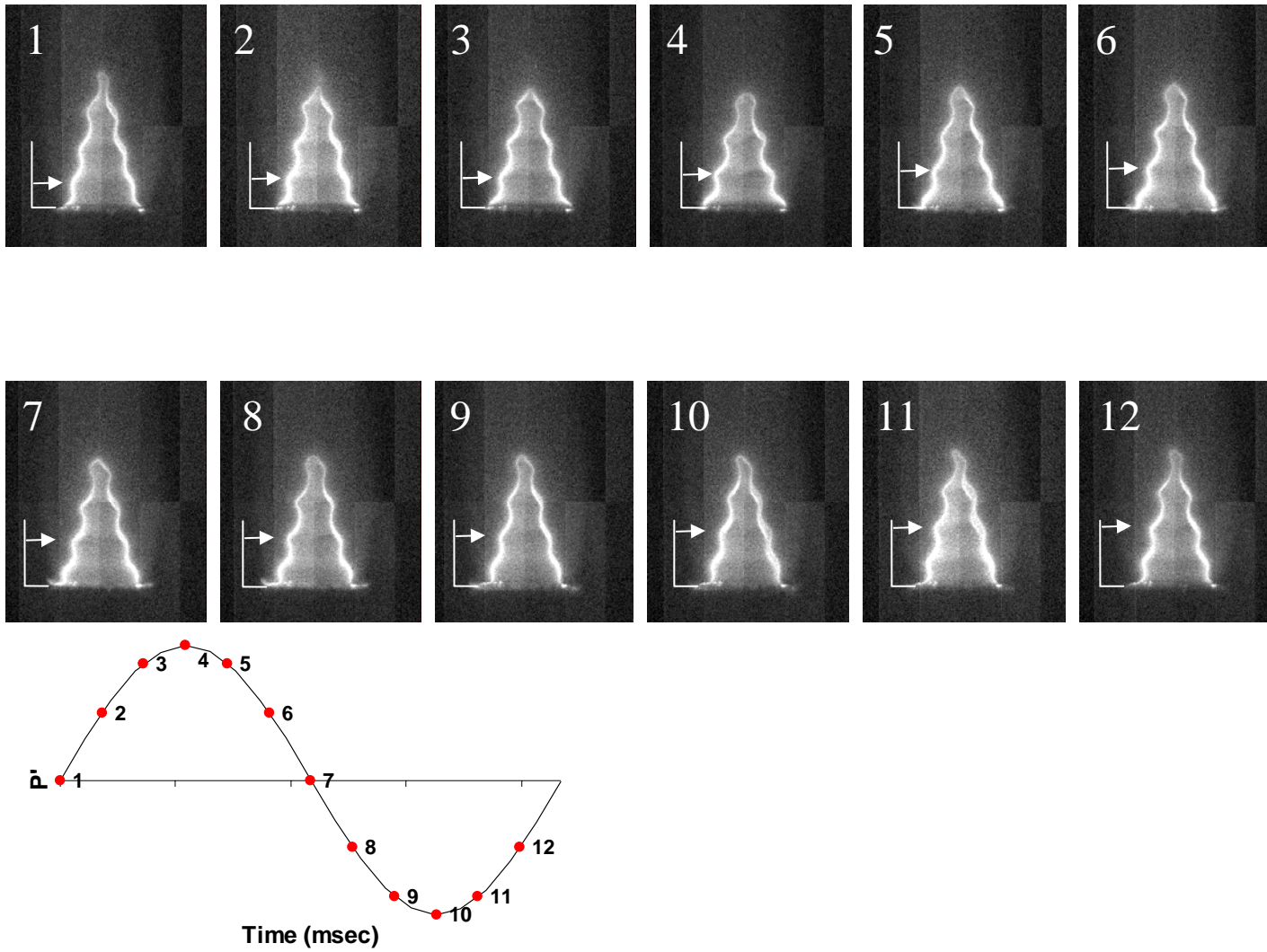


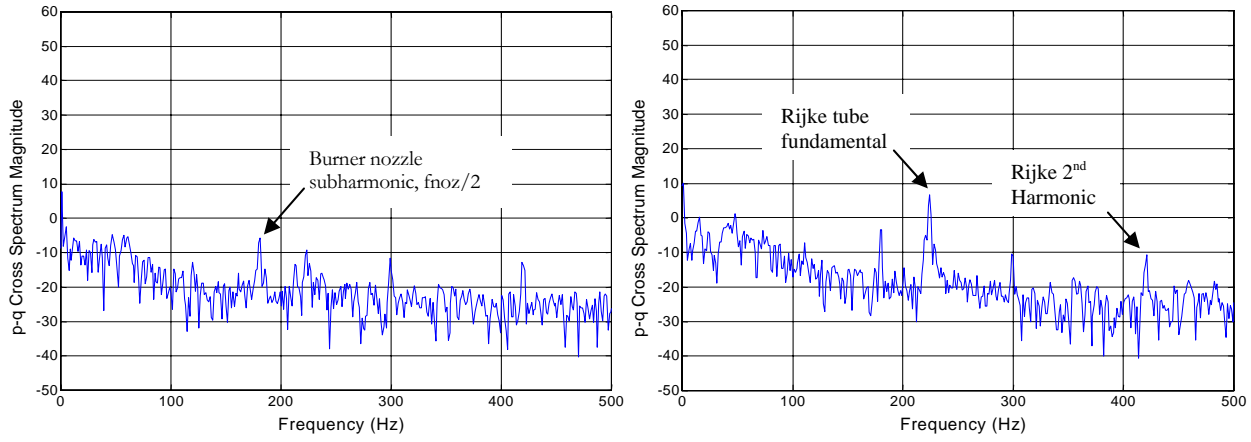
Figure 7.3: Phase-resolved images of a self-excited flame referenced to the pressure cycle. Arrow follows progression of cusp during one period of oscillation.

Phase-resolved images of a self-excited flame oscillating at 230 Hz referenced to the pressure cycle are illustrated in [Figure 7.3](#). The images are in increments of 30° of phase and clearly demonstrate the progression of the cusps propagating downstream along the flame surface (arrow). Given $St_D = 3.0$, the distance traveled by the cusp over a cycle produces a propagation velocity of $C = 1.54$ m/sec. Thus the disturbance propagates along the flame surface at the nozzle exit mean flow rate ($C/V_{\text{mean}} = 1.0$). This would tend to suggest that the disturbance is purely acoustic in nature meaning that it is irrotational. These results agree with Bourehla and Baillot¹⁴ who has suggested that for oscillating flames in which $St_D \leq 1.4$ the disturbance takes on an aero-acoustic (rotational, vortex-driven) behavior, but is more acoustic (irrotational) for $St_D > 1.4$. Further discuss on the propagation velocity will follow in Chapter 10 when phase-resolved measurements of the flow field are presented.

The Rayleigh Criteria, as given in Equation 2.1 and repeated below, provides a means of

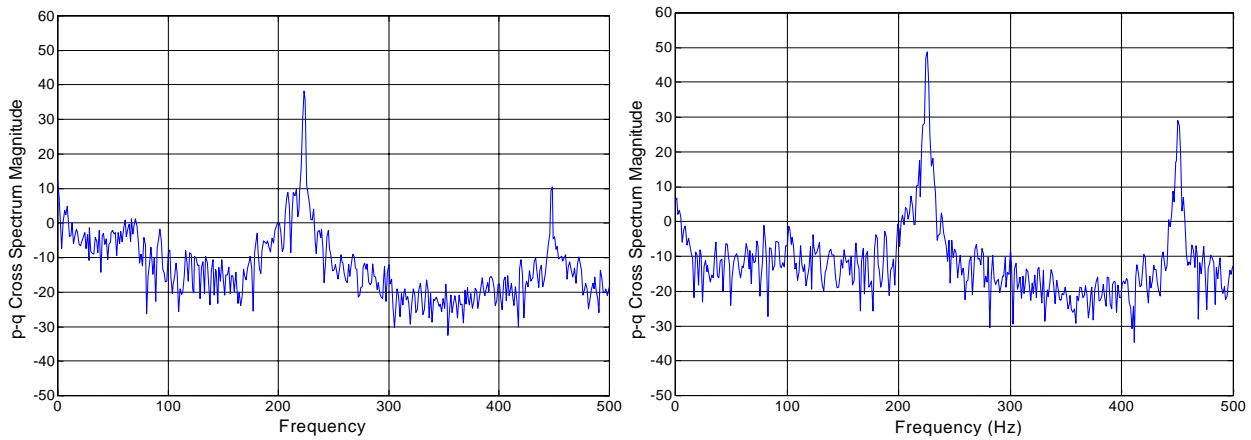
$$Ra = \int_0^T q'(t)P'(t)dt \quad 2.1$$

quantifying the stability of a thermoacoustic system. In essence this relationship is a cross correlation between variations in the acoustic pressure and heat release rate. The cross spectrum density function, which is a Fourier transform of the cross correlation, between the acoustic pressure and heat release rate variations for several operating conditions is plotted in Figure 7.4a-d. Flame stability is characterized by a lack of correlation in the Rayleigh Criteria and thus results in the absence of any prominent peaks above the background noise as shown in the cross spectra of Figure 7.4a ($\phi = 0.6$, $V_{\text{mean}} = 1.54$ m/sec). Here a small peak appears at the sub-harmonic frequency of the burner nozzle, $f_{\text{noz}}/2 = 180$ Hz, but the amplitude of this peak is small and its response is defined by a lack of acoustic velocity at the nozzle exit. Acoustic damping within the tube ensures that the stable response shown in Figure 7.4a is characterized by broadband noise as opposed to isolated peaks. However, as shown in Figure 7.4b, for $\phi = 0.68$ and $V_{\text{mean}} = 1.54$ m/sec where the flame considered to be marginally stable, several peaks are identifiable in the cross-spectra analysis. A small peak is obtained at the first resonant response, or fundamental frequency ($f_{\text{tube}} = 224$ Hz), which over the range of operating conditions is between 219-230 Hz as the average post-flame temperature varies in the tube. Additional peaks occur just above the broadband noise at $f_{\text{noz}}/2 = 180$ Hz and $2f_{\text{tube}} = 421$ Hz. The higher of these two frequencies, $2f_{\text{tube}} = 421$ Hz, is the second harmonic, or resonant, frequency for the tube.



a) Cross-spectra of pressure and heat release rate for stable flame, $U = 1.54$ m/sec and $\phi = 0.6$.

b) Cross-spectra of pressure and heat release rate for “marginally” stable flame, $U = 1.54$ m/sec and $\phi = 0.68$.



c) Cross-spectra of pressure and heat release rate for self-excited flame, $U = 1.54$ m/sec and $\phi = 0.7$.

d) Cross-spectra of pressure and heat release rate for self-excited flame, $U = 1.54$ m/sec and $\phi = 1.0$.

Figure 7.4: Frequency cross-spectra of analog signals

As the flame becomes more unstable, Figure 7.4c and d, energy is feed into the tube fundamental resonance and its harmonics, which begin to eclipse the sub-harmonic signal of the burner nozzle, $f_{noz}/2$. At these conditions the strong correlation between the heat release and acoustic pressure is characterized by the large amplitude peaks shown in Figures 7.4 c and d. The amplitude of the disturbance remains constant at a given operating condition, however as energy is added to the system through a change in equivalence ratio or flow rate (results shown later indicate flow rate has little influence on the amplitude of the instability) the magnitude of the instability grows until a saturation limit is reached. Evidence of this saturation behavior will be discussed below.

The acoustic response as measured by the rms pressure signal at the nozzle exit is shown in Figure 7.5 and appears to be independent of the flow rate with the RMS pressure dropping off quickly

at conditions leaner than $\phi = 0.8$ and richer than $\phi = 1.0$ for all flow. These regions are considered the limits of stability, or stability boundaries, of the Rijke tube burner assembly used for this study. For the lean flame case, a measurable disturbance is observed at $\phi = 0.7$, thus the actual stability limit extends down to this equivalence ratio. A difference of approximately 80 Pa separates the peak rms pressure measured in a self-excited flame from that of a stable flame. This difference is rather significant based on observations of acoustically forced flames exposed to slightly higher rms pressures that resulted in flame blow-off. The boundaries at the limits of stability ($\phi = 0.68$ and 1.1) are considerably steep relative to the rest of the operational regime and has a profound effect on control of thermoacoustic instabilities as a stable combustor operating near a boundary may easily slip into an unstable condition by a small operational change. More discussion on the significance of the stability boundaries is included later in this chapter.

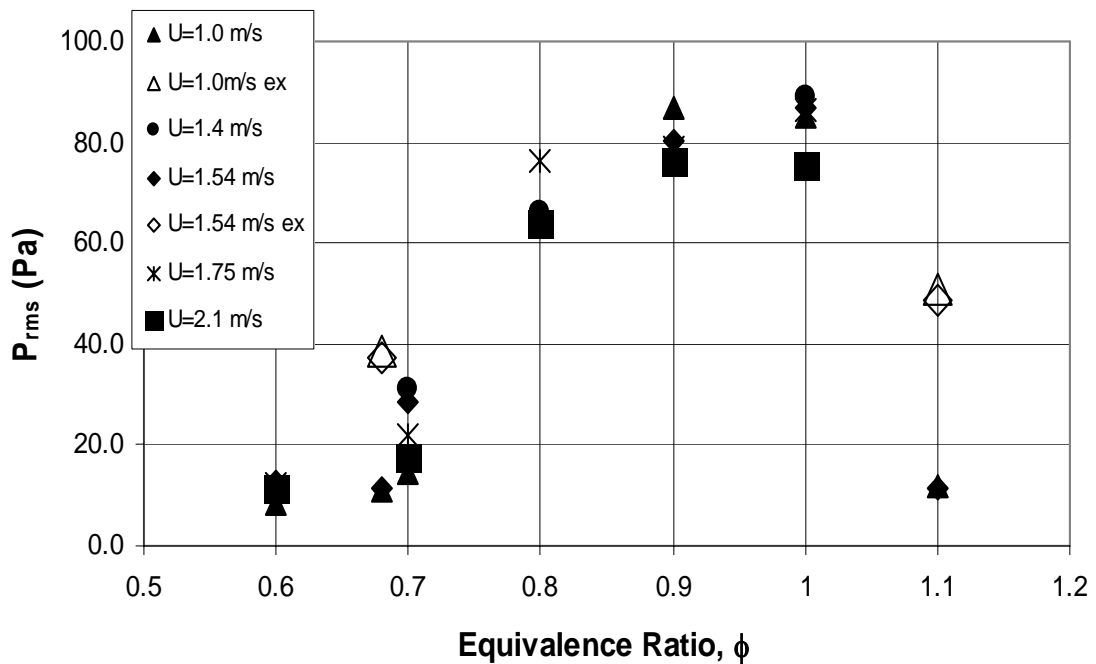


Figure 7.5: Amplitude of RMS pressure as a function of equivalence ratio at various nozzle exit velocities.

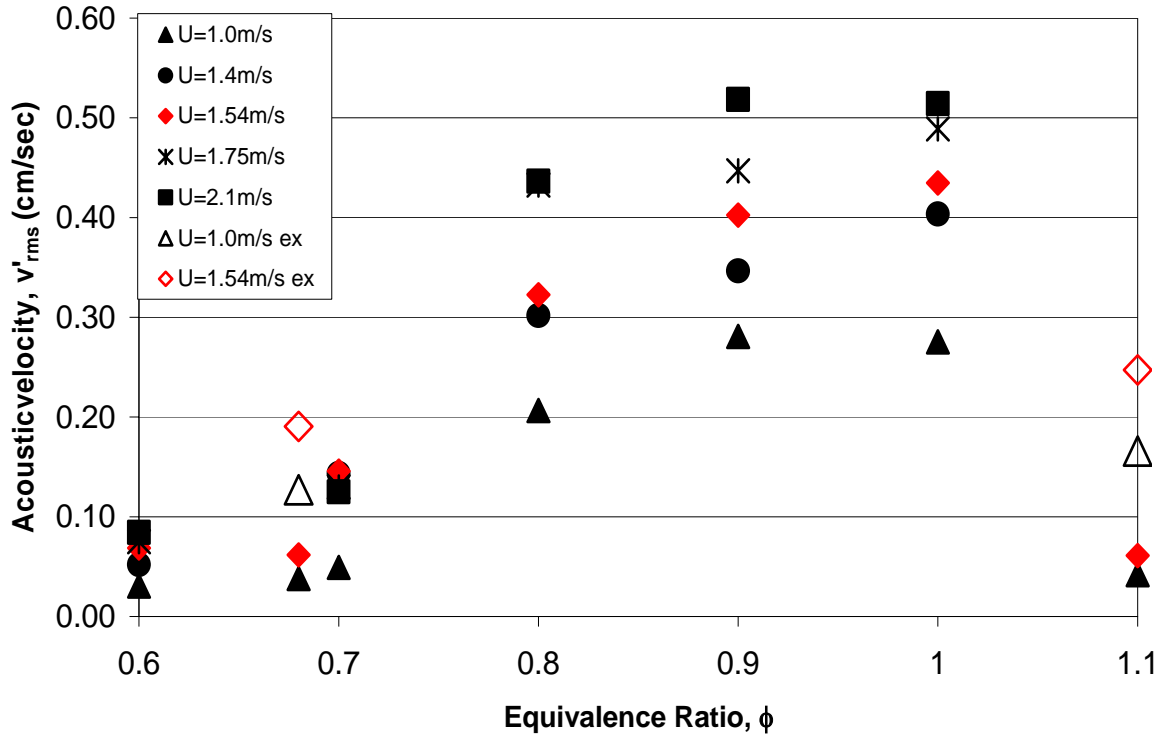


Figure 7.6: rms amplitude of the acoustic velocity as a function of equivalence ratio at various nozzle exit velocities.

The rms amplitude of the acoustic velocity, v' , shown in Figure 7.6 appears to have a similar trend as the rms of the acoustic pressure, with peak amplitude of $v' = 0.28 - 0.51$ cm/sec occurring between $\phi = 0.9-1.0$. Unlike the rms pressure, the acoustic velocity has considerably more variation across the mean flow rates. This would indicate that the rms amplitude of the acoustic velocity is dependent on the mean flow as well as the equivalence ratio. Indeed a plot of the acoustic velocity versus the burner power, estimated from the mixture enthalpy and mass flow rate of the reactants, displays a nearly linear relationship at conditions corresponding to an inherently unstable flame. Khanna⁵⁸ showed that a greater percentage increase in the mean energy content could be obtained by increasing ϕ at a constant V_{mean} as compared to increasing V_{mean} at a constant ϕ . This appears to be in agreement with the results presented in Figures 7.7.

A comparison between the acoustic velocity, v' , and the heat release rate, q'_{rms} , in Figure 7.8 reveals a strong linear relationship below $v' < 0.2$ cm/sec as indicated by the solid line. As the amplitude of the disturbance continues to grow there is increasing variance with flow rate in the heat

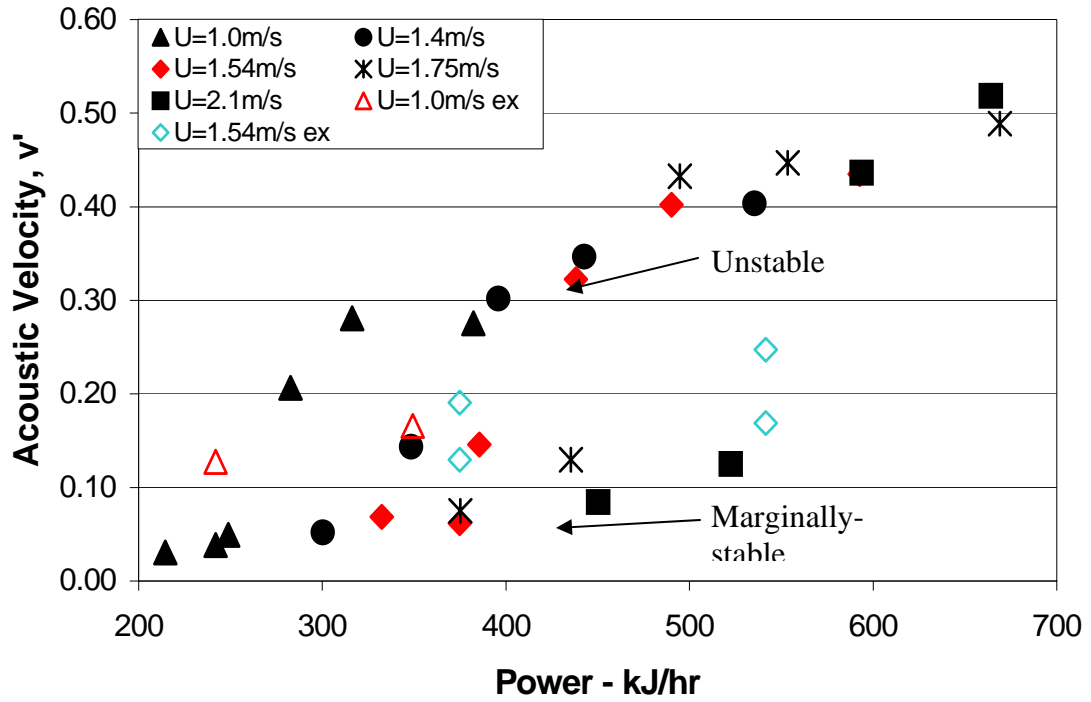


Figure 7.7: Acoustic intensity as a function of burner power.

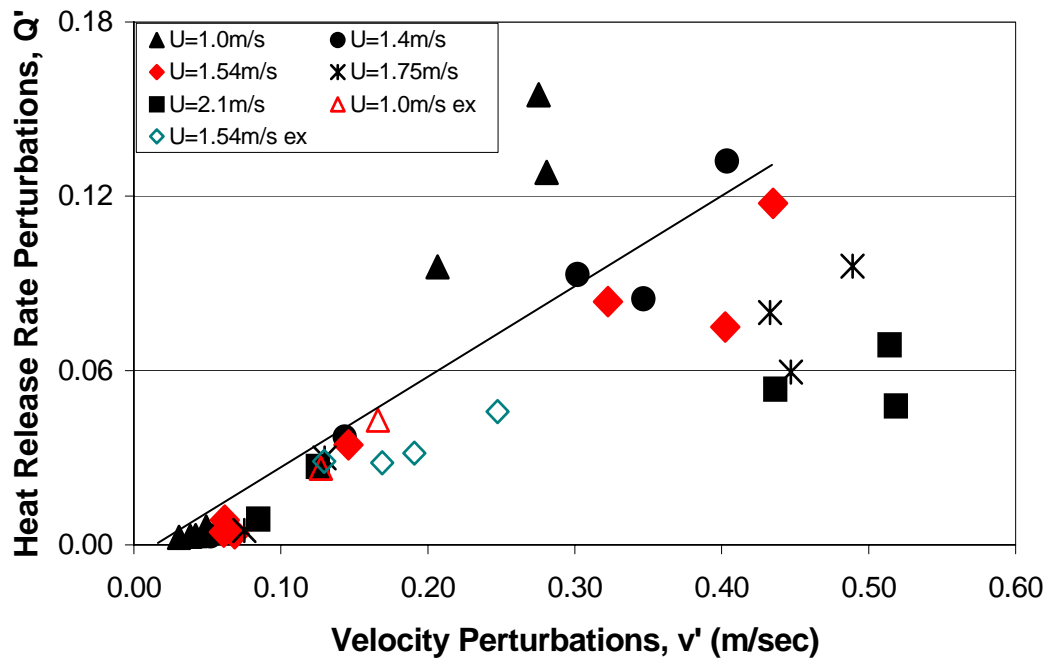


Figure 7.8: Velocity intensity, $i_p = v'/V_{mean}$, as a function of equivalence ratio at various nozzle exit velocities.

release response. This variance in the heat release rate perturbations appears to be dependent on the mean flow rate through the burner such that as the amplitude of the disturbance continues to grow the heat release rate perturbations are stronger at low flow rates than at higher values. This occurs although as will be shown later the mean flow rate has no apparent effect on the flame surface area, thus this may be a time delay effect.

For a sinusoidal signal, knowledge of the phase angle provides information regarding a zero time reference and is obtained from a Fourier transform of the time history of the parameter in question. In the study of thermoacoustic instabilities the phase relationship between parameters is important in understanding the mechanisms that drive the instability. Comparing Figure 7.5 with Figure 7.9, we see that the maximum instability occurs as the difference in phase angle between the heat release rate and pressure approaches 0° , indicating that these two quantities are in phase, as specified by the Rayleigh Criteria. At stable and marginally stable conditions identification of the phase difference becomes difficult as the periodic signal is overtaken by random noise. In these cases the phase difference is determined at the instability frequency for the closest unstable flame. Thus at lean stable conditions ($\phi \leq 0.68$) the phase angle difference was determined at a frequency of $f = 220$ Hz which was the frequency of oscillations for the unstable flame at $\phi = 0.7$. Conditions at $\phi \leq 0.68$

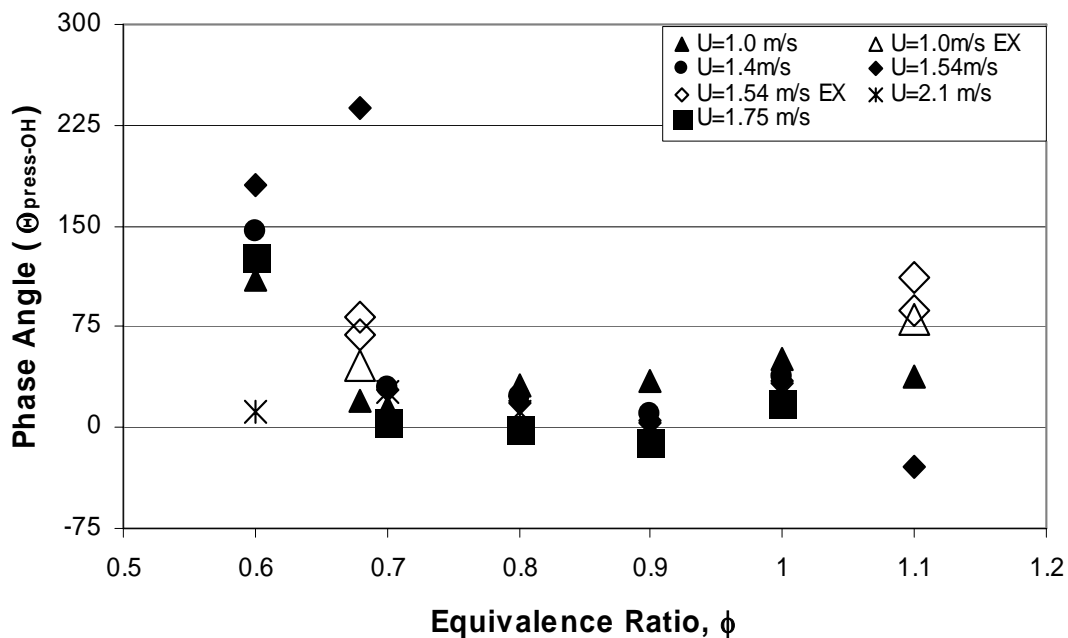


Figure 7.9: Phase angle between acoustic pressure and OH* perturbations as a function of equivalence ratio.

exhibit the random behavior that is typical of the lack of signal periodicity with the phase difference varying widely between flow rates with $\Theta = 25^\circ - 225^\circ$, thus not satisfying the Rayleigh criteria.

Further comparisons between Figures 7.5 - 7.9 show that while it was possible to acoustically drive a stable flame ($\phi = 0.68$ and 1.1) by means of an externally mounted speaker (no change in impedance) to a similar acoustic and heat release amplitudes as the self-excited cases just across the stability boundary, the large difference in phase angle ($\Theta_{\text{driven}} = 75^\circ$ compared to $\Theta_{\text{self-ex}} = 0^\circ$) shown in Figure 7.9 clearly indicates that the excited cases do not satisfy the Rayleigh criteria.

Examining the phase difference between the acoustic velocity and the heat release rate perturbations, we see that as the flame transitions from stable to slightly unstable between $\phi = 0.7 - 0.75$ there is a sharp decline and a tighter grouping amongst the flow rates of the phase angle difference. At an equivalence ratio of $\phi = 0.8$ there is a significant increase in the amplitude of the instability as shown in Figure 7.5, and the accompanying phase difference in v'

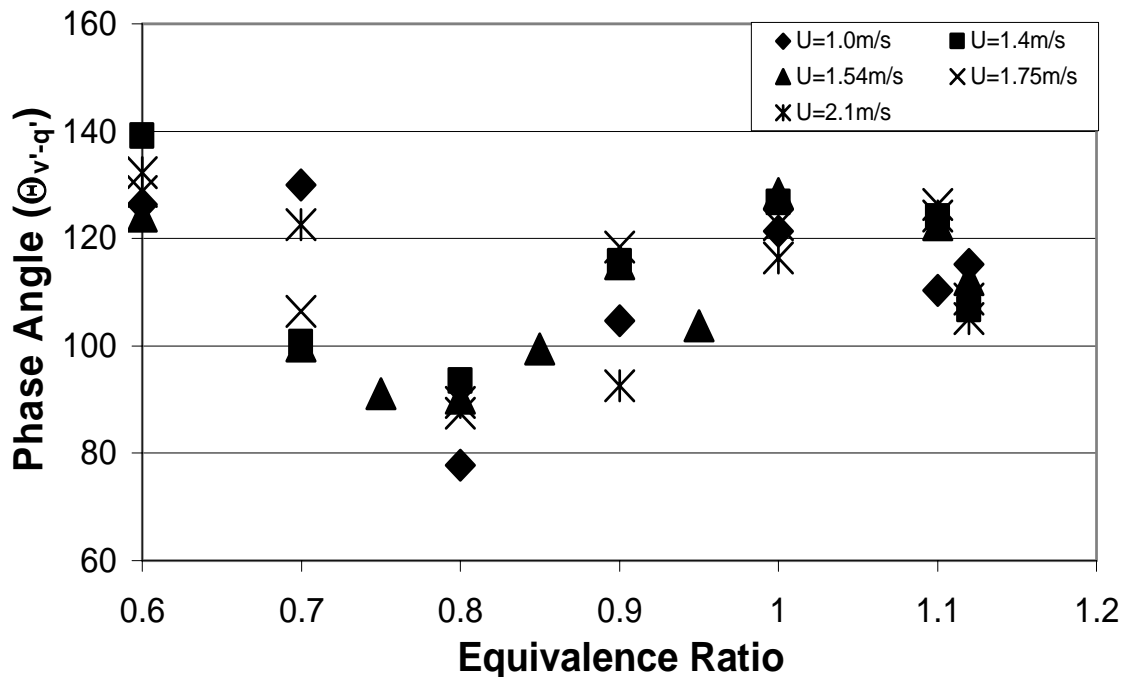


Figure 7.10: Phase angle between acoustic velocity and OH* perturbations as a function of equivalence ratio.

and q' is approximately $\theta_{v'-q'} = 90^\circ$ (Figure 7.10). The phase difference increases to approximately $\Theta = 100^\circ$ - 120° during peak instability thus suggesting an influence from equivalence ratio. Additional data is presented regarding the relationship between the acoustic velocity, flame surface area and heat release in Chapters 8 and 9.

7.2 Stability Boundary Analysis and Flame Excitation

A detailed analysis of the stability boundary in thermoacoustic systems such as the Rijke tube combustor is beyond the scope of this study as it would consume volumes on its own. Nonetheless, the following section forms some general conclusions based on the limited analysis performed as part of this thesis and recommendations for future work are discussed.

The stability boundary on both the lean and rich side of operation is characterized by a sudden change in the response of the flame with only a minor change in equivalence ratio at all flow conditions tested. As previously stated the sharp gradient between a stable and unstable flame could significantly hamper a stable turbine that may operate near the stability boundary as a small change in equivalence ratio or fuel composition could transition it into an unstable regime. An equivalence ratio difference of $\Delta\phi = 0.02$ separates stable and unstable flames on the lean end of the stability spectrum while a measured difference of $\Delta\phi = 0.1$ was obtained on the rich side. In order to investigate the stability boundary, flames that were just outside the unstable regime were made to oscillate by “externally” driving (Figure 3.9b) the flame with a 5 W sinusoidal input to the burner at the frequency exhibited by the unstable flame just inside the unstable regime. With the loudspeaker in this configuration more input power was required in order to obtain a response from the flame due to the loss of acoustic power outside the burner. Thus the 5 W response depicted here is considerably different than that discussed in Chapter 9 with the loudspeaker as shown in Figure 3.9c. A distinct advantage to exciting the flame with the externally located speaker is that there is no change to the acoustic impedance of the fuel nozzle.

Figures 7.11 – 7.14 are images of self-excited and acoustically-driven flames at operating conditions that straddled the stability boundary of the burner. Images of the stable flames at the same conditions as the “driven” cases can be seen in Table 7.1. Notice the stark contrast in the flame shape between the self-excited and forced cases especially at $\phi = 1.0 - 1.1$ (Figures 7.12 and 7.14). This radical change in the flame response, between self-excited and stable, was accompanied by a reduction

in the rms pressure and heat release and is attributed to a change in equivalence ratio of $\Delta\phi = 0.1$. With just an incremental change in the equivalence ratio the flame, with $V = 1.54$ m/sec, more than doubles its length from 3.0 cm to 7.2 cm and pressure perturbations drop from $p' = 87.6$ Pa ($\phi=1.0$) to $p' = 11.3$ Pa ($\phi=1.1$), indicating that the flame is rather sensitive to changing in equivalence ratio. Exciting the flame it was possible to obtain an acoustic pressure rms amplitude comparable to the self-excited quantity, $p' = 50$ Pa.

It should be noted that the response of the flame on the rich side of the stability boundary should be considered with some prejudice. To some degree the flame was expected to respond differently once the equivalence ratio exceeded stoichiometric ($\phi > 1.0$) due to the fact that above stoichiometric conditions the flame becomes closer to a partially-premixed system as opposed to fully-premixed. Altering from premixed to partially-premixed one would expect a change in the flame height and even qualitative conclusions are questionable. Also of importance is the fact that additional heat release occurs away from the flame due to continual mixing downstream of the flame. This could potentially alter the acoustic characteristics downstream of the flame and thus acoustic waves may interact differently with the region downstream of a partially-premixed flame in comparison to that of a fully premixed flame. In effect the transition from an unstable to stable flame shown in this study to occur under fuel rich conditions may be more related to flame stoichiometry than to a change in the coupling process between the heat release and burner acoustics.

Although the transition from self-excited (unstable) to stable flame occurs with just a small change in equivalence ratio for both lean and rich operation, the two stability boundaries result in a very different response from the flame. During lean operation the margin between unstable and stable flames was considered to be much narrower due to the consistent response of the flame at $\phi = 0.7$ and 0.68 in comparison to the fuel rich boundary. Unlike the fuel rich stability boundary, the lean boundary may be the result of a loss of gain or a phase shift between the acoustics and variations in the heat release rate.

Examining the characteristics of the flame response at the lean stability boundary ($\phi = 0.68$ -0.7, $V_{\text{mean}} = 1.54$ m/sec) subject to stable, self-excited and acoustically driven conditions as well as acoustically driven non-reacting flows excited at the same input amplitude, Figure 7.15, may give some insight into the phenomena that is occurring. At an equivalence ratio of $\phi = 0.7$ the flame is inherently unstable producing a self-excited response of $p'_{\text{self-ex}} = 38$ dB at a frequency of $f = 223$ Hz. A

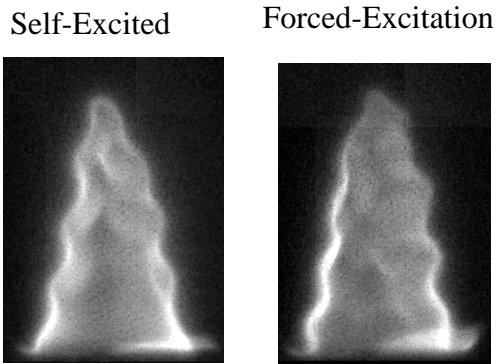


Figure 7.11: Flame images for $V = 1.54$ m/sec. Self-excited, $\phi = 0.7$; Forced-excitation, $\phi = 0.68$.

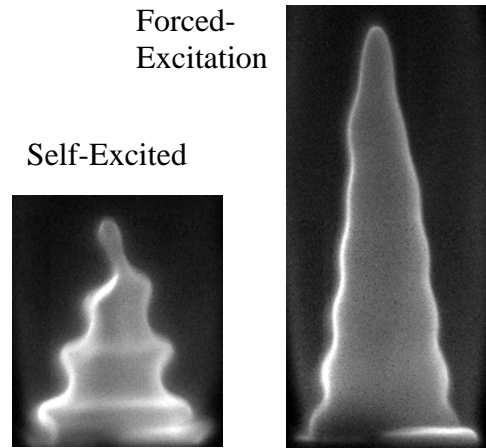


Figure 7.12: Flame images for $U = 1.54$ cm/sec. Self-Excited, $\phi = 1.0$; Forced-Excitation, $\phi = 1.1$.

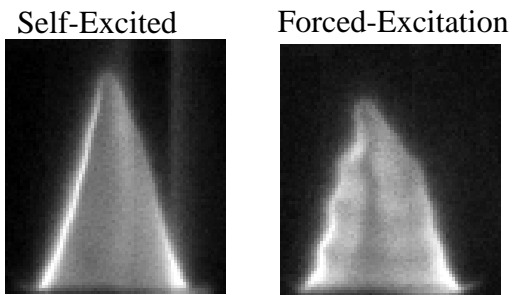


Figure 7.13: Flame images for $U = 1.0$ cm/sec. Self-Excited, $\phi = 0.7$; Forced-Excitation, $\phi = 0.68$.

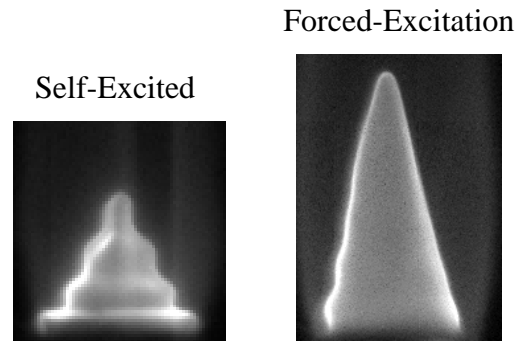


Figure 7.14: Flame images for $U = 1.0$ cm/sec. Self-Excited, $\phi = 1.0$; Forced-Excitation, $\phi = 1.1$.

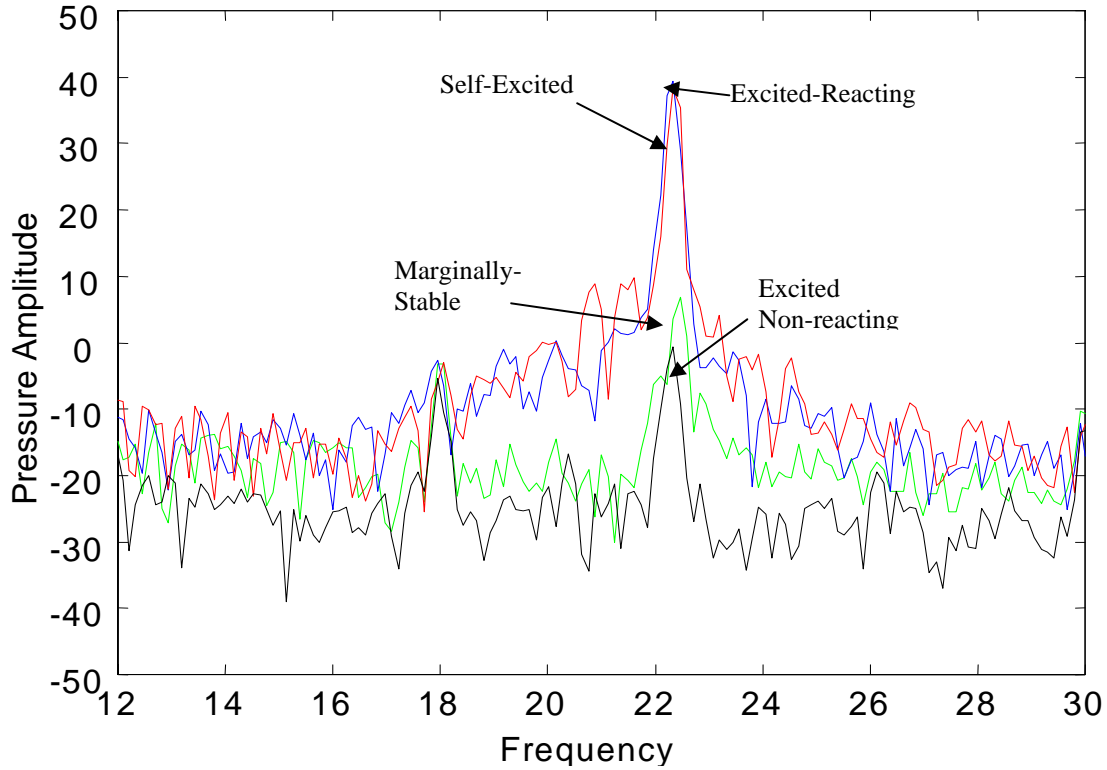


Figure 7.15: Frequency response of the nozzle exit pressure for self-excited, stable, and acoustically forced reacting and non-reacting flows for $V_{\text{mean}} = 1.54$ m/sec and $\phi = 0.95$.

reduction in the equivalence ratio of $\Delta\phi = 0.02$ decreases the measured response at $f = 223$ Hz to just less than $p'_{\text{stable}} = 5$ dB. Acoustically driving the flame, it is possible to duplicate the amplitude response of the self-excited flame ($p'_{\text{driven}} = 40$ dB) but the energy input from the speaker needed to produce such a disturbance is much less than would be expected as shown by comparing the response of the excited, non-reacting flow.

Extinguishing the acoustically-forced flame we see that the actual input energy from the speaker is relatively low, producing an amplitude of only $p'_{\text{nonreact-driven}} = -1.0$ dB at the burner nozzle outlet. Thus in order to obtain the amplified response from the acoustically-driven flame, positive feedback from the flame must be added back into the system, Figure 7.16, however this does not occur in the open-loop system of the non-reacting flow. This is in contrast to results shown in Chapter 9 in which the flame is excited by the in-line speaker configuration shown in Figure 3.9c. Plots comparing the rms pressure amplitude of the acoustically-driven flame to that of the non-reacting flow at the same level of input excitation from the speaker with the burner in the configuration of Figure 3.9c indicate a purely open-loop response in which the rms amplitudes

measured at the burner nozzle outlet are nearly identical, thus there is no positive feedback from the flame. This matter emphasizes the importance of the burner impedance on thermoacoustic instabilities. The addition of the in-line speaker alters the acoustic characteristics (impedance) within the burner nozzle while the externally located speaker does not. Without altering the acoustic impedance in the nozzle from that of the self-excited flame much less energy input from the speaker was needed to obtain an unstable flame. The additional energy required to drive the flame at similar conditions would indicate the lack of acoustic coupling or the absence of driving mechanisms and may suggest that experimentally derived transfer functions based on acoustically-driving inherently stable flames are inaccurate unless the characteristic impedance is taken into consideration, thus supporting the two-port model approach, which will be discussed further in Chapter 9.

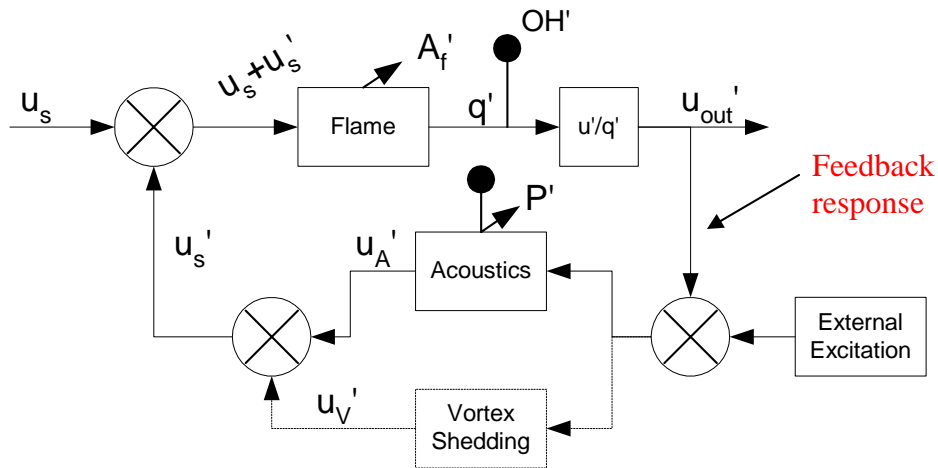


Figure 7.16: Block diagram representation of Rijke tube combustor with arrow indicating the feedback response from the flame.

This chapter was limited to a general presentation of the response of the flame which proved to be inherently unstable at a number of operating conditions. Satisfaction of the Rayleigh Criteria was shown to occur during periods of instability through the analysis of the phase-gain relationship between the system acoustics and heat release rate. However, there was no discussion of the coupling mechanisms that must act in order to form the positive feedback loop need to drive the instabilities. Several of these mechanisms will be the topic of concern in Chapters 8 and 10.

Chapter 8 Flame Surface Area

A number of studies have attempted to relate variations in the heat release rate to fluctuations in the flame surface area, brought on through interactions with an oscillating flow, and have been reviewed in Chapter 2. In this section, we investigate the analytical model developed by Fleifel et al.³⁹ along with results from the Blackshear¹¹ study and further work performed by Ducruix et al.³³ and Bourehla and Baillet¹⁵. A comparison is made between the results from those studies to the experimental results of this study in which image analysis is used to obtain the instantaneous flame surface area of an oscillating flame.

8.1 Review of Flame Surface Variations, Fleifel et al.³⁹.

The model developed in Fleifel et al.³⁹ (here-in referred to as the Fleifel model) has been quoted in several past works and was used as a point of reference for this study. For a detailed analysis of the Fleifel model the reader is directed to the reference, however a brief review is provided below

The Fleifel model was intended to describe the unsteady heat release from a laminar flame based on the variation in the flame surface area due to its interaction with an oscillating flow. Assuming a constant flame speed, the flame surface must respond to velocity modulations at the burner outlet. In the case of a harmonic distortion in the flow the flame reacts by forming period “cusp” or undulations along the surface ([Figure 8.1](#)).

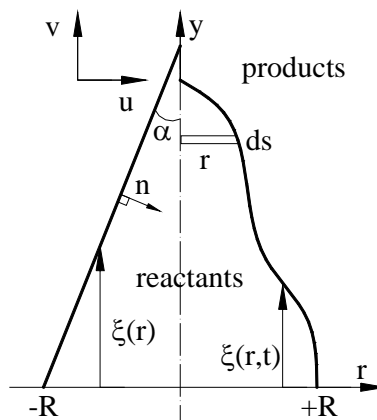


Figure 8.1: Sketch of flow and flame parameters under (a) stable and (b) unstable conditions (Ducruix³⁰).

The instantaneous surface area of the flame can be obtained by integrating the axial displacement, ξ , of the flame front over the annulus

$$A_f = \int_0^R 2\pi r \sqrt{\left(\frac{\partial \xi}{\partial r}\right)^2 + 1} dr \quad 8.1$$

Axial displacement variations as a function of the radius can be described by the following

$$\frac{\partial \xi}{\partial t} = V(r, t) + S_u \cos(\alpha) \frac{\partial \xi}{\partial r} \quad 8.2$$

The α term, which denotes the half angle of the steady flame, in Equation 8.2 was added by Ducruix et al³³ to account for shorter flames that may have a significant cone angle.

Equation 8.2 is valid only if S_u , laminar burning velocity, is assumed constant along the flame front. This assumption may be too strong, because the flame speed changes with curvature and strain rate (Ducruix et al.³³). Fleifil simplified their model by neglecting the effects of flame stretch through the assumption of a constant flame speed. Law⁶⁷ distinguishes the effects of stretch as those caused by hydrodynamic forces, which changes the flame surface area and thus the volumetric burning rate, but does not affect flame intensity. Based on the definition proposed by Law⁶⁷, Fleifil's model assumes constant flame intensity by using a non-stretched laminar flame speed, and evaluates the impact of hydrodynamic stretch through surface area perturbations on the global heat release from oscillating flames. In this study flame stretch will refer to a change in flame intensity and its effects on variations in the flame surface area will be neglected.

The flow field of Fleifil's model is composed of a mean and perturbed term where the perturbed term can be considered uniform in space while harmonic in time:

$$v' = \varepsilon V \sin(\omega t), \quad u' = 0 \quad 8.3$$

where ε is the relative intensity of the perturbation and ω is the frequency of the acoustic mode. An acoustic intensity of $\varepsilon = 0.1$ or 10% of the mean velocity was assumed for their study. This is

comparable to the intensity obtained in this study in which the disturbance ranged from $\varepsilon = i_p = 0.025 - 0.28$, as shown in Table 7.1.

The authors solved Equations 8.1 and 8.2 by identifying a non-dimensional flame Strouhal number ($G = \omega R/S_u$) where ω is the angular frequency, R is the burner radius, and S_u is the laminar, non-stretched flame speed, and obtained a relationship for the instantaneous flame surface area perturbations normalized by their mean which was found to be strongly dependent on G and a linear function of the relative intensity of velocity perturbation, $i_p = v'/V_{mean}$.

$$\frac{A_f'}{A_f} = \frac{2i_p}{G^2} \left[(1 - \cos(G)) \sin(\omega t) - G \left(1 - \frac{1}{G} \sin(G) \right) \cos(\omega t) \right] \quad 8.4$$

A plot of the normalized perturbation of the flame surface area against G , assuming a small flame cone angle, at different instants of time during one cycle is reproduced in [Figure 8.2](#).

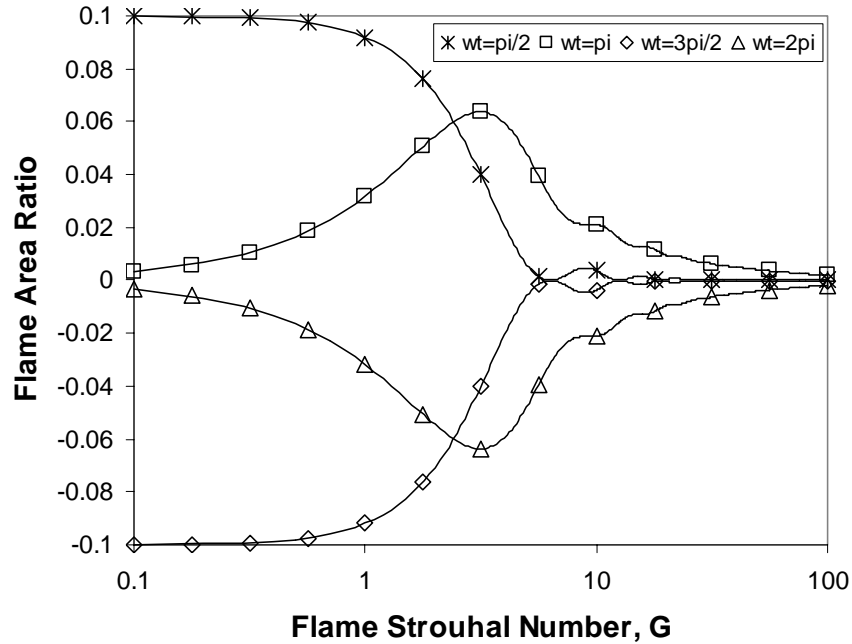


Figure 8.2: Normalized perturbation in flame area as a function of the flame Strouhal number at different instants in time for $i_p = 0.1$ (Fleifil et al.³⁵).

The total rate of heat release can be assumed proportional to the flame surface area and the flame speed as given by the following

$$Q(t) = \rho S_u A_f(r,t) \Delta q_r \quad 8.5$$

where ρ is the mixture density, S_u is the flame speed, A_f is the flame surface area and Δq_r is the heat of reaction per unit mass of the mixture. The flame surface area can be decomposed into a mean and fluctuating component, Equation 8.6.

$$A_f(r,t) = \bar{A}_f(r) + A_f'(r,t) \quad 8.6$$

This allows a similar decomposition of the heat release rate which assumes that perturbations in the heat release rate can be directly associated with variations in the flame surface area and can be expressed as

$$\frac{Q'}{Q} = \frac{A_f'}{A_f} \quad 8.7$$

The Fleifil analysis shows that although the flame surface becomes more wrinkled at larger values of G , the amplitude of the area ratio approaches zero. Utilizing the kinematic response of the flame surface to the applied velocity field given above, Fleifil developed a linear transfer function between perturbations in the heat release rate and velocity that was dependent on the non-dimensional flame Strouhal number. The magnitude of the first-order model used to approximate the transfer function was shown to decrease with an increase in frequency, while the phase shift was smallest at low frequencies and approach a maximum value at high values of G . Similar findings were obtained by Bourehla and Baillet¹⁵ and Ducruix et al.³³.

Results from the Blackshear¹¹ study also suggested that the flame speed had a significant impact on the phase relationship between the area and flow perturbations, and like Fleifil showed that the phase lag of the $a_p = A_f'/A_{\text{mean}}$ behind $i_p = v'/V_{\text{mean}}$ increase as the flame speed decreased. These results are considered in the next section which discusses the experimental evaluation of the relationship between a varying flame surface area and heat release rate.

8.2 Experimental Determination of the Instantaneous Flame Surface Area

For the methane/air flames studied here, much of the visible chemiluminescence is due to C₂ (436-563nm) and CH (432nm) emissions from the flame. Studies such as those conducted by Najm et al.^{85,86} have shown that these species are relatively short-lived within the flame structure and thus provide a reasonable approximation for the flame surface. Assuming the flame surface to be axisymmetric and a thin interface between reactants and products, integration of the spatial gradient of the measured flame surface (Equation 8.1) leads to a determination of the flame surface area.

Chemiluminescent images of the flame surface were recorded at a rate of 1000 Hz by a high speed Kodak Motion Analyzer (CCD Model 1000 HRC) with an electronic exposure time of 1/5000 sec. The short exposure time was well above the expected flame perturbation rate ($1/f_{\text{pert}} = 1/230$ sec) to ensure images were instantaneous representations of the flame surface location. The number of images collected at each operating conditions was limited to 682 based on the memory capacity of the Kodak system, resulting in images being acquired every 82.8° of phase ([Figure 8.3](#)) for a 230 Hz oscillation. This adequately captured the motion of the flame surface over a period of oscillation and because of the mismatch between the oscillation and sampling frequency for this example it is possible to reconstruct the images to obtain up to 3.6° of phase resolution. Proper data alignment was ensured by references the short pulse emitted by the camera at the beginning of each frame with the measured pressure signal at the nozzle exit, [Figure 8.4](#). The first recorded pulse would then be considered the first record and previously recorded data would be discarded.

Each image was imported into MATLAB as a two-dimensional array of pixel intensities and normalized by the maximum. The image was then cropped to include only the region of interest (ROI), and gradients of the pixel intensity over a span of 5 horizontal elements was obtained in order to identify the flame surface. The software analyzes the image row by row and identifies a contour representation of the flame surface by locating the maximum gradient in the pixel intensity. Once an element of the surface has been identified for a row, the algorithm shifts to the first pixel in the next row and repeats the process until the entire ROI is complete, [Figure 8.5](#). Assuming symmetry, only one side of the flame surface needed to be defined in order to calculate the flame surface area. [Figure 8.6](#) provides a symbolic representation of the procedure which was used to determine the flame location, calculate the flame surface area and perform correlation studies with heat release rates and pressure oscillations.

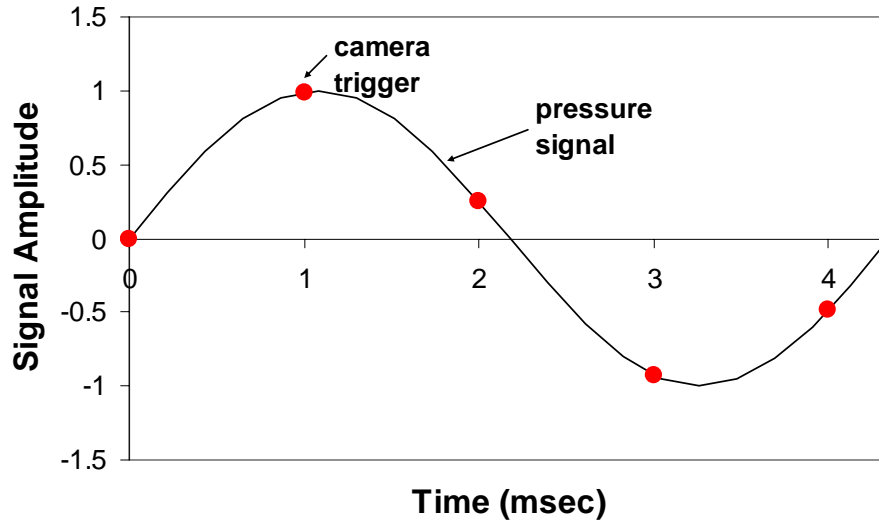


Figure 8.3: Time alignment of image trigger with data acquisition and pressure perturbations.

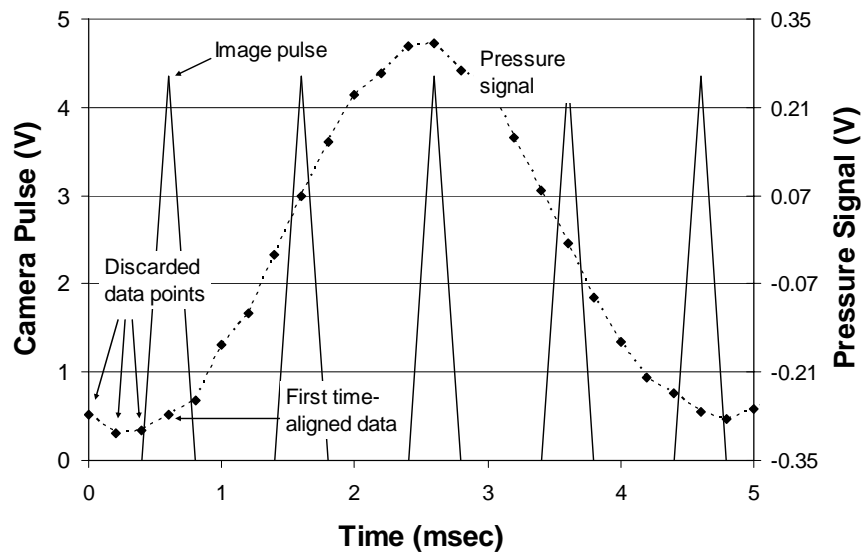


Figure 8.4: Time alignment of image trigger with data acquisition and pressure perturbations.

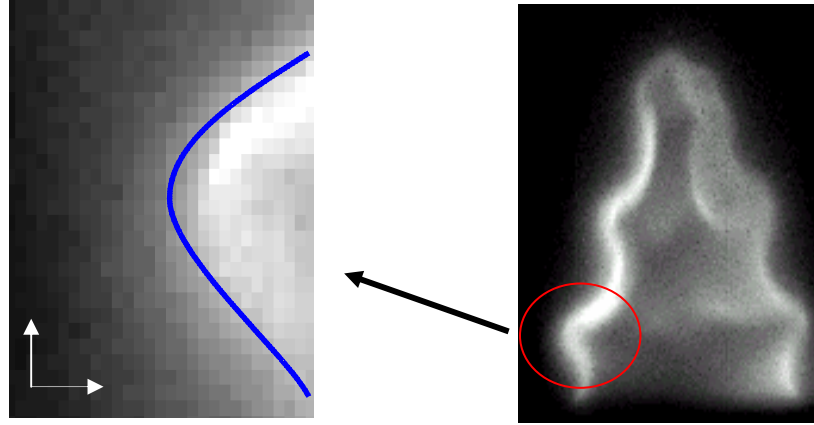


Figure 8.5: Pressure amplitude trace during peak oscillations ($U=150$ cm/sec, $\phi=1.0$) upstream and downstream of nozzle restriction.

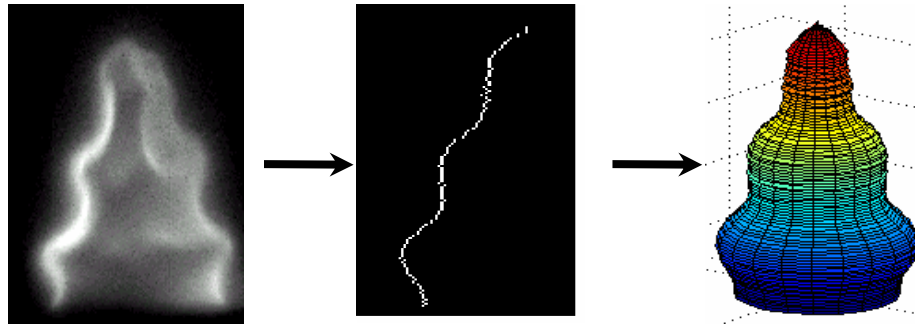


Figure 8.6: Representation of algorithm to determine the flame surface area from digital image of flame.

8.2.1 Experimental Results and Discussion

The test conditions discussed here are the same used to construct Table 7.1 which included stable, self-excited and acoustically forced flames with the Rijke tube combustors in the configurations shown in Figure 3.9(a) and 3.9(b). Nozzle exit velocities ranged from $V_{\text{mean}} = 1.0 - 2.1$ cm/sec ($Re \approx 1140 - 2380$) and equivalence ratios of $\phi = 0.6 - 1.1$. Marginally stable flames at $\phi = 0.68$ and $\phi = 1.12$ were acoustically-driven to experimentally evaluate the regions in which the flame transitions across the stability boundary.

Assuming that the flame surface area consists of a time-dependent fluctuation super-imposed on a steady mean ($A_f(t) = A_{f_mean} + A_f'(t)$ and $\overline{A_f(t)} = A_{f_mean}$), comparisons can be made between the average, or mean, surface area of a self excited flame to that of a reference stable flame at similar

operating. To obtain the reference flame, limited data from PIV results (Chapter 10) obtained while the burner was in configuration 3.9c were used, and assuming the flame is symmetrical about the longitudinal axis, the flame surface area of a stable conical flame can be approximated from simple geometric principles relating the flame height and radius at the base, $A_f = \pi rL$. Where r is the flame base radius and L is the length of the flame surface from the base to the tip, [Figure 8.7](#). For a Stable flame with a height of $H_f = 3$ cm the resulting surface area is $A_f = 9.9$ cm².

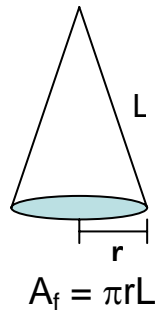


Figure 8.7: Geometrical relationship used to determine the flame surface area in stable flame. Assuming symmetry along the centerline.

[Figure 8.8](#) and [8.9](#) show the mean flame area and average flame length of the flame at stable, self-excited and acoustically-forced conditions. The stable reference conditions are shown by the open circles connected by the dashed line with the $A_{f,mean} \approx 8 - 11$ cm² and $H_{f,mean} \approx 2.7 - 4.1$ cm. Measurement uncertainty was addressed by considering measurements made of the stable flame that resulting in an uncertainty of approximately 4% of the mean value. Both plots show relatively similar trends with the minimal values being attained at equivalence ratios corresponding to the laminar flame speeds of $S_L = 32 - 44$ cm/sec ($\phi = 0.85 - 1.0$). As the flame speeds slows due to an increase or decrease of the equivalence ratio from stoichiometric, the flame lengthens and there is an increase in the mean surface area. At very lean or rich conditions there is a substantial increase in the flame length as well as the mean flame area. For the rich case ($\phi > 1.0$) this is related to the partially pre-mixed conditions that occur. Consequently, minimal values in [Figure 8.8](#) and [8.9](#) also occur at peak instabilities, but with the excitation of marginally stable flames at $\phi = 0.68$ and 1.12 producing similar results as the respective stable flames and adjacent unstable flames at $\phi = 0.7$ and 1.0 . The effects of flame stability appear to have a minimal impact on average values of surface area and length. However, comparing the results of the stable reference flame to those of the self-excited case it can be

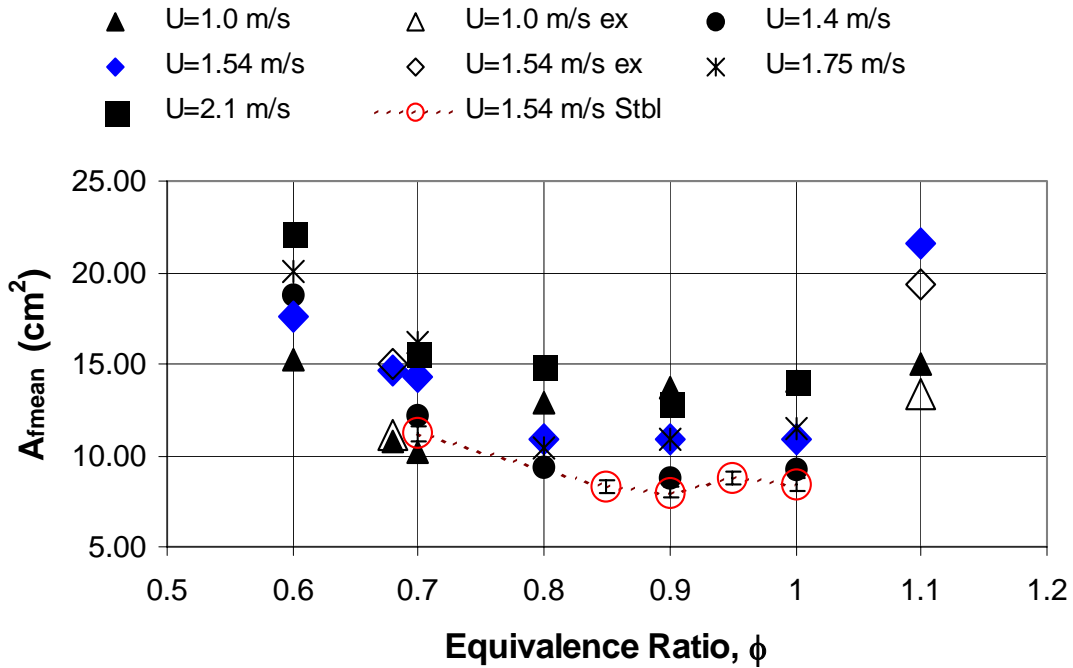


Figure 8.8: Measured mean flame surface area as a function of equivalence ratio. Stable flame reference provided.

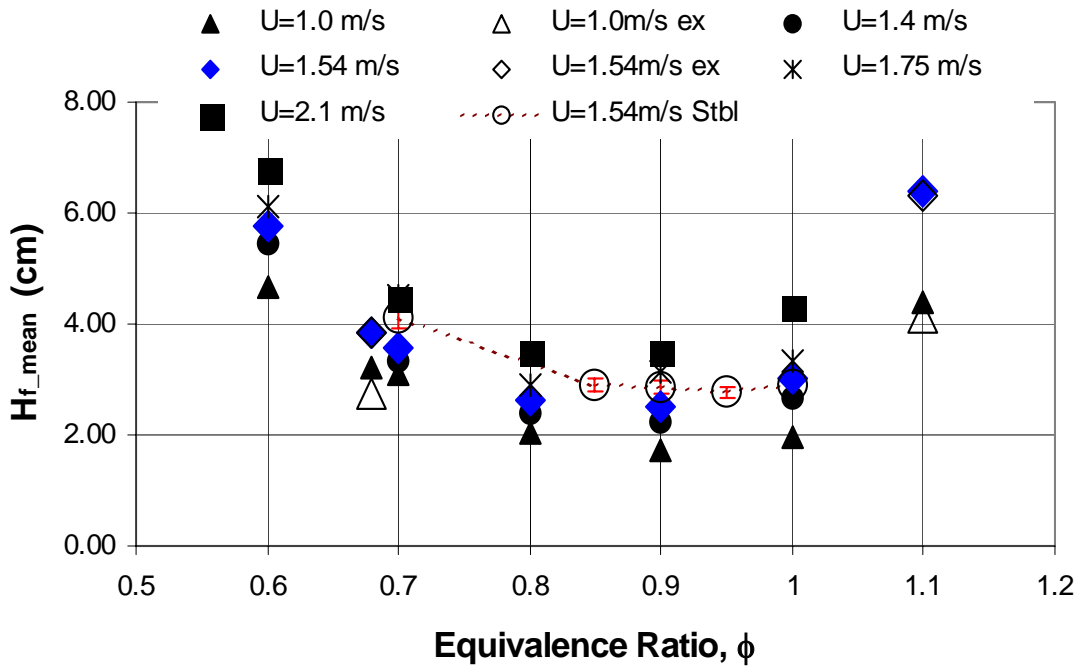


Figure 8.9: Measured mean flame height as a function of equivalence ratio. Stable flame reference provided.

seen that although there is a similar agreement of the flame length ([Figure 8.9](#)), the average flame surface area of the self-excited flame is on average 31.3% larger than that of the stable reference flame ([Figure 8.8](#)). This is contrary to results from Bourehla and Baillot¹⁵ and Baillot et al⁶ who suggested that on average wrinkling of the front does not have a global influence on the flame and the mean-time average of the unstable flame surface area should equal that of the unperturbed flame. However, although the cause of the difference shown in this study is not fully understood, one can speculate that a possible source of this discrepancy is a difference in flame speed between the stable flame and that of a self-excited flame. For the relationship in [Figure 8.8](#) to occur, the flame speed of the stable flame would have to be greater than that of the self-excited flame, $S_{f_self-ex} < S_{f_stable}$. Flame stretch, which has been neglected in this analysis, could produce local variations in the flame speed especially near the base of the flame where effects may be observed in the surface area, but not the flame length.

8.2.2 Spectral Analysis of Oscillating Flames

For this study, the phase-gain relationship between the instantaneous flame surface area, acoustic modulation and heat release rate is of interest. An example of the instantaneous surface area and pressure trace for a flame during peak instability ($V_{mean} = 1.54$ m/sec, $\phi = 0.9$ and $St_D = 3.0$) is shown in [Figure 8.10](#). Although somewhat noisy, variations in the instantaneous surface area appear to be nearly sinusoidal and in phase with the pressure signal. A spectral analysis ([Figure 8.11](#)) shows that indeed there is a strong coupling between the dynamics of the flame front and the acoustic perturbations with agreement between the surface area and acoustic pressure oscillation frequencies.

The signal coherence between the surface area, OH*, and pressure perturbations at the oscillation frequency was determined to be greater than 0.85 for all of the conditions studied with $\phi > 0.68$ for the self-excited unstable cases (see example in [Figure 8.12](#)). At equivalence ratios of $\phi < 0.68$ the flame was stable and no oscillations in the flame response were detectable

Examples of the frequency spectra for stable, acoustically-forced and self-excited flames at a mean flow of $V_{mean} = 1.54$ m/sec are given in [Figures 8.13](#), [8.14](#), [8.15](#), and [8.16](#), respectively. The examples shown are cross-correlations of: (a) pressure and heat release, (b) pressure and flame surface area, (c) surface area and heat release, (d) surface area and flame height.

[Figure 8.13a](#) is the cross-correlation of the acoustic pressure and heat release rate at $V_{mean} = 1.54$ m/sec and $\phi = 0.68$, and although this was considered a stable flame, peaks in the frequency spectrum are still visible, with detectable oscillations occurring at the Rijke tube fundamental

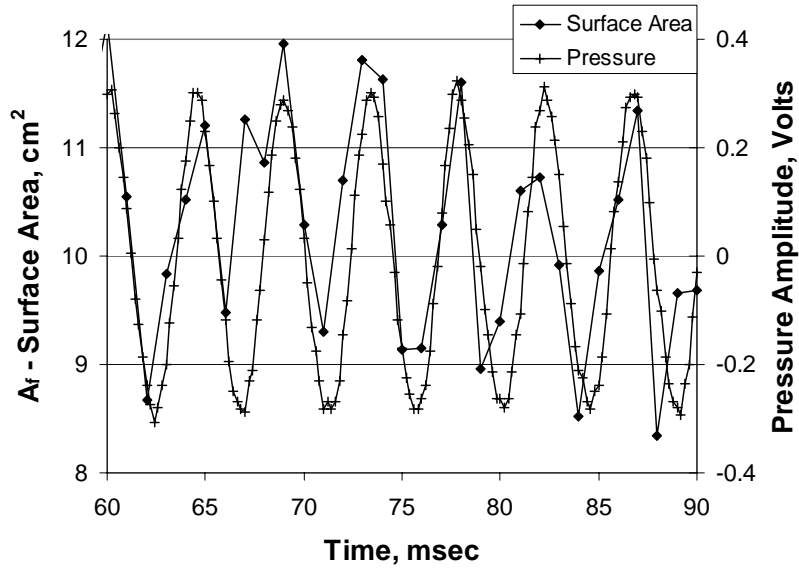


Figure 8.10: Flame images for $U = 75$ cm/sec. Unstable flame, $\phi = 1.0$; Excited flame, $\phi = 1.1$.

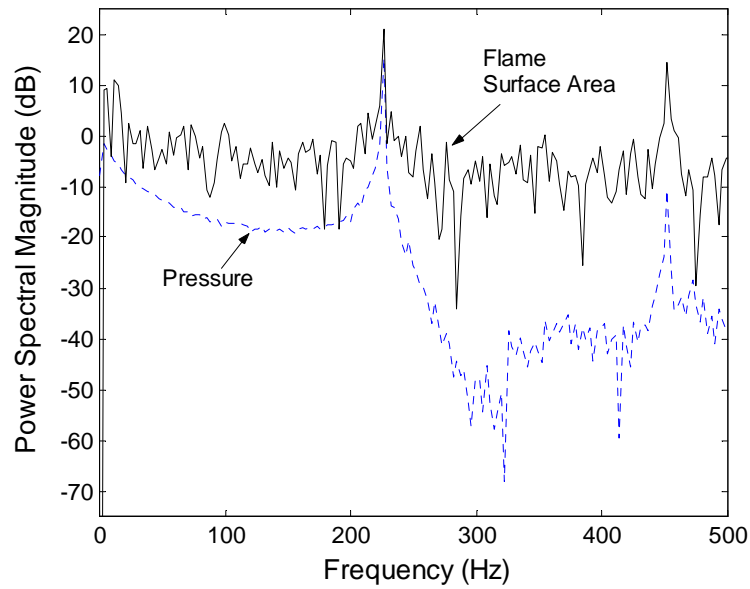


Figure 8.11: Flame images for $U = 75$ cm/sec. Unstable flame, $\phi = 1.0$; Excited flame, $\phi = 1.1$.

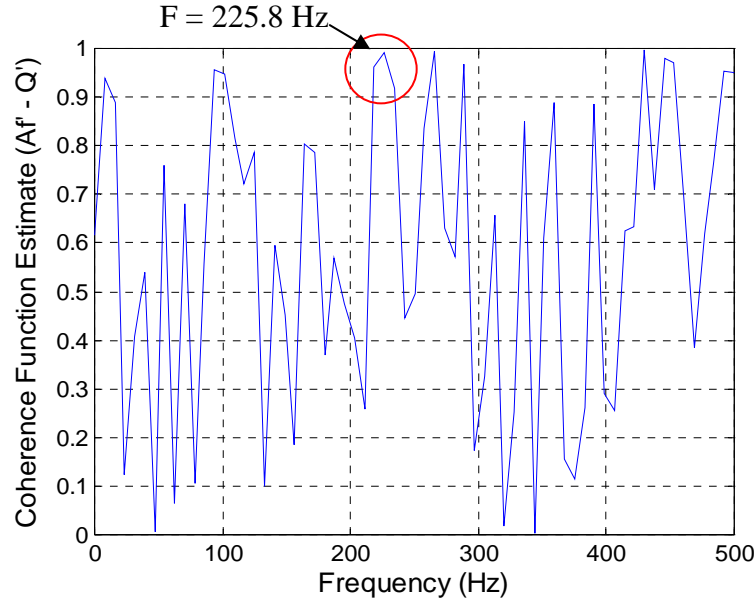
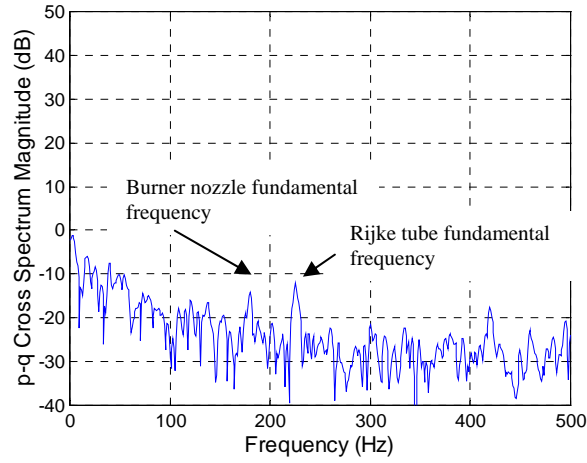


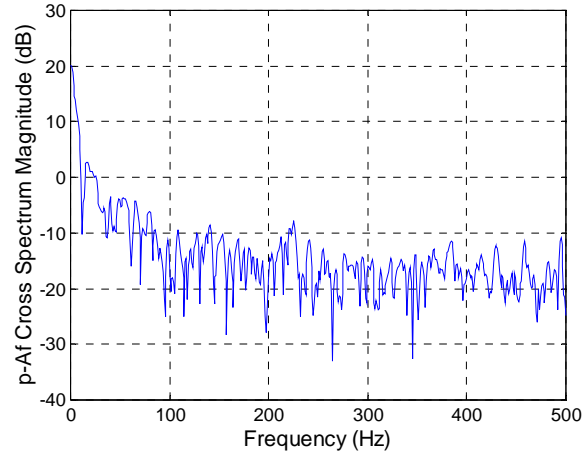
Figure 8.12: Signal coherence between area and heat release perturbations for $U = 1.54$ m/sec and $\phi = 0.9$. Coherence is near 1.0 for instability frequency (225.8 Hz).

frequency, f_{fund} , of approximately $f_{\text{fund}} = 220$ Hz. An additional peak occurs at $f = 182$ Hz which is associated with the resonant frequency of the burner nozzle, f_b . The amplitudes of the cross-correlation between pressure and heat release at these two frequencies are comparable although small, while the correlations between the other parameters ([Figures 8.13b-d](#)) more closely resembles the broadband noise typical of signatures from stable flames.

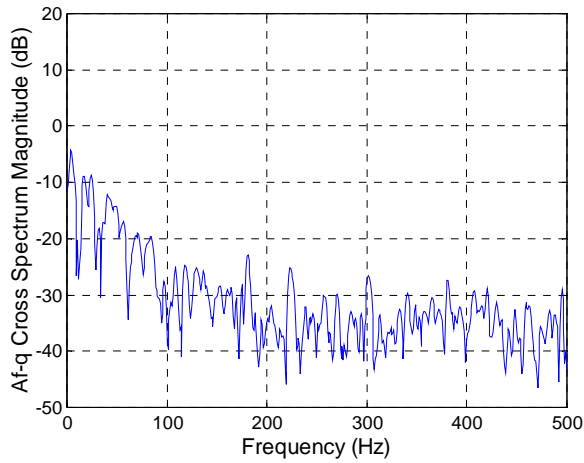
Acoustically-forcing this stable flame ($V_{\text{mean}} = 1.54$ m/sec and $\phi = 0.68$) with the externally located speaker arrangement (Figure 3.9b) at a frequency of $f_{\text{acoust-force}} = 220$ Hz and a velocity intensity of approximately $i_p = 0.07$ (estimated from acoustic pressure intensity) lead to the cross spectral response shown in [Figures 8.14a-d](#). As would be expected, the cross-spectra is dominated by a peak at $f_{\text{acoust-force}} = 220$ Hz and the second harmonic at $f = 440$ Hz, a small peak still persists at f_b , but is nearly masked by the response at 220 Hz. As was shown in Figure 7.14, with only a small addition of acoustic energy ($P_{\text{acoust-amp}} < 0$ dB) the flame response is increased substantially, $P_{\text{acoust-force}} = 40$ dB, an increase of almost 35 dB over the stable response shown in Figure 8.13. In order for this to occur the excitation of the marginally stable flame must force a coupling between the acoustics and variable heat release rate that is similar to the mechanisms driving the self-excited flames. The large increase in the amplitude of the cross-spectra in [Figure 8.14a](#) over that of [Figure 8.13a](#) indicate the presence of the appropriate coupling mechanisms.



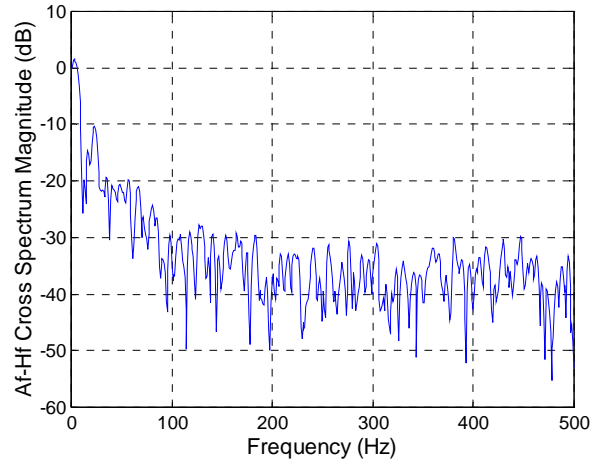
a) Cross-spectra of pressure and heat release rate



b) Cross-spectra of pressure and flame surface area

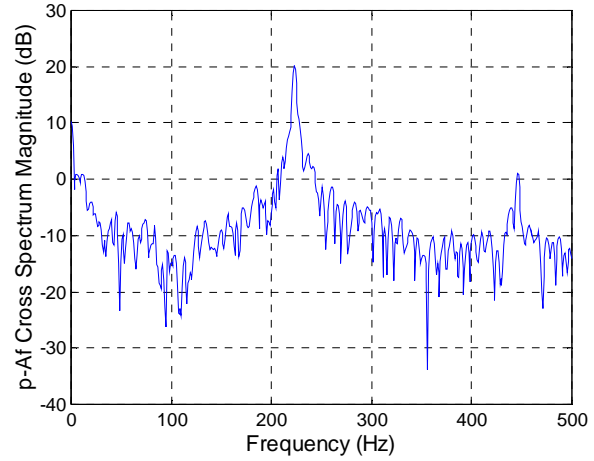
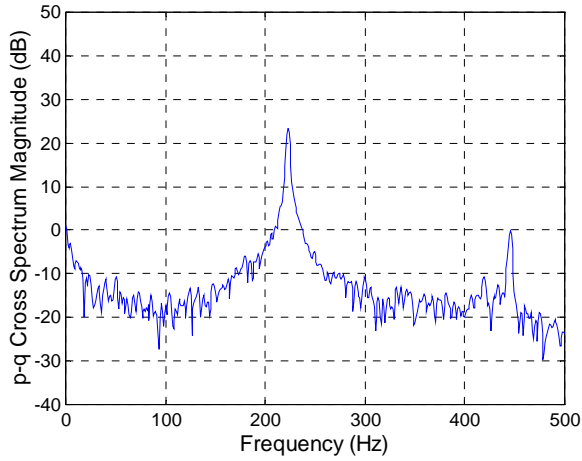


c) Cross-spectra of surface area and heat release rate

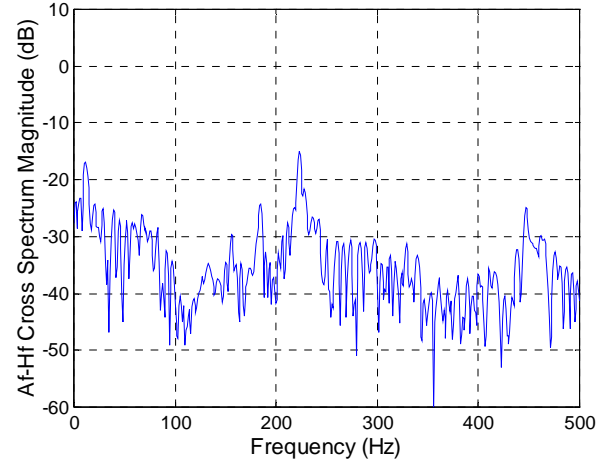
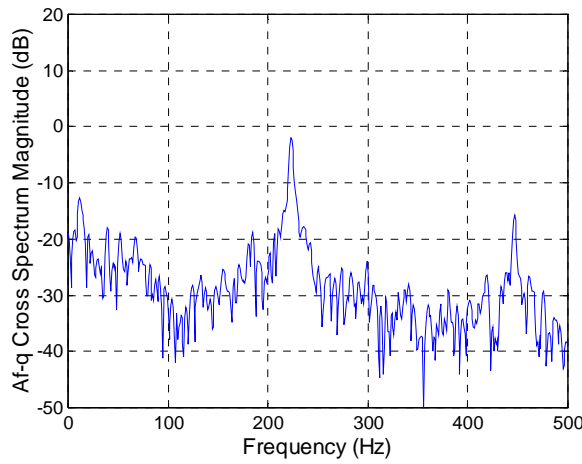


d) Cross-spectra of surface area and flame height (flapping)

Figure 8.13: Frequency cross-spectra of analog signals stable flame at $V_{\text{mean}} = 1.54$ m/sec and $\phi = 0.68$. a) Cross-spectrum of P^2 - Q' , b) Cross-spectrum of P^2 - Af^2 , c) Cross-spectrum of Af^2 - Q' , d) Cross-spectrum of Af^2 - Hf^2 .

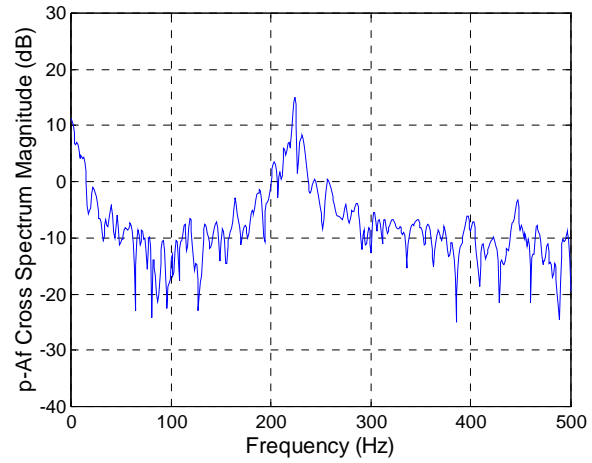
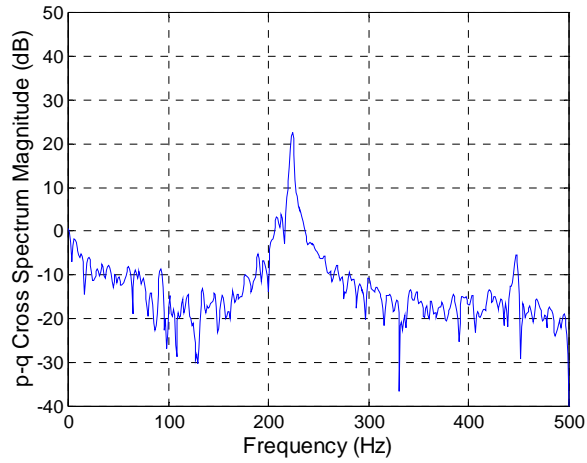


a) Cross-spectra of pressure and heat release rate b) Cross-spectra of pressure and flame surface area

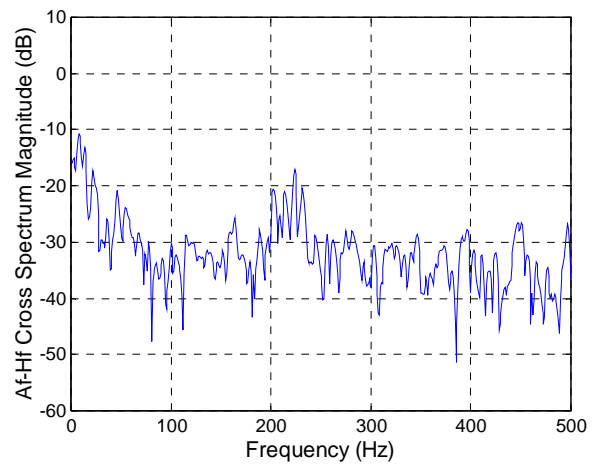
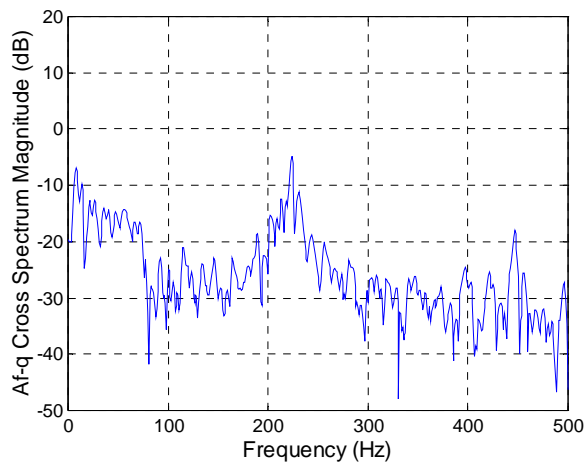


c) Cross-spectra of surface area and heat release rate d) Cross-spectra of surface area and flame height (flapping)

Figure 8.14: Frequency cross-spectra of analog signals forced flame at $V_{\text{mean}} = 1.54$ m/sec and $\phi = 0.68$, a) Cross-spectrum of P^2 - Q^2 , b) Cross-spectrum of P^2 - Af^2 , c) Cross-spectrum of Af^2 - Q^2 , d) Cross-spectrum of Af^2 - Hf^2 .

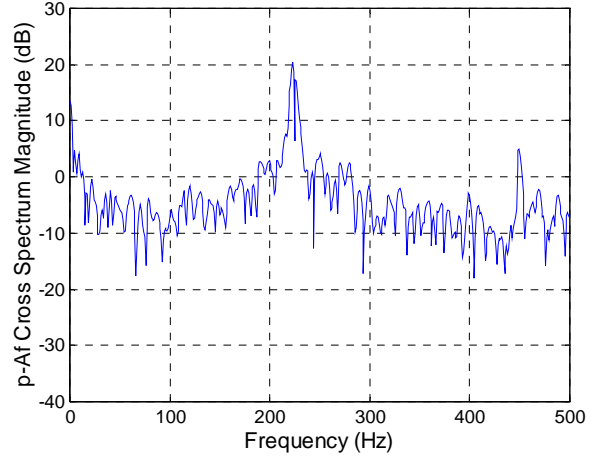
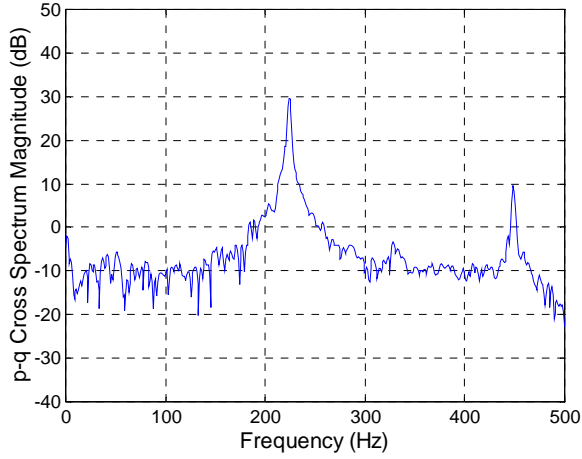


a) Cross-spectra of pressure and heat release rate b) Cross-spectra of pressure and flame surface area

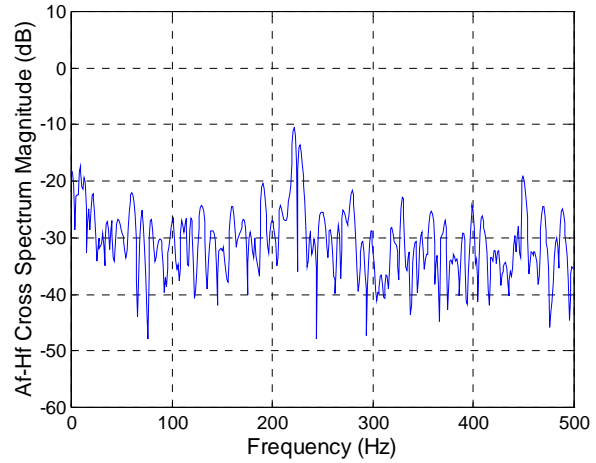
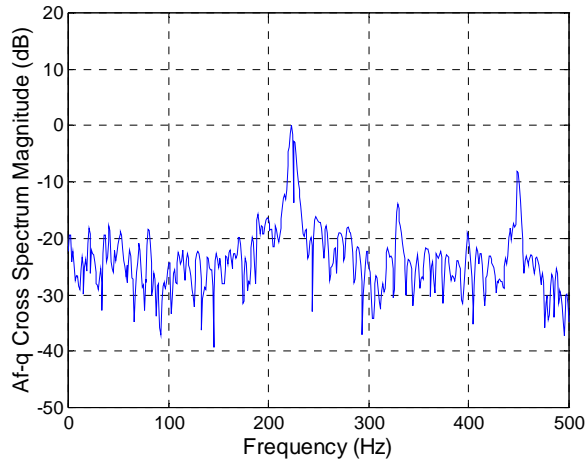


c) Cross-spectra of surface area and heat release rate d) Cross-spectra of surface area and flame height (flapping)

Figure 8.15: Frequency cross-spectra of analog signals self-excited flame at $V_{\text{mean}} = 1.54$ m/sec and $\phi = 0.70$. a) Cross-spectrum of P' - Q' , b) Cross-spectrum of P' - Af' , c) Cross-spectrum of Af' - Q' , d) Cross-spectrum of Af' - Hf' .

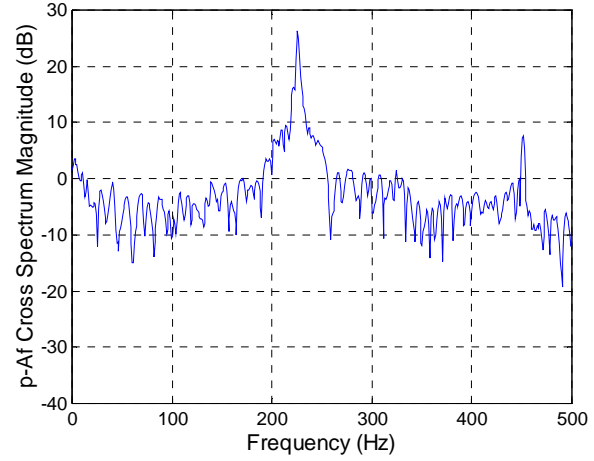
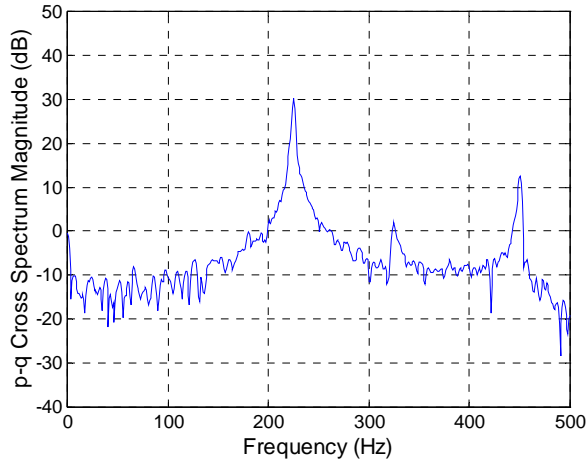


a) Cross-spectra of pressure and heat release rate b) Cross-spectra of pressure and flame surface area

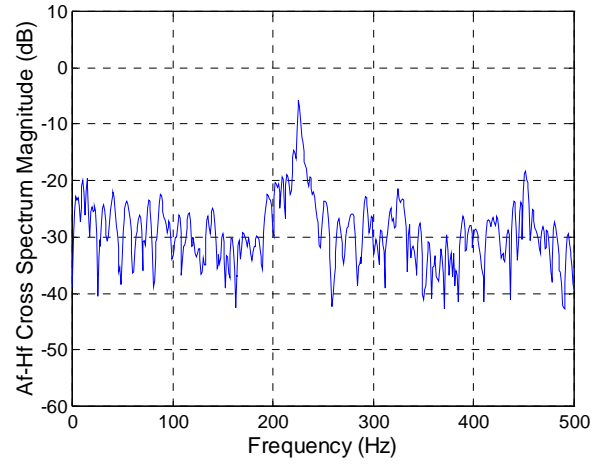
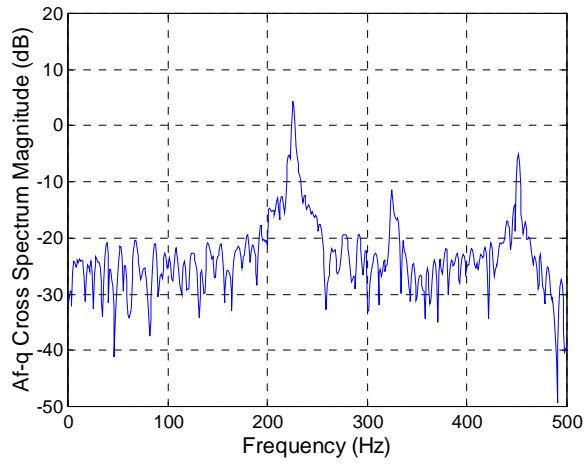


c) Cross-spectra of surface area and heat release rate d) Cross-spectra of surface area and flame height (flapping)

Figure 8.16: Frequency cross-spectra of analog signals self-excited flame at $V_{\text{mean}} = 1.54$ m/sec and $\phi = 0.80$. a) Cross-spectrum of P^2 - Q' , b) Cross-spectrum of P' - Af , c) Cross-spectrum of Af - Q' , d) Cross-spectrum of Af - Hf .

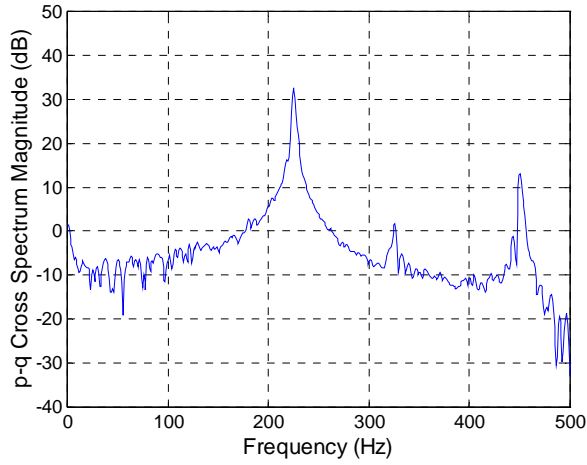


a) Cross-spectra of pressure and heat release rate b) Cross-spectra of pressure and flame surface area

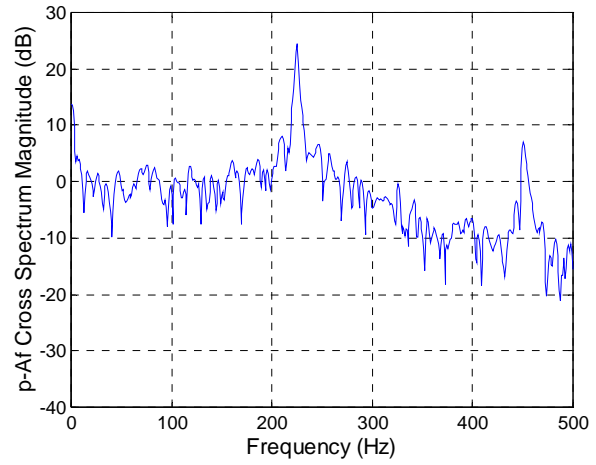


c) Cross-spectra of surface area and heat release rate d) Cross-spectra of surface area and flame height (flapping)

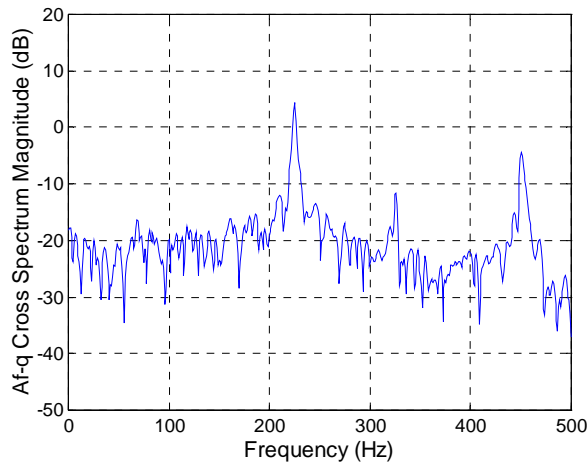
Figure 8.17: Frequency cross-spectra of analog signals self-excited flame at $V_{\text{mean}} = 1.54$ m/sec and $\phi = 0.90$. a) Cross-spectrum of P^2 - Q' , b) Cross-spectrum of P^2 - Af , c) Cross-spectrum of Af - Q' , d) Cross-spectrum of Af - Hf .



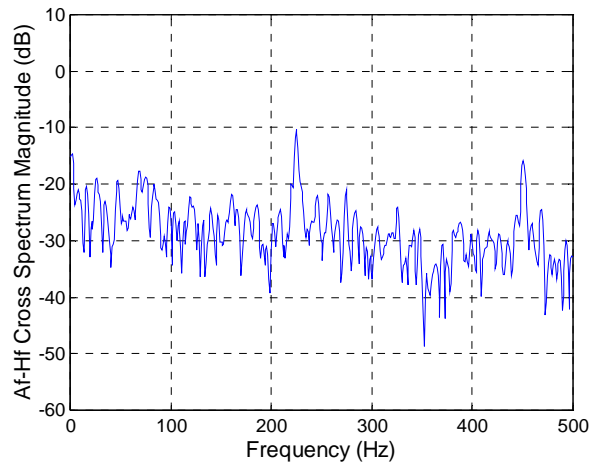
a) Cross-spectra of pressure and heat release rate



b) Cross-spectra of pressure and flame surface area



c) Cross-spectra of surface area and heat release rate



d) Cross-spectra of surface area and flame height (flapping)

Figure 8.18: Frequency cross-spectra of analog signals self-excited flame at $V_{\text{mean}} = 1.54$ m/sec and $\phi = 1.0$. a) Cross-spectrum of P' - Q' , b) Cross-spectrum of P' - Af' , c) Cross-spectrum of Af' - Q' , d) Cross-spectrum of Af' - Hf' .

The self-excited, unstable flame of [Figure 8.15a-d](#) is obtained by adjusting from $\phi = 0.68$ to $\phi = 0.7$, a change of only $\Delta\phi = 0.02$. As previously noted, this small change in equivalence ratio resulted in a 60% increase in P'_{rms} . Similar to the acoustically-forced case, the spectrum is dominated by a single frequency at f_r , however a broadening of the peak masks the identification of a peak at f_b . Aside from the broadening of the peaks, the closed-loop response of the flame in [Figure 8.15](#) is quite similar to the open-loop response of [Figure 8.14](#). The broadening of the peaks is an indication that at low amplitude excitations the excitation frequency may not be fixed and the correlations are not strong, particularly between the flame surface area and the flame height, [Figure 8.15d](#).

The strong similarities between [Figures 8.14](#) and [8.15](#) supports the hypothesis that acoustically-forcing the flame by this means produces a similar response as when the flame is self-excited. As will be seen in Chapter 9, this form of acoustic-forcing invokes a significantly different response than the inline speaker method ([Figure 3.9c](#)), a method which is typically used to in developing empirically derived system response models of self-excited flames. This supports the notion that the acoustic impedance is an important parameter in predicting the occurrence of thermoacoustic instabilities, as it is essentially the only parameter that is affected by changing the experimental configuration from [Figure 3.9b](#) to [3.9c](#).

In [Figure 8.16](#), the equivalence ratio is increased to $\phi = 0.8$, the acoustic pressure amplitude increases to $P'_{\text{rms}} = 64$ Pa and the magnitude of the cross-spectrum between the pressure and heat release rate increases to $C_{p-q} = 30$ dB from $C_{p-q} = 22$ dB at $\phi = 0.7$. As the amplitude of the self-excited instability increases more energy is directed into the second harmonic ($f_{2F} = 450$ Hz) and we begin to see more of a correlation at the burner nozzle frequency, $f_b = 325$ Hz, between the various parameters. However, the amplitude of the cross-spectrum between the flame surface area and the flame height, although slightly higher and narrower centered at $f_F = 225$ Hz, remains relatively low. A possible explanation offered by Baillot, Durox and Prud'Homme¹¹⁸ is that the tip oscillates at a different frequency (flapping frequency) than the rest of the flame and is control by buoyancy effects; however spectral analysis of the varying flame height did not reveal any additional oscillation frequencies. A more likely explanation is that the varying tip region has only a minor influence on the overall variation in the surface area, and thus suggesting that its effects on the overall variations in the heat release rate are negligible.

The cross-spectral density for the self-excited flame during periods of maximum instability ($V_{\text{mean}} = 1.65$ m/sec, $\phi = 0.9$ and 1.0) is shown in [Figure 8.17a-d](#) and [Figure 8.18a-d](#), respectively. As

the previous plot, these figures are dominated by a peak at the fundamental frequency of the burner, $f_{\text{fund}} = 228\text{--}230\text{ Hz}$, which has shifted slightly due to the increase in temperature within the burner. The amplitude of the p' - q' cross-spectrum peak at f_f and f_{2f} has not increased substantially from that given in [Figure 8.16a](#), although there has been a slight increase at f_b . This would suggest that nonlinearities contributed to the behavior as the harmonic frequencies tend to distort the sound wave and thus limit the amount of energy that could be fed back into the coupling process that drives the instabilities.

Similar trends were observed at other flow rates over the same equivalence ratio ranges. This leads one to conclude that the coupling mechanisms that drive the thermoacoustic instability are more dependent on equivalence ratio, ϕ , than the mean flow rate through the burner. This is further supported by the data presented in the remaining pages of this section that look at the peak instabilities and phase angle relationships between parameters for flames operated at the conditions specified in [Table 7.1](#).

[Figure 8.19](#) is a plot of the flame area ratio ($a_f = A_f'_{\text{rms}}/A_{f_{\text{mean}}}$) for different flow rates over a range of equivalence ratios. Aside from a few outliers the area ratio is relatively small for stable and marginally stable flames, as expected. These outliers in the lean flame are thought to primarily be the result of a flame that is statically unstable at these conditions as opposed to dynamically unstable flames. Transitioning between stable and self-excited flames results in a reduction of surface area intensity of up to a 50%. On the lean side of the stability boundary, excitation increased the flame area ratio by 120% - 170% and approached levels comparable to the self-excited flame. However at levels above stoichiometric ($\phi = 1.1$), stable flame excitation had a minimal effect. A possible explanation for this difference at the two stability boundaries is varying heat release from other surfaces through diffusion in the outer layer of the rich flame and to the flame anchor. Another possibility is that under lean conditions the flame surface may experience a higher degree of flame stretch thus variations in the flame may have more of an impact on the surface. If this is the case, this would presumably indicate that rich flames (such as diffusion flames) may better damp instabilities in the flow and prevent or reduce the amplitude of thermoacoustic instabilities. However, more work is needed to verify the possibility of a reduction in “flame damping” due to lean burner.

As the flame becomes dynamically unstable, the amplitude of the area ratio increases and begins to converge. Results plotted in [Figure 8.20](#) of the area ratio shown as a function of the acoustic intensity, p'_{rms} , demonstrate this more clearly with the area ratio converging to approximately $A_f' = 0.13$ at conditions of peak instability. Comparing [Figure 8.21](#), which is a plot of the rms of the variable heat

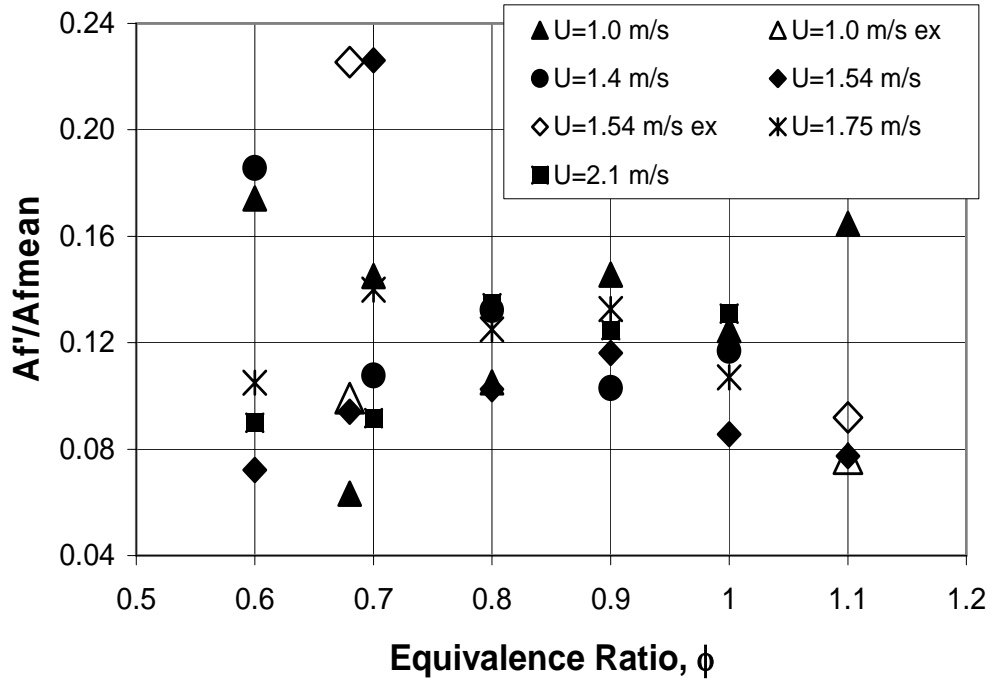


Figure 8.19: Normalized amplitude of RMS flame surface area as a function of equivalence ratio at various nozzle exit velocities.

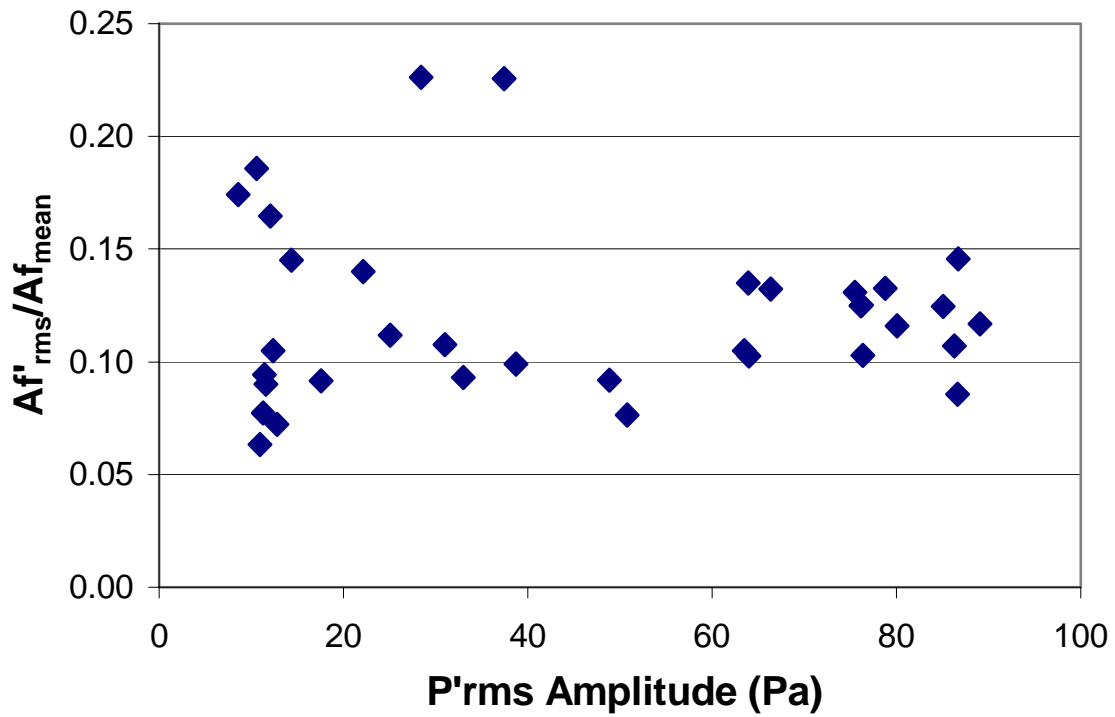


Figure 8.20: Amplitude of flame area ratio as a function of the acoustic pressure.

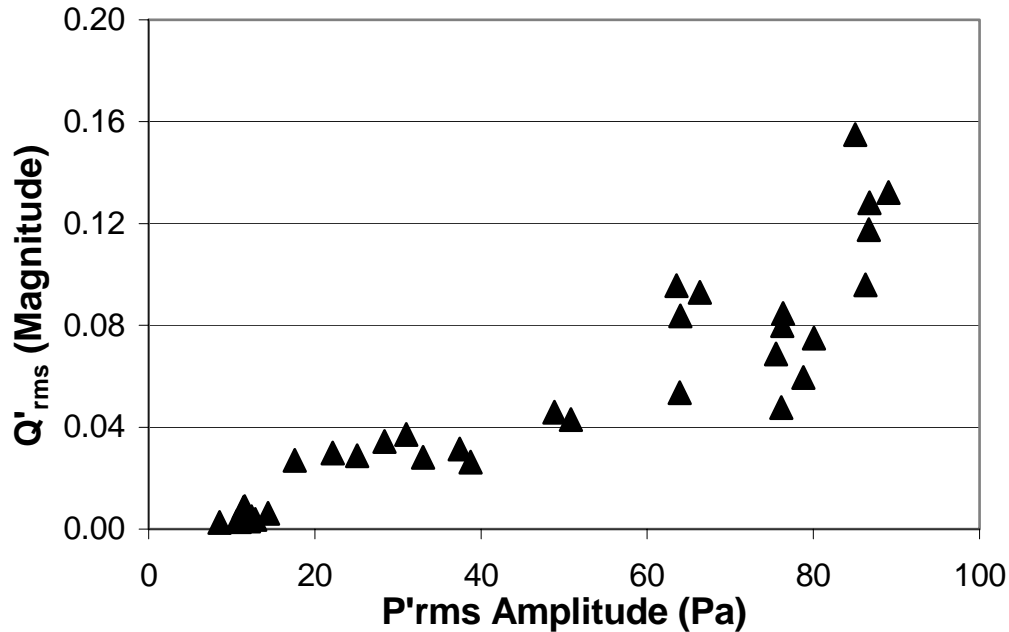


Figure 8.21: Amplitude of the variable heat release rate as a function of the acoustic intensity.

release rate versus the acoustic intensity, with [Figure 8.20](#) we see that although variations in the flame surface area appear to plateau the amplitude in the heat release rate perturbations continue to grow with an increase in the acoustic intensity. This would suggest that the relationship between flame surface area and heat release rate is more complicated than this simple relationship given in [Equations 8.5 and 8.7](#). Comparing the two plots reveals that the variations in the flame surface area reach a limit while perturbations in the heat release rate continue to grow as the instability is amplified. Although perturbations in the heat release rate may be the result of variations in the flame surface area once the saturation limit in the surface area is reached continual growth in the amplitude of the variable heat release rate is the result of additional mechanisms that may or may not have been previously active. This results in a nonlinear relationship between the heat release rate and flame surface area. As the amplitude of the instability grows past the limit of surface area variability, the flame surface may continue to react through local variations in flame stretch which in turn alter the localized heat release rate by imposing a stretch flame speed. These effects persist until the flame surface begins to stretch to extinction and the flame becomes statically unstable.

In [Figure 8.2](#) which plots the flame area ratio over a wide range of flame Strouhal numbers ($G = \omega D / 2S_w$), Fleifil et al.³⁹ demonstrates a strong dependence of the area ratio on G . Unfortunately for the work done for this thesis which allowed the flame to oscillate under self-excited conditions the

flame Strouhal numbers obtained were rather limited with $G \approx 35 - 60$. Nonetheless, a comparison between the predictive results of the Fleifil model and the experimental results of this study are possible at similar values of G , [Figure 8.22](#). Results indicate that the Fleifil model under predicts the amplitude of the flame area ratio for the range of flame Strouhal numbers evaluated in this study.

The measured phase difference between the heat release rate and the flame surface area is given in [Figure 8.23](#) over a range of equivalence ratios and flow rates. Phase data beyond the limits of instability $\phi < 0.68$ and $\phi > 1.1$ is essentially meaningless as the flame was not oscillating at these conditions and thus has been excluded from these plots. The phase angles were taken from the cross

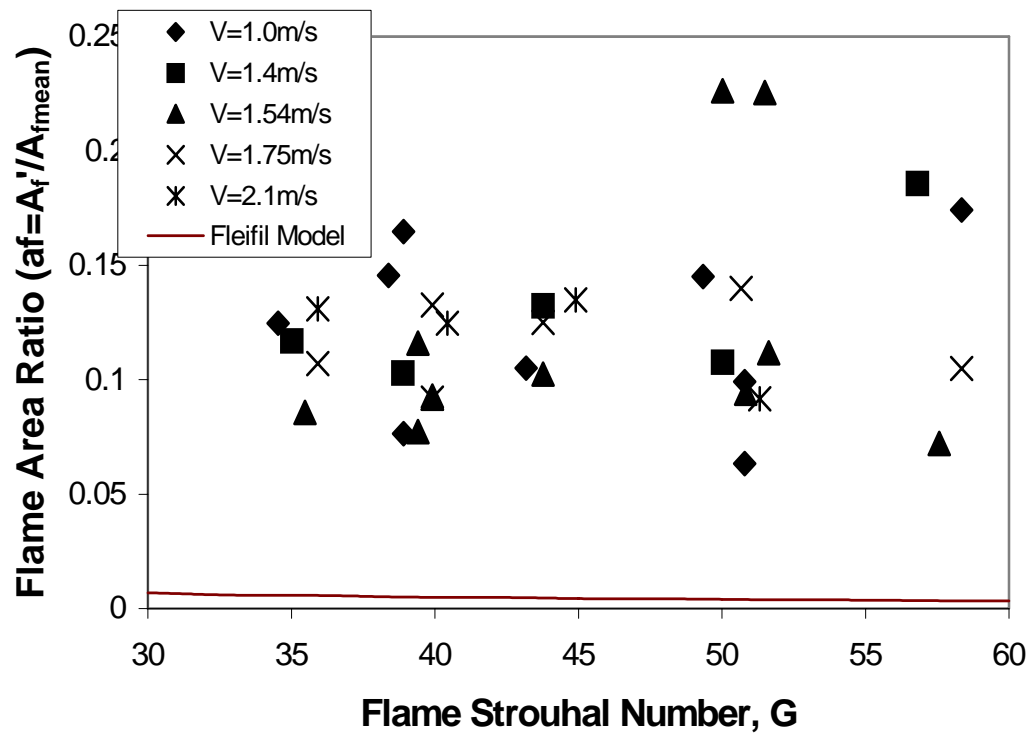


Figure 8.22: Flame area ratio plotted against the non-dimensional frequency, or flame Strouhal number comparing experimental results to those predicted by the Fleifil model.

spectral density at the peak oscillation frequency. In analyzing the phase relationship between these two parameters one must give some consideration to the methods of detection. As previously noted the heat release rate is determined by measuring OH^* emissions while the flame surface area is extracted from chemiluminescence images of C_2 and CH emissions. In determining the phase relationship between heat release and surface area the assumption must be made that the chemical times of the reactions that produce these species are unaffected by the presence of thermoacoustic

instabilities or are affected at the same rate. The validation of this assumption is beyond the scope of this study however it is believed that the acoustic pressures experienced here are not significant enough to vary the reaction rates of the processes that create these species. Understanding that there is a time delay between the acoustic velocity and perturbations of the flame surface area (acoustic velocity is discussed in Chapters 9 and 10) and given the above statements regarding measurement techniques it is interesting that there is a phase angle difference between perturbations in the flame surface area and the heat release rate. This may emphasize the importance of flame stretch and the fact that a simple characteristic time delay may not be able to describe the phase relationship between the heat release rate and the acoustic velocity or flame surface area.

In the kinematic model developed by Fleifel et.al³⁹, it was assumed an acoustic velocity disturbance that resulted in a variance in the flame surface area preceded it by a characteristic time that was dependent upon the flame Strouhal number and according to Equation 8.5, perturbations in the heat release rate were in phase with the flame surface area. Thus while a phase difference should exist between the velocity disturbance and the heat release rate, no difference should be present between the flame surface area and the heat release. Figure 8.24 is a plot of the measured phase angle differences between the flame surface area and heat release rate along with the phase angle difference between the acoustic velocity and the heat release rate predicted by the Fleifel model. The interesting thing to note here is that even the phase angle difference between the acoustic velocity and the heat release rate predicted by Fleifel is consistently less than that of the measured difference between the flame surface area and heat release. Ducruix et. al³³ also believed that the Fleifel model under predicts the phase difference at $G > 10$ and again suggests a more complicated relationship than a simple time delay.

In Figure 8.23 at $\phi = 0.68$ a low amplitude oscillation is detected at the fundamental frequency of the burner, however there is still some considerable variability in the phase angle difference between the flame surface area and heat release rate, Θ_{AF-q} , at this weakened state. As the flame transitions through the lean stability boundary ($\phi = 0.68-0.7$) there is a significant change in Θ_{AF-q} with a shift from $\Theta_{AF-q} = 110^\circ$ for a weakly unstable flame at $V_{mean} = 1.0$ m/sec and $\phi = 0.68$ to $\Theta_{AF-q} \approx 200^\circ$ for the respective self-excited flame at $\phi = 0.7$. In addition to the strong gradient across the boundary, the data spread across the flow rates has greatly reduced. Excitation of the weakly unstable or marginally stable flame at $\phi = 0.68$ produced a response similar to the self-excited flames at $\phi = 0.7$. However, it is interesting to note that although the phase difference obtained at the rich limit is quantitatively

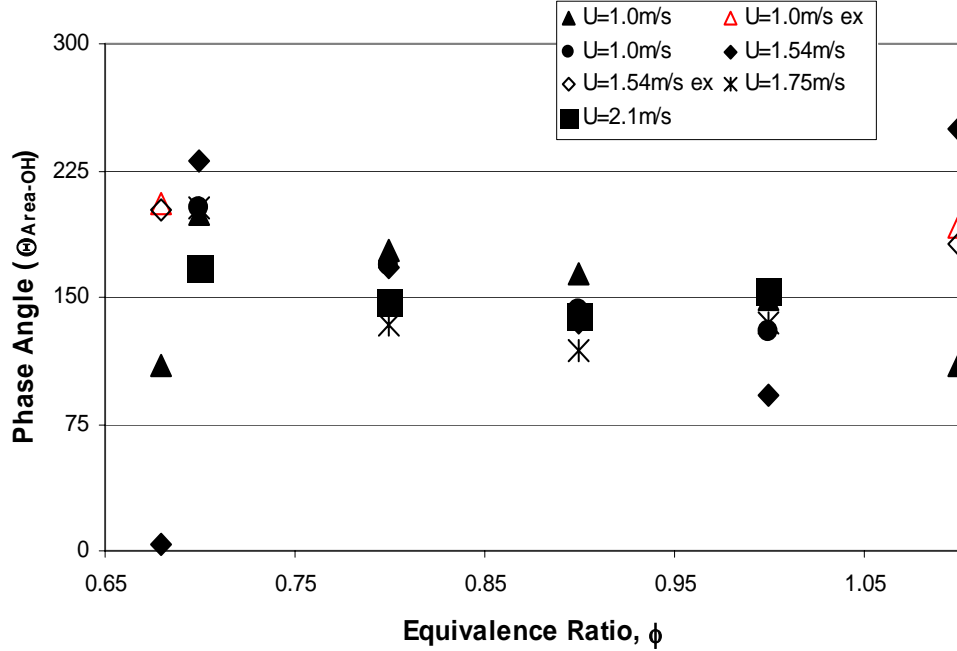


Figure 8.23: Phase angle between surface area and OH* perturbations as a function of equivalence ratio.

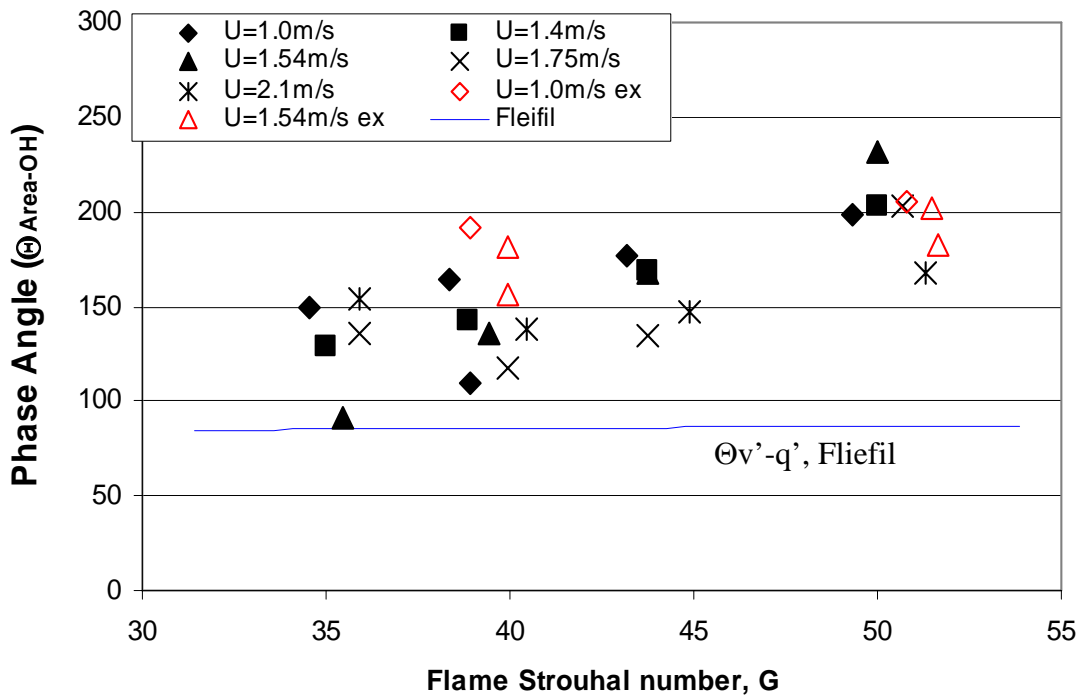


Figure 8.24: Phase angle between surface area and OH* perturbations as a function of flame Strouhal number.

similar to that of the acoustically-forced flame at the lean stability boundary, it is considerably different than the respective self-excited flame at $\phi = 1.0$. Ignoring the differences across the flow rates, the average phase angle difference at $\phi = 1.0$ is approximately $\Theta_{AP-q'} = 140^\circ$, compared to the phase angle difference of the acoustically-forced flame which is $\Theta_{AP-q'} = 185^\circ$ at $\phi = 1.1$. At the lean stability boundary ($\phi = 0.68$) the acoustically-forced flame produces a phase angle difference of $\Theta_{AP-q'} = 200^\circ$, which is equal to the flow averaged quantity for the self-excited flame at $\phi = 0.7$. A comparison of the power spectrums on non-reacting and reacting flows in the acoustically-driven cases (Figure 7.13) indicated that there was an amplification of the flame response due to feedback within the combustor as the amplitude of the power spectrum at the excitation frequency for the excited reacting flow far exceeded that of the excited non-reacting flow and marginally stable flame. Thus the phase response of the acoustically-driven flame at these conditions is not solely an open-loop response, nor is this phase angle difference explained by a simple time delay.

There are several features that stand out in comparing these results. First the rms amplitude of the acoustic response for both the lean and rich acoustically-forced flame at both flow rates is comparable to each other ($P_{rms} = 38 - 48$ Pa) as well as the rms amplitude of the acoustic pressure of the self-excited flame at $\phi = 0.7$ ($P_{rms} = 30$ Pa). However this quantity is much lower than that of the

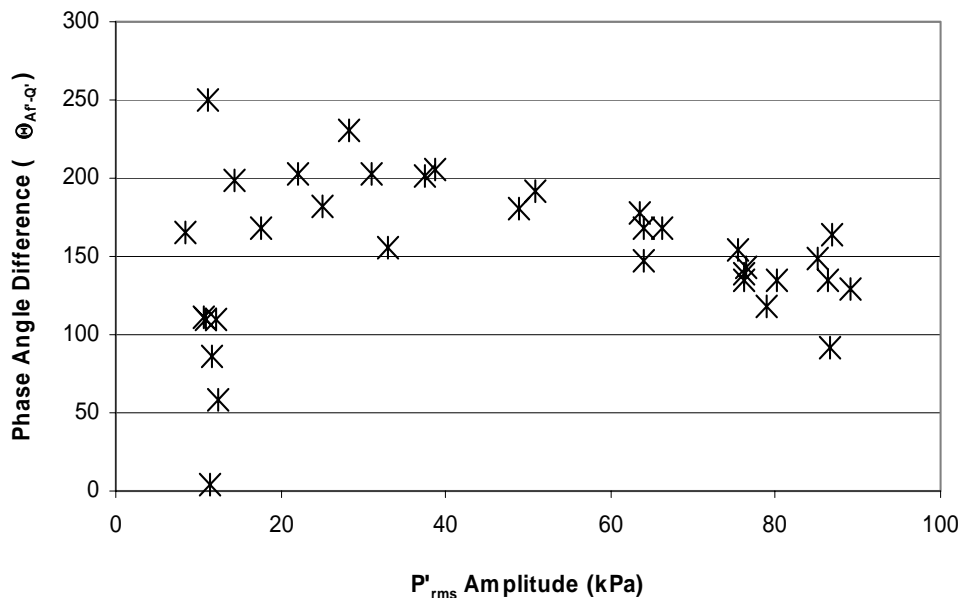


Figure 8.25: Phase angle difference between flame surface area and heat release rate given at increasing amplitudes of thermoacoustic instabilities.

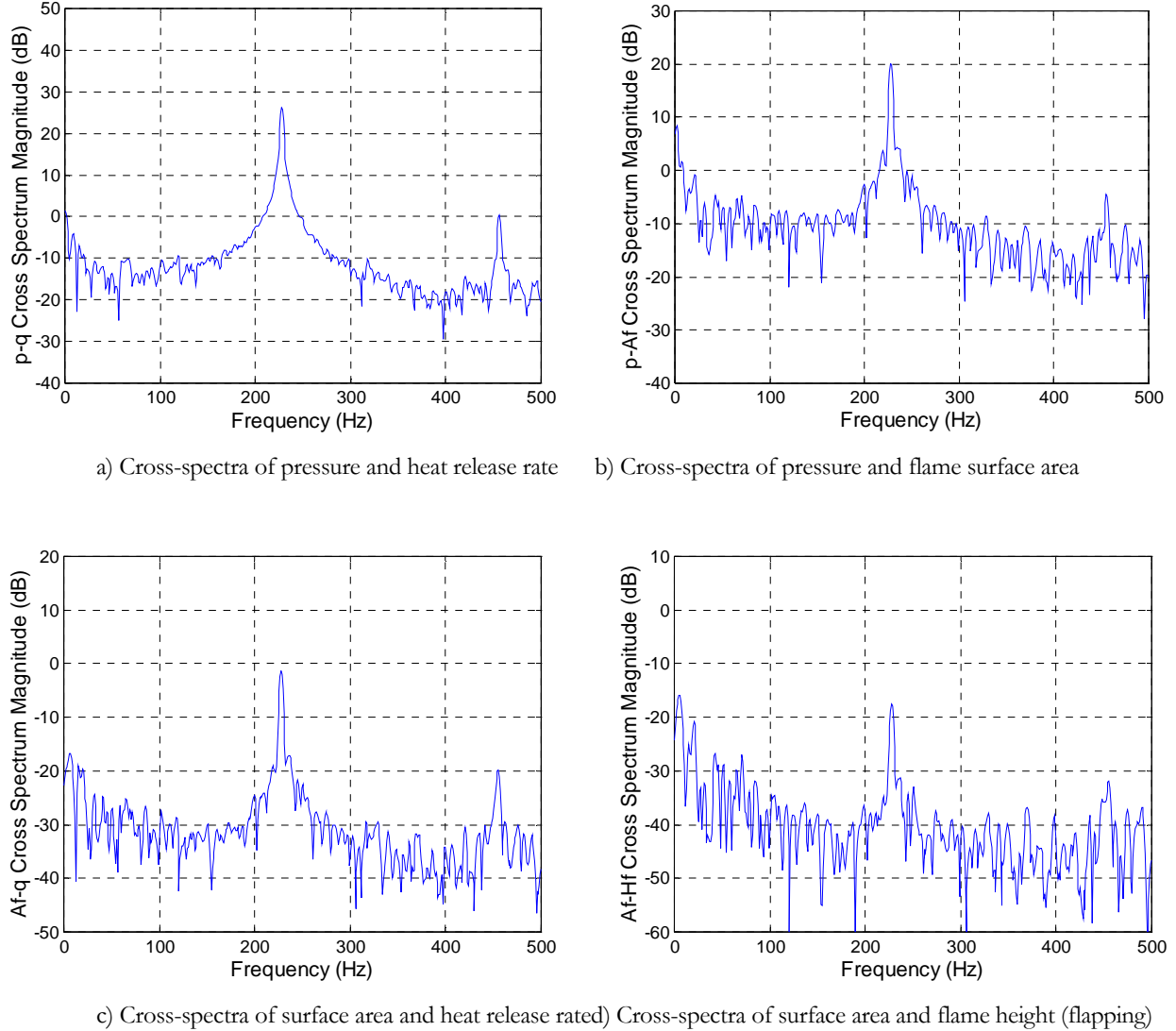


Figure 8.26: Frequency cross-spectra of analog signals from acoustically-forced flame at $V_{\text{mean}} = 1.54$ m/sec and $\phi = 1.1$. a) Cross-spectrum of $P' - Q'$, b) Cross-spectrum of $P' - Af'$, c) Cross-spectrum of $Af' - Q'$, d) Cross-spectrum of $Af' - Rd'$, e) Cross-spectrum of $Af' - Lf'$

self-excited flame at $\phi = 1.0$ with $P_{\text{rms}} > 80$ Pa. We have already spoke of the fundamental differences in the flame response when operated above stoichiometric conditions, but we can not overlook the similarities in the acoustically-driven and marginally- unstable flames. [Figure 8.25](#) is a plot of this phase angle difference against the rms value of the acoustic pressure and indicates that for unstable flames, in which $P_{\text{rms}} > 30$ Pa, $\Theta_{AP-q'}$ collapses to a steadily decreasing monotonic line ending at $\Theta_{AP-q'} \approx 135^\circ$. Thus the actual amplitude of the disturbance may be significant in determining the phase difference between perturbations in the flame surface area and the variable heat release rate.

Another interesting point is the similarities in the cross-spectrum between the lean and rich acoustically-forced flame and the weakly unstable flame at $\phi = 0.7$, and its difference compared to the spectrum of the self-excited flame at $\phi = 1.0$. For a flow rate of $V_{\text{mean}} = 1.54$ m/sec, plots of the cross-spectrums for the acoustically-forced flame at $\phi = 0.68$, the self-excited flame at $\phi = 0.7$ and at $\phi = 1.0$ are given in [Figures 8.14, 8.15](#) and [8.18](#), respectively. For comparative purposes the cross-spectrums for the acoustically-forced flame at $V_{\text{mean}} = 1.54$ m/sec and $\phi = 1.1$ is given in [Figure 8.25](#). There are obvious similarities in both the amplitude and overall spectrum between the plots of [Figure 8.25](#) and those of [Figure 8.14](#) and [8.15](#) with the spectrum being dominated by the peak at the burner fundamental frequency ($f_r \approx 225\text{-}230$ Hz) and a smaller peak at its second harmonic ($f_{2r} = 450\text{-}460$ Hz). Comparing these spectra with their respective plots in [Figure 8.18](#) indicates that at the higher amplitude an additional peak appears at the nozzle fundamental frequency ($f_b = 330$ Hz). Additionally this peak occurs in the spectra for the all flames at $f = 0.8\text{-}1.0$. It is the presence of this additional peak that may account for the variation in $\Theta_{\text{AF-q}}$ across the operation conditions shown here. This along with the possible effect of the acoustic amplitude emphasizes that the phase angle relationship is more than just a simple characteristic time delay and that both acoustic state variables (v' and p') play an active role in determining the phase angle relationship between heat release mechanisms and the actual heat release rate. The practical implication is that the evaluation of the flame response based on flame surface area perturbations alone will not describe the phase necessary for closed loop stability.

The decrease in $\Theta_{\text{AF-q}}$ observed in [Figure 8.24](#) also occurs as the equivalence ratio increases to $\phi = 1.0$, thus there is also an increase in the laminar flame speed and this decrease appears to be independent of the mean flow rate. Allowing the burner to operate in self-excited mode does not allow the opportunity to control the amplitude of excitation at each operating condition. Therefore it is difficult to differentiate the effects of laminar flame speed and from those of the amplitude of the acoustic disturbance. The results presented in [Chapter 9](#) and [10](#) attempt to address these concerns, however as will be seen, exciting the flame through the configuration shown in [Figure 3.9c](#) brings about its own complications.

Chapter 9 Flame Excitation

9.1 Various Modes of Flame Excitation

Figure 9.1 (reproduction of Figure 4.1) is a block diagram representation of the feedback loop that drives thermoacoustic instabilities in the Rijke tube combustor used in this study. With simple modifications, this block diagram can be used to represent the three different experimental configurations shown in Figure 9.2 (reproduction of Figure 3.9). Removal of the box labeled “external excitation” provides a representation of the self-excited flame configuration given in Figure 9.2a. In this configuration, due to closed-loop feedback between the acoustics and the heat release, the flame is inherently unstable over most of the burner’s operating range. However, with a slight change in equivalence ratio under lean ($\phi < 0.68$) or rich ($\phi > 1.05$) conditions the inherently unstable flame becomes stable. With a speaker placed just outside the open-ended Rijke tube, as shown in Figure 9.2b, it is possible to impose a controlled acoustic disturbance to get the flame to begin to oscillate under the marginally stable conditions of $\phi < 0.68$ or $\phi > 1.05$. This is represented in the block diagram of Figure 9.1 by reinstating the “external excitation” box. Comparisons between the power spectra of non-reacting and reacting stable and excited flows, given in Figure 7.14, indicated that this method of excitation actually promotes a coupling between the heat release and acoustics that amplifies the overall response of the marginally stable flame. This suggests that

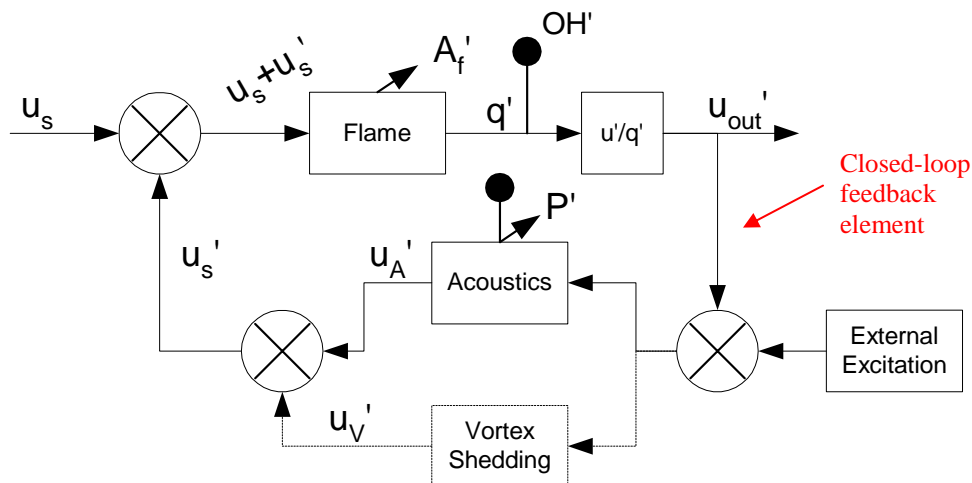


Figure 9.1: Block diagram representation of the feedback loop that drives thermoacoustic instabilities in the Rijke tube combustor.

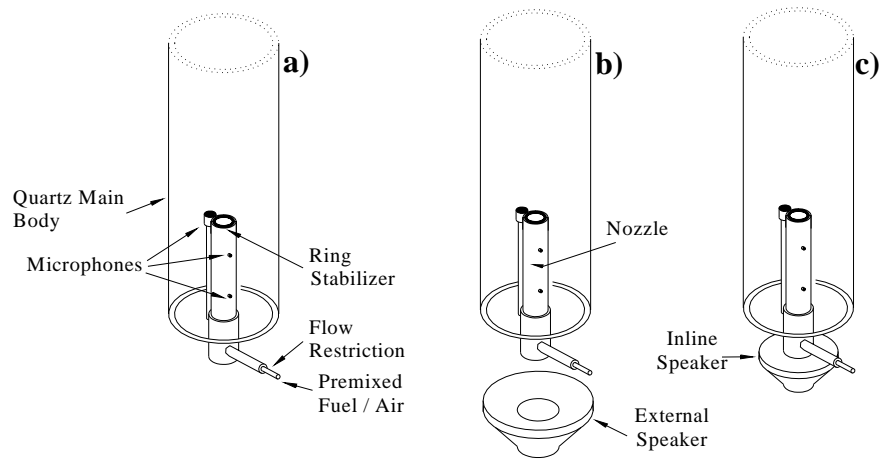


Figure 9.2: Three experimental configurations utilizing various method of excitation; (a) self-excited, (b) acoustically-forced by external speaker, and (c) acoustically-forced by inline speaker.

the energy is added to the acoustic response from the flame and a closed-loop feedback cycle is formed as opposed to just a simple open-loop system. This allows one to study the full feedback mechanisms with controlled input to the flame.

Prediction of thermoacoustic instabilities in gas turbine engines is dependent on the derivation of accurate flame transfer functions. Experimental methods such as open-loop acoustic-forcing is often employed to generate simple n-port models that define the flame transfer function, however there is some concern as to if this practice leads to the development of a valid model that can be used to predict closed-loop stability in a reduced-order model. These transfer functions form the mathematical definitions of the boxes labeled “flame” and “ u'/q ” in Figure 9.1 and may be a one-port model, typically using an input of acoustic velocity to predict the flame response, or a multi-port model using additional inputs such as acoustic pressure, or impedance, equivalence ratio perturbations, etc. The model developed by Fleifil et. al³⁹ is one example of a one-port models that is based on the acoustic velocity. For these models to be valid the heat release signature from an acoustically-forced flame should be comparable to that of a self-excited flame provided that it is excited in such a way as to have the similar inputs. Comparing self-excited to acoustically-forced flames in the same burner would provide an opportunity to evaluate this hypothesis. Unfortunately, as the experimental derivation of these transfer functions require that the flame be acoustically-

driven and free of the mechanisms that drive self-excited combustion, burners that are often used must be inherently stable and do not permit operation in both modes at similar conditions thus making comparisons impossible.

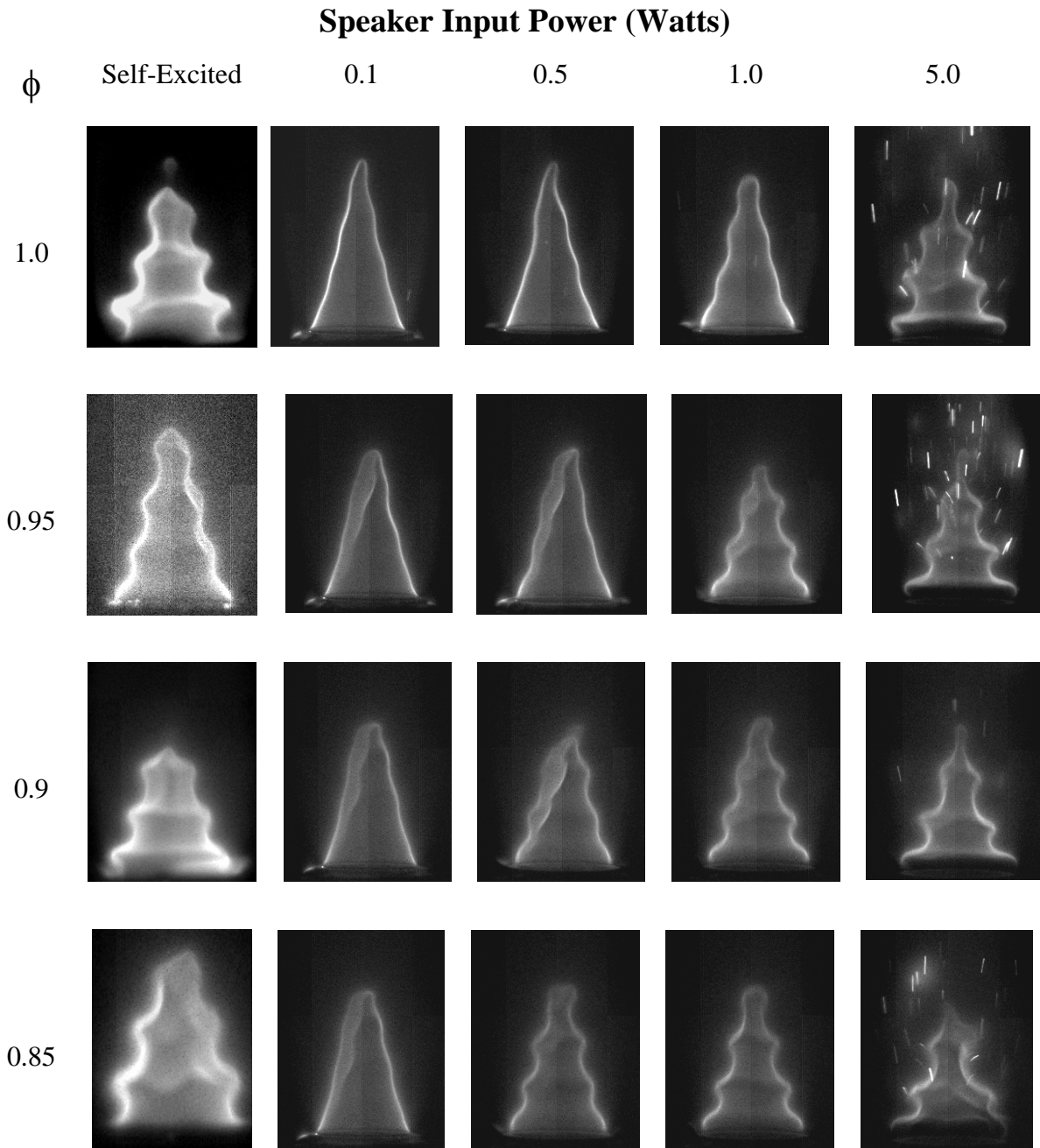
The Rijke tube burner used in this study is unique in that it is inherently unstable, however open-loop forcing of a stable flame is possible using the arrangement presented in Figure 9.2c. Replacing the rigid boundary at the base of the burner nozzle with a loudspeaker sufficiently alters the acoustic impedance which helps to stabilize the flame. An advantage of this configuration is that the burner modification at the nozzle base does not alter the downstream boundary conditions at the nozzle exit / flame anchor.

Although the derivation of transfer functions describing the response of the flame is not the scope of this study, an effort was made to evaluate the ability of acoustically-forced stable flames to reproduce a closed-loop response (one-port vs. two port). Comparisons between the self-excited and acoustically-driven flame at various amplitudes of acoustic intensity provide an opportunity to study the phase-gain relationship between heat release and acoustic velocity in both modes. For the one-port model to be valid, excitation of the stable flame to an acoustic velocity amplitude comparable to that of a self-excited flame at the same operating conditions should produce similar perturbations in the heat release rate in terms of gain and phase.

9.2 Self-excited and acoustically-forced flames

Table 9.1 shows images of the physical response of the flame to various excitation levels ranging from a steady, stable flame to one that is unstable with a velocity perturbation intensity as high as $i_p (v^2/V_{\text{mean}}) = 0.18$. The amplitude of the self-excited flame response is completely dependent upon the thermoacoustic feedback mechanism of the overall burner – flame system, while for the acoustically-driven flames the amplitude of the disturbance was varied by increasing or decreasing the input power to the loudspeaker with the burner in the configuration shown in Figure 9.2(c). The bright streaks appearing in the images of Table 9.1 for the flame driven at an input power of 5.0 Watts are incandescent traces of particles that remained in the air delivery line after performing Particle Image Velocimetry (PIV). Comparison with previous data indicated that these particles did not influence the response of the flame.

Table 9.1: Chemiluminescent images of flame at $V_{\text{mean}} = 1.65$ m/sec operating at various equivalence ratios and degrees of excitation.



9.2.1 Flame Front Perturbations

In Table 9.1 an interesting phenomena was observed in the acoustically-forced flames as the equivalence ratio was reduced from $\phi = 1.0$ to $\phi = 0.85$. Maintaining a constant power to the speaker at the base of the nozzle, the flame surface becomes more perturbed as the equivalence ratio is decreased. Similar behavior was observed by Blackshear¹¹ in studying the ability of a flame to damp an imposed acoustic wave. The author was somewhat ambiguous regarding the definition of flame damping and suggested a relation between the reflected and transmitted acoustic energy for a given incident wave. This definition ignores the flames' ability to absorb the acoustic energy which can be subsequently released as heat, thus satisfying the conservation of energy across the flame surface. However, given air as the media the absorption coefficient is relatively low at approximately $10^{-4} - 10^{-2}$ dB/m for $f \approx 230$ Hz and $T = 20^\circ - 2000^\circ\text{C}$ (Kinsler⁶²).

Blackshear¹¹ found in tests conducted in a configuration similar to that shown in Figure 9.2c that by decreasing the equivalence ratio the voltage required to drive a speaker at a constant sound intensity in the burner was reduced. This was interpreted to indicate that the damping characteristics of the flame were reduced with a decrease in flame speed. Limited analysis prevented conclusive findings of the effect of flame speed on damping.

The analysis by Fliefil et.al³⁹ also suggests an influence from the flame speed. Figure 8.2 illustrates the relationship developed by Fliefil to describe perturbations in the flame surface area as a function of the flame Strouhal number ($G = \omega R/S_w$). At low values of G (high S_w) the flame is shown to respond with large perturbations that decrease in amplitude, but increase in number, as the flame Strouhal number increases (decreasing S_w). The flame Strouhal number for the disturbances shown in Table 9.1 is approximately $G \approx 35 - 50$ which coincides with low amplitude area perturbations of Figure 8.2. The decrease in surface fluctuations with G shown by Fliefil et. al³⁹ is opposite of the effect that occurs in this study in which front deformations are actually increasing in amplitude as the flame speed decreases (increasing G).

Fliefil's model assumes that the flame speed remains constant along the flame surface; however this assumption may be too strong. As will be shown in Chapter 10, the application of PIV measurements to the reacting flow-field provide a means of obtaining the dilatation rate field, $\nabla \cdot V$, or rate of volume expansion. For incompressible flows, the rate of volume expansion is directly caused by the heat release rate of the flame (Mueller et. al⁸¹). Inconsistencies in the dilatation rate measured along the surface of an oscillating flame suggest localized variations in the heat release

rate. It is believed that these variations are the result of altered regions of positive and negative flame stretch which would be accompanied by a stretched laminar flame speed that would vary along the flame surface. Future analysis is planned to investigate the presence and affect of flame stretch on heat release variations.

Aside from the flame speed, the flame temperature is also greatly influenced by a change in equivalence ratio and can have a subsequent effect on the combustor acoustic response. In an open-closed pipe configuration such as the burner nozzle in which the pipe is driven at $x = 0$ and open at $x = L$, acoustic energy radiates from the open end into the surrounding medium. However at $x = L$ the amplitude of the reflected pressure wave is only slightly less than that of the incident wave but differs in phase by 180° (Kinsler⁶²). On the contrary, the incident and reflected velocity waves are nearly in phase resulting in the amplitude at the nozzle exit of almost twice that of the incident velocity wave alone. This results in a relatively small quantity for the impedance which is equal to the radiation impedance given by

$$Z_{open} = z_o \left(\frac{k_o^2 r_o^2}{4} + 0.6ik_o r_o \right) \quad 9.1$$

Although the impedance is small and much of the acoustic energy is reflected at the open end of the nozzle, the difference in the characteristic acoustic impedance, z_o , brought on by the temperature discontinuity across the flame can influence the amount of acoustic energy that is reflected by or transmitted through the flame front. When an acoustic wave encounters the flame, which can be thought of as a thin interface separating the low temperature reactants and the high temperature products, reflected and transmitted waves are generated (Chu²⁰). The ratio of the amplitude of the reflected or transmitted acoustic pressure (P_r and P_t , respectively) to that of the incident wave depends upon the difference in the characteristic acoustic impedance ($z = \rho c$) up- and downstream of the flame (Kinsler et.al⁶²).

The study of the scattering of acoustic waves at a media discontinuity, such as a flame, is a complex matter due in part to the angle of incident and shape of the boundary and is thus beyond the scope of this analysis and the reader is directed to Chu²⁰ and Lieuwen^{71,72}. However, a simplified analysis can be obtained by considering a normally incident acoustic wave that encounters a planar flame, Figure 9.3.

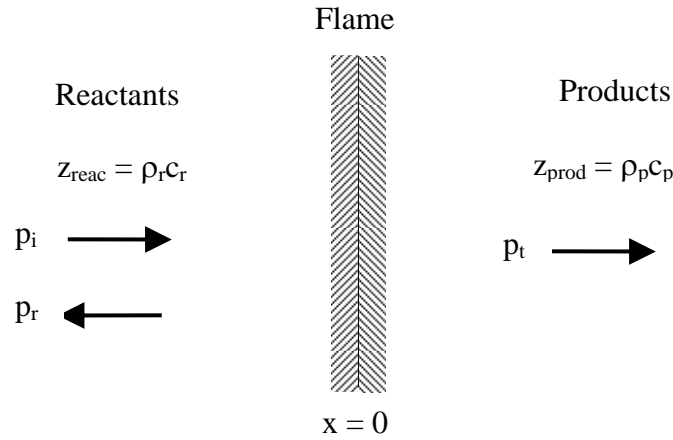


Figure 9.3: Reflection and transmission of acoustic wave incident on flame boundary.

Here p_i , p_r and p_t are the acoustic pressure of the incident, reflected and transmitted waves, respectively, and can be defined in terms of the pressure amplitude (\mathbf{P}), wave number ($k = \omega c$), oscillation frequency (ω) and speed of sound (c) by the following

incident wave	$p_i = \mathbf{P}_i e^{j(\omega t - k_{react} x)}$	
reflected wave	$p_r = \mathbf{P}_r e^{j(\omega t + k_{react} x)}$	
transmitted wave	$p_t = \mathbf{P}_t e^{j(\omega t - k_{prod} x)}$	9.2

The reflection and transmission coefficients are defined by the function of the acoustic impedance up- and downstream of the flame front

$$\mathbf{R} = \mathbf{P}_r / \mathbf{P}_i = \frac{1 - z_{react} / z_{prod}}{1 + z_{react} / z_{prod}}$$

$$\mathbf{T} = \mathbf{P}_t / \mathbf{P}_i = \frac{2}{1 + z_{react} / z_{prod}}$$

9.3

The acoustic reflection coefficient, \mathbf{R} , ranges from $-1 \leq R \leq 1$ and within this range four types of reflections are possible: 1) $z_{\text{prod}} \ll z_{\text{react}}$, $R \rightarrow 1$, a rigid boundary in which most of the acoustic energy is reflected without a change in phase; 2) $z_{\text{prod}} \gg z_{\text{react}}$, $R \rightarrow -1$, pressure release boundary in which most of the acoustic energy is reflected with a 180° shift in phase; 3) $z_{\text{prod}} = z_{\text{react}}$, $R = 0$, no reflection; 4) $z_{\text{prod}} \approx z_{\text{react}}$, $-1 < R < 1$, acoustic energy is reflected with some change in phase.

Assuming an inlet temperature of 20°C and using air to approximate both reactants and products, the upstream characteristic impedance is found to be $z_{\text{react}} = \rho_{\text{react}} c_{\text{react}} = 415 \text{ Pa}\cdot\text{sec}/\text{m}$. Setting the downstream temperature equal to the adiabatic flame temperatures for air – methane flames the temperature ratio across the flame and the downstream characteristic impedance are given in Table 9.2 as a function of equivalence ratio.

Table 9.2: Variation in the post-flame characteristic impedance and reflection coefficient for methane-air flame based on ϕ and temperature ratio across the flame.

ϕ	$T_{\text{prod}}/T_{\text{react}}$	c_{prod}	z_{prod}	R
0.80	6.76	952	148.6	-0.47
0.85	6.85	957	147.8	-0.472
0.90	6.92	962	147.0	-0.474
0.95	6.99	966	146.4	-0.476
1.00	7.06	970	145.8	-0.477

The temperature rise across the flame boundary results in a decrease in the acoustic impedance ($z_{\text{prod}} < z_{\text{react}}$), thus some acoustic energy is reflected, and given $R < 0$ (Figure 9.4) a positive pressure wave is reflected as a negative pressure which acts to progressively cancel more acoustic energy as R approaches -1 until the resulting pressure amplitude at the boundary is equal to zero (pressure release boundary).

The increase in flame perturbation is a result of an additional acoustic energy being transmitted through the flame which would occur as the difference in characteristic impedance across the flame reduced through a decrease in equivalence ratio, although the narrow increase in product impedance with equivalence ratio reduction does not seem significant enough to account for the large alteration in flame shape illustrated in Table 9.1. However, the upstream temperature assumption may be too strong as the temperature in the pre-flame region is likely higher, due to

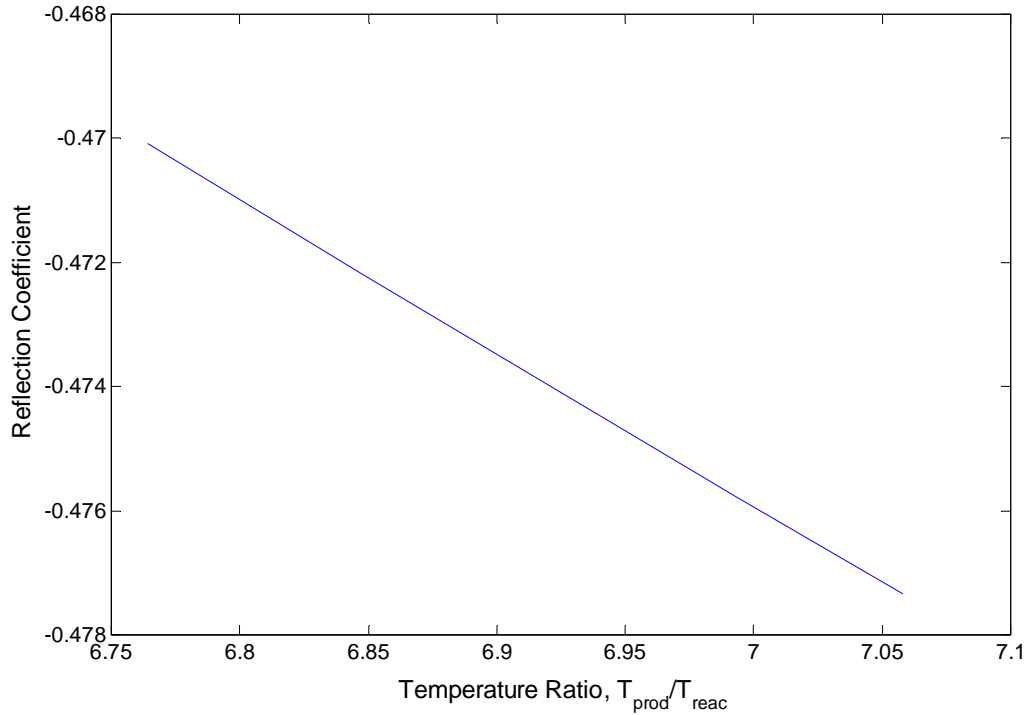


Figure 9.4: Plot of the changes in the reflection coefficient, R , as a function of the temperature ratio across the flame.

back-mixing and heating of the flame anchor, which would result in a reduction of the reactant characteristic impedance. Unfortunately as this was not the main focus of this study only a limited amount of data addressing this issue was collected and additional investigation is needed to accurately identify the source of this phenomena.

9.2.2 Response from acoustically-forced flame

The rms values of the acoustic pressure and acoustic velocity for acoustically-forced and self-excited flames with $V_{\text{mean}} = 1.65$ m/sec are given in Figure 9.5 and 9.7, respectively, as a function of equivalence ratio. Accompanying these figures are plots of the phase difference between perturbations in the acoustic pressure and heat release rate, and acoustic velocity and heat release rate perturbations as a function of equivalence ratio in Figures 9.6 and 9.8, respectively. In Chapter 7 pressure data were obtained from a single microphone at the exit of the nozzle, however here the data for these plots were obtained by the two-microphone method discussed in Chapter 6 in which the nozzle acoustic state variables were extrapolated through linear acoustic relationships from

measurements made from two microphones located upstream of the flame. The p' - q' ($\Theta_{p',q'}$) and the v' - q' ($\Theta_{v',q'}$) phase angle differences were obtained from the frequency response plots of the cross-spectrum between the two parameters taken at the frequency that corresponds to the fundamental mode. The rms pressure amplitude ranged from 0.5 – 3.5% of the operating pressure ($P_{\text{atm}} = 1.01 \times 10^5 \text{ Pa}$), while the acoustic intensity ($i_p = v'/V_{\text{mean}}$) was equal to $i_p = 0.04 - 0.18$. Attempts to drive the flame at amplitudes greater than $\epsilon_{\text{ex}} = 5.0 \text{ W}$ resulted in blow-off. Repeatability of the rms values of the acoustic state variables (p' and v') and the heat release rate (q') along with the reported phase angles was exceptionally good with a percent difference of less than 10% of the mean for all the cases tested.

It can be inferred from the Rayleigh criteria that higher amplitude thermoacoustic instabilities occur as the phase difference between the acoustic pressure and variable heat release rate approaches zero. This phenomenon is observed in Figures 9.5 and 9.6 for the self-excited flame, in which the amplitude of the rms pressure of the self-excited flame operating under lean conditions (Figure 9.5) increases as the equivalence ratio increases until it reaches a maximum value at $\phi = 0.95 - 1.0$. At these same conditions $\Theta_{p',q'}$ for the self-excited flame attains a minimum value of approximately zero (Figure 9.6). The overall $\Theta_{p',q'}$ for the self-excited flame is relatively narrow with values ranging from $\Theta_{p',q'} = -12^\circ - 16^\circ$. Thus under lean conditions ($\phi < 0.8$) the self-excited flame experiences a significant decrease in the amplitude with only a slight change in phase.

Between $\phi = 0.75$ and $\phi = 0.8$ the amplitude of the acoustic intensity for the self-excited flame increases from $i_p = 0.12$ to 0.14 , Figure 9.7. Over this same range there was no change in phase angle difference between the acoustic velocity and heat release rate ($\Theta_{v',q'}$), Figure 9.8. Once the flame becomes self-excited, the acoustic intensity appears to be relatively independent of equivalence ratio with an amplitude of $i_p \approx 0.14$ at $\phi = 0.8 - 1.0$. Under peak instability the phase angle difference is equal to $\Theta_{v',q'} = 120^\circ - 130^\circ$, but overall appears to be linearly variant with $\Theta_{v',q'} = 85^\circ - 130^\circ$ for $\phi = 0.8-1.0$. Given the relatively constant time-averaged flame height shown in Figure 8.9 for $\phi = 0.8-1.0$ and $V_{\text{mean}} = 1.54 \text{ m/sec}$, the linear variation of $\Theta_{v',q'}$ with ϕ supports the notion of a reaction dependent phase lag as suggested by Crocco's $n-\tau$ model²².

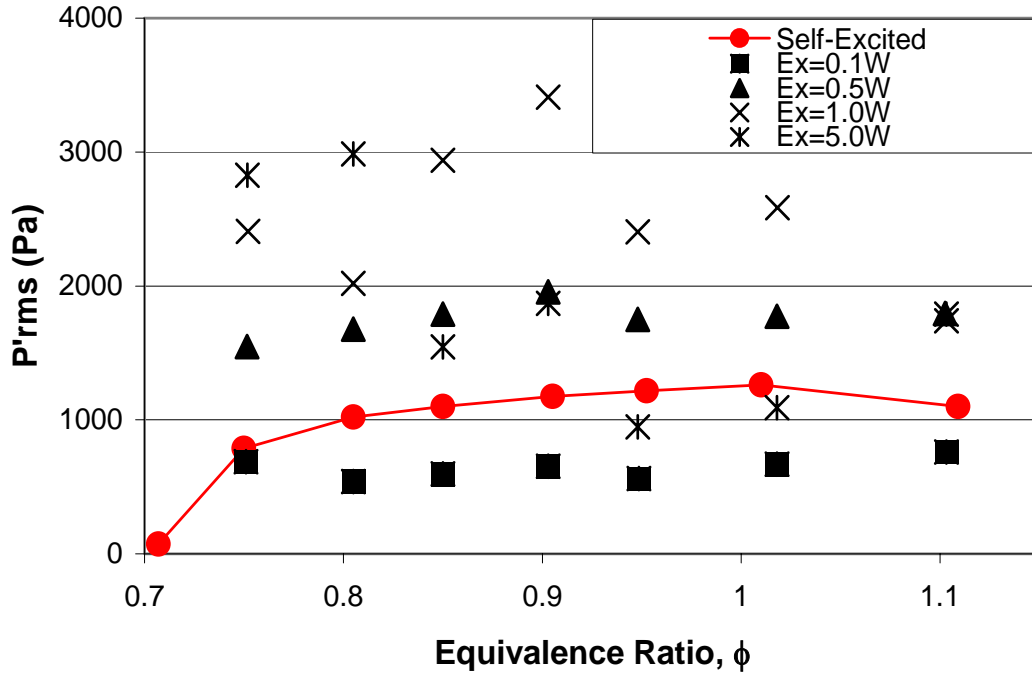


Figure 9.5: RMS pressure variation with equivalence ratio and excitation intensity as measured by the two-microphone method in an oscillating laminar flame at $V_{\text{mean}} = 1.65$ m/sec, $\phi = 0.95$ and $f_{\text{ex}} = 230$ Hz.

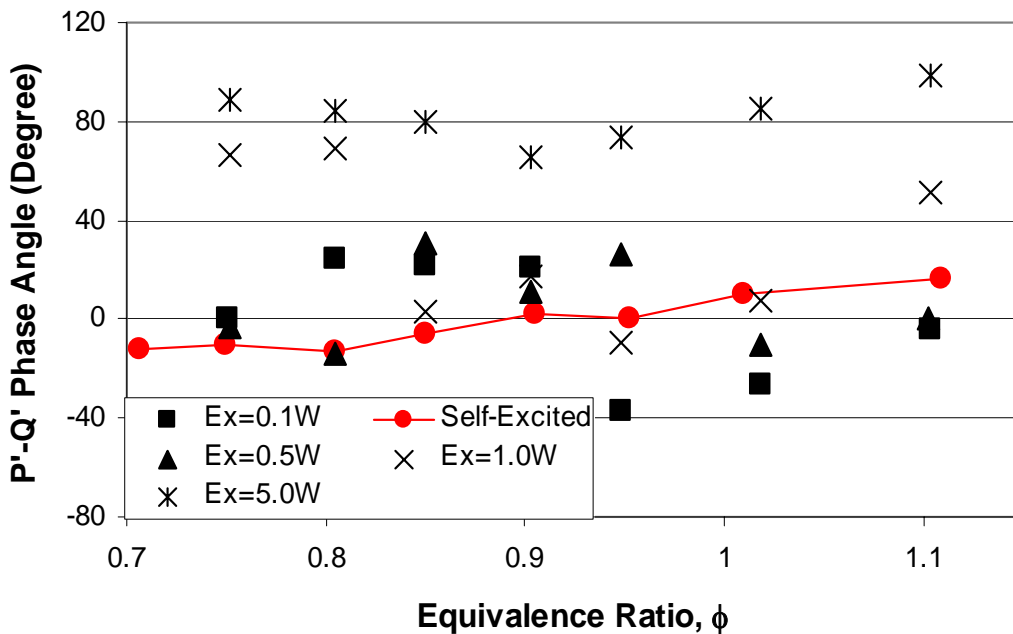


Figure 9.6: Phase difference between the acoustic pressure and heat release as a function of equivalence ratio and excitation intensity as measured by the two-microphone method in an oscillating laminar flame at $V_{\text{mean}} = 1.65$ m/sec and $\phi = 0.95$.

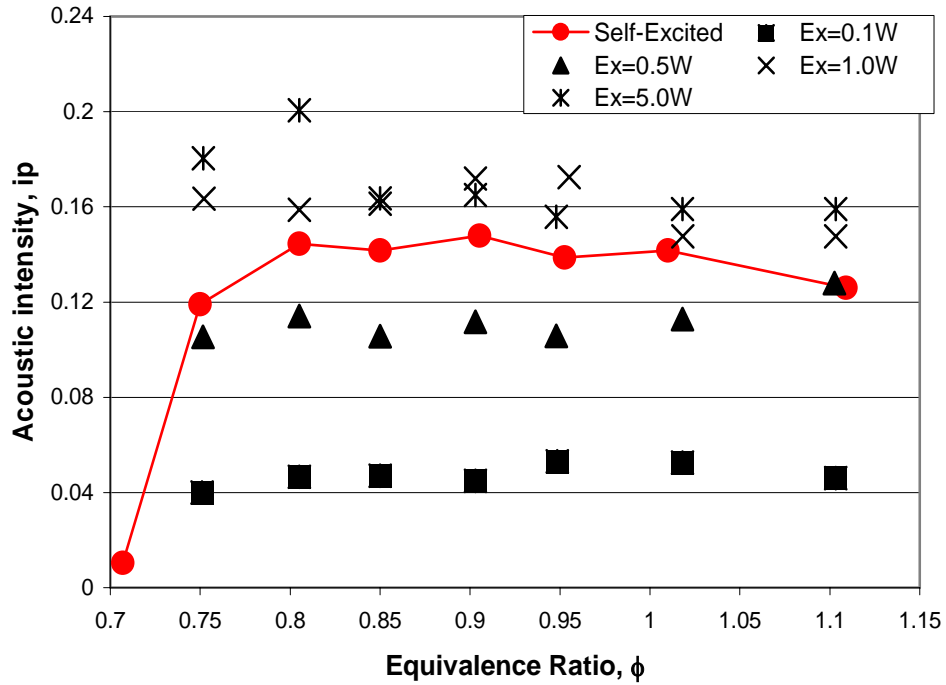


Figure 9.7: Acoustic intensity, $i_p = v'/V_{\text{mean}}$ as a function of equivalence ratio and excitation intensity as measured by the two-microphone method in an oscillating laminar flame at $V_{\text{mean}} = 1.65$ m/sec, $\phi = 0.95$ and $f_{\text{ex}} = 230$ Hz.

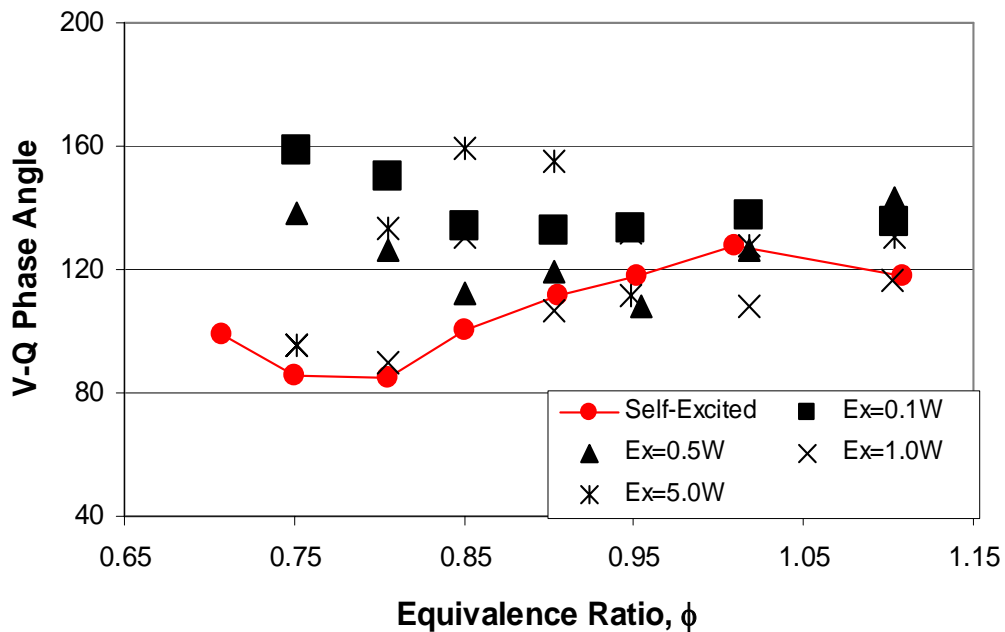


Figure 9.8: Phase difference between the acoustic velocity and variable heat release rate as a function of equivalence ratio and excitation intensity as measured by the two-microphone method in an oscillating laminar flame at $V_{\text{mean}} = 1.65$ m/sec, $\phi = 0.95$ and $f_{\text{ex}} = 230$ Hz.

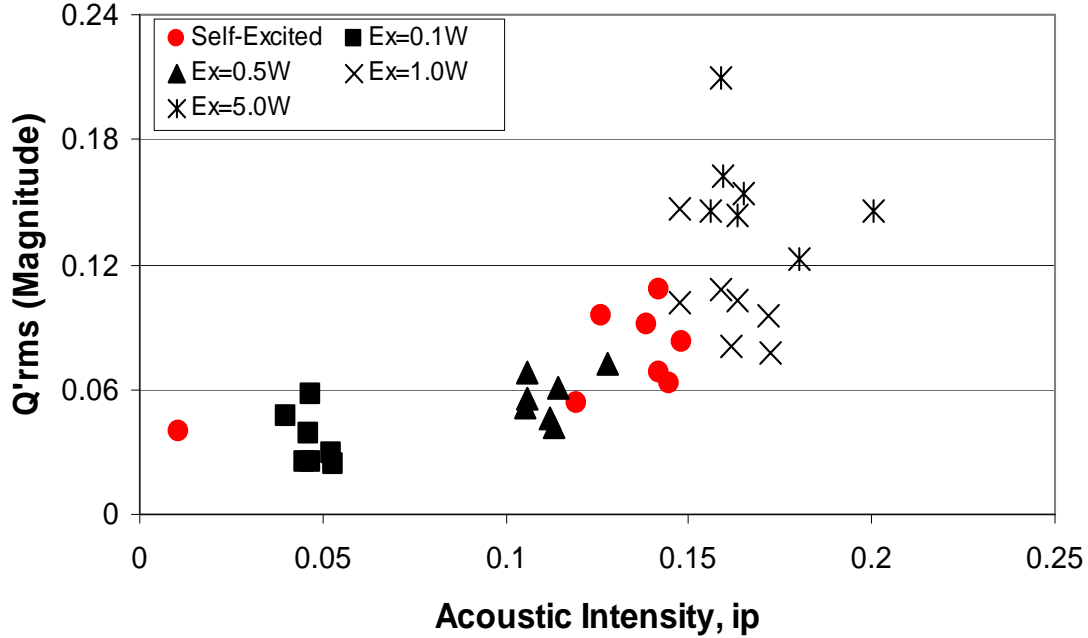


Figure 9.9: Amplitude of the heat release rate perturbations as a function of the acoustic intensity for methane-air flame at $V_{\text{mean}} = 1.65$ m/sec, $\phi = 0.95$ and $f_{\text{ex}} = 230$ Hz.

The addition of the speaker at the base of the nozzle alters its acoustic characteristics allowing the inherently unstable flame to become stable. Excitation of the flame under these conditions is often utilized to develop transfer function sub-models describing the response of the flame to an acoustic disturbance. Unlike the rms pressure of the self-excited flame which steadily increases from a minimum at $\phi = 0.7$ to a maximum of 1.2% over the operating pressure at $\phi = 0.95-1.0$, the response of the acoustically-forced flame remains relatively constant at 0.6% and 1.7% for excitation levels of $\epsilon_{\text{ex}} = 0.1$ and 0.5 Watts, respectively (Figure 9.5), indicating that the amplitude of the rms pressure is independent of the equivalence ratio for these low amplitude excitations similar to the self-excited flame. Under these conditions the system is responding to an open-loop input and the pressure amplitude is free of any feedback from the flame. Although the forced instability of the flame is not a result of thermoacoustic coupling $\Theta_{p',q'}$ remains relatively low, however there is considerable more variability compared to the self-excited flame.

As the amplitude of the acoustic excitation increases the rms pressure becomes very erratic with ϕ , although the test-to-test repeatability remains within 10%. There is a sudden change in the phase angle difference at $\epsilon_{\text{ex}} = 1.0$ W from $\Theta_{p',q'} \approx 70^\circ$ at $\phi = 0.75-0.8$ to $\Theta_{p',q'} \approx 0^\circ$ at $\phi = 0.85 - 1.0$.

Increasing the excitation amplitude to $\epsilon_{\text{ex}} = 5.0 \text{ W}$ results in a continuation of the irregular rms pressure response, however $\Theta_{p',q'}$ is now relatively constant at $\Theta_{p',q'} \approx 80^\circ$. Although the exact cause of the variation in the rms pressure and $\Theta_{p',q'}$ at these higher excitation amplitudes is unclear, the relatively flat response of the acoustic intensity for $\epsilon_{\text{ex}} \geq 1.0 \text{ W}$ shown in Figure 9.7 along with the exponential increase in q'_{rms} for $i_p > 0.14$, as shown in Figure 9.9, may suggest that saturation had been reached. The primary finding here is that the flame responds differently to low and high amplitude excitations and this difference must be accounted for in the predictive models.

A comparison of the cross spectrum of $p'-q'$ at the different levels of excitation for $\phi = 0.95$, Figure 9.10, may provide some insight into the difference in the characteristic response of the acoustically-forced flame. A peak at the sub-harmonic frequency $F_{\text{ex}/2} \approx 115 \text{ Hz}$ can be seen in the $p'-q'$ cross spectrum for $\epsilon_{\text{ex}} = 0.1 - 1.0 \text{ W}$, but is not present in the cross-spectrum at $\epsilon_{\text{ex}} = 5.0 \text{ W}$ or the self-excited flame. The similarity in amplitude of the $p'-q'$ response at $F_{\text{ex}} = 230 \text{ Hz}$ for $\epsilon_{\text{ex}} = 1.0-5.0$ would suggest that saturation has been reached and excess energy continues to leak into the sideband regions. Starting with $\epsilon_{\text{ex}} = 0.1 \text{ W}$, as the excitation amplitude is increased we begin to see more energy leaking into the sideband frequencies and is evident through a broadening of the response at frequencies immediately surrounding $F_{\text{ex}} = 230 \text{ Hz}$. The exact cause of the loss of the sub-harmonic frequency $F_{\text{ex}/2} = 165 \text{ Hz}$ at $\epsilon_{\text{ex}} = 5.0 \text{ W}$ is not completely understood.

One can speculate that the characteristics of the saturated response force a cancellation of the sub-harmonic as additional energy is supplied by the loudspeaker at $F_{\text{ex}} = 230 \text{ Hz}$. Looking specifically at the amplitude of the $p'-q'$ cross spectrum at $\epsilon_{\text{ex}} = 5.0 \text{ W}$ in Figure 9.11 we see that while the amplitude of the fundamental frequency remains constant there is some variation in the sideband regions with equivalence ratio.

Figure 9.9 compares the amplitude of the heat release rate to that of the acoustic intensity with each data point representing the response at a different equivalence ratio. The self-excited results shown here are a subset of the plot shown in Figure 7.6 which indicates a fairly linear relationship between the heat release rate and the acoustic intensity for self-excited flames at various flow rates. Here however, we see that the equivalence ratio has very little influence on the heat release perturbations except at $\epsilon_{\text{ex}} = 5.0 \text{ W}$. At low intensity levels the acoustically-driven flames has a very similar response as the self-excited (e.g. $i_p = 0.12$ and $i_p = 0.19$), but as the intensity level increases to greater than $i_p = 0.2$ there is an exponential increase in the heat release rate that is not apparent in the self-excited flame results shown in Figure 7.6. Thus under self-excited conditions

the v' - q' relationship appears to be linear, but under forced excitation saturation is reached and the relationship becomes non-linear. This suggests that under self-excited conditions the thermoacoustic response of the flame does not reach saturation (although this may be flow dependent) and care must be taken in order to not push the flame into a saturated response when acoustically-forcing the flame in order to obtain empirically derived transfer functions.

Although Figures 7.6 and 9.9 appear to support the use of one-port models to predict the characteristics of the heat release response from an oscillating flame directly from the acoustic intensity, this may not prove conclusive in determining the overall thermoacoustic response from the flame. Because thermoacoustic instabilities are the result of a coupling between the acoustics and the heat release rate, one also needs to have an understanding of the phase relationship between these two parameters. Previous discussion of Figure 9.8 was limited to the linear response of the self-excited over $\phi = 0.8 - 1.0$ and supported the assumption of a chemical kinetic time delay that led to the shift in $\Theta_{v'-q'}$ with ϕ . The v' - q' phase difference during lean operation for the acoustically-forced flame is fairly consistent with a decreasing trend towards $\Theta_{v'-q'} = 120^\circ$ at $\phi = 0.95$ which is approximately equal to the self-excited flame response at this equivalence ratio. And although there is agreement in $\Theta_{v'-q'}$ between the self-excited and acoustically-forced flames at operating conditions that produce peak instabilities in the self-excited flame, there is a large discrepancy near the lean stability margin. Recall from Table 9.1 that the amplitude of the wrinkles was greatest during lean operation as the reflection coefficient approaches zero. Thus the difference in the lean results may be an indication of multi-dimensional near-field acoustics or a change in the acoustic impedance. This would suggest that while a transfer function derived from acoustically-forcing a flame with an acoustic disturbance may be able to describe the gain and phase response of a thermoacoustic instability during periods of peak oscillation, it may not be capable of predicting the onset of combustion instabilities at conditions near the edge of stability. Thus one-port models can not capture the true essence of the coupling process between acoustics and perturbations in the heat release rate.

This concept is further illustrated by results shown in Figure 9.12 from a limited study in which attempts were made to quantitatively match the p' - q' cross spectrum response of a self-excited flame by acoustically-driving it with the base-mounted speaker. Operating the burner at the flow and equivalence ratio necessary to produce peak instability in the self-excited flame ($V_{\text{mean}} =$

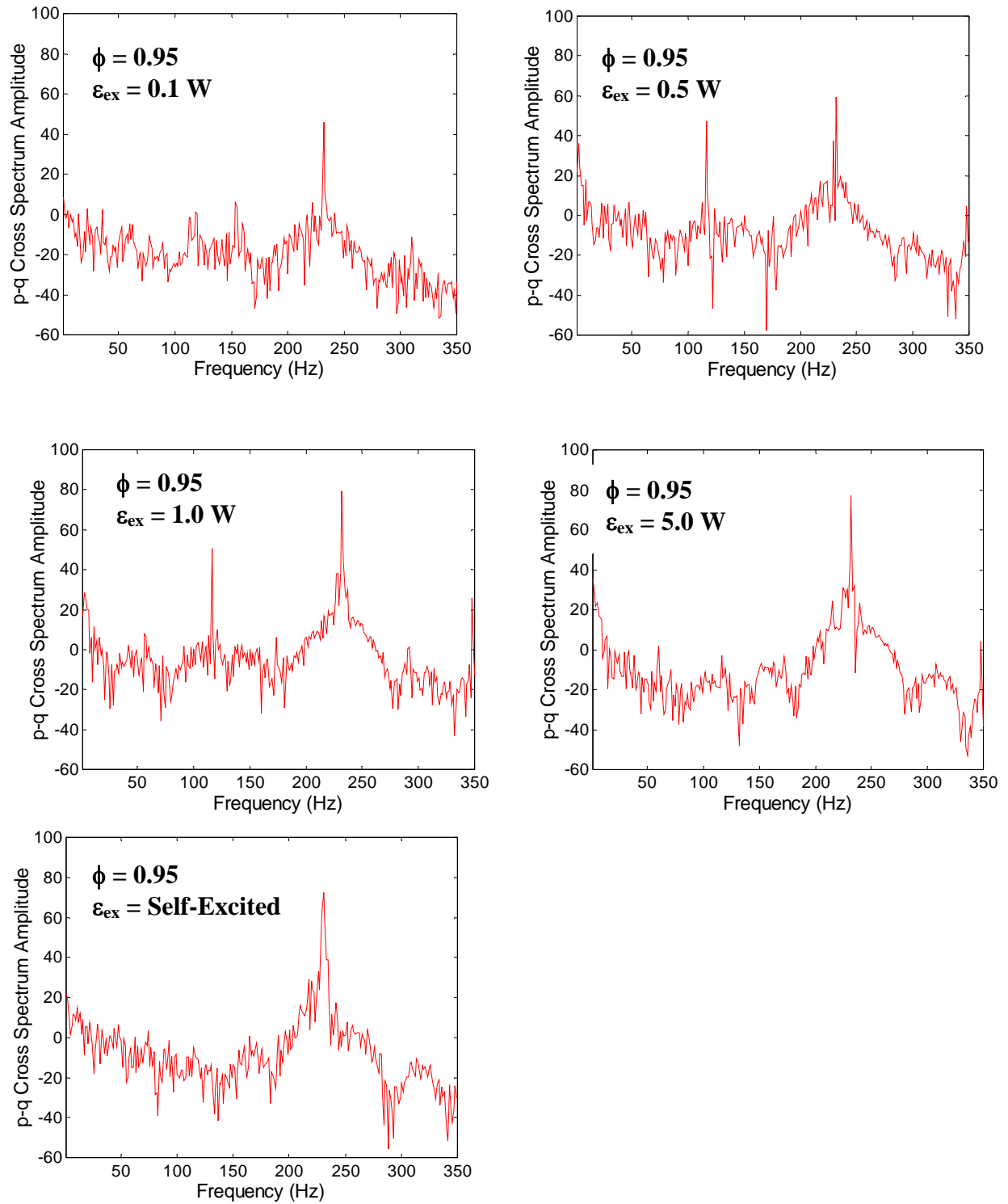


Figure 9.10: Cross spectrum analysis of acoustic pressure, p' , and heat release rate perturbations, q' , at various degrees of excitation for $V_{mean} = 1.65 \text{ m/sec}$, $\phi = 0.95$ and $f_{ex} = 230 \text{ Hz}$.

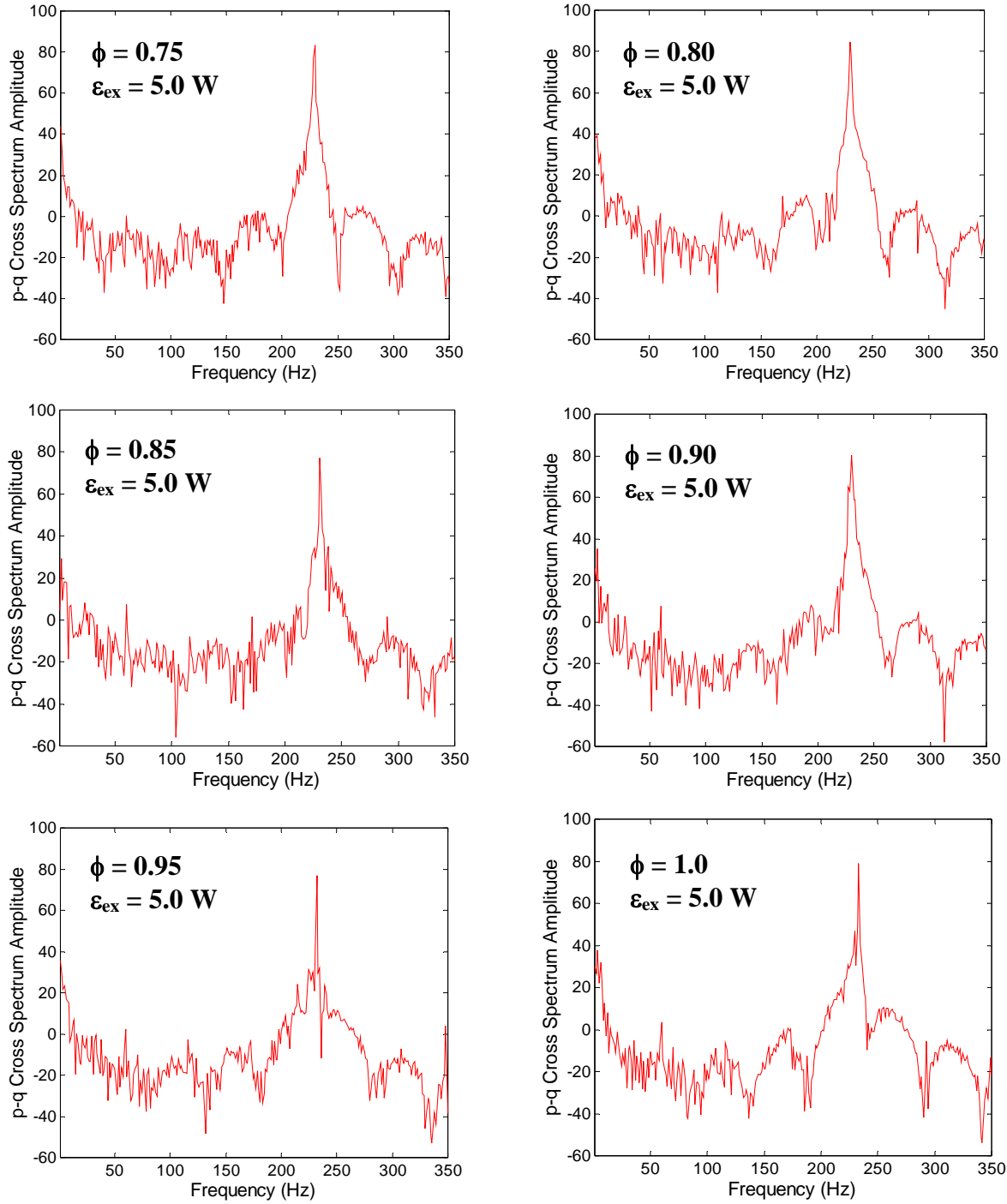


Figure 9.11: Cross spectrum analysis of acoustic pressure, p' , and heat release rate perturbations, q' , at $\epsilon_{ex} = 5.0\text{W}$ and equivalence ratios ranging from $\phi = 0.75 - 1.0$, where $V_{mean} = 1.65\text{ m/sec}$ and $f_{ex} = 230\text{ Hz}$.

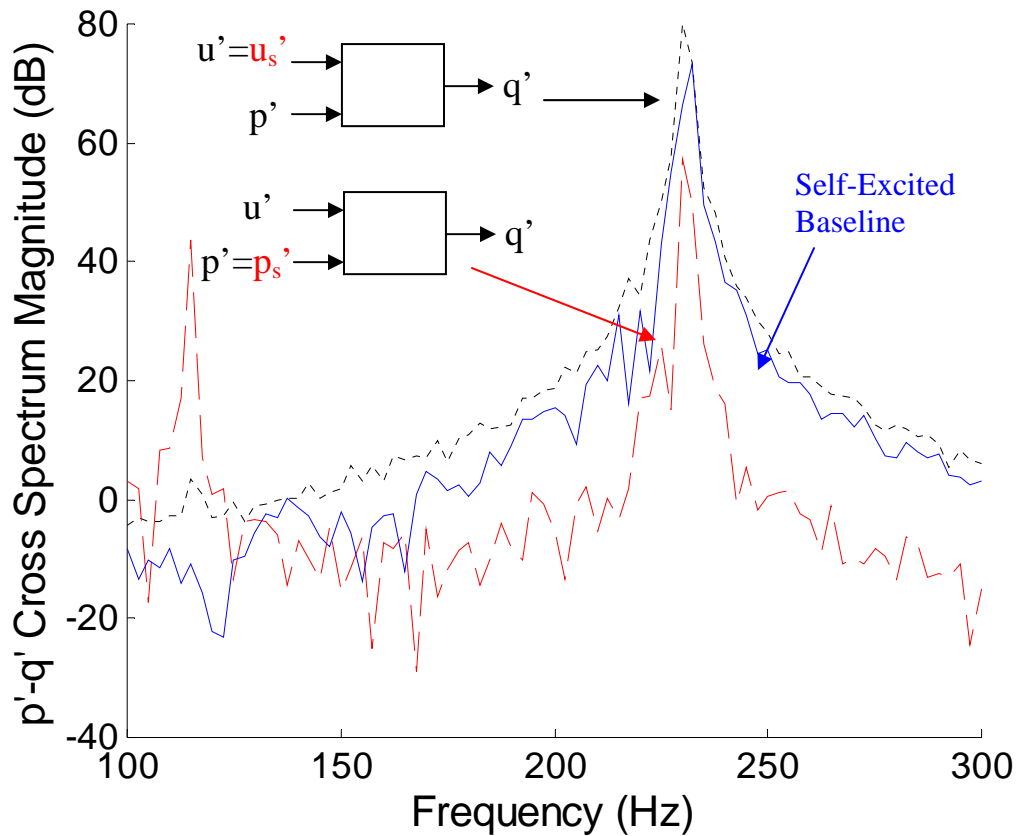


Figure 9.12: Comparison of cross-spectrum analysis between the acoustic pressure, p' , and heat release perturbations, q' for self-excited and acoustically-forced flame such that the amplitude of either the forced acoustic velocity or pressure equaled that of the self-excited flame with $V_{\text{mean}} = 1.65$ m/sec and $\phi = 0.95$.

1.54 m/sec and $\phi = 0.95$), the flame was driven by the base-mounted speaker with an input at $F_{\text{ex_forced}} = F_{\text{ex_self}}$ at amplitudes as to produce comparable levels of acoustic pressure or acoustic velocity at the nozzle exit. Figure 9.12 shows that in neither instance was the same p' - q' cross spectrum response obtained from the flame as when the flame was self-excited and would tend to support the notion that one-port models are inadequate at predicting the overall thermoacoustic response from the flame.

For the case of one-port model, the derived transfer function includes not only the heat release response of the flame but also the response of the additional acoustic elements (i.e. step expansion) to a given acoustic intensity. A change in one of the elements would result in a change in the flame response. Thus in order to maintain validity of these models the upstream acoustic impedance must remain constant, therefore making these models quite system specific. The inability

of one-port models can be addressed by the application of two-port models as suggested by Paschereit and Polifke⁹².

The burner used in this study, as well as in most experimental analyses, consists of a step change that is used to anchor the flame and eventually lead into the combustion chamber from the mixture nozzle. In modeling this system, the nozzle and subsequent combustion chamber constitute separate acoustic elements that are often lumped into one regardless if considered a one-port or multi-port. The multi-port methodology can accommodate this black box approach by taking the acoustic impedance and / or both acoustic variables into consideration. This is not to say that the flame response is directly dependent on the acoustic pressure. The amplitude of the acoustic pressure is much too low to create perturbations in the parameters that determine the heat release rate from the flame. However, the acoustic pressure, or acoustic impedance, does influence the characteristics of the acoustic especially in the near-field of the flame.

Results presented in this chapter suggest that one-port models, in which a single input such as acoustic velocity, can not adequately reproduce the response of a flame to an acoustic disturbance under all conditions. However, one-port models can be a useful tool in trying to understand the general influence of a particular mechanism on combustion instabilities. As an example, if the input of a velocity modulation could actually be separated from its environment its influence on the flame response would be rather straightforward, but what is difficult to predict is how the response of the flame is affected by the acoustic characteristics of its environment and how the flame can alter those characteristics. Thus it is not the actual one-port model that is inadequate but its application to a particular system and the underlying assumptions that go along with its application.

Utilizing the appropriate inputs, two-port or multi-port models can account for specific acoustic characteristics of a given system. Transfer functions developed as one-port models may be combined with additional parameters to develop multi-port models that can predict the influence of the local environment on the various mechanisms. However additional studies such as those by Kruger et al^{64,65} and Paschereit et. al^{92,93} are needed to determine the full capability of multi-port models. For the Rijke tube combustor the next step would be to include a model such as Fliefil et. al³⁹ into a full acoustic model of the combustor. This model would need to account for multi-dimensional near-field acoustics which are discussed in Chapter 10.

Chapter 10 PIV Results and Discussion

Up to this point links have been shown between the acoustic velocity and variations in the heat release rate during thermoacoustic instabilities. However the analysis of the phase-gain relationship of these parameters has thus far revealed inconsistencies that are not accounted for by reduced-order models. It has been previously mentioned that fluid dynamics contribute to the occurrence of thermoacoustic instabilities through the generation of structures that result in variations in the heat release rates. Flow non-uniformities and flame curvature may also contribute to localized peaks in the heat release rate by producing alternating regions of flame stretch (Mueller et. al⁸¹). Several studies including Lee and Lieuwen⁶⁸, Khanna⁵⁸ and Ducruix et. al³³, have commented on the potential effect from multi-dimensional flows in the near-field of the flame; however there has been little experimental evaluation of this behavior.

In Chapter 5 the methodology behind particle image velocimetry (PIV) measurements was discussed along with analysis parameters specific to this study. Special consideration for using PIV in reacting flows, such as an increased seeding density, were also addressed. This chapter will focus on the presentation and discussion of measurements made using PIV. Data is reported for laminar cold flow, acoustically-forced cold flow, stable laminar flames, self-excited unstable flames, and high frequency acoustically-forced flames. Analysis and discussion focuses on near-field acoustic effects, acoustic forcing and variations in flame structure

10.1 Non-Reacting Flows

10.1.1 Laminar, non-reacting flow

Figure 10.1a and b are a negative image of the laser illuminated non-reacting flow ($V_{\text{mean}} = 1.4$ m/sec, $Re = 1340$) without excitation and the corresponding instantaneous velocity field, respectively. The edges of the cold flow image mark the interface between the moving seeded flow and the initially stagnant unseeded surrounding air. No valid data were obtained in the outer edges of the jet due to low particle seeding in these regions.

In the absence of acoustic excitation, the cold flow at the nozzle exit is a laminar plug flow with a quasi, top-hat profile which evolves little over several diameters downstream (Figure 10.1b). Given the axisymmetric nature of the problem cylindrical coordinates are adopted in which the r -axis is planar to the burner radius with $r = 0$ along the burner centerline, and the z -axis is coincident with the burner centerline. By assuming axisymmetric flow it is possible to neglect the angular velocity, V_{θ} .

Axial flow ($V_z = V$) is positive going from bottom ($z/D=0$) to top, and radial velocity ($V_r = U$) is taken to be positive for flow out from the nozzle centerline ($r/R = 0$). Vorticity is defined as $\omega = (\partial U/\partial z - \partial V/\partial r)$, along with strain rates $\epsilon_{rr} = \partial U/\partial r$, $\epsilon_{zz} = \partial V/\partial z$, shear-strain rate $\epsilon_{rz} = \frac{1}{2}(\partial U/\partial z + \partial V/\partial r)$ and flow dilatation $\nabla \cdot \mathbf{V} = U/r + \partial U/\partial r + \partial V/\partial z$.

In Figure 10.1b, vorticity contours indicate a small zone of recirculation at the top edge of the ring stabilizer ($z/D = 0$ and $r/R = -1.1$ or 1.1) and small-scale vorticity within the jet shear layer, but otherwise the flow is stable. Kelvin-Helmholtz vortices begin to develop further downstream at $z/D > 2.5$, however this is beyond the maximum extent of the flame ($z/D \approx 1.3$).

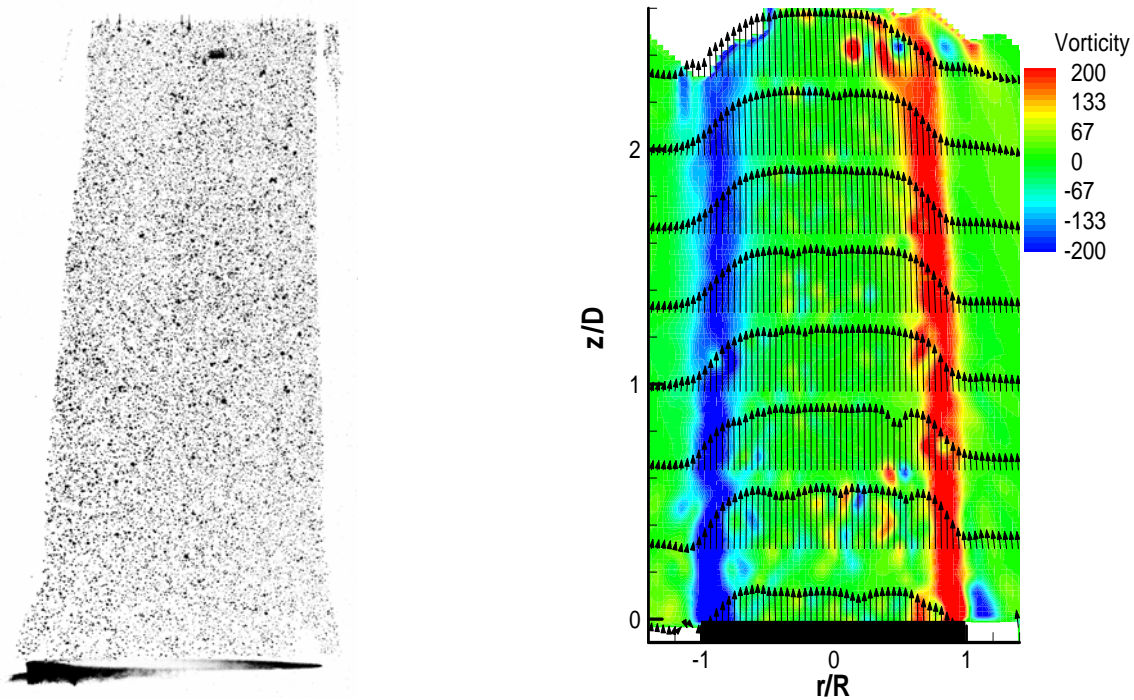
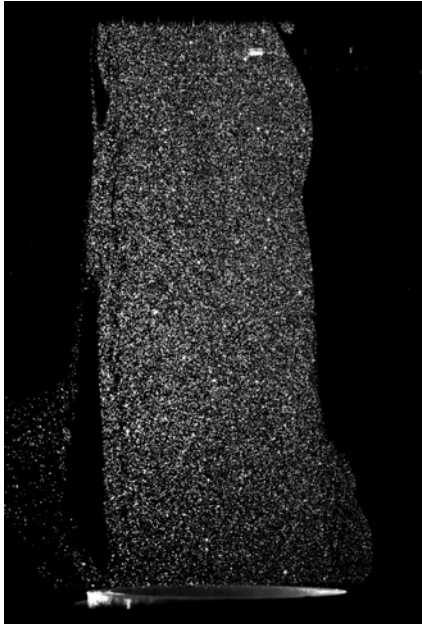
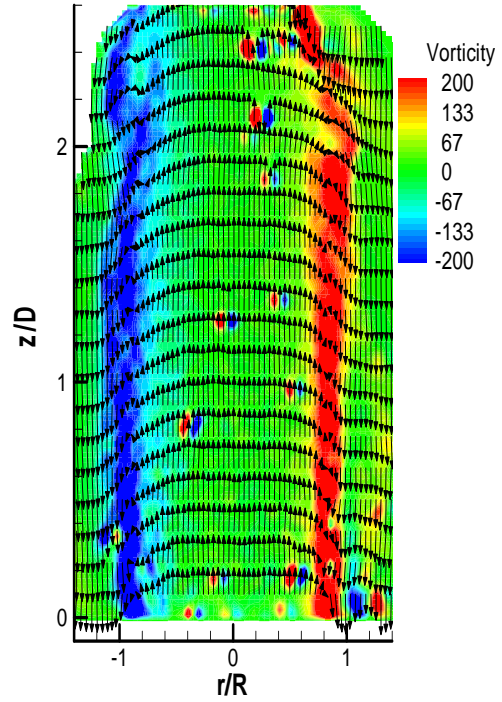


Figure 10.1: (a) Negative image of MIE scattering from particles in a non-reacting flow field near the nozzle exit of the Rijke tube burner. (b) Corresponding velocity field and vorticity contours of the non-reacting flow shown in (a).

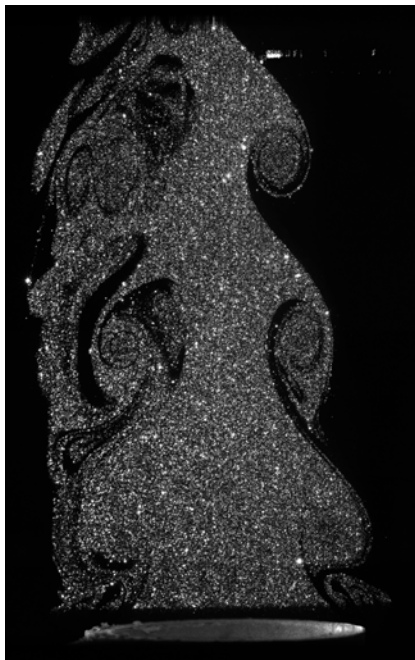


(a)

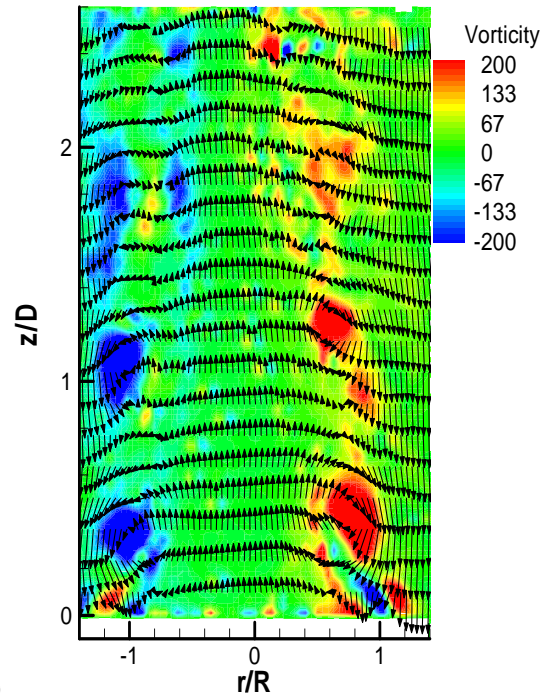


(b)

Figure 10.2: (a) MIE scattering, PIV image of acoustically driven flow field at $f_{\text{ex}} = 230$ Hz ($St_D = 2.49$). (b) Velocity vectors and vorticity contours corresponding to (a).



(a)



(b)

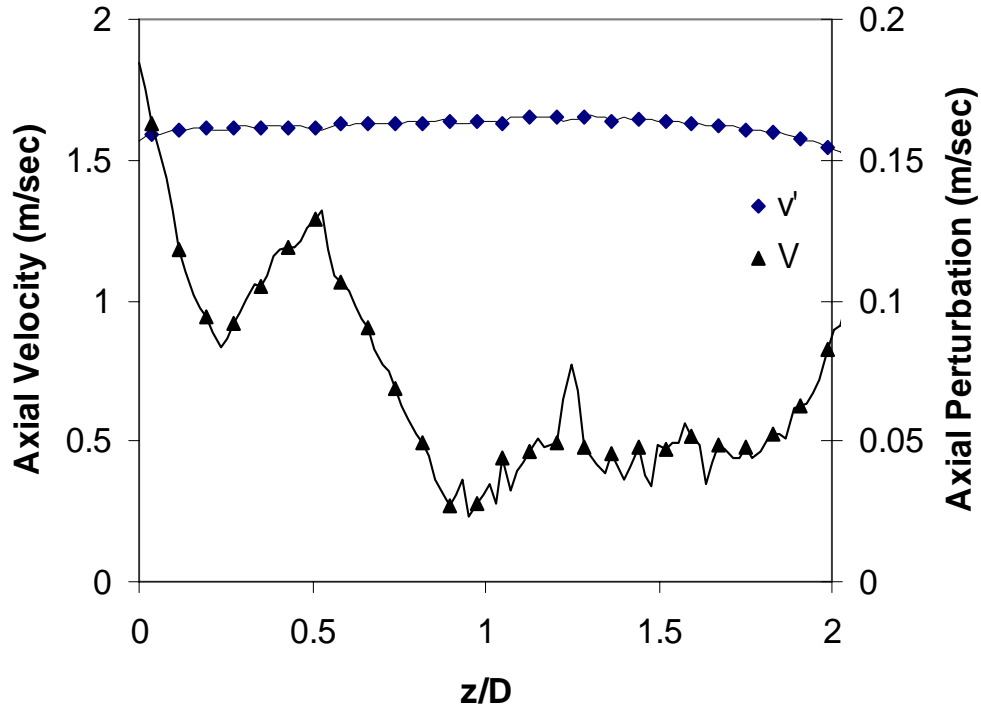
Figure 10.3: (a) MIE scattering, PIV image of acoustically driven flow field at $f_{\text{ex}} = 75$ Hz ($St_D = 0.81$). (b) Velocity vectors and vorticity contours corresponding to (a).

10.1.2 Acoustically forced, non-reacting flow

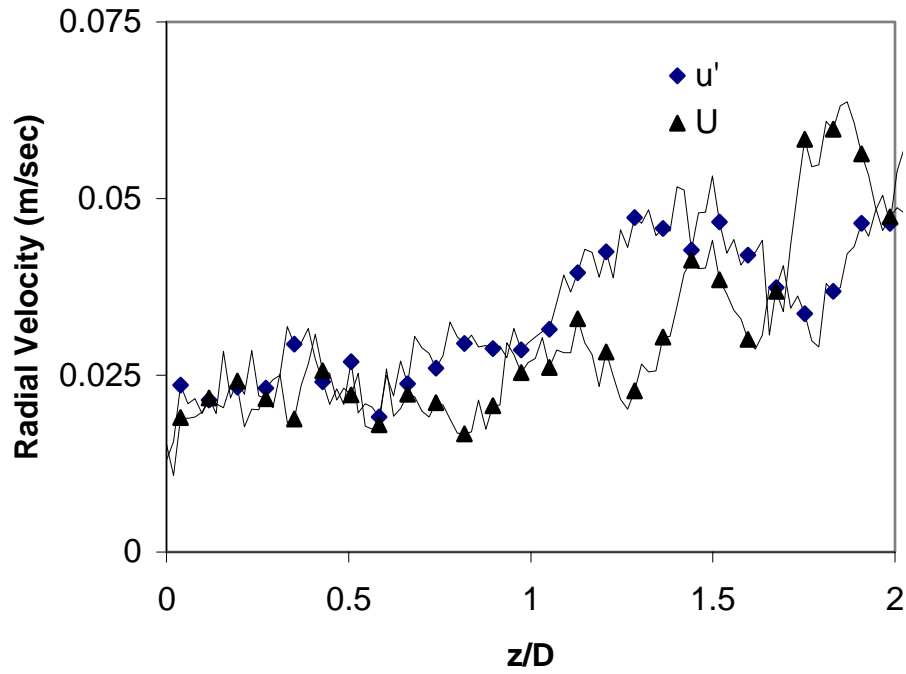
With the burner in configuration 3.9c, the loudspeaker provides an external sinusoidal perturbation at frequency F_{ex} . Holding the amplitude of the excitation at approximately $v'/V_{mean} = 0.14$, or $i_p = 14\%$, one observes a dramatic difference in the flow response depending of the excitation frequency, F_{ex} . Figure 10.2a, b and 10.3a, b gives an indication of the difference by comparing the flow response for an excitation at $F_{ex1} = 225$ Hz and $F_{ex2} = 75$ Hz, respectively. In both figures 10.2b and 10.3b, the average axial exit velocity has been subtracted in order to highlight the flow vorticity. Given an excitation of 225 Hz (Figure 10.2) the velocity profile does not alter significantly from the non-perturbed flow field until approximately $z/D = 1.85$ where vortices begin to form. However, as previously noted this is beyond the extent of the flame as the self-excited flame had a height of $H_f = 27$ mm ($z/D = 1.3$).

The low frequency ($F_{ex2} = 75$ Hz) excited flow is characterized by large structures that begin to form at the exit of the burner nozzle, Figure 10.3(a) and (b). The regions of low seeding within the jet core indicate areas where the surrounding ambient air has been entrained into the flow. Phase resolved images obtained for the low frequency non-reacting flow provide a means of obtaining time resolved measurements such as the average flow rates and the root mean square (rms) velocities, v' and u' . Profiles of the mean (V , U) and rms (v' , u') axial and radial velocities along the centerline axis ($r/R = 0$) are shown in Figures 10.4(a) and (b). The mean axial velocity along the centerline of the flow varies little over a downstream length equivalent to one diameter of the burner nozzle ($z/D = 1.0$). It remains close to $V_{cl,mean} = 1.6$ m/sec over this distance indicating that the stream has not yet begun to slow and little mixing with the surrounding ambient air has taken place. Beyond $z/D = 1.0$ the flow begins to decelerate due to boundary layer separation and quickly drops off at $z/D > 1.6$ until low seeding density at the image extremes results in a loss of signal. The amplitude of v' is highest at the exit of the nozzle ($z/D = 0$) reaching a value of $v' = 0.18$ m/sec ($i_p = 0.11$). The quantity steadily decreases to $v' = 0.087$ m/sec ($i_p = 0.054$) at $z/D = 0.22$. Here there is a momentary rebound in the amplitude up to $v' = 0.12$ m/sec ($i_p = 0.075$) as the core region is weakly affected by the expanding vortices and then again decreases. Although both the mean and rms radial velocities increase slightly, their values are quite small along the burner axis, Figure 10.4b

Radial profiles of the time-averaged axial and radial velocities, as well as the rms components, taken at two locations downstream from the nozzle exit ($z/D = 0.0$ and 0.3) are



(a)



(b)

Figure 10.4: Axial distribution of centerline velocities for acoustically-forced flow at 75 Hz ($St_D = 0.81$). (a) Axial mean and rms velocities. (b) Radial mean and rms velocities.

shown in Figure 10.5(a)-(d) for the same flow conditions as Figure 10.4a and b. Similar to the non-excited flow, the exit flow at $z/D = 0.0$ has a plug flow or top-hot profile with the mean axial velocity nearly constant at $V_{\text{mean}} = 1.4$ m/sec. The rms axial velocity, v' , is a maximum at $z/D = 0.0$ reaching $v' = 0.18$ m/sec at the centerline and is nearly constant across the nozzle exit. Two small humps appear towards the edge of the jet and are primarily due to flow recirculation at the ring-stabilizer. At $z/D = 0.3$ the mean axial profile remains flat and has only slightly widened. The amplitude of v' has decreased to $v' = 0.095$ m/sec at the centerline and the recirculation humps have nearly disappeared.

In the cold flow cases shown thus far, the flow emitted from the nozzle is predominately one-dimensional in the axial direction. However, excitation at $F_{\text{ex}} = 75$ Hz has resulted in the two-dimensional flow even at the nozzle exit. Profiles of the mean and perturbed radial velocities are shown in Figure 10.5(b) and (d), and as previously noted the radial velocity is positive away from the centerline. At $z/D = 0.0$ (Figure 10.5(d)) the mean radial flow is identically zero at the centerline ($r/R = 0.0$) and reaches a maximum of $u' \approx 0.1$ m/sec at the radial extents of the nozzle, $r/R = -1$ and 1 . The sudden increase in velocity at $r/R = -1$ and 1 is primarily the result of rotational flow due to the recirculation zone along the boundary of the nozzle and vortex formation exiting the nozzle. The rms velocity exceeds the mean radial velocity over the entire flow field, and as expected exhibits a minimum at the centerline. However, the two-dimensionality of the acoustic velocity is apparent by the consistent increase in the rms velocity away from the centerline although inside the region subjected to rotational flow due to vortex formation. As the flow progresses downstream to $z/D = 0.3$ (Figure 10.5(b)) the time-averaged radial flow indicates a slightly negative flow suggesting that the rotational motion of the vortices forces the flow toward the centerline. The rms radial velocity is now constant from $-0.3 < r/R < 0.3$ indicating that the two-dimensional evanescent acoustic wave has decayed. Again at the off-axis bounds of the nozzle the radial rms velocity is high due to the passage of the vortex structures.

Within the confines of the nozzle the imposed disturbance is a planar acoustic wave and the phase angle between the pressure and acoustic velocity is constant. As the flow emerges from the nozzle, vortical structures begin to form (Figure 10.3(b)) whose magnitude are dependent upon the shedding characteristics of the nozzle exit shear layer and the frequency of the imposed acoustic disturbance. These structures propagate downstream at a phase speed (celerity), C_{ph} , which may not necessarily equal the flow velocity (Lieuwen¹²⁰). Utilizing results from PIV measurements it is

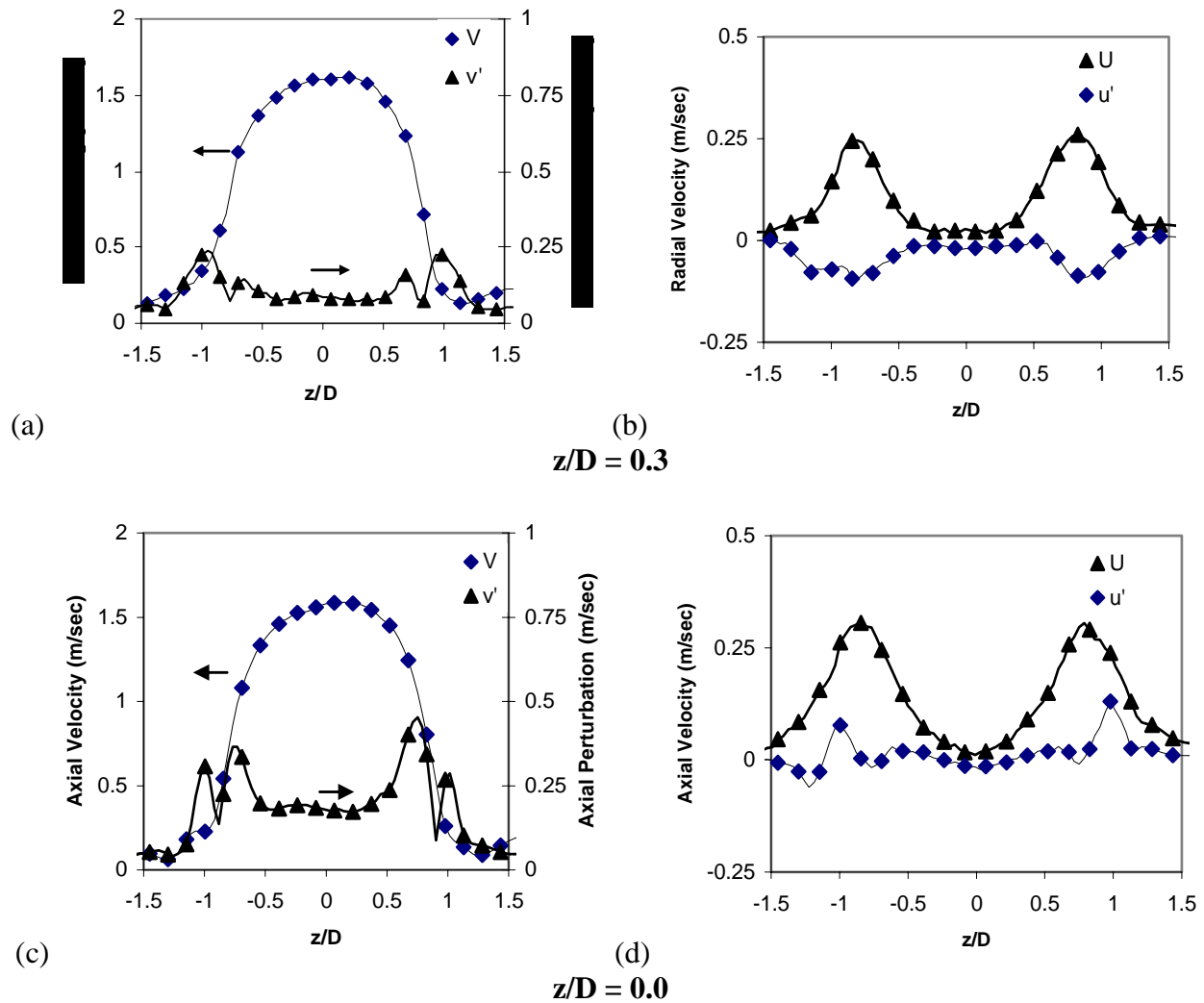


Figure 10.5: Radial profiles of non-reacting flow acoustically-forced at $f_{ex} = 75$ Hz ($StD = 0.81$) at different axial distances from the nozzle exit. (a) Axial mean and rms velocity and (b) radial mean and rms velocity at $z/D = 0.3$, and (c) axial mean and rms velocity and (d) radial mean and rms velocity at $z/D = 0.0$.

possible to obtain the distance, δ , between the vortex cores, which from Figure 10.3(b) is $\delta = 12.5$ mm ($y/D = 0.625$). Thus given a forcing frequency of $F_{ex} = 75$ Hz the propagation speed is determined to be $C_{ph} = \delta F_{ex} = 0.94$ m/sec which is approximately 33% below the mean axial velocity of $V_{mean} = 1.4$ m/sec. This is surprisingly similar to the results of Baillet et. al⁶ who also showed the celerity of vertical disturbances of similar frequency to be 33% of the mean flow velocity.

The presence of the vortical structures and acoustic forcing result in an aero-acoustic characteristic that produces a phase shift between the local velocity fluctuations as the flow propagates

downstream. The phase variation is indicated by a shift in the peak of the sinusoidal centerline velocity at locations downstream of the nozzle ($z/D = 0.0$) as shown in Figure 10.6. The figure shows examples at $z/D = 0.0$ and 0.2 of the time-resolved measurements obtained at 20° increments (referenced to the measured nozzle exit acoustic pressure) for the flow forced at 75 Hz ($St_D = 0.81$).

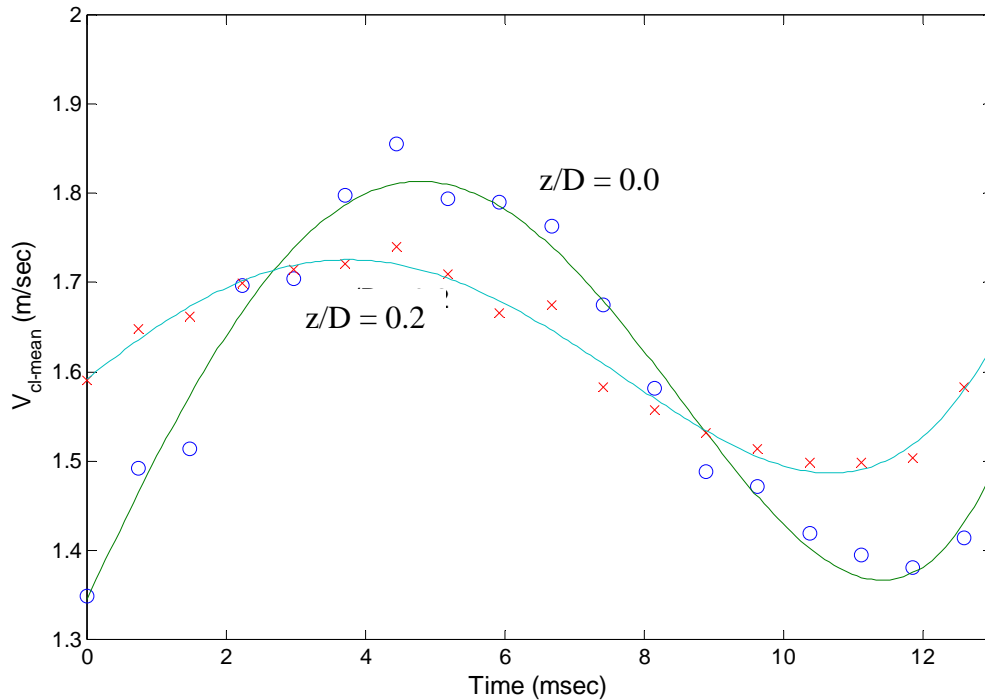


Figure 10.6: Phase variation of the acoustic velocity along the burner centerline axis for flow subject to low frequency, $f_{ex} = 75\text{ Hz}$ ($St_D = 0.81$), excitation.

A fourth-order polynomial fit was applied to the time-resolved results in order to approximate the evolution of the phase angle difference of the velocity perturbations along the centerline with respect to the speaker input signal. Using the phase angle difference between the measured nozzle exit pressure and velocity fluctuations at $z/D = 0$ as a reference (Θ_o), the phase angle progress is plotted against z/D in Figure 10.7. The negative difference that occurs between $z/D = 0.075$ and $z/D = 0.2$ indicates an increase in the wave speed as the phase angle difference between the pressure and acoustic velocity decreases from its initial value at $z/D = 0.0$.

Between $z/D = 0.2$ and $z/D = 0.4$ the phase angle difference continues to be less than the initial difference at $z/D = 0.0$, although it is now constant at $\Delta\Theta = -38^\circ$. Beyond $z/D = 0.4$ the phase difference increases (wave speed decreases) as the boundary layer thickens and the flow

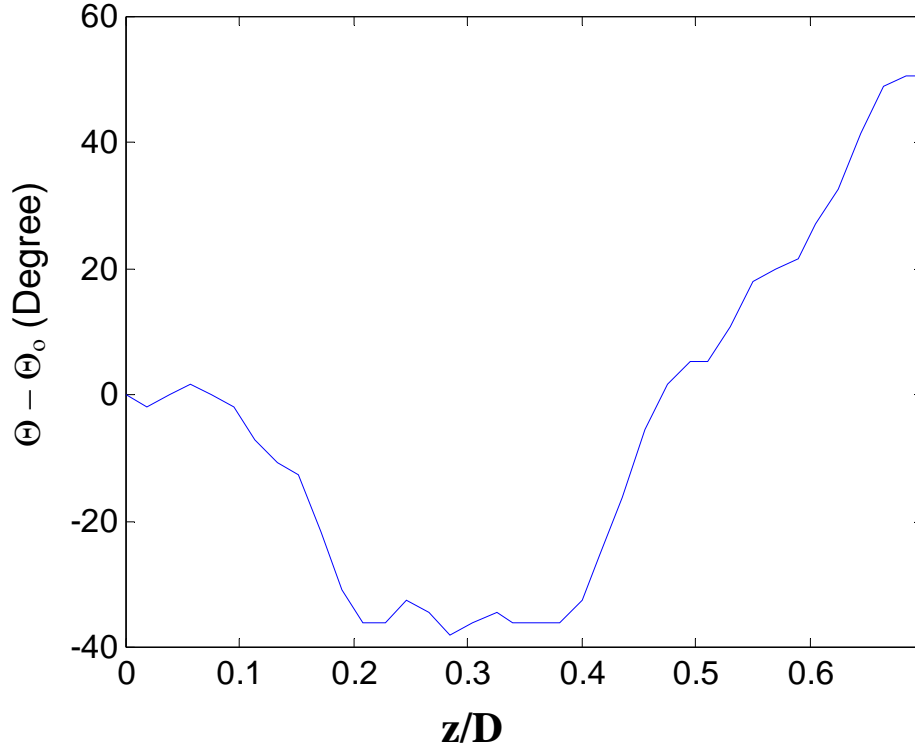


Figure 10.7: Axial variation of the phase difference between the axial rms velocity and the nozzle exit pressure along the burner centerline for an acoustically forced flow at $V_{\text{mean}} = 1.65$ m/sec and $f_{\text{ex}} = 75$ Hz ($St_D = 0.81$).

velocity retards. Although the rotational flow of the vortices does not appear to extend into the centerline within $z/D = 0.4$, comparison with Figure 10.3(b) indicates a correlation between the variation in phase speed difference (wave speed) and the initial growth of the vortex.

10.2 Reacting Flows

Chapter 5 discussed some of the difficulties of performing PIV in reacting flows. In this section, results obtained from PIV measurements in stable, laminar flames, as well as self-excited and acoustically-forced flames are presented along with some comparison to non-reacting flows. From these results we will see how the flow field varies in response to the presence of the flame and how the flame responds to acoustic disturbances that are propagating through the flow field.

The application of PIV to stable laminar flames is not new and has been discussed by Mungal and Lourenco⁸³. These authors proved the capability of performing PIV simultaneously in the cold and hot regions of the flame and showed that dilatation ($\nabla \cdot \mathbf{V} = U/r + \partial U/\partial r + \partial V/\partial z$) is an

adequate marker of the flame zone as it is directly related to a change in density through conservation of mass. The use of dilatation as a flame marker is corroborated by utilizing continuity and ideal gas laws to relate dilatation to a temperature gradient such as across the flame surface (Mueller et al.⁷⁶).

$$\nabla \cdot \mathbf{V} = \frac{1}{T} \left[\frac{\partial T}{\partial t} + \bar{\mathbf{V}} \cdot \nabla T \right] \quad (10.1)$$

10.2.1 Stable Laminar Flames

Figure 10.8 is an example image of a stable laminar flame anchored above the Rijke tube combustor nozzle, $\phi = 0.95$ and $V_{\text{mean}} = 1.65$ m/sec ($Re = 1435$). Without excitation (self-excited or acoustically-forced) the flame is steady and nearly conical. The visible light, composed primarily of CH (435 nm) and C2 (516 nm) for methane air flames, captured by a standard CCD (Kodak) is shown in Figure 10.8(a) and is a suitable indicator of the reacting surface although it exaggerates its thickness (typically 1-3 mm) due to the sustained chemiluminescence of these species downstream from the reaction zone. A separate MIE scattered image taken by illuminating the alumina oxide seeding particles used for PIV by a 200 mJ, 6 nsec laser pulse provides a slightly different image of the flame, Figure 10.8(b). As discussed in Chapter 5, the heavier seeding level marks the region in the flow up to the pre-heat zone and the temperature gradient across the reaction zone forces a volume expansion that greatly reduces the seeding density.

Along the sides of a similar Bunsen flame Mungal and Lourenco⁸³ noted that the pre-heat zone was relatively constant at approximately 0.3 mm. However, at the tip of the flame the pre-heat zone is much thicker (1.4 mm) due to focused heating of the central streamtube. In oscillating flames, such as the one discussed later in this section, cusps that form along the edge and propagate downstream may have properties similar to those of the flame tip. If this is the case, then the flame surface along the cusps would be subjected to significant stretch, defined as a localized change in the area of the flame surface, similar to what occurs at the flame tip.

Flame stretch may be either positive or negative, with positive stretch occurring on outwardly propagating flames and the opposite for negative stretch (e.g. Bunsen flame tip). Unlike the flame tip, cusps that form along the surface would consist of alternating regions of positive and negative stretch which in turn have been shown to decrease / increase the flame

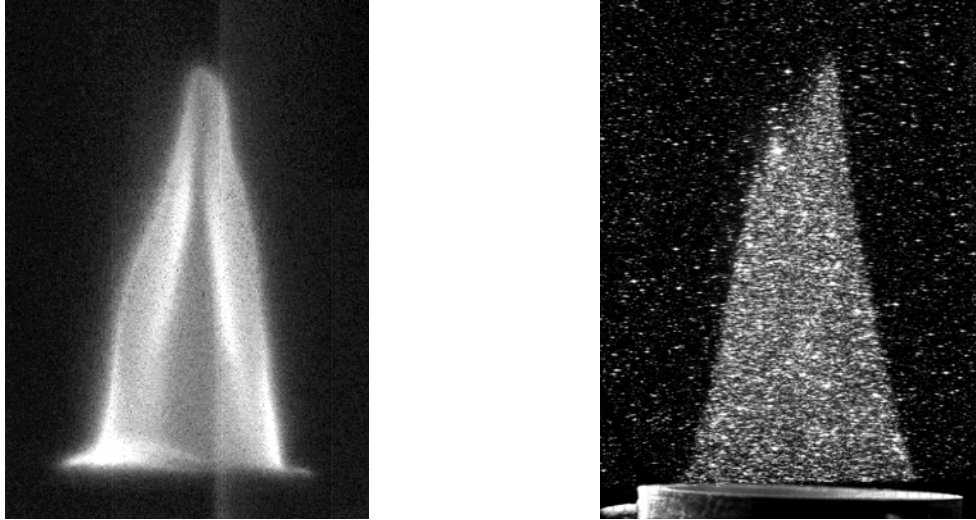


Figure 10.8: (a) Chemiluminescent image and (b) MIE scattering image of laser illuminated particles in a stable, laminar flame with $V_{\text{mean}} = 1.65$ m/sec and $\phi = 0.95$.

propagation, respectively (Sinibaldi et al¹¹⁶). Driscoll et al³² noted that the local peak reaction rate (as measured by the dilatation rate) decreases significantly in the presence of large positive flame stretch, and increases in regions where negative stretch enhances local reaction rates. Thus alternating regions that form along the cusps in oscillating flames may contribute to the driving or damping of thermoacoustic instabilities.

Figure 10.9(a) and (b) are pictorial representations of a series of isotherms and flow lines that illustrate the temperature and flow distribution along the side and at the tip of a laminar flame based on the general description provided by Lewis and von Elbe⁷⁰. Along the side of the flame, Figure 10.9(a), the normal velocity component, V_{n1} , is equal to the laminar flame speed. The temperature increase across the flame surface results in a volume expansion that is restricted to the normal direction only, and this expansion results in an increase in the normal velocity component while the tangential component, V_{t1} , remains constant.

At the tip, the heat flow converges toward the on-coming flow due to the decreased radius of curvature. This forces the temperature increase to move forward against the flow stream creating the curvature shown in Figure 10.9(b), thus increasing the burning velocity above the laminar flame speed while forcing a divergence in the mass flow at the tip resulting in only a small increase of the normal velocity across the flame surface above that of the already accelerated flow. Due to the mass flow divergence there is a considerable loss of reactants prior to the flame tip. In some cases, particularly when operating near the limit of flammability, the loss may be large enough to cause

flame extinction at the tip. The reduced flow of reactants within the tip suggests a reduction in the heat release rate in this region. A similar phenomenon may occur within the cusps that form along the surface of an oscillating flame.

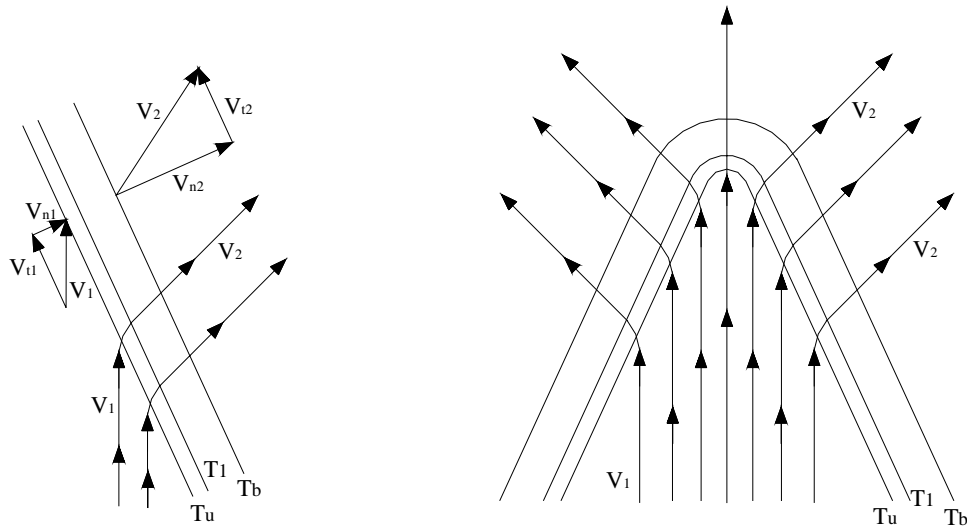


Figure 10.9: Temperature and flow distribution along the sides (a) and tip (b) of a laminar Bunsen flame.

An example of a typical velocity field of a stable flame is shown on a grid of 127×127 points in Figure 10.10. Each point on the grid represents the average vertical and horizontal velocity for a $0.38 \times 0.38 \text{ mm}^2$ box. A limited number of grid points are shown with the mean axial velocity, $V_{\text{mean}} = 1.54 \text{ m/sec}$, subtracted to improve clarity. The dark lines are contours of constant dilatation. As previously mentioned, flow dilatation marks the volume expansion that occurs in the flow due to the temperature increase across the flame front, thus providing an excellent mechanism for marking the flame front.

The initial velocity profile, at $z/D = 0$, is slightly more parabolic than the non-reacting flow which has a somewhat top-hat profile (Figure 10.1). The strong flow turning associated with the conservation of the tangential velocity component and the increasing normal (to the flame surface) component consistent with the volume expansion is evident as the flow reaches the pre-heat zone along the sides of the flame with an increase of almost 200% in the velocity from 1.58 m/sec to 2.9 m/sec across the flame. The high velocities in the post-flame regions resulting from the volume expansion easily exceed the maximum speeds of the incoming reactants.

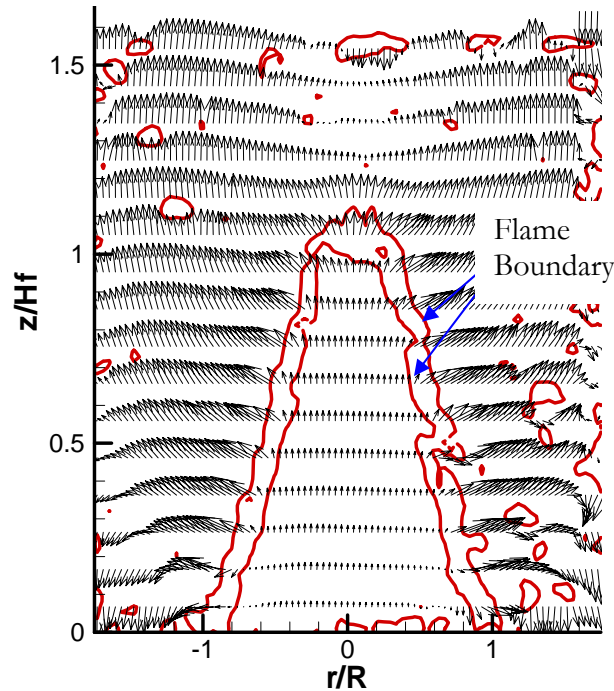


Figure 10.10: Measured velocity field and flow dilatation iso-contours for a stable flame similar to that shown in Figure 10.8.

The core streamtube in Figure 10.10 begins to narrow away from the nozzle exit. The expansion effect of the flow appears to be similar along the sides of the flame until the tip region where the post-flame gas forms a wake-like profile with a minimum velocity along the jet centerline. A similar wake-like profile was observed by Mungal and Lourenco⁸³ and is attributed to the large volume expansion along the sides of the flame. The low pressure region within the wake curves the expanding post-flame gases back towards the centerline thus satisfying the conservation of momentum.

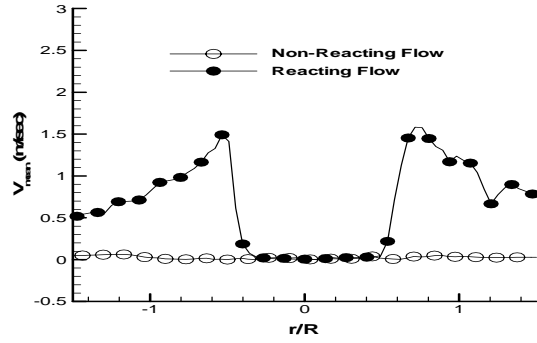
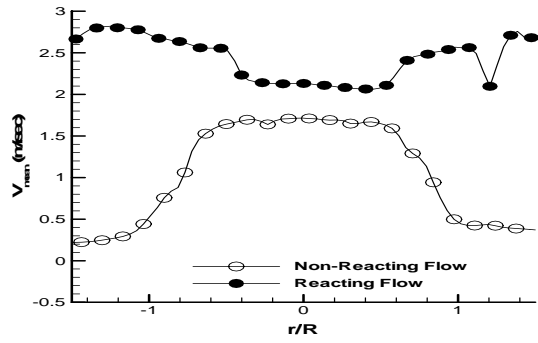
Detailed discussion of flame stretch and peak dilatation rates measured in flames may be found in a number of references including Law⁶², Choi and Puri¹⁹, Echehki and Mungal³⁶, Sinibaldi et al¹¹⁶, and Mueller et al⁸¹. For this study dilatation rate is used primarily as a tool for identifying the flame surface, and although variations of dilatation rate and flame stretch are mentioned a rigorous analysis of how these parameters vary with instability is beyond the scope thesis, and thus is the topic of future analysis planned by the author.

Dilatation rate contours are also shown in Figure 10.10 mark the boundary of the flame with the contour indicating a line of constant dilatation at $\nabla \cdot \mathbf{V} = 200 \text{ sec}^{-1}$. Although it had a localized

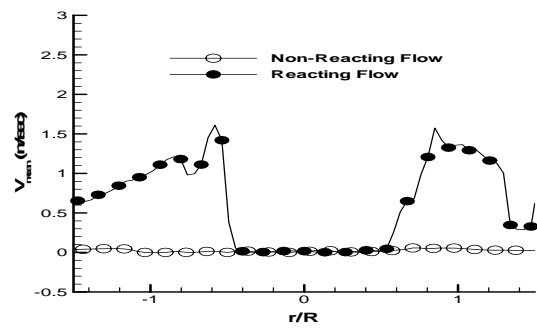
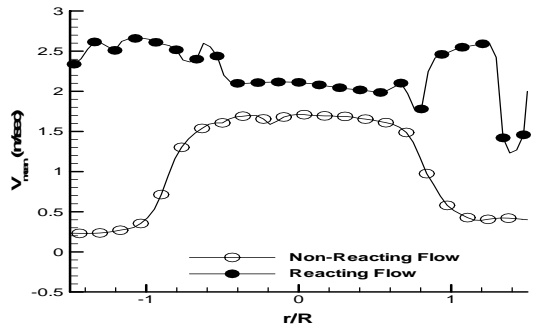
peak dilatation rate of $\nabla \cdot \mathbf{V} \approx 1200 \text{ sec}^{-1}$, the stable flame displayed an average peak value along the lengths of the flame front was $\nabla \cdot \mathbf{V} \approx 600 \text{ sec}^{-1}$.

A comparison between the axial and radial velocity profiles of stable reacting and non-reacting flows are shown in Figure 10.11 as a function of the radial location (r/R) at different axial locations, z/D , where D is the nozzle diameter and the flame height to diameter ratio is $H_f/D = 1.3$. A combination of symbols and lines are used to represent data acquired from the PIV images. The initial axial velocity profiles (at $z/D = 0.0$) are very similar for the cold flow region of the stable flame and the non-reacting laminar flow with the flow exiting with a “top-hat” profile. This would suggest that heat from the flame, which is immediately downstream of this location, does not have a significant influence on the flow at the nozzle exit. However, the radial flow at $z/D = 0$ does show some effect with an increase at the bounds of the ring stabilizer ($r/R = -1, 1$) where the flame is anchored. This acceleration of velocity through the flame is the result of the volume expansion across the flame surface due to the large temperature difference between the cold and hot gases.

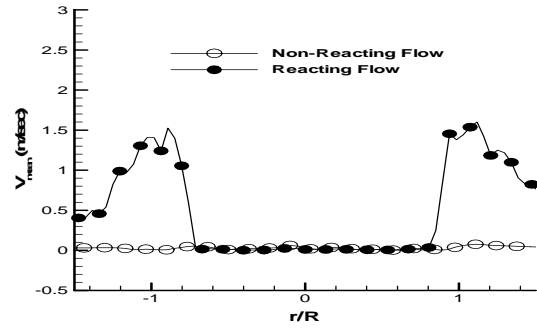
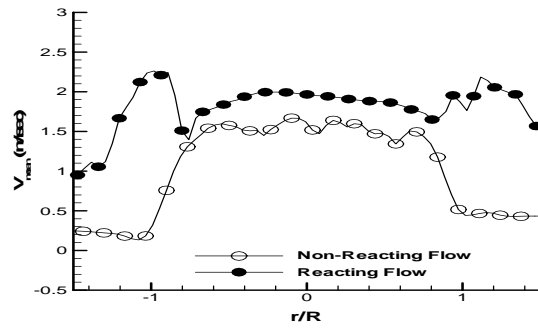
Just downstream at $z/D = 0.25$ the influence of the flame is now clearly apparent in the plot of the axial velocity. While the non-reacting axial velocity is unchanged, the reacting flow acceleration at $r/R = -1, 1$ is evidence of the encroachment of the flame toward the centerline with an increase in flow over the non-reacting axial velocity at $r/R = -1, 1$ of $V_{\text{non-reacting}, r/R=-1} \approx 0.3 \text{ m/sec}$ to $V_{\text{reacting}, r/R=-1} \approx 2.25 \text{ m/sec}$. In addition the flow along the centerline has increased from a maximum of $V_{\text{non-reacting}, r/R=0} \approx 1.5 \text{ m/sec}$, which it maintains through $z/D = 1.0$, to $V_{\text{reacting}, r/R=0} \approx 2.0 \text{ m/sec}$. Thus heat from the flame has now radiated inward to sufficiently increase the flow rate in the cold pre-combustion flow. The flat, negligible radial flow accelerates from $U_{\text{mean}} = 0.0$ to approximately $U_{\text{reacting}} \approx 1.5 \text{ m/sec}$ at $r/R = -1, 1$. This indicates that like the non-reacting flow, the pre-combustion stable flame flow emitted from the nozzle is one-dimensional until it reaches the flame front. Although both the axial and radial flows continue this trend of the volume expansion across the flame front, the difference between the pre-combustion and post-combustion axial velocities narrows while the radial difference remains nearly constant regardless of the flame front location. This indicates that the pre-combustion flow of the stable flame is indeed one-dimensional, and that although the radiative heating from the flame surface causes an acceleration of the one-dimensional axial flow it does not influence flow turning prior to the flow crossing the flame surface.



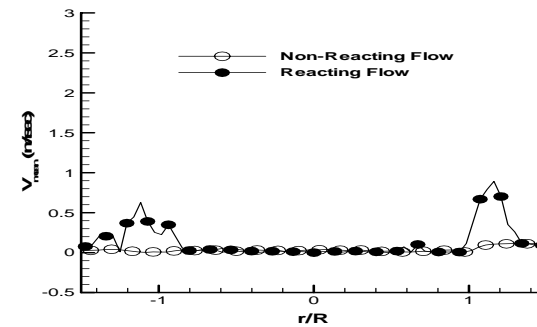
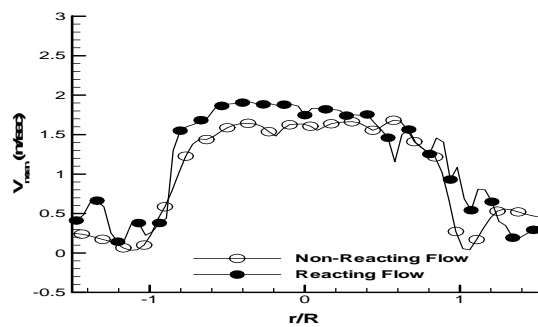
$z/D = 1.0$



$z/D = 0.75$



$z/D = 0.25$



$z/D = 0.0$

Figure 10.11: Comparison of radial profiles at various axial distances from the burner nozzle exit for axial and radial mean velocities for reacting and non-reacting flows at $V_{mean} = 1.65$ m/sec and $\phi = 0.95$.

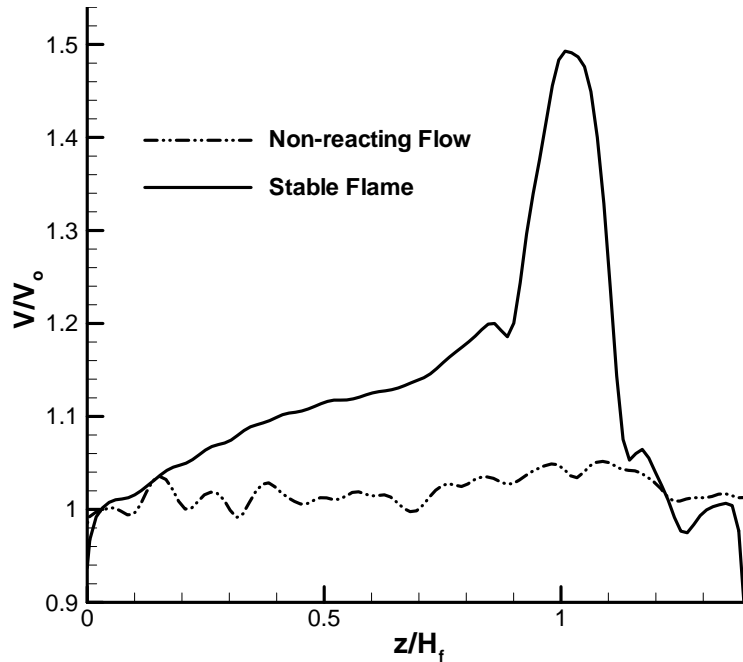


Figure 10.12: Centerline profile of the mean axial velocity, V_{mean} , normalized by the nozzle exit mean flow, V_o , for reacting ($\phi = 0.95$) and non-reacting stable, laminar flow with $V_{\text{mean}} = 1.65$ m/sec.

The axial velocity along the centerline for the stable flame is plotted in Figure 10.12 accompanied by the axial velocity profile from the non-reacting steady flow. The velocity profiles were both normalized by their corresponding centerline velocities at the nozzle exit and the axial coordinate is given a ratio of the axial distance from the nozzle exit and the stable flame height ($H_f = 27$ mm). The pre-combustion, cold flow shows a relatively constant value over its length although there is a slight increase as the flame encroaches on the centerline that can be seen and is similar to the behavior shown in Figure 10.11. Once the cold gas reaches the pre-heat region there is a sudden acceleration as the flow is introduced to the flame with a maximum velocity obtained at the flame surface ($z/H_f = 1.0$). Here in the tip region of the flame the gas velocity has increased to just over 150% of that at the nozzle exit. In the post flame region the flow quickly decelerates reaching a minimum of $V/V_o = 0.96$ which is below that of the nozzle inlet velocity. The reduction in flow forms a wake region just downstream of the tip and is visible in Figure 10.10. This wake region, which has been seen in other studies (Mungal and Lourenco⁸³) and will be discussed in length later in this chapter is the result of a low pressure region which must form in order to curve the expanding post flame gases back toward the centerline.

10.2.2 Unstable, Oscillating Flames

PIV data was collected from self-excited and acoustically-forced flames with intensities ranging from $i_p = 0.0 - 0.18$. Cycle-resolved results were obtained for a self-excited flame ($i_p = 0.14$) and a flame acoustically-driven at approximately the same frequency ($St = 2.49$ and $H_f/\lambda \approx 0.02$) and intensity ($i_p = 0.17$). All of the results shown were obtained with an average nozzle exit flow of $V_{\text{mean}} = 1.65$ m/sec ($Re = 2200$) and an equivalence ratio of $\phi = 0.95$.

Figure 10.13a and b are examples of a typical PIV image and velocity vector plots for a self-excited, unstable flame ($i_p = 0.14$), and Figure 10.14a-f are examples of PIV measurements from the flame under various degrees of excitation ranging from self-excited to acoustically-forced to stable. In Figure 10.13b lines of constant flow dilatation ($\nabla \cdot \mathbf{V} = 250 \text{ sec}^{-1}$) mark the boundary of the flame surface, while shaded contours indicate regions of high axial velocity in the post-flame regions. Like the stable flame PIV image shown in Figure 10.7, the heavy and light seed areas of the MIE scattered flame image in Figure 10.13(a) separate the cold, pre-flame and hot, post-flame regions respectively in Figure 10.13a. Even the sharp transitions marking the boundary of the cusp regions are clearly visible in the image of the illuminated particles. Velocity vectors in Figure 10.13b indicate the corresponding velocity field with the mean flow subtracted and has a number of similarities to that of the stable flame shown in Figure 10.9 and Figure 10.14f.

Results from low frequency studies ($St_D < 1.4$) of Baillot et al.⁶ have suggested that the acoustic disturbances are convected along with the mean flow. This was determined by measuring the phase angle difference between the velocity perturbations along the centerline and the initial vibration of the driver, similar to Figure 10.7. In Chapter 7 we discussed the propagation of the cusps along the flame surface and determined that during periods of instability, the distance between the cusps could be determined by assuming they are convected with the mean flow. Given an acoustic disturbance at $St_D = 2.49$ the convected wavelength would be $\lambda_c = V_o/f = 7.17$ mm. This is well within the measurement resolution of the PIV system (grid – $0.38 \times 0.38 \text{ mm}^2$) and if a convected disturbance did exist the flow would appear to oscillate over this distance.

Looking at the flow fields in the self-excited ($i_p = 0.14$) and acoustically-driven flames at higher excitation amplitudes ($i_p = 0.17, 0.19$) in Figures 10.14a, d and e respectively and the centerline profiles of the unstable flames given in Figure 10.21, we see that although the velocity profile in the pre-flame region along the centerline is not flat as in the previous cases there is no

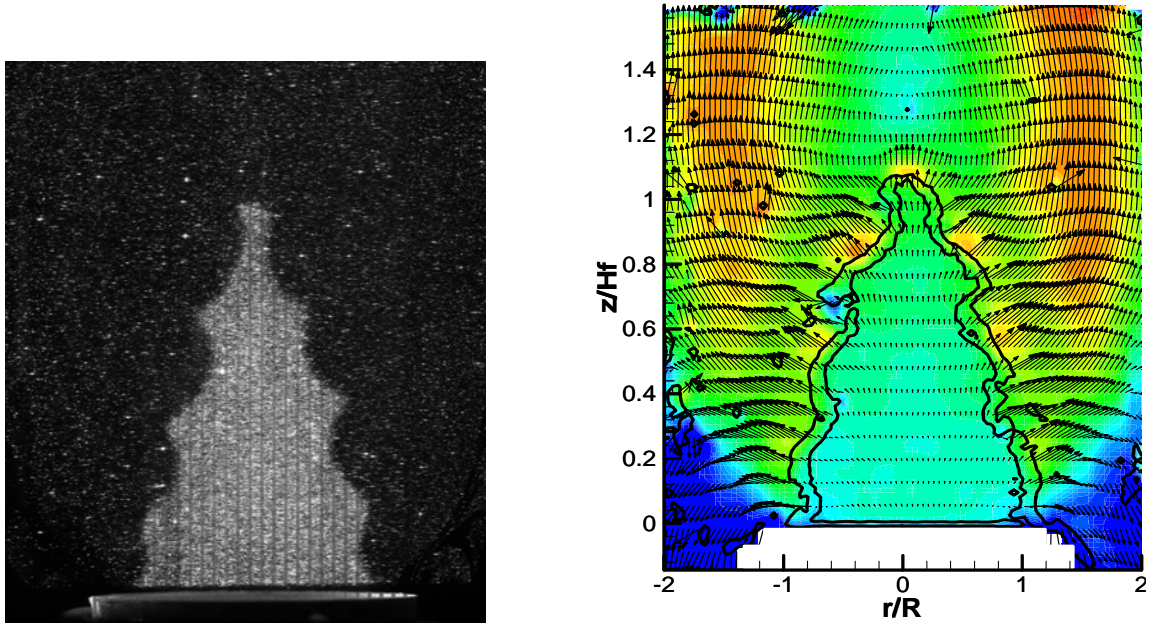


Figure 10.13: (a) Example MIE scattering image of self-excited flame use to perform PIV; (b) Image of Velocity Vectors obtained from PIV analysis for self-excited flame.

apparent indication of a convected acoustic disturbance. This would suggest that the unsteady velocity field is independent of the mean flow even for intensities approaching 20% ($i_p = 0.19$).

Given the bulk fluid motion of the flow field, it appears that the cusps that form along the surface are not the result of a local disturbance (i.e. vortex shedding) occurring at that instance at the flame front downstream from the nozzle exit. The kinematic model proposed by Fliefil et al.³⁹, as well as the characteristic method proposed by Baillot et. al⁶, were able to capture the formation of cusps along the surface given a time-varying perturbation like that measured in this study where pulsations in the flow at the nozzle exit force the orientation of the flame front to vary in response. Because the front propagates in a direction normal to its instantaneous position, the resulting convex / concave shape and amplitude of cusps along the surface are dictated by the intensity of the disturbance at the nozzle exit, and although the acoustic disturbance decays quickly away from the nozzle exit the cusps persist through the tip of the flame even resulting in a variation in the flame height and surface area.

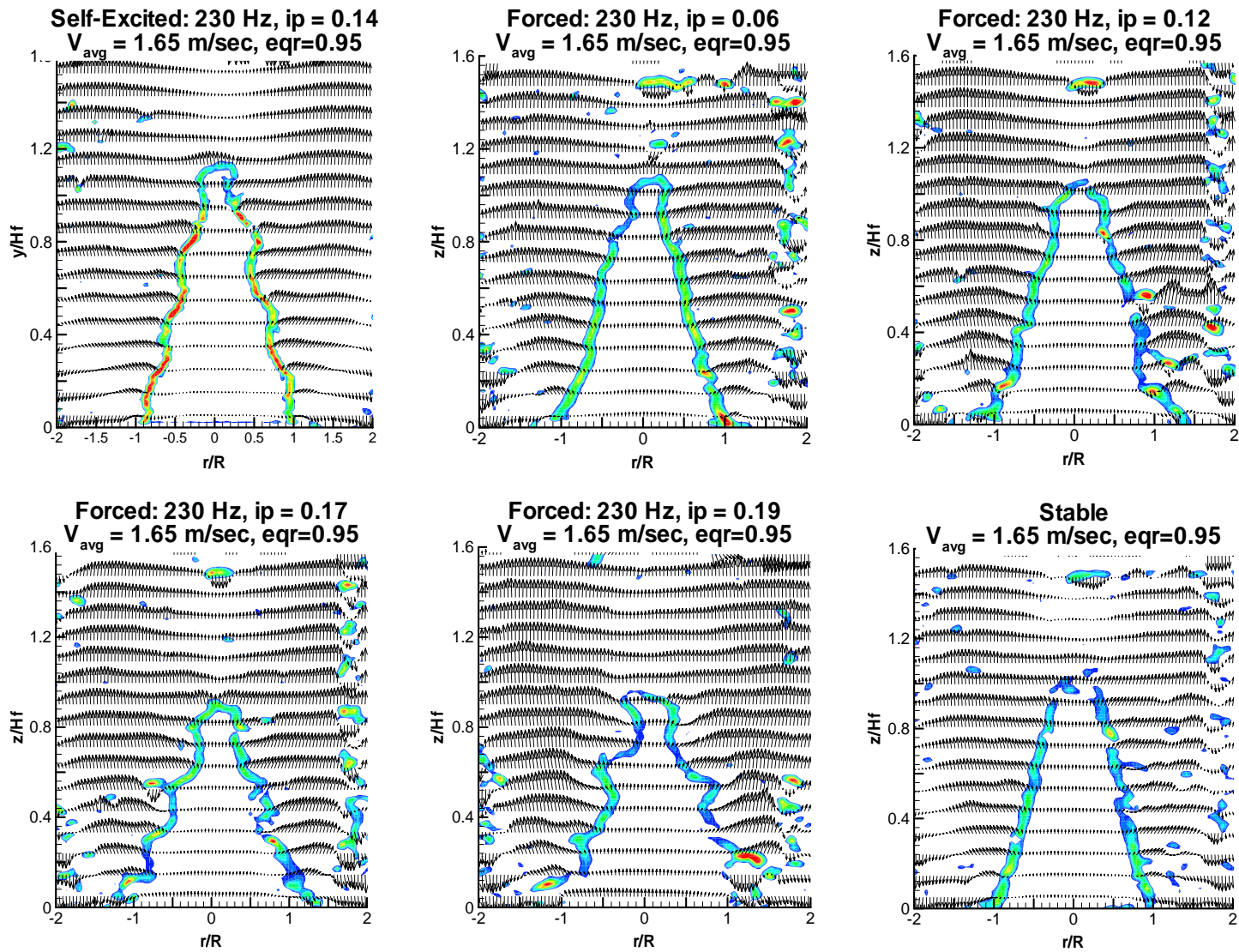


Figure 10.14: Velocity vectors and dilatation contours of the Rijke tube burner flame, $V_{\text{mean}} = 1.65 \text{ m/sec}$, $\phi = 0.95$ and $H_f/\lambda = 0.02$, experiencing various degrees of instability. Acoustically-forced flames were driven by speaker located in the base of the burner nozzle; (a) self-excited, $ip = 0.14$; (b) acoustically-forced, $ip = 0.06$; (c) acoustically-forced, $ip = 0.12$; (d) acoustically-forced, $ip = 0.17$; (e) acoustically-forced, $ip = 0.19$; (f) Stable.

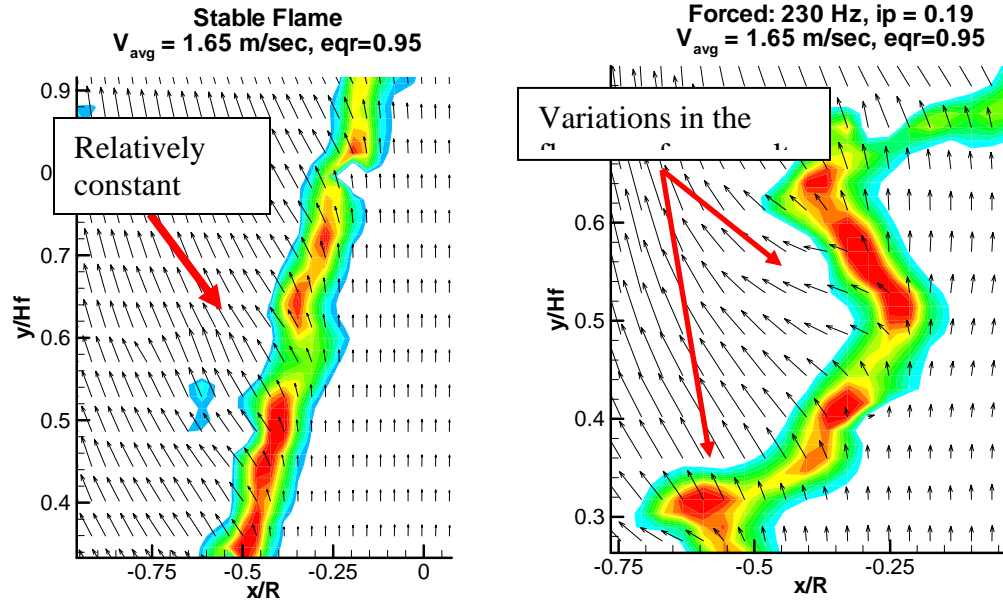


Figure 10.15: PIV velocity vectors and dilatation contours of flame indicating the effect that the flame contour has on the flow velocity as it crosses the flame surface. (a) Stable flame; (b) Acoustically-forced flame, $i_p = 0.19$.

As previously stated the position or curvature of the flame front does not appear to affect the velocity field in the near-field. However, as the flow enters the pre-heat region and crosses the flame surface, we begin to see the influence of flame curvature, and subsequently intensity, on the local velocity field. The occurrence of flow turning as the flame enters the pre-heat zone has been previously discussed and is clearly visible in the measured velocity fields shown in Figures 10.15a and b. The effects of this turning were excluded from the kinematic model presented by Fliefil et al.³⁹ and its subsequent effect on heat release rate may explain some of the discrepancies between experimental and theoretical results.

Along the smooth sides of the stable and low amplitude disturbance flames ($i_p = 0.06$ and 0.12 , Figure 10.14b and c), the flow upon crossing the pre-heat and flame front respond by increasing the velocity component normal to the surface which is at a relatively constant angle to the oncoming flow. This is apparent in the stable flame results shown in Figure 10.15a. As the intensity increases, cusps and wrinkles begin to form along the front and local regions of the flow are now required to diverge at various angles in response to the flame front, Figure 10.15b. Although the effects of flame stretch were not explicitly discussed in this study, altering regions of positive (convex - with the flame surface collapsing towards reactants) and negative (concave - with the flame surface expanding from the reactants) stretch that forms along the flame front subsequently

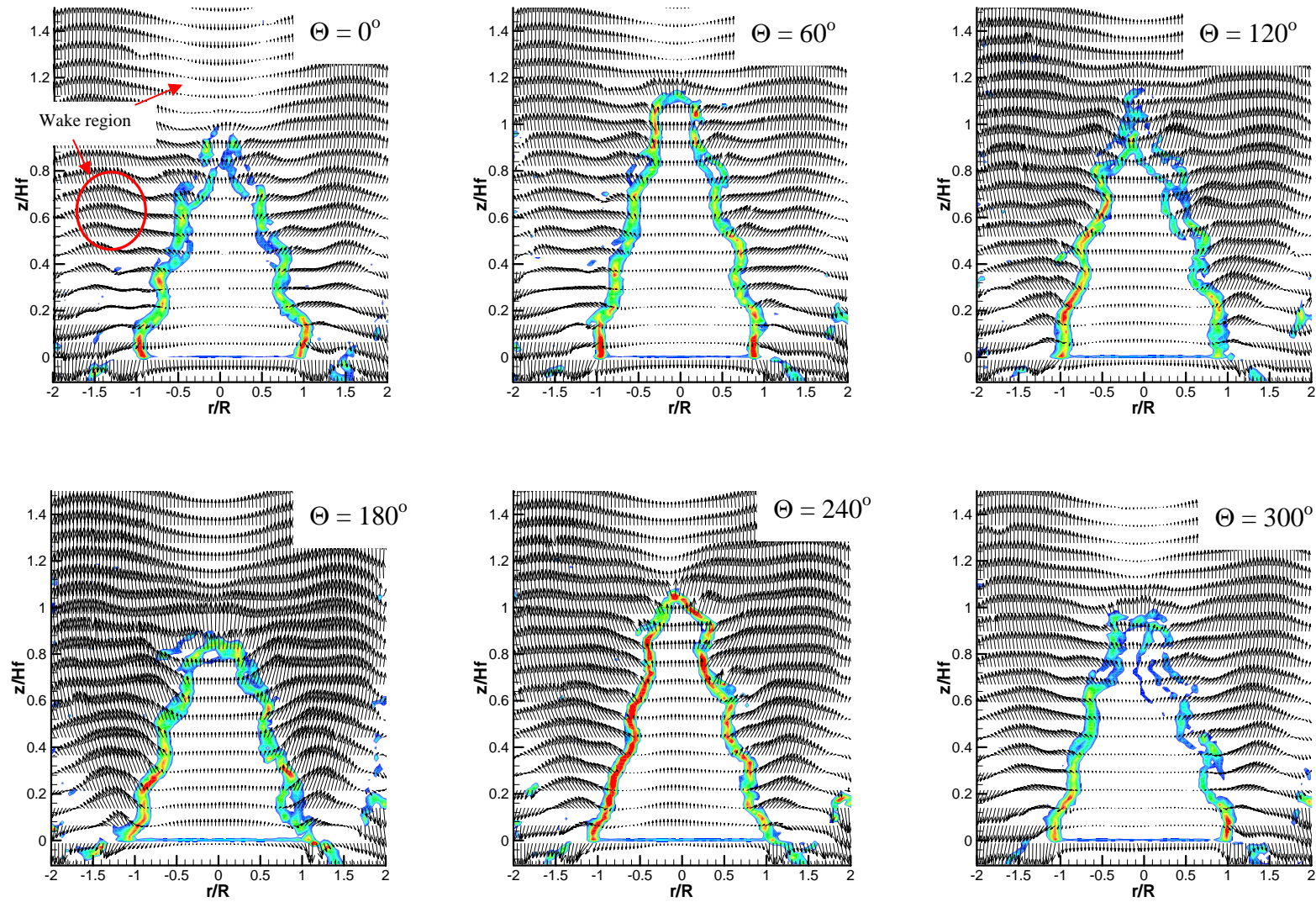


Figure 10.16: Phase resolved velocity vector fields and dilatation contours for self-excited flame with $St_D = 2.49$, $V_{\text{mean}} = 1.65$ m/sec and $f = 0.95$. Acoustic pressure measured made at nozzle exit used for phase angle

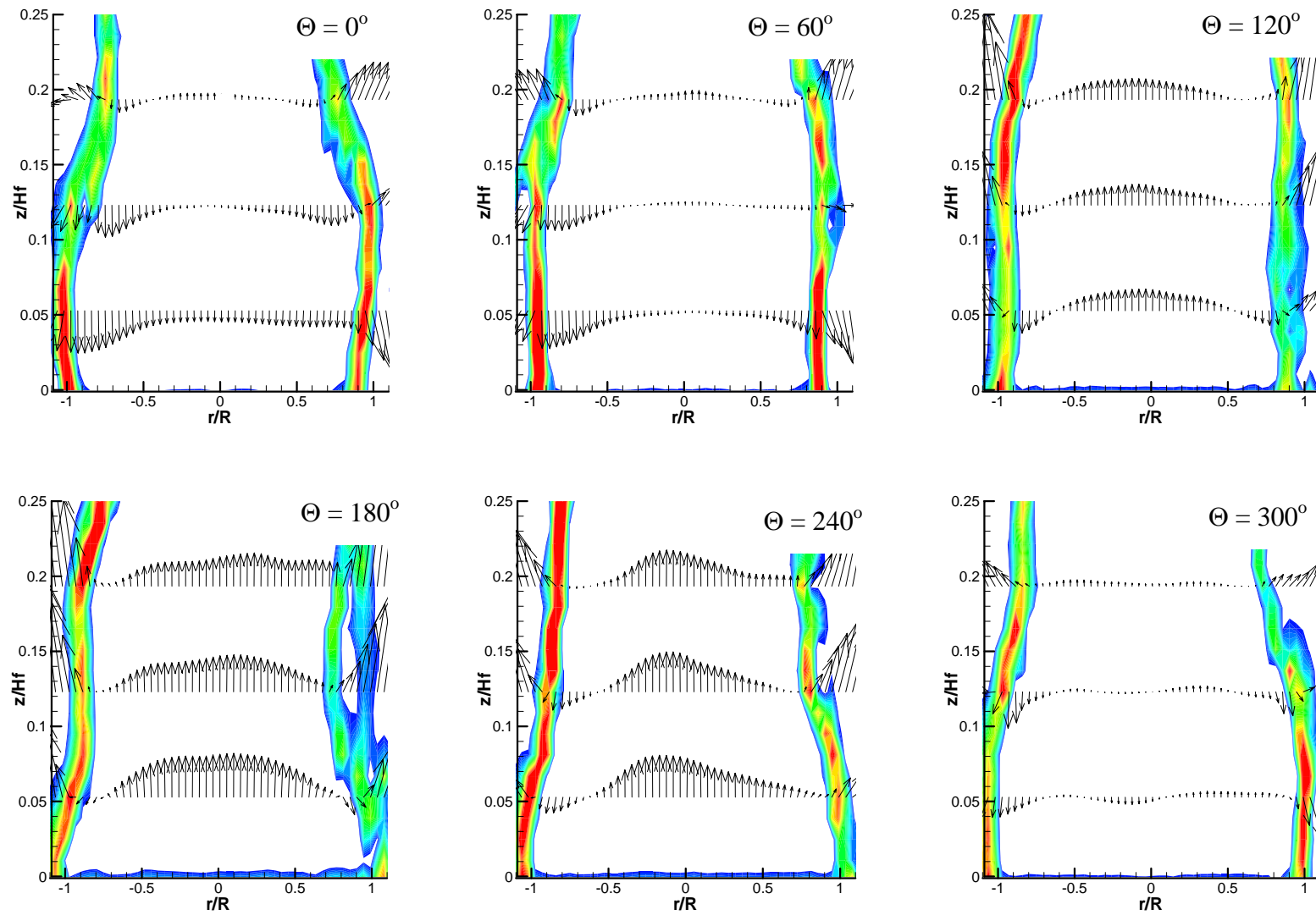


Figure 10.17: Close-up of phase resolved velocity vector fields and dilatation contours for self-excited flame shown in Figure 10.16. Enlarged area shows oscillating velocity vectors in the cold-flow.

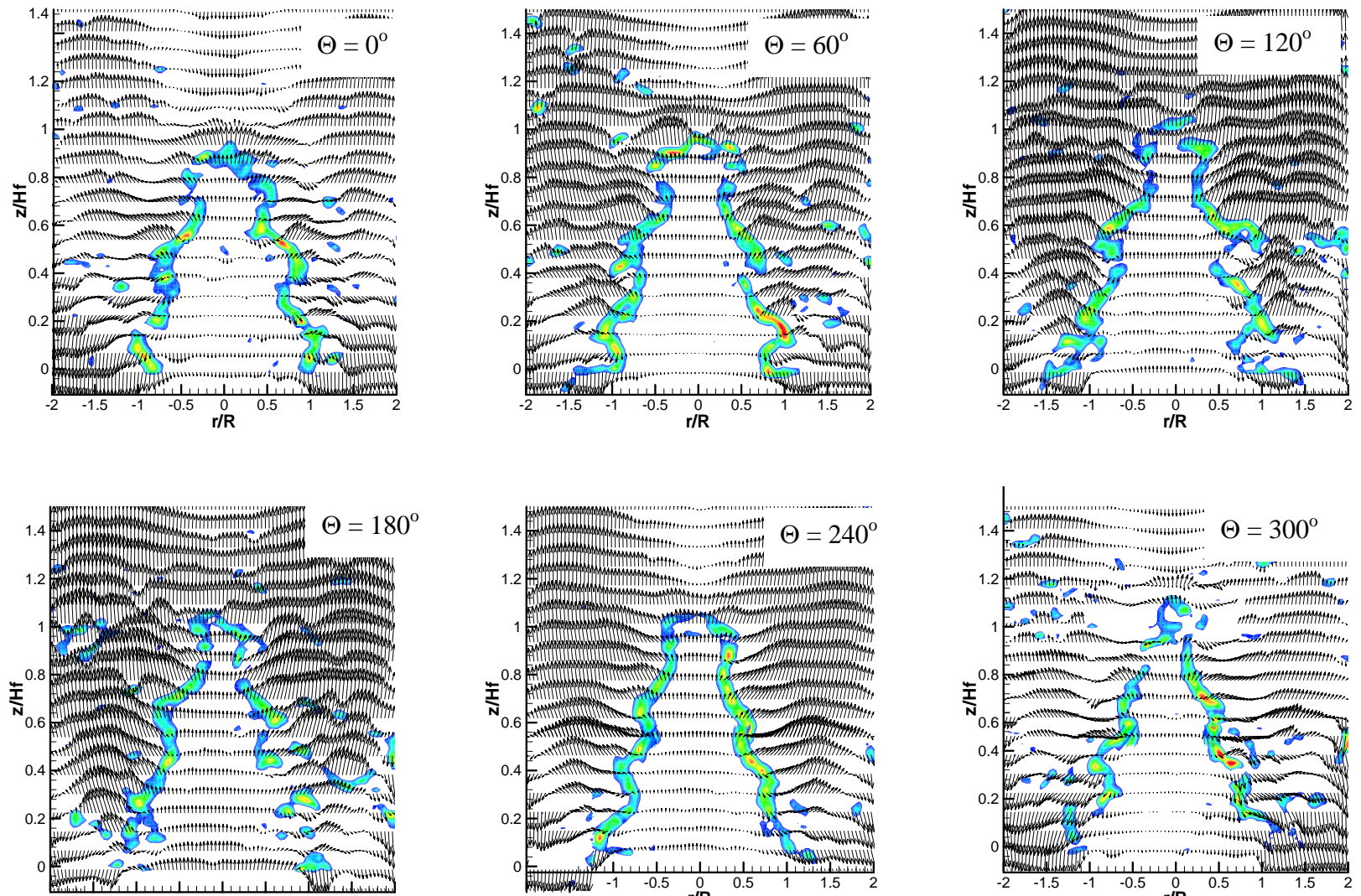


Figure 10.18: Phase resolved velocity vector fields and dilatation contours for acoustically-forced flame with $St_D = 2.49$, $V_{\text{mean}} = 1.65$ m/sec and $\phi = 0.95$. Acoustic pressure measured made at nozzle exit used for phase angle reference.

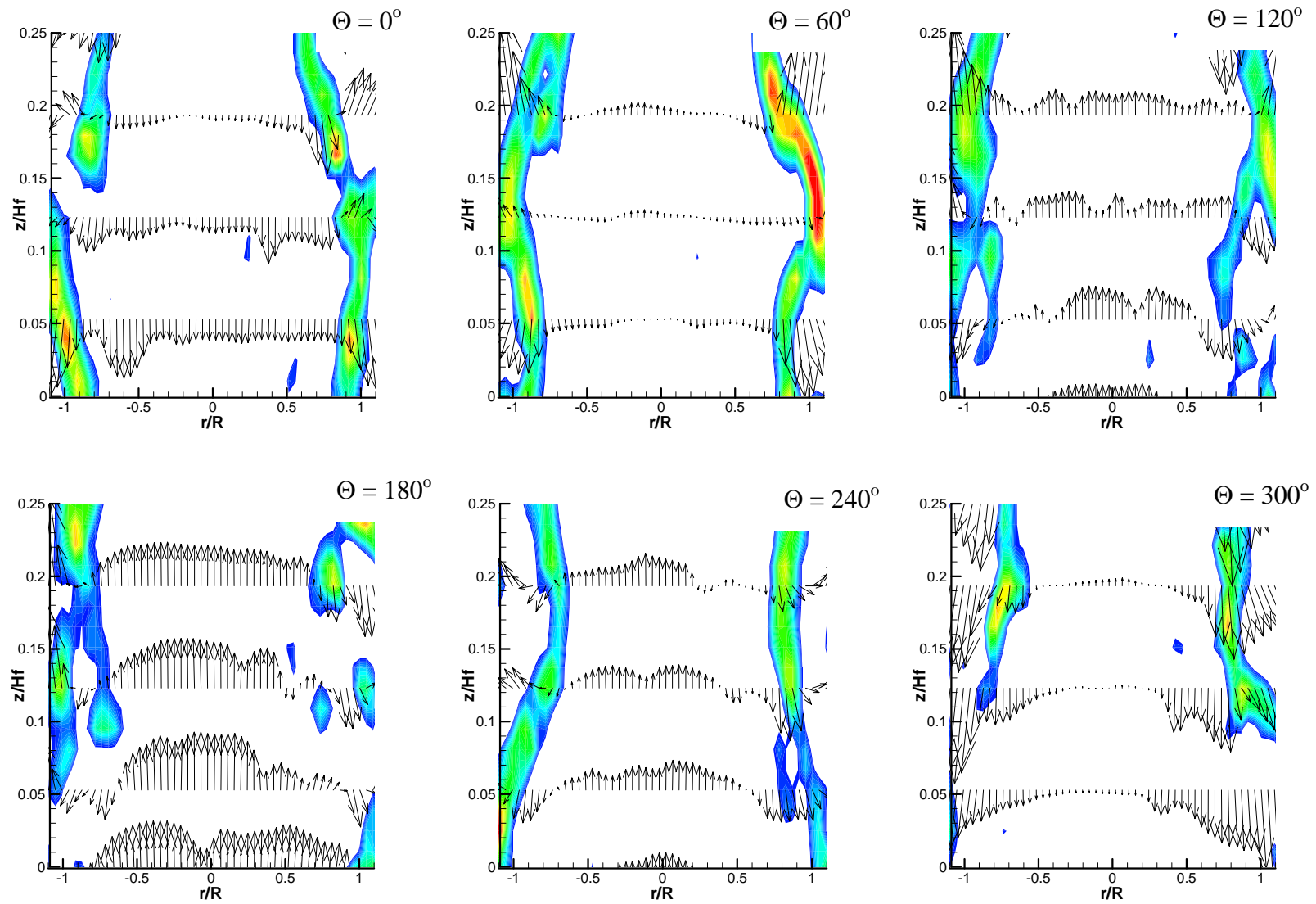


Figure 10.19: Close-up of phase resolved velocity vector fields and dilatation contours for self-excited flame shown in Figure 10.18. Enlarged area shows oscillating velocity vectors in the cold-flow.

produce perturbations in the flame surface area and additionally force variations in the near-field and post flame flows. These flow field variations may periodically alter the heat release emitted from the flame and account for the phase discrepancies that exist between the flame surface area or velocity perturbations at the nozzle exit and the heat release rate. This study is the first to propose that the local flame structure must be accounted for in order to accurately describe the phase response, and additional study of this phenomenon is needed in order to obtain quantitative results.

10.2.3 Unstable, Oscillating Flames: Phase-Resolved

In order to obtain cycle resolved images of the flow field, the PIV system was phase-locked to the nozzle outlet pressure signal as described in Chapter 3.6.3 and 6.1, allowing images to be acquired in increments of 10° of phase. Thirty-six instances of the flow field were obtained over a cycle with 3-5 image pairs being averaged together to obtain one instance. Because this process was quite time-consuming it was only performed on two occurrences of an oscillating flame: self-excited ($i_p = 0.14$) and acoustically forced ($i_p = 0.17$), in which the average nozzle exit flow was $V_{\text{mean}} = 1.65$ m/sec and $\phi = 0.95$.

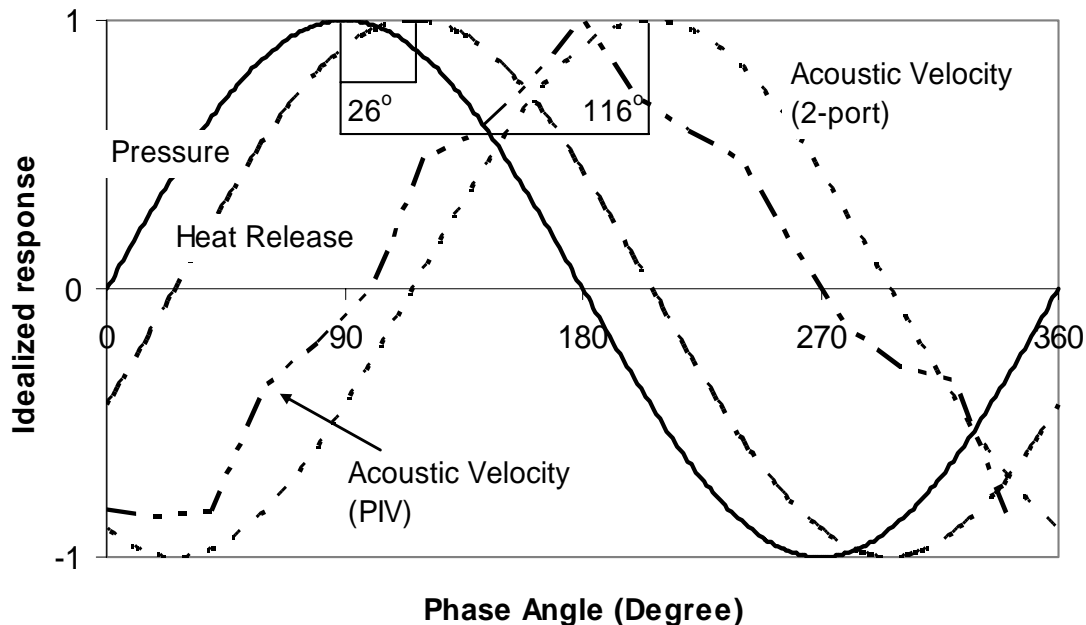


Figure 10.20: Measured Flame difference between the acoustic pressure, perturbations in the heat release rate and acoustic velocity for self-excited flame at $V_{\text{mean}} = 1.65$ m/sec, $\phi = 0.96$ and $St_D = 2.49$.

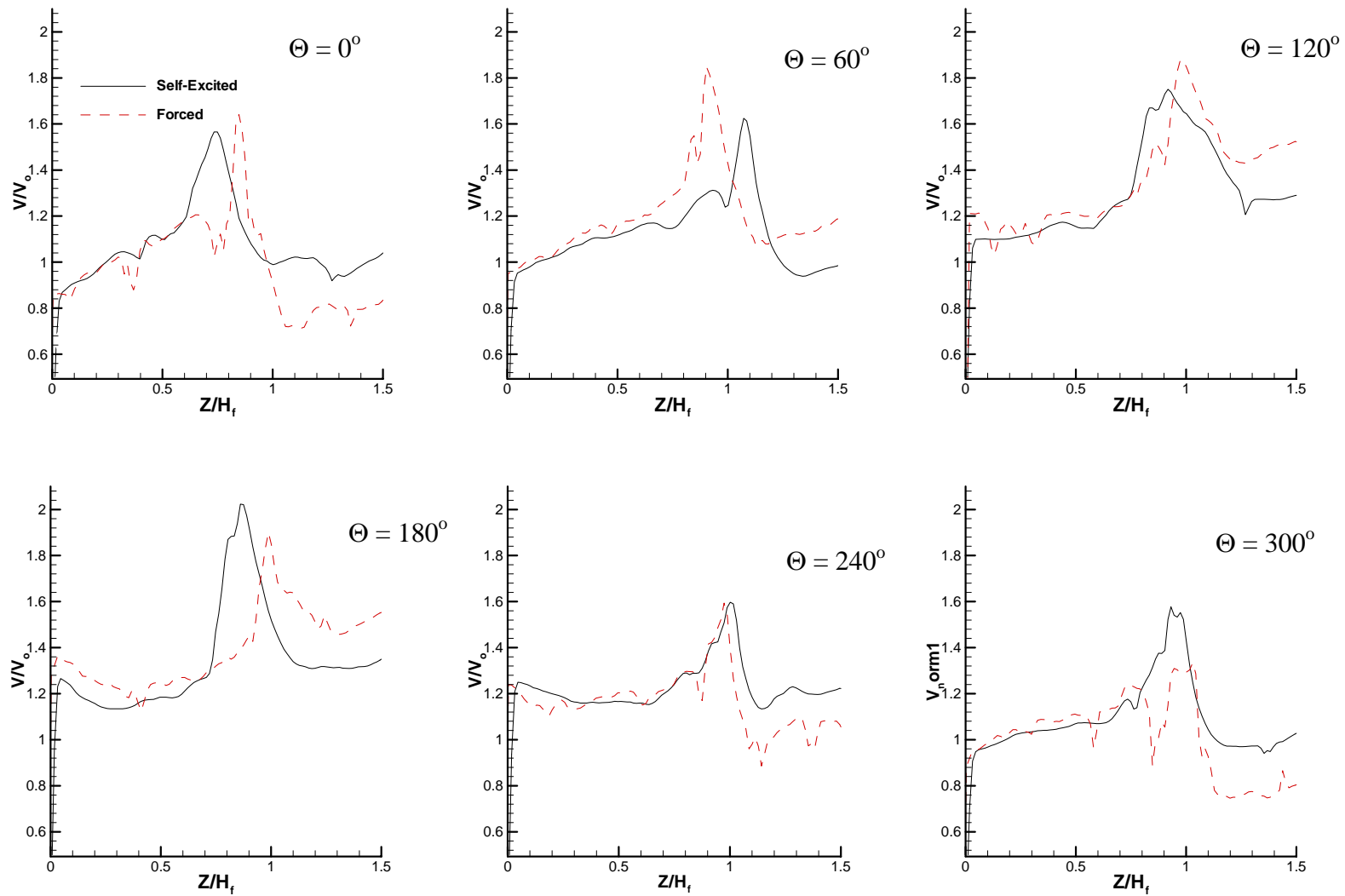


Figure 10.21: Phase resolved axial velocity profiles along the centerline for self-excited and acoustically-forced flames at $V_{\text{mean}} = 1.65$ m/sec, $\phi = 0.95$ and $St_D = 2.49$. Acoustic pressure at nozzle exit used as phase reference.

Figure 10.16 through 10.19 show examples of the velocity fields at several phase angles, with reference to the nozzle exit pressure, for a self-excited ($i_p = 0.14$) and acoustically driven flame ($i_p = 0.17$). The mean axial velocity, measured at the nozzle exit from $-0.7 = x/R = 0.7$, was subtracted from the flow to emphasize the acoustic perturbations. Figure 10.17 and 10.19 are close-up images of the velocity field that clearly show the oscillatory motion of the flow. As a qualitative comparison, it would be expected that the oscillatory motion of the flow at the nozzle exit agree with the phase measurements performed in Chapter 9 using the two-port analysis. The idealized cycle responses of the acoustic pressure and velocity along with the heat release rate are given in Figure 10.20 separated in phase by the measured difference obtained from the two-port method. At the operation conditions listed above, the self-excited flame had a phase difference between the pressure and heat release rate of 26° of phase and 116° for the pressure and acoustic velocity. A comparison of these results, along with the normalized PIV measured velocity response, indicates a relatively good qualitative agreement with the two-port analysis as the initial acoustic velocity at 0° is negative and becomes positive between 60° and 120° (116°). The velocity at the nozzle exit begins to reach its peak between $180^\circ - 240^\circ$ before it decreases over the remaining cycle. Thus there is general agreement in the direction of the acoustic velocity as measured by the two-port method of Chapter 9 and the PIV phase-locked method shown here.

Phase resolved plots of the centerline axial velocity normalized by the time-averaged value at the nozzle exit (V_o) for self-excited and acoustically-forced flames are shown in Figures 10.21a-f. These plots illustrate a general trend for both forms of oscillating flames consisting of a relatively flat profile leading to a sudden increase due to the thermal expansion across the flame tip followed by a sharp deceleration as the flow enters the wake region described earlier. This is in agreement with experimental results presented by Mungal et. al⁸³. Good agreement is obtained between self-excited ($i_{p_self} = 0.14$) and acoustically-forced ($i_{p_fc} = 0.17$) flames as shown in the individual phase-resolved profiles. The effects of the acoustic velocity are clearly visible at $z/H_f = 0.0$ as the amplitude of the normalized velocity oscillates about $V/V_o = 1.0$ over the course of the cycle. Downstream of the nozzle exit, the flow increases or decreases as it converges to approximately $V/V_o \approx 1.1$ at $z/H_f = 0.6$, suggesting that the axial acoustic disturbance has damped prior to the centerline flow reaching the flame tip. This is in qualitative agreement with the minimum and maximum numerical predictions presented by Lee and Lieuwen⁶⁸ and is more apparent when considering the actual rms axial velocity measured along the centerline as shown in Figure 10.22. Also shown in Figure 10.22 plots the rms values for the axial centerline velocity for both the

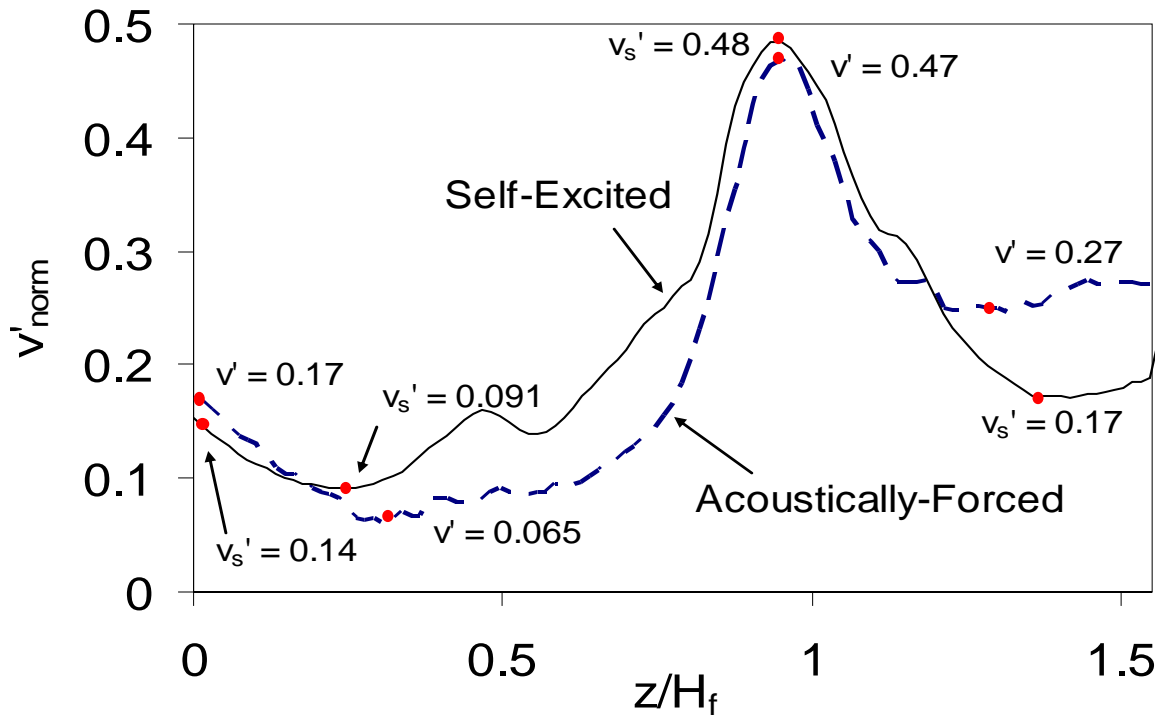


Figure 10.22: Measured rms axial velocity along the centerline normalized by mean nozzle exit velocity for self-excited and acoustically-forced flame. Approximately 50% reduction in amplitude from $z/H_f = 0.0$ to $z/H_f = 0.38$.

acoustically-forced and self-excited flames as a function of the axial distance from the nozzle exit normalized by the average flame height (z/H_f). The reported axial acoustic intensity (v') is measured at the nozzle exit ($z/H_f = 0.0$) where the rms velocity is shown to have a local maximum. Losses in the flow allow the amplitude of the velocity perturbations to reach a minimum at $z/H_f \approx 0.3$ that is equal to approximately half the amplitude of v' at $z/H_f = 0.0$. As the flow enters the preheat and reaction zones ($z/H_f > 0.5$) there is a significant increase in the rms value for both flames, but can be attributed to the movement of the flame tip as opposed to an acoustic effect. However, even though the acoustic disturbance is not the primary driver for the increase in velocity perturbations within this region, the peak axial velocity (as a result of the flow crossing the reaction zone) does seem to vary with the acoustic disturbance.

Although the acoustic disturbance in the reactant flow was shown to be relatively small prior to the flow entering the preheat region of the flame a comparison of the velocity at the flame tip, obtained from Figure 10.20, shows that the amplitude of the velocity at the flame tip varies in phase with the acoustic velocity measured at $z/H_f < 0.5$. This would not be expected given the

diminished quantity of the rms component at $z/H_f = 0.5$. An additional peculiarity in relation to the acoustic damping occurs along the flame surface. Assuming that the cusps that form along the flame surface are a result of the acoustic disturbance in the cold reactant flow, one would expect their amplitude to decrease with the rms amplitude from the nozzle exit. However, although the quantitative analysis of the cusp amplitude is beyond the scope of this study, a qualitative evaluation of Figures 10.15 and 10.17 suggest that the amplitude of the cusps remains relatively constant along the entire length of the flame. This would suggest that although the acoustic velocity within the reactant flow has essentially damped, the downstream flame surface is still being influenced by the acoustic disturbance. While further analysis is necessary, an explanation of this phenomenon may exist in the product flow downstream of the flame surface.

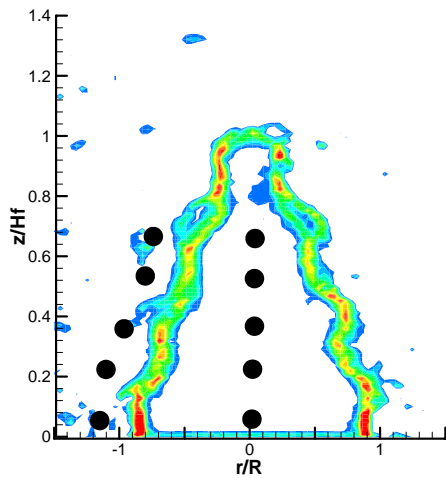


Figure 10.22: Flow dilatation contours for self-excited flame. Filled circles indicate locations where data was obtained to generate Figures 10.23 and 10.24.

Table 10.1: rms velocities at outboard (v') and along the centerline (v'_{cl}) at axial positions (y/H_f)

r/R	z/H_f	v'	v'_{cl}
-1.2	0.0	0.19	0.17
-1.0	0.23	0.19	0.08
-0.9	0.35	0.21	0.07
-0.7	0.51	0.17	0.07
-0.5	0.65	0.19	0.04

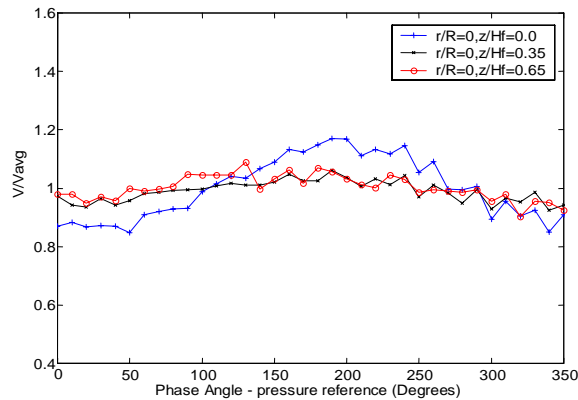


Figure 10.23: Axial velocity, normalized by nozzle exit mean axial velocity, measured along the centerline in the pre-combustion flow for Self-Excited flame.

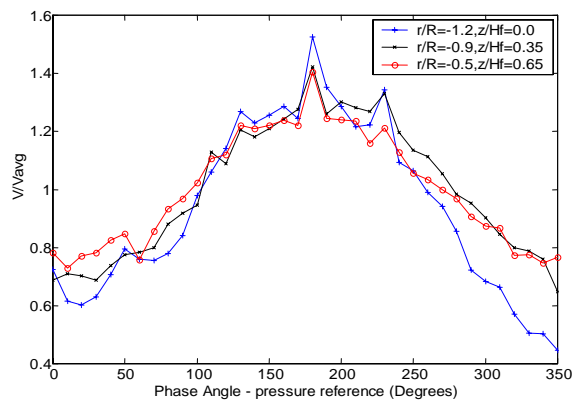


Figure 10.23: Axial velocity, normalized by nozzle exit mean axial velocity, measured at off axis locations in the product flow for Self-Excited flame.

The PIV results of Figures 10.15 – 10.18 indicate a wake region that forms not only downstream of the flame tip, but also along the sides of the flame (Figure 10.15(a)). As PIV has not been performed in oscillating flames, these wake regions have not previously been observed. The flame, anchored at the nozzle exit, propagates upstream and downstream in response to the acoustic velocity which is highest at the base of the flame. As discussed earlier, the flow normal to the flame surface increases due to the volume expansion, thus as the flame surface varies in response to the reactant flow so too does the product flow forming the wake regions observed in Figures 10.15 and 10.17. However, unlike the acoustic disturbance in the reactant flow that has greatly diminished by $z/H_f = 0.65$, Table 10.1 and Figures 10.23-10.24 indicate that the perturbations in the product flow are actually amplified by the volume expansion across the flame surface and persist much further downstream. Figures 10.23 and 10.24 are plots of the rms velocity measured along the centerline in the reactant flow (Figure 10.23) and at radial locations downstream of the flame surface in the product flow (Figure 10.24) but along the same axial plane as indicated on Figure 10.22. Figures 10.23 and 10.24 are plotted along the same y-axis scale which clearly shows that the amplified acoustic response of the product flow is maintained downstream in comparison to the disturbance that quickly decays in the reactant flow.

Although additional analysis in the area is needed as it was not the main focus of this study, one could speculate that the downstream deformations of the flame surface may primarily be the result of the amplified acoustic disturbance in the product flow. This differs from conventional practices in which flame response models aimed at predicting the heat release rate are based solely on a uniform acoustic disturbance in the upstream reactant flow. Based on the preliminary results from this study, this methodology may lead to under-predicting the deformations in the flame surface as the persistent flame amplified product flow acoustic disturbance is not taken into consideration. However, as this phenomenon was not the main focus of this study, additional analysis is necessary to further understand this effect on the heat release rate from the flame.

10.2.4 Unstable, Oscillating Flames: Near-Field Acoustics

The axial velocity perturbation v' measured at various locations along the centerline over one oscillation period are given for the self-excited and acoustically-forced flames in Figures 10.25 and 10.26, respectively. In both cases, the normalized axial rms component is a maximum near the base of the flame with $v'_{\text{self}}/V_0 = 0.14$ and $v'_{\text{forced}}/V_0 = 0.17$, and begins to decay as the flow proceeds

downstream. Comparing the traces it is apparent that the velocity oscillations are in phase at each axial location. The data shown here for the moderately high frequency of $f_{\text{ex}} = 230$ Hz ($H_f/\lambda = 0.02$) for both the self-excited and acoustically-forced cases is in agreement with the results shown by Bourehla and Baillot¹⁵ which indicated that at higher frequencies v' becomes independent of the mean flow and depends only on acoustics, thus the celerity or phase speed of the disturbance would be equal to zero. Preliminary data not shown here indicated a varying wave speed along the centerline for relatively low frequency excitations ($f_{\text{ex}} = 75$ Hz) in which $H_f/\lambda = 0.006$.

The amplitude of the axial-acoustic wave decays beyond the step expansion of the nozzle exit from $v'_{\text{self}} = 0.14$ and $v'_{\text{forc}} = 0.17$ to a minimum amplitude of $v'_{\text{self}} = 0.091$ and $v'_{\text{forc}} = 0.065$ at $z/H_f = 0.55$ (Figure 10.21). This is a reduction of 35% and 62% in the axial-acoustic velocity amplitude, respectively, while there was little change in the mean flow over the same distance. As previously mentioned, modeling efforts assumed the acoustic disturbance to be uniform through the cold flow region.

The radial perturbation (u') was also measured at the off-axis positions identified in Table 10.2 and shown in Figure 10.27. Given that the radial acoustic component increased away from the centerline, the locations of the sampling points were chosen to minimize the influence from the flame. A graph demonstrating the same in-phase sinusoidal behavior as the axial acoustic velocity is given by Figure 10.28 and 10.29, and affirms the acoustic description of the radial velocity perturbation. Figure 10.30 presents the ratio of the radial perturbation velocity to the centerline axial perturbation velocity with the experimental data showing that the magnitude of u' is comparable with v' even at 50% of the flame height.

Figure 10.30 provides experimental evidence of the radial acoustic velocity at the base of the flame and agrees quite well with the theoretical results proposed by Lee and Leiuwen⁶⁸. The amplitude of the radial disturbance, along with the agreement in phase with the axial disturbance, suggests that its neglect in models such as Fleifil et. al³⁹ and Ducroix³³ could contribute to inconsistencies experienced when compared to experimental results. The next step in this analysis would be to include two-dimensional acoustic effects in Fleifil's model in order to improve its prediction in the near-field.

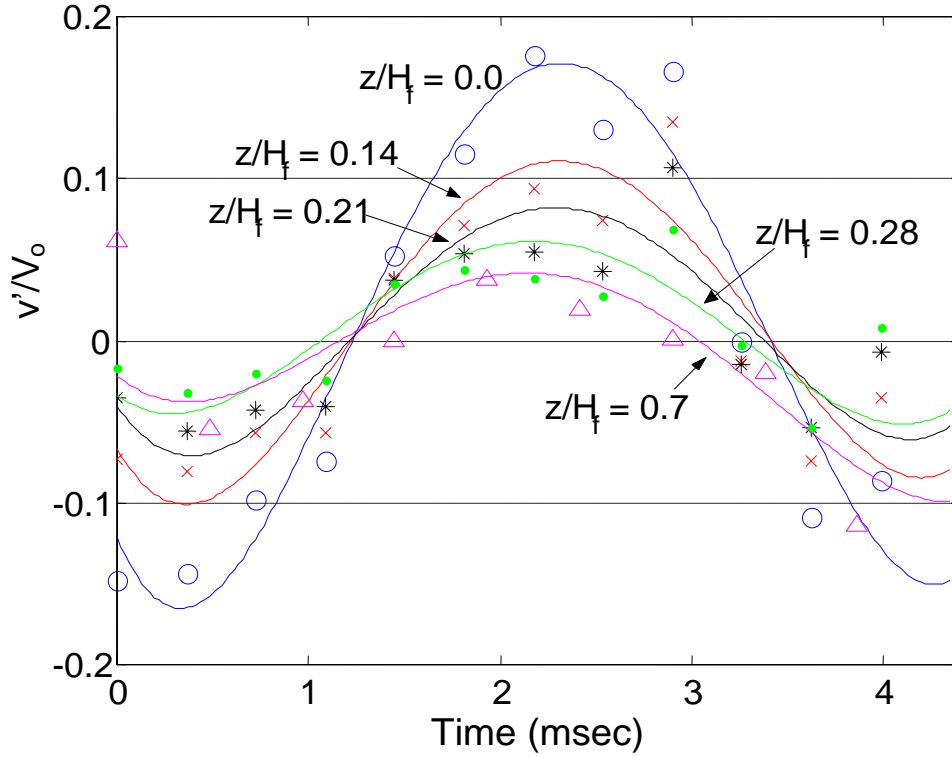


Figure 10.25: Normalized axial acoustic velocity component, v'/V_{mean} , for self-excited flame measured along the centerline at axial distances indicated by z/H_f .

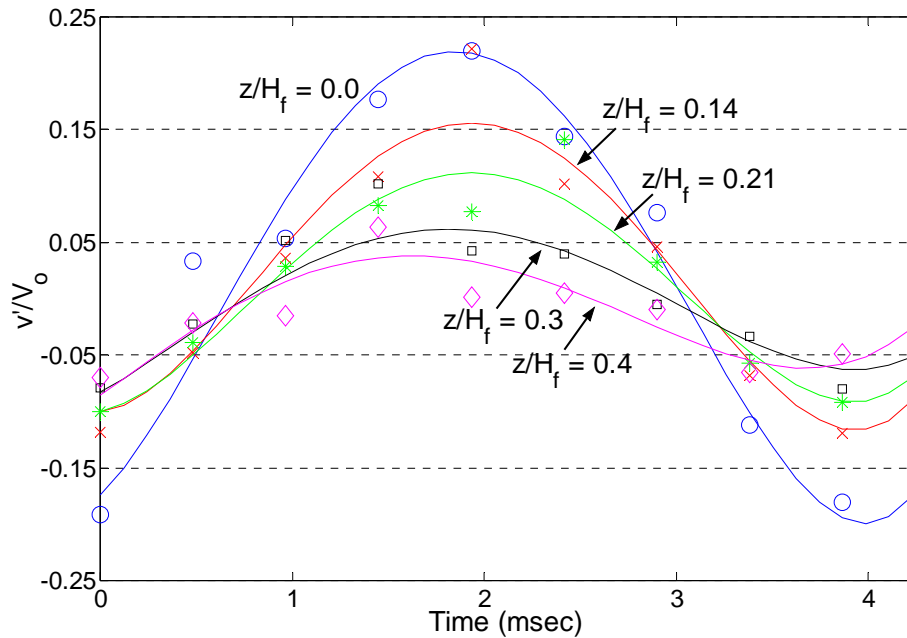


Figure 10.26: Normalized axial acoustic velocity component, v'/V_{mean} , for acoustically-forced flame measured along the centerline at axial distances indicated by z/H_f .

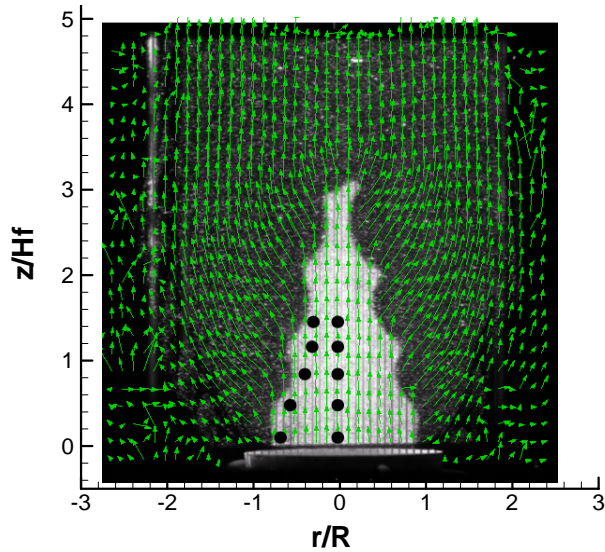


Figure 10.27. Seeded oscillating flame, black dots indicate the positions referenced in Table 2.

Table 10.2
Sample locations within the pre-flame region corresponding to PIV images (Fig.3).

Outboard Location	Centerline
$r/R = -0.65, z/H_f = 0$	$z/H_f = 0$
$r/R = -0.46, z/H_f = 0.14$	$z/H_f = 0.14$
$r/R = -0.4, z/H_f = 0.27$	$z/H_f = 0.27$
$r/R = -0.28, z/H_f = 0.40$	$z/H_f = 0.40$
$r/R = -0.28, z/H_f = 0.54$	$z/H_f = 0.54$

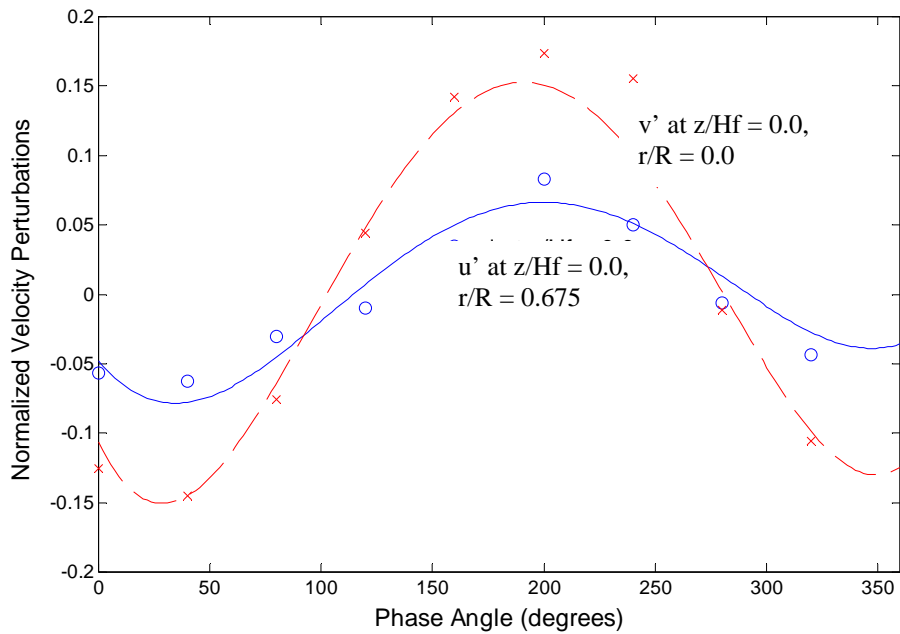


Figure 10.28: Plots of radial, u' , and axial acoustic velocities, v' , measured at the burner nozzle exit for the Self-Excited flame. Axial component measured along the centerline and radial acoustic velocity measured off axis within the pre-combustion region.

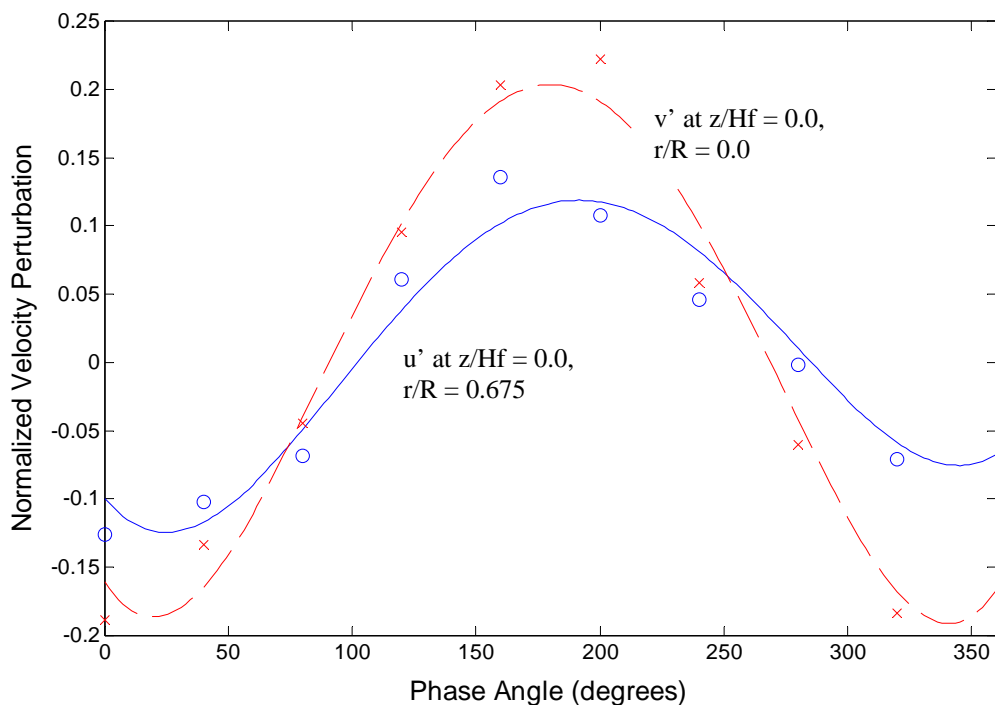


Figure 10.29: Plots of radial, u' , and axial acoustic velocities, v' , measured at the burner nozzle exit for the acoustically-forced flame. Axial component measured along the centerline and radial acoustic velocity measured off axis within the pre-combustion region.

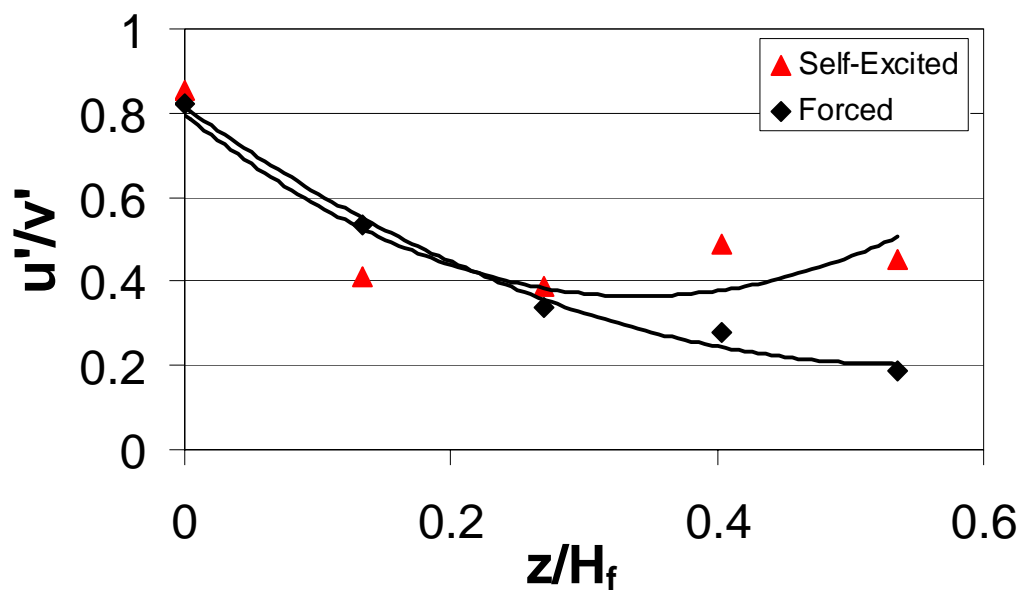


Figure 10.30: Axial dependence of the ratio of the radial to centerline axial velocity perturbations measured in self-excited and acoustically-forced flames. Solid lines are polynomial fits of actual data indicated by symbols.

Chapter 11 Conclusions and Recommendations

11.1 Summary and Conclusions

The land-based turbine industry has made considerable progress in the reduction of NO_x emissions through the use of various technologies such as lean-premixed (LPM) combustion. Unfortunately, LPM combustion is susceptible to thermoacoustic instabilities which can degrade engine and emission performance and can even prove to be destructive to the engine and its components. Although advancements have been made in the mitigation and control of these unwanted dynamics, dealing with their presence continues to cost turbine manufacturers millions of dollars each year. Problems with combustion instabilities is expected to worsen as turbines begin to increase utilization of Liquefied Natural Gas (LNG) and coal-derived syngas, both of which may have variable fuel properties.

The intent of this study was to provide a simplified experimental platform in order to isolate individual mechanisms that may be responsible for driving thermoacoustic instabilities so as to further our fundamental understanding of the problem. Significant findings were noted in each section and are summarized here.

The Rijke tube combustor utilized for this study provided the necessary acoustic boundaries in order for the flame to experience self-excited thermoacoustic instabilities. The combustor offered a unique opportunity to study the flame under various degrees of stability ranging from stable to self-excited to acoustically-forced. The flame proved to be inherently unstable over much of its operating range and with only an incremental change in the equivalence ratio the flame transitioned from unstable to stable resulting in significant changes in the phase-gain relationships between the acoustic pressure and velocity and the variable heat release rate. This emphasizes the need to understand the coupling process between the acoustics and heat release as only slight variations in operating conditions (possibly due to variable fuel properties) can activate a dynamic instability.

Periodic disturbances in the heat release rate are thought to primarily result from variations in the flame surface area brought on by velocity oscillations due to the systems acoustic response. Theoretical analysis by Fliefel et al³⁹ and Blackshear⁷ supported this hypothesis, however experimental findings have not previously been available. Utilizing flame chemiluminescence recorded on high speed media it was possible to experimentally evaluate variations in the flame surface area of an inherently unstable flame at various equivalence ratios and flow rates. Comparison of the time-averaged results suggested that the mean flame surface area from unstable flames is slightly larger

than that of stable flames, however the time-averaged height of the unstable flame was slightly less. This implies that the significant differences in response are occurring at the sides of the flame and not the tip as offered by Bourehla and Baillot¹⁵ and Baillot et al⁶. Experimental results of the gain between the flame surface area and heat release indicated that at low amplitudes of instability there is a linearly increasing relationship between these parameters however at higher amplitudes of the instability perturbations in the flame surface area saturate while the amplitude of the heat release rate variations continues to rise. The Fliefil et al³⁹ model, in addition to not capturing this nonlinear behavior, under predicted the gain and phase response between the heat release and flame surface area. The phase relationship between the heat release and flame surface area appeared to agree qualitatively with the findings of Blackshear⁷ who suggested a dependence of this relationship on flame speed. Fliefil et al³⁹'s assumption of a constant flame speed may be the source of the discrepancy at higher amplitude instabilities as the assumption does not take variable flame stretch along the flame surface into consideration.

Prediction of thermoacoustic instabilities in gas turbine engines is dependent on the derivation of accurate flame transfer functions. Experimental methods such as open-loop acoustic-forcing is often employed to generate simple n-port models that define the flame transfer function, however there is some concern as to if this practice leads to the development of a valid model that can be used to predict closed-loop stability in a reduced-order model. The unique design of the Rijke tube combustor used for this study provided the ability to operate under conditions of self-excited flame or acoustically-forcing a stable flame. Although the burner in its baseline configuration was inherently unstable, stable flame operation was made possible by slightly altering the nozzle geometry well upstream of the flame, and thus flow dynamics leading into the flame were unaltered. The geometry modification, made by replacing a rigid boundary at the base of the nozzle with an in-line speaker, altered the acoustic impedance within the tube which helped stabilize the flame.

Comparisons between the self-excited and acoustically-driven flame at various amplitudes of acoustic intensity provide an opportunity to study the phase-gain relationship between heat release and acoustic velocity in both modes. The amplitude of the self-excited flame response is completely dependent upon the thermoacoustic feedback mechanism of the overall burner – flame system, while for the acoustically-driven flames the amplitude of the disturbance is based on open-loop forcing and was varied by increasing or decreasing the input power to the in-line loudspeaker. The addition of the speaker at the base of the nozzle alters its acoustic characteristics allowing the inherently unstable flame to become stable. This method is

often utilized to develop reduced-order models describing the response of the flame to an acoustic disturbance there was a desire to evaluate the difference in response between the open-loop forcing and closed-loop feedback.

Gain and phase response from the unstable flame differed depending upon the method of excitation. The self-excited flame exhibited a sharp change in gain at the lean and rich stability boundaries although the phase angle difference between the acoustic pressure and heat release remained relatively constant having only a slight increase with equivalence ratio. The phase angle difference between the acoustic velocity and heat release rate displayed a similar trend although expanding over a greater range. At relatively low amplitudes neither the acoustic pressure nor the acoustic velocity from the acoustically-forced flame appeared to exhibit much change with equivalence ratio, however there was a change in sign of the $p'-q'$ phase angle at the equivalence ratio corresponding to the peak self-excited instability. The $v'-q'$ phase angle difference did show some influence from equivalence ratio as the quantity converged to the same phase angle difference as the self-excited flame at the equivalence ratio corresponding to the peak instability. However, during lean operation the $v'-q'$ phase angle difference of the acoustically-forced flame was considerably different than that of the self-excited case. Thus the difference in the lean results may be an indication of multi-dimensional near-field acoustics or a change in the acoustic impedance. This would suggest that an empirically derived transfer function obtained by acoustically-forcing a flame with an acoustic disturbance may not be capable of predicting the onset of combustion instabilities over some portion of the operating range, and thus indicating that one-port models can not capture the true essence of the coupling process between acoustics and perturbations in the heat release rate.

Utilizing dense flow seeding, time resolved measurements from self-excited and acoustically-forced flames under varying intensity provided velocity field information in both the cold and hot flow regimes. By obtaining velocity field measurements in both the non-reacting and reacting flows permitted the detection of the volume expansion, or flow dilatation, due to the temperature difference across the flame surface which provided an excellent means of identifying the instantaneous surface of a flame subject to an instability.

Although the effects of flame stretch were not explicitly discussed in this study, altering regions of positive (convex - with the flame surface collapsing towards reactants) and negative (concave - with the flame surface expanding from the reactants) stretch that forms along the

flame front subsequently produce perturbations in the flame surface area and additionally force variations in the near-field and post flame flows. These flow field variations may periodically alter the heat release emitted from the flame and account for the phase discrepancies that exist between the flame surface area or velocity perturbations at the nozzle exit and the heat release rate. This study is the first to propose that the local flame structure must be accounted for in order to accurately describe the phase response, and additional study of this phenomenon is needed in order to obtain quantitative results.

The time resolved data acquisition permitted the identification of the acoustic velocity throughout the flow field. Measurements made in the hot product flow indicated an axial acoustic velocity of much higher amplitude and much longer lived than in the pre-flame flow. Oscillations in the post-flame velocity field resulting from perturbations in the volume expansion across an oscillating flame surface may help to drive variations in the surface as the flame progresses downstream of the nozzle. The resulting variations along the flame surface may in turn produce the aforementioned regions of variable flame stretch that may contribute to perturbations in the heat release rate from the flame. Neither of these concepts have previously been include in dynamic models of thermoacoustic systems and may account for some of the discrepancy that exist in predicting the gain and phase relationship between a variable heat release rate and its suspected mechanisms.

A final concept that has historically been neglected in reduced-order models of thermoacoustic flame instabilities is the effect of multi-dimensional acoustic velocities in the near-field region of the flame. Recent experimental and theoretical studies reviewed in the text have discussed the presence of evanescent acoustic waves in the near-field. Through the use of time-resolved PIV the radial velocity at the base of the flame in the near-field was measured and found to agree quite well with the theoretical results proposed by Lee and Leiuwen⁶⁸. The amplitude of the radial disturbance, which was found to be comparable in magnitude and have agreement in phase with the axial centerline acoustic velocity, suggests that its neglect in models such as Fleifil et. al³⁹ and Ducroix³³ could contribute to inconsistencies experienced when compared to experimental results. The next step in this analysis would be to include two-dimensional acoustic effects in Fleifil's model in order to improve its prediction in the near-field.

11.2 Recommendations for Future Work

The research effort described in this dissertation was focused on providing an experimental evaluation of theoretical predictions regarding the contribution of various heat release mechanisms to

driving combustion instabilities in laminar, premixed methane-air flames. During the course of this study, a number of topics were uncovered that could help to further our fundamental understanding of thermoacoustic instabilities. Due to the need to limit this analysis these areas were left for future studies with a brief discussion of these topics provided below.

11.2.1 Evaluation of marginal stability boundary

Analysis of the self-excited flame at various equivalence ratio revealed a very sharp transition between stable and unstable flame with the definition of stable being no measurable disturbance above the random noise. This sharp transition occurred under both lean ($\phi = 0.68$) and slightly beyond stoichiometric ($\phi = 1.1$) conditions, however due to the partial-premixed nature of the flame operating slightly richer than stoichiometric this condition is not directly applicable to the study of fully premixed flames.

Operating the Rijke tube combustor at an equivalence ratio of $\phi = 0.7$, the flame exhibited a noticeable instability with an acoustic pressure peak of approximately $P_{\text{amp}} = 38$ dB at $f_{\text{ex}} = 224$ Hz. Decreasing the equivalence ratio to $\phi = 0.68$ while maintaining a constant flow rate resulted in a reduction of the peak acoustic pressure to $P_{\text{amp}} = 5$ dB (also at $f_{\text{ex}} = 224$ Hz). This decrease was much greater than experienced at any other as the equivalence ratio was swept from $\phi = 0.6 - 1.1$. Accompanying this sharp decline in magnitude was a significant difference in the trend of the phase angle difference between pressure and heat release rate with changes in equivalence ratio. Over most of the range of equivalence ratios tested, the flame was inherently unstable and the phase angle difference between the pressure and heat release rate ranged from $\Theta_{\text{p-q}} = 0^\circ - 35^\circ$. However, as the flame transitions from unstable ($\phi = 0.7$) to marginally stable ($\phi = 0.68$) there was a drastic change in the phase angle difference from $\Theta_{\text{p-q},\phi=0.7} \approx 20^\circ$ at $V_{\text{mean}} = 1.54$ m/sec to $\Theta_{\text{p-q},\phi=0.68} \approx 230^\circ$ at $f_{\text{ex}} = 224$ Hz and $V_{\text{mean}} = 1.54$ m/sec. Further reduction in equivalence ratio to $\phi = 0.6$ resulted in a phase difference of $\Theta_{\text{p-q},\phi=0.6} \approx 150^\circ$.

The specific cause of the sharp transition in both gain and phase at the stability boundary for the burner utilized in this study has yet to be determined. In actuality the source identification of this phenomenon may provide significant insight into the pressure-heat release coupling process required to drive thermoacoustic instabilities. Thus there is a “burning” need to continue this investigation.

11.2.2 Further investigate of periodic variations in the flame structure (flame stretch)

Through the use of the time-resolved PIV measurements obtained simultaneously in both the cold, reactant flow and the hot, product gases the volume expansion (flow dilatation) across the flame surface was obtained at various location during periods of instability. Previous research has correlated steep gradients in flow dilatation measured in reacting flows with the presence of the flame surface or primary heat release.

Limited analysis of the results presented in this study revealed some periodic variations in the peak heat release along the flame surface with minimum and maximum dilatation occurring in regions susceptible to positive and negative flame stretch, respectively. These heat release variations along the flame surface may account for disparities observed in the phase / gain relationship between the acoustic velocity and variable heat release rate and warrant further analysis.

In addition, preliminary indications exist that the cusps along the flame surface alter the post-flame, product flow in an oscillatory manner that may in fact exacerbate undulations in the flame surface after the evanescent acoustic wave has decayed in the pre-flame flow. Obtaining phase-resolved PIV at a number of additional flow rates and equivalence ratios may provide the necessary data to obtain conclusive results on this matter.

11.2.3 Variable fuel prosperities to simulate LNG and coal-derived syngas

The small change in equivalence ratio that resulted in the flame transitioning from stable to unstable operation emphasizes the need to better understand the effects of variable fuel properties on combustion instabilities. The demand for LNG and coal derived syngas fuels is on the rise, however as these fuels are susceptible to variations in their composition there is a real danger of instabilities appearing in what had previously been a quietly operating turbine. Thus there is a need to quantify an acceptable variance in fuel composition for LNG and syngas applications. Analysis may show a much different transition from stable to unstable as shown at the stability boundary of the methane-air flame of this study; however the possibility for more severe dynamics does exist.

References

1. Abom, M., "A Note on the Experimental Determination of Acoustical Two-Port Matrices", *J. Sound Vib.*, 155: 185-188, 1992.
2. Adrian, R.J., "Limiting Resolution of Particle Image Velocimetry for Turbulent Flow", *Adv. In Turb. Res.*, pp 1-19, 1995.
3. Adrian, R.J., "Dynamic Ranges of Velocity and Spatial Resolution of Particle Image Velocimetry", *Meas. Sci. Technol.*, 8, pp1393-1398, 1997.
4. Adrian, R.J., "Uses, Analysis and Interpretation of PIV Data", *30th AIAA Fluid Dynamics Conference*, AIAA-99-3753, 1999
5. Baade, P.K., "Design Criteria and Models for Preventing combustion Oscillations", *ASHRAE Symposium on Combustion Driven Oscillations*, Atlanta, GA, 1979.
6. Baillot, F., Bourehla, A., and Durox, D., "The Characteristics Method and Cusped Flame Fronts", *Combust. Sci. and Tech.*, 112: 327-350, 1996.
7. Baillot, F., Durox, D., and Prud'Homme, R., "Experimental and Theoretical Study of a Premixed Vibrating Flame", *Combustion and Flame*, 88: 149-168, 1992.
8. Barrere, M., and Williams, F.A., "Comparison of Combustion Instabilities found in Various Types of Combustion Chambers", pp 169-181, 1968.
9. Becker, K.H., Kley, D., Norstrom, R.J., "OH* Chemiluminescence in Hydrocarbon Atom Flames", *Fourteenth Symposium (International) on Combustion*, pp. 405-411, 1977.
10. Beer, J.M., "Clean Combustion in Gas Turbines: challenges and technical responses – a review", *J. Inst. Energy*, V 68, pp 2-10, March 1995.
11. Blackshear, P.L., "Driving Standing Waves by Heat Addition", *Fourth Symposium (International) on Combustion*, pp 553-566, The Williams and Wilkins Co., Baltimore, 1952.
12. Boden, H. and Abom, M., "Modelling of Fluid Machines as Sources of Sound in Duct and Pipe Systems", *Acta Acustica*, 3: 549-560, 1995.
13. Bolinder, J., "On the Accuracy of a Digital Image Velocimetry System", Technical Report: ISSN 0282-1990, Lund Institute of Technology, Dept. of Heat and Power Eng., 1999.
14. Borghi, R., "Turbulent Combustion Modelling", *Prog. Energy Combust. Sci.*, 14, pp. 245-292, 1988.
15. Bourehla, A. and Baillot, F., "Appearance and Stability of a Laminar Conical Premixed Flame Subjected to an Acoustic Perturbation", *Combustion and Flame*, 144:303-318, 1998.
16. Candel, S., "Combustion Instabilities Coupled by Pressure Waves and Their Active Control", *Twenty-Fourth Symposium (International) on Combustion*, pp. 1277-1296, 1992.
17. Carrier, G.F., "The Mechanics of the Rijke Tube", *Q. Appl. Math*, 12, pp. 383-395, 1955.
18. Christensen, K. T., Soloff, S. M. & Adrian, R. J., "PIV Sleuth -Integrated Particle Image Velocimetry Interrogation/Validation Software", TAM Report No. 943, University of Illinois at Urbana-Champaign, 2000.
19. Choi, C. and Puri, I., "Response of Flame Speed to Positively and Negatively Curved Premixed Flames", Tech. Mtg. Central States Combust. Instit., 2002.
20. Chu, B.T., "Stability of Systems Containing a Heat Source – The Rayleigh Criteria", NACA RM 56D27, 1956.
21. Cheng, J. and Blaser, D., "Transfer Function Method of Measuring In-Duct Acoustic Properties", *J. Acoust. Soc. Am.*, 68(3): 907-913, 1980.
22. Crocco, L., "Aspects of Combustion Stability in Liquid Rocket Motors", *J. Am. Roc. Soc.*, Part 1: V 21, p. 163, Nov-Dec 1951; Part 2: V 22, p. 7, Jan-Feb 1952.
23. Crocco, L., Grey, J., Harrje, D.T., "Theory of Liquid Propellant Rocket Combustion Instability and Its Experimental Verification", *Am. Rocket Soc. J.*, 30, pp 159-168, 1960.

24. Crocco, L. and Mitchell, C.E., "Nonlinear Periodic Oscillations in Rocket Motors with Distributed Combustion", *Combust. Sci. and Tech.*, 1, pp. 147-169, 1969.
25. Culick, F., "Stability of Longitudinal Oscillations with Pressure and Velocity Coupling on a Solid Propellant Rocket", *Combust. Sci. Tech.*, 2: 179-201, 1970.
26. Culick, F., "Non-Linear Growth and Limiting Amplitude of Acoustic Oscillations in Combustion Chambers", *Combust. Sci. Tech.*, 3: 1-16, 1971.
27. Culick, F., "A Note on Rayleigh's Criteria", *Comb. Sci. and Tech.*, V 56, pp 159-166, 1987.
28. Dandy, D. and Vosen, S., "Numerical and Experimental Studies of Hydroxyl Radical Chemiluminescence in Methane-Air Flames", *Combust. Sci. and Tech.*, 82, pp. 131-150, 1992.
29. Darling, D., Radhakrishnan, K., Oyediran, A., Cowan, E., "Combustion_Acoustic Stability Analysis for Premixed Gas Turbine Combustors", AIAA-95-2470, 1995.
30. Dowling, A.P., "Nonlinear Self-Excited Oscillations in a Ducted Flame", *J. Fluid Mech.*, V 346, pp271-290, 1997.
31. Dowling, A.P., "The Calculation of Thermoacoustic Oscillations", *J. Sound Vib.*, V 180, pp 557-581, 1995.
32. Driscoll, J., Sutkus, D., Roberts, W., Post, M., and Goss, L., "The Strain Exerted by a Vortex on a Flame-Determined from Velocity Field Images", *Combust. Sci. and Tech.*, 96: 213-229, 1994.
33. Ducruix, S., Durox, D., and Candel, S., "Theoretical and Experimental Determination of the Transfer Function of a Laminar Premixed Flame", *Twenty-Eighth Symposium (International) on Combustion*, pp. 765-773, 2000.
34. Durox, D., Baillet, F., Searby, G., and Boyer, L., "On the Shape of Flames Under Strong Acoustic Forcing: a Mean Flow Controlled by an Oscillating Flow", *J. Fluid Mech.*, 350: 295-310, 1997.
35. Durox, D., Ducruix, S., and Candel, S., "Experiments on Collapsing Cylindrical Flames", *Combustion and Flame*, 125: 982-1000, 2001.
36. Echehki, T., and Mungal, M., "Flame Speed Measurements at the Tip of a Slot Burner: Effects of Flame Curvature and Hydrodynamic Stretch", *Twenty-Third Symp. (Intl.) Combust.*, The Combustion Institute, 455-461, 1990.
37. Edwards, C.H. and Penney, D., "Calculus and Analytic Geometry", Prentice-Hall, New Jersey, 1986.
38. Feldman, K.T., "Review of the Literature on Rijke Thermoacoustic Phenomena", *J. Sound Vib.*, 7, pp. 83-89, 1968.
39. Fleifil, M., Annaswamy, A.M., Ghoneim, Z.A., and Ghoniem, A.F., "Response of a Laminar Flame to Flow Oscillations: A Kinematic Model and Thermoacoustic Instability Results", *Combustion and Flame*, 106, pp. 487 – 510, 1996
40. Franklin, G.F., Powell, J.D. and Emami-Naeini, A., *Feedback Control on Dynamic Systems*, Addison-Wesley, New York, 1994.
41. Friedlander, M., Smith, T., Powell, A., "Experiments on the Rijke-Tube Phenomena", *J. Acoust. Soc. Am.*, 36, pp. 1737-1738, 1964.
42. Gaydon, A.G., and Wolfhard, H.G., *Flames-Their Structure, Radiation and Temperature*, Chapman and Hall, London, 1953.
43. Gentemann, A., Hirsch, C., Kunze, K., Kiesewetter, F., Sattelmayer, T., and Polifke, W., "Validation of Flame Transfer Function Reconstruction for Perfectly Premixed Swirl Flames", ASME, GT-2004-53776, 2004.
44. Gomez, A. and Rosner, D.E., "Thermophoretic Effects on Particles in Counterflow Laminar Diffusion Flames", *Combust. Sci. and Tech.*, 89, pp335-362, 1993.

45. Gutmark, E., Schadow, K.C., Sivasegaram, S., Whitelaw, J.H., "Interaction Between Fluid-Dynamic and Acoustic Instabilities in Combusting Flows Within Ducts", *Comb. Sci. and Tech.*, V 79, pp 161-166, 1991.
46. Haber, L., Vandsburger, U., Saunders, W.R., Khanna, V., "An Examination of the Relationship Between Chemiluminescent Light Emissions and Heat Release Rate Under Non-Adiabatic Conditions", ASME, 2000-GT-0121, 2000.
47. Harrije, D.T. and Reardon, F.H., *Liquid Propellant Rocket Combustion Instability*, NASA SP-194, 1971.
48. Higgins, B., "On the Sound Produced by a Current of Hydrogen Gas Passing Through a Tube", *J. Natural Philosophy, Chemistry and the Arts*, 1, pp 129-131, 1802.
49. Hobson, D.E., Fackrell, J.E., Hewitt, G., "Combustion Instabilities in Industrial Gas Turbines – Measurements on Operating Plant and Thermoacoustic Modeling", *Trans. ASME*, V 122, 2000.
50. Huang, H., Dabiri, D. and Gharib, M., "On Errors of Digital Particle Image Velocimetry", *Meas. Sci. Technol.*, 8, pp 1427-1440, 1997.
51. Hubbard and Dowling (2000)
52. Janus, M.C. and Richards, G.A., "A Model for Premixed Combustion Oscillations", Technical Note DOE/METC-96/1026, 1996.
53. Jarosinski, J., "The Thickness of Laminar Flames", *Combustion and Flame*, 56, pp. 337-342, 1984.
54. Johnson, M.R., Kostiuik, L.W., Cheng, R.K., "A Ring Stabilizer for Lean Premixed Turbulent Flames", *Combustion and Flame*, 114, pp. 594-596, 1998.
55. Kaskan, W.E., "An Investigation of Vibrating Flames", *Fourth Symposium (International) on Combustion*, pp 575-591, The Williams and Wilkins Co., Baltimore, 1952.
56. Keller, J.J., "Thermoacoustic Oscillations in Combustion Chambers of Gas Turbines", *AIAA Journal*, 33, 1995.
57. Keller, J.O. and Saito, K., "Measurements of the Combusting Flow in a Pulse Combustor", *Combust. Sci. and Tech.*, 53, pp. 137-163, 1987.
58. Khanna, V.K., "A Study of the Dynamics of Laminar and Turbulent Fully and Partially Premixed Flames", Ph.D. Thesis, VA Polytechnic Institute, 2001.
59. Khanna, V.K., Vandsburger, U., Saunders, W.R., and Baumann, W.T., "Measurement of Acoustic Velocity Fluctuations using the Two Microphone Technique", Technical Report VACCG-TR-002-2000, 2000.
60. Khanna, V.K., Vandsburger, U., Saunders, W.R., Baumann, W.T., and Hendricks, A.D., "Dynamic Analysis of Burner Stabilized Flames, Part 1: Laminar Premixed Flame", *AFRC International Symposium*, Newport Beach, CA, 2000.
61. Khanna, V.K., Vandsburger, U., Saunders, W.R., and Baumann, W.T., "Dynamic Analysis of Swirl Stabilized Turbulent Gaseous Flames", ASME, GT-2002-30061, 2002.
62. Kinsler, L., Frey, A., Coppens, A., and Sanders, J., *Fundamentals of Acoustics*, 3rd Ed., John Wiley and Sons, New York, 1982.
63. Konrad, W., Brehm, N., Kameier, F., Freeman, C., Day, I.J., "Combustion Instability Investigations on the BR710 Jet Engine", *Trans. ASME*, V 120, 1998.
64. Kruger, U., Huren, J., Hoffman, S., Krebs, W., Flohr, P., Bohn, D., "Prediction and Measurement of Thermoacoustic Improvements in Gas Turbines with Annular Combustion Systems", ASME, 2000-GT-0095, 2000.
65. Kruger, U., Huren, J., Hoffman, S., Krebs, W., Bohn, D., "Prediction of Thermoacoustic Instabilities with Focus on the Dynamic Flame Behavior for a 3A-Series Gas Turbine of Siemens KWU", ASME, 99-GT-111, 1999.

66. Lavrentjev, J., and Abom, M., "Characterization of Fluid Machines as Acoustic Multi-Port Sources", *J. Sound Vib.*, 197: 1-16, 1996.
67. Law, C.K., "Dynamics of Stretched Flames", *Twenty Second Symposium (International) on Combustion*, pp. 1381-1401, 1988.
68. Lee, D.H. and Lieuwen, T.C., "Acoustic Nearfield Characteristics of a Premixed Flame in a Longitudinal Acoustic Field", ASME, 2001-GT-0040, 2001.
69. Lee, S.Y., Seo, S., Broda, J.C., Pal, S. and Santoro, R.J., "an Experimental Estimation of Mean Reaction Rate and Flame Structure During Combustion Instability in a Lean Premixed Gas Turbine Combustor", *Twenty-Eighth Symposium (International) on Combustion*, pp. 775-782, 2000.
70. Lewis, B. and von Elbe, G., *Combustion, Flames and Explosions of Gases*, Academic Press, Inc., Orlando, FL, 3rd Ed., 1987.
71. Lieuwen, T., "Measurements of Incoherent Acoustic Wave Scattering from Turbulent Premixed Flames", *Proc. Comb. Inst.*, V 29, 2002.
72. Lieuwen, T., "Modeling Premixed Combustion – Acoustic Wave Interactions: A Review", *J. Propulsion and Power*, V 19, 2003.
73. Lieuwen, T. and Neumeier, Y., "Nonlinear Pressure-Heat Release Transfer Function Measurements in a Premixed Combustor", *Proc. Comb. Inst.*, 29, 2002.
74. Lieuwen, T., Torres, H., Johnson, C., Zinn, B.T., "A Mechanism of Combustion Instability in Lean-Premixed Gas Turbine Combustors", ASME, 99-GT-3, 1999.
75. Maling, G.C., "Simplified Analysis of the Rijke Phenomena", *J. Acoust. Soc. Am.*, 35, pp. 1058-1060, 1963.
76. Markstein, G.H., *Nonsteady Combustion Propagation*, Pergamon Press, Oxford, England, 1964.
77. Merk, H.J., "An Analysis of Unstable Combustion of Premixed Gases", *Sixth Symposium (International) on Combustion*, pp. 500-512, 1956.
78. Melling, A., "Tracer Particles and Seeding for Particle Image Velocimetry", *Meas. Sci. Technol.*, 8: 1406-1416, 1997.
79. Mitchell, C.E., "Analytical Models for combustion Instability", *Liquid Rocket Engine Combustion Instability*, V 169, AIAA, 1994.
80. Mongia, R., Dibble, R., Lovett, J., "Measurement of Air-Fuel Ratio Fluctuations Caused by Combustor Driven Oscillations", ASME, 98-GT-304, 1998.
81. Mueller, C., Driscoll, J., Reuss, D. and Drake, M., "Effects of Unsteady Stretch on the Strength of a Freely-Propagating Flame Wrinkled by a Vortex", *Twenty-Sixth Symposium (International) on Combustion*, Combustion Institute, 347-355, 1996.
82. Mugridge, B.D., "Combustion Driven Oscillations", *J. Sound Vib.*, 70, pp. 437-452, 1980.
83. Mungal, M.G., Lourenco, L.M., and Krothapalli, A., "Instantaneous Velocity Measurements in Laminar and Turbulent Premixed Flames Using On-Line PIV", *Combust. Sci. and Tech.*, 106, pp. 239-265, 1995.
84. Munjal, M.L., *Acoustics of Ducts and Mufflers*, Wiley-Interscience, New York, 1987.
85. Najm, H., Paul, P., Mueller, C., Wyckoff, P., "On the Adequacy of Certain Experimental Observables as Measurements of Flame Burning Rate", *Combustion and Flame*, 113, pp. 312-332, 1998.
86. Najm, H., Kino, O.M., Paul, P., Wyckoff, P., "A Study of Flame Observables in Premixed Methane – Air Flames", *Combust. Sci. and Tech.*, 140, pp. 369-403, 1998.
87. Neuringer, J.L. and Hudson, G.E., "An Investigation of Sound Vibrations in a Tube Containing a Heat Source", *J. Acoust. Soc. Am.*, 24, pp 667-674, Nov. 1952.
88. Oran, E. and Gardner, J., "Chemical-Acoustic Interactions in Combustion Systems", *Prog. Energy Combust. Sci.*, 11, pp. 253-276, 1985.

89. Otsuka, T. and Wolanski, P., "Particle Image Velocimetry (PIV) Analysis of Flame Structure", *J. Loss Prevention in the Process Industries*, V 14, pp 503-507, 2001.
90. Paschereit, C.O., Gutmark, E., Weisenstein, W., "Structure and Control of Thermoacoustic Instabilities in a Gas-Turbine Combustor", *Combust. Sci. and Tech.*, 138, 213-232, 1998.
91. Paschereit, C.O., Gutmark, E., Weisenstein, W., "Control of Combustion Driven Oscillations by Equivalence Ratio Modulations", ASME, 1999.
92. Paschereit, C.O. and Polifke, W., "Investigation of the Thermoacoustic Characteristics of a Lean Premixed Gas Turbine Burner", ASME, 98-GT-582, 1998.
93. Paschereit, C.O., Schuermans, B., Polifke, W., and Mattson, O., "Measurement of Transfer Matrices and Source Terms of Premixed Flames", ASME, 99-GT-133, 1999.
94. Paul, P.H. and Najm, H.N., "Planar Laser-Induced Fluorescence Imaging of Flame Heat Release Rate", *Twenty-Seventh Symposium (International) on Combustion*, pp. 43-50, 1998.
95. Peracchio, A.A. and Proscia, W.M., "Nonlinear Heat-Release / Acoustic Model for Thermoacoustic Instability in Lean Premixed Combustors", ASME, 98-GT-269, 1998.
96. Poinot, T., Echekki, T., and Mungal, M., "A Study of the Laminar Flame Tip and Implications for Premixed Turbulent Combustion", *Combust. Sci. and Tech.*, 81: 45-73, 1992.
97. Poinot, T., Trounev, A., Veynante, D., Candel, S., Esposito, E., "Vortex-Driven Acoustically Coupled Combustion Instabilities", *J. Fluid Mech.*, 177, pp. 265-292, 1987.
98. Preetham and Lieuwen, T., "Nonlinear Flame-Flow Transfer Function Calculations: Flow Disturbance Celerity Effects", Fortieth AIAA/ASME/SAE/ASEE Joint Propulsion Conference, AIAA 2004-4035, 2004.
99. Putnam, A.A., and Dennis, W.R., "Organ-Pipe Oscillations in a Flame-Filled Tube", *Fourth Symposium (International) on Combustion*, pp 566-575, The Williams and Wilkins Co., Baltimore, 1952.
100. Putnam, A.A., and Dennis, W.R., "A Study of Burner Oscillations of the Organ-Pipe Type", *Trans. ASME*, 75, pp 15-28, 1953.
101. Putnam, A.A., and Dennis, W.R., "A Survey of Organ-Pipe Oscillations in Combustion Systems", *J. Acoust. Soc. Am.*, 28, p 246, 1956.
102. Putnam, A. A. *Combustion Driven Oscillations in Industry*, American Elsevier Publishing, New York, NY (1971).
103. Raffel, M., Willert, C., and Kompenhans, J., *Particle Image Velocimetry: A Practical Guide*, pp 3-8, Springer-Verlag, Berlin, 1998.
104. Rayleigh, J.W.S., *The Theory of Sound*, 2, p. 226, Dover, New York, 1945.
105. Reuss, D.L., Adrian, R.J., and Landreth, C.C., "Two-Dimensional Velocity Measurements in Laminar Flame Using Particle Image Velocimetry", *Combust. Sci. and Tech.*, 67, pp. 73-83, 1989.
106. Reuss, D.L., Adrian, R.J., Landreth, C.C., French, D.T. and Fansler, T.D., "Instantaneous Planar Measurements of Velocity and Large-Scale Vorticity and Strain Rate in an Engine Using Particle-Image Velocimetry", SAE 890616, 1989.
107. Richards, G.A. and Janus, M.C., "Characterization of Oscillations During Premix Gas Turbine Combustion", ASME International Gas Turbine and Aeroengine Congress and Exhibition, Orlando, FL, June 1997, 97-GT-244.
108. Richards, G.A. and Robey, E.H., "Dynamic Response of Premix Fuel Injector", ASME TurboExpo Land, Sea, Air 2001, New Orleans, LA, June 2001, 2001-GT-XXX.
109. Rijke, P.L., "Notice of a New Method of Causing a Vibration of the Air Contained in a Tube Open at Both Ends", *Phil. Mag.*, 17, pp. 419-422, 1859.
110. Samaniego, J.M., Egolfopoulos, F.N., and Bowman, C.T., "CO₂* Chemiluminescence in Premixed Flames", *Combust. Sci. and Tech.*, 109, pp. 183-203, 1995.

111. Schadow, K.C., Gutmark, E., Parr, T.P., Parr, D.M., Wilson, K.J., and Crump, J.E., "Large-Scale Coherent Structures as Drivers of Combustion Instability", *Combust. Sci. and Tech.*, 64, pp. 167-186, 1989.
112. Schadow, K.C. and Gutmark, E., "Combustion Instability Related to Vortex Shedding in Dump Combustors and Their Passive Control", *Prog. Energy Combust. Sci.*, 18, pp. 117-132, 1992.
113. Scholtz, M.H. and Dipietro, S.M., "Field-Experience on DLN Typhoon Industrial Gas Turbine", ASME, 97-GT-61, 1997.
114. Schuermans, B., Polifke, W., and Paschereit, C.O., "Modeling Transfer Matrices of Premixed Flames and Comparison with Experimental Results", ASME, 99-GT-132, 1999.
115. Shih, W.P., Lee, J., Santavicca, D.A., "Stability and Emissions Characteristics of a Lean Premixed Gas Turbine Combustor", *Twenty-Sixth Symposium (International) on Combustion*, 1996.
116. Sinibaldi, J., Driscall, J., Mueller, C., Donbar, J., Carter, C., "Propagation Speeds and Stretch Rates Measured Along Wrinkled Flames to Assess the Theory of Flame Stretch", *Combustion and Flame*, 133: 323-334, 2003.
117. Spenik, J.L., "An experimental investigation of particle motion in pulsating turbulent pipe flow", MS Thesis, West Virginia University, 1989.
118. Sung, C.J., Law, C.K. and Axelbaum, R.L., "Thermophoretic Effects on Seeding Particles in LDV Measurements of Flames", *Combust. Sci. and Tech.*, 99, pp. 119-132, 1994.
119. Sung, C.J., Kistler, J.S., Nishioka, M. and Law, C.K., "Further Studies on Effects of Thermophoresis on Seeding Particles in LDV Measurements of Strained Flames", *Combustion and Flame*, 105, pp. 189-201, 1996.
120. Turns, S.R., *An Introduction to Combustion*, McGraw-Hill, Inc., New York, 1996.
121. Wagner, T.C. and Ferguson, C.R., "Bunsen Flame Hydrodynamics", *Combustion and Flame*, 59, pp. 267-272, 1985.
122. Westerweel, J., "Fundamentals of Digital Particle Image Velocimetry", *Meas. Sci. Technol.*, 8, pp. 1379-1392, 1997.
123. Williams, F., *Combustion Theory*, Perseus Books, Massachusetts, 2nd Ed., 1985.
124. Yoon, H.G., Peddieson, J. and Purdy, K.R., "Mathematical Modeling of a Generalized Rijke Tube", *Intl. J. Eng. Sci.*, 36, pp 1235-1264, 1998.